MEASUREMENT AND MODELING OF SOOT FORMATION AND DEPOSITION IN FUEL RICH HIGH PRESSURE KEROSENE COMBUSTION

by

Rufat F. Kulakhmetov

A Dissertation

Submitted to the Faculty of Purdue University

In Partial Fulfillment of the Requirements for the degree of

Doctor of Philosophy

School of Aeronautics and Astronautics

West Lafayette, Indiana

December 2020

THE PURDUE UNIVERSITY GRADUATE SCHOOL

STATEMENT OF COMMITTEE APPROVAL

Dr. Timothée L. Pourpoint, Chair

School of Aeronautics and Astronautics

Dr. Stephen D. Heister

School of Aeronautics and Astronautics

Dr. Terrence R. Meyer

School of Mechanical Engineering

Dr. Ananda Himansu

Air Force Research Laboratory, Edwards AFB

Dr. Ranjan S. Mehta

CFD Research Corporation

Approved by:

Dr. Gregory A. Blaisdell

To my family, friends, educators and mentors who've supported me throughout my pursuits

ACKNOWLEDGMENTS

First and foremost, I would like to thank my advisor Dr. Timothée Pourpoint for originally taking me on as master's student and providing me with an opportunity to work on exciting experimental research at the Zucrow Laboratories. This work would not have been possible without his support and guidance. I would also like to thank my committee: Dr. Stephen Heister, Dr. Ananda Himansu, Dr. Ranjan Mehta and Dr. Terrance Meyer for the valuable discussions that helped guide my approach towards understanding soot formation and deposition at rocket engine environments. I would specifically like to thank Dr. Ranjan Mehta for the extremely valuable discussion on how to model soot and for his suggestion and guidance with incorporating the Method of Moments with Interpolative Closure to the plug flow reactor model.

I would also like to thank the NASA Space Technology Research Fellowship and my NASA Collaborator Sandra Greene for supporting my work and allowing me the opportunity to intern during my summers at both NASA Marshall Space Flight Center and the Air Force Research Laboratory at Edwards Air Force Base. Sandra has been awesome with providing feedback and helping guide the experimental effort. My internship at NASA Marshall provided me an opportunity to develop my modeling ability under the guidance of both Brian Richardson and Jeff West, to whom I'm extremely grateful for teaching me about how to properly run CFD. At AFRL, I was able to both further develop my CFD skills and advance the numerical effort in my PhD with incredible help from the folks in the RQRC branch including: Dr. Venke Sankaran, Dr. Ingrid Wysong, Dr. Ananda Himansu, Dr. Matthew Harvazinski, and Dr. Tomas Houba. The numerical approach in this work was pretty much developed based on many valuable discussions during my internship at AFRL.

Thanks to Dr. Pourpoint's research group for all the experimental discussion and assistance. Specifically, I would like to thank Jason Gabl for helping with the experimental design reviews and test readiness reviews by pointing out issues that could be potentially problematic, as well as the extensive help with running the experiment; Dr. Philip Piper for many productive discussions on designing experimental hardware, what fittings are good and why, why certain regulators or valves are preferred over others…; and Michael Orth for providing extremely valuable input on safely operating gaseous hydrogen and oxygen systems safely, and from his extensive machining experience on how to simplify experimental design drawings for machining by removing or

modifying features that are not important for the experiment but increase machining difficulty. In addition, I owe extreme gratitude for the undergrads (and some who are now grad students) in the lab for helping out with both research tasks and with building the feed-system for the experimental hardware – which was an extremely time and labor-intensive effort – including: Joey Cavanaugh, Baker Noonan, Andrew Vuong, Louis Villa, Josh Zubik, Kevin Wallace.

I would also like to thank Swanand Sardeshmukh and Kota Mikoshiba for their help with running, debugging and post-processing GEMS as well as the informative discussion on my modeling approach or providing a sanity check to see if my calculations made sense or I was crazy. Additionally, I would like to thank Tristan Fuller and Dasheng Lim for the extensive discussions on designing torch igniters, fluid systems and general experimental knowledge from their extensive testing experience. It was always interesting stepping into their office.

The torch igniter troubleshooting in the experiment was significantly aided by discussion with Robin Osborne at Marshall Space Flight Center and Darren Tinker from Vanderbilt University (Now at NASA Marshall Space Flight Center), whom I owe a great deal of thanks.

I would like to acknowledge Zucrow staff for facilitating my PhD experience including: Jen Ulutas for helping me out with all administrative tasks including replacing my Zucrow keys after losing them in kayaking accident; Sheri Tague for helping out with any and all account balance issues and helping out with many administrative chores, Tania Bell for quickly processing all my orders and providing outstanding assistance when a package got lost, and Christine Wyant for helping with several administrative tasks and package package delivery. I would also like to thank Scott Meyer and Rohan Gejji for aiding with designing the feed system and answering all questions about running experiments at Zucrow. I owe a great amount of gratitude to Rob McGuire and Toby Lamb machining my experimental hardware. I would also especially like to thank Toby Lamb for the extensive machining discussion that taught me a lot about various machining techniques and definitively improved my machining ability.

The experimental effort in the project would not have been possible without the Bechtel Innovation Design Center (BIDC) which provided a place for me to machine a large amount of my experimental hardware for free. Machining the hardware myself definitely help improve my design skills after personally fabricating hardware and learning why some design features are difficult. I would like to thank David Huddleston at the BIDC for sharing his extensive knowledge of best machining practices and helping salvage several parts that became damaged after 15-20

hours of machining due to oversight on some machining features. I would also like to thank David McMillan at the BIDC for reviewing my design drawings in depth and suggesting ways to simplify the drawing or my experiment to make it easier to machine or collect data or suggesting where I can find the exact experimental hardware that I need.

The soot deposit measurements would not have been possible without the help of Dr. Steven Schneider and Dr. Brandon Chynoweth by letting me extensively use their Zygo Zegage Optical Profilometer to take soot thickness measurements.

Furthermore, my six years spent at Purdue would not have been nearly as enjoyable without the wonderful friends I made at Purdue including: Nyansafo Aye-Addo, Dr. Lida Ahmadi, Dr. Wes Anderson, Dr. Valeria Andreoli, Dr. James Braun, Dr. Timo Buschhagen, Dr. David Cuadrado, Akshay Deshpande, George Georgalis, Jake Harry, Dr. Paht Juangphanich, Doug Matthews, Dr. Zhe Liu, Francisco Lozano, Dr. Mario Migliorino, Marina Sala de Medeiros, Dr. Monique McClain, Dr. Lalit Rajendran, Jocelino Rodrigues, Dr. Vlad Podolsky, Dr. Francois Sanson, Dr. Mike Smyser, Bhavini Singh. Studying for quals with the Magnificent Seven made the experience more tolerable and enjoyable. I would like to especially thank Miss Maisy Ahmadi-Podolsky for always being excited to greet me at the door and ask for belly-rub whenever I came back from lab or just whenever I had any type of cheese.

Last but certainly not least, I would like to thank my parents Zema and Fuad and my brother Marat for encouraging and supporting me from kindergarten all the way through the 20th grade.

TABLE OF CONTENTS

LIST OF TABLES

LIST OF FIGURES

NOMENCLATURE

Variables

α = Soot Surface Site Fraction

β_{ij} = Collision Coefficient Between Particle Plasses i,j

γ = Specific Heat Ratio

δ = Dirac Delta Function

ϵ = Van der Waals enhancement factor

κ = Thermal Conductivity

ϕ = Equivalence Ratio

ω = Species Production Rate

π_r = Reduced Aggregate Moment

ρ = Gas Density

μ = Dynamic Viscosity

μ_r = Reduced Moment

τ_{res} = Residence Time

τ_w = Wall Shear Stress

A = Area

C^* = C-star velocity

C_D = Discharge Coefficient

C_{soot} = Soot Particle Concentration

C_V = Flow Coefficient

c_p = Specific Heat at Constant Volume

c_v = Specific Heat at Constant Pressure

D = Diameter

D_{drop} = Droplet Diameter

d_{Bolt} = Bolt Diameter

F_{PBolt} = Bolt Preload Force

F_{SBolt} = Bolt Separation Force

f_v = Soot Volume Fraction

G = Soot Coagulation Rate

H = Soot Aggregation Rate

h = Specific Enthalpy

h_{conv} = Convection Coefficient

h_f = Enthalpy of Formation

h_{vap} = Latent Heat of Vaporization

K_{lube} = Bolt Lubrication Factor

m = Gas Mass

$\dot{m}$ = Mass Flow Rate

M = Mach Number

M_r = Soot Concentration Moment

M_W = Molecular Weight

N_i = Soot Particle Number Density of Particle Size i

P = Pressure

P' = Perimeter

$\dot{Q}$ = Heat

r = Radial Coordinate

R = Soot Nucleation Rate

R_e = Reynolds Number

s = Surface Growth Rate

S_c = Schmidt Number

S_{PBolt} = Bolt Proof Load

T = Temperature

T_{Bolt} = Bolt Torque

t = Time

t_s = Soot Deposit Thickness

$\dot{t}$	= Soot Thickness Growth Rate	$\vec{V}$	= Velocity
U	= Internal Energy	V_{br}	= Brownian Deposition Velocity
u	= Specific Internal Energy	V_{th}	= Thermophoretic Drift Velocity
u_z	= Axial Component of Velocity	W	= Soot Surface Growth Rate
u_r	= Radial Component of Velocity	Y	= Species Mass Fraction
V	= Volume	z	= Axial Coordinate

Constants

k_b	=	Boltzmann constant (1.380649e-23 J/K)
σ_{SB}	=	Stefan-Boltzmann constant (5.67e-8 W/m^2-K^4)
R_u	=	Universal Gas Constant (8.314563 J/mol-K)
N_a	=	Avogadro Constant (6.022140/mol)

Subscripts

c	=	Chamber
e	=	Exit
g	=	Gas
l	=	Liquid
s	=	Soot
t	=	Total/Stagnation Property
i	=	Reference to ith species or ith moment
in	=	inlet
out	=	outlet
w	=	wall

Acronyms

1D	=	One-Dimensional
2D	=	Two-Dimensional
CFD	=	Computational Fluid Dynamics
DAQ	=	Data Acquisition

FOF	=	Fuel-Oxidizer-Fuel Injector
GEMS	=	Generic Equation and Mesh Solver
HACA	=	Hydrogen-Abstraction-Acetylene-Addition
P&ID	=	Plumbing and Instrumentation Diagram
PEBCAK	=	Problem Exists Between Chair and Keyboard
MOMIC	=	Method of Moments with Interpolative Closure
MR	=	Mixture Ratio
OF	=	Oxidizer to Fuel Ratio (Same thing as Mixture Ratio)
PID	=	Proportional-Integral-Derivative Controller
RP	=	Rocket Propellant
RP1	=	Rocket Propellent-1
RP2	=	Rocket Propellant-2
GOx	=	Gaseous Oxygen
GH_2	=	Gaseous Hydrogen
WSR	=	Well Stirred Reactor (Same thing as Perfectly Stirred Reactor or Continuously Stirred Reactor)
PFR	=	Plug Flow Reactor
PSD	=	Particle Size Distribution
VI	=	Virtual Instrument

ABSTRACT

Combustion of kerosene propellants often deposits soot on chamber walls. These deposits act as a thermal barrier and can significantly affect the analysis of cooling systems. This is especially vital for reusable engines since the accumulated soot deposit can make the wall heat flux vary between every firing. This dissertation discusses a computational and experimental effort to understand the main drivers of these soot deposits. The computational approach employs the Method of Moments with Interpolative Closure (MOMIC) model to predict soot particle dynamics; Brownian and thermophoretic diffusion for particle transport to the chamber surface; and the Hydrogen-Abstraction-Acetylene-Addition (HACA) mechanism for soot surface growth. These models were incorporated in a 1D plug flow reactor. Two-dimensional axisymmetric reacting CFD simulations were also run to understand the flow field influence on the near wall gas phase chemistry. Simultaneously, a fuel rich kerosene and gaseous oxygen experiment was developed and fired to obtain soot deposit thickness measurements for model comparison. The results show the reduced order plug flow model can satisfactorily predict the soot thickness and that thermophoresis is the dominant deposition mechanism. However, though the model can predict deposit mass trends, it underpredicts the absolute values for some conditions and may need an additional mechanism.

1. INTRODUCTION

1.1 Motivation

Kerosene fuels are burned in a variety of propulsive applications. Kerosene combustion is a complex process and can lead to production of soot. Soot is not only a pollutant, but it can affect engine performance and particulate deposit on the wall is known to affect heat transfer properties. Since heat flux scales with pressure, the deposits can become a larger concern at higher chamber pressures. Though the deposits act as a thermal barrier coating, the nonuniformity in the deposition can lead to thermal hot spots and potentially chamber failure. The deposits can also significantly affect design of a cooling system and neglecting it in a model can result in large differences in heat flux estimates compared to experiments [1]. This is particularly important in rocket engines, where pressures can be tens to hundreds of atmospheres. Furthermore, advancements in the performance reusability of hydrocarbon/LOX booster engines calls for operation at pressures upwards of 3000 psia, and reusability for up to 50 missions [2], which makes understanding the deposition process even more important in order to design efficient cooling scheme.

Current cooling techniques in rocket engines include regenerative cooling, where coolant (usually fuel) flows through passages along the chamber and nozzle walls; and fuel film cooling, where a liquid fuel film is produced via ports around the injector plate or the chamber wall. Fuel film cooling is effective at reducing the heat flux at the chamber wall, however since the fuel is not combusted efficiently the engine performance can drop significantly [3]. Designing an efficient fuel film cooled combustion to reduce performance loss while keeping the chamber within temperature limits can also pose several challenges. As discussed by Himansu [1], these include interfacial hydrodynamic and transport effects between the core flow gases and fuel film, as well as discontinuities in flow properties. Further complicating the design is carbon deposition on the chamber wall. This deposit affects heat transfer and can result in hot spots due to nonuniformity in deposits, or increased corrosion that could reduce life span of a potential re-usable booster engine. The deposits are thought to arise from pyrolysis of the liquid fuel film and transport of core flow soot to the walls. However, there is little understanding of the physics and chemistry that govern the deposit. In addition, existing correlations of deposits in actual engines are based on measurements at the end of a test-fire after the engine has gone through several transients and

purge cycles such as in [4]. The varying engine operations can produce a varying amount of deposit during the hot-fire and this can make it difficult to understand the mechanisms of carbon deposit formation on the chamber wall. Literature on fuel film cooling at rocket conditions is also lacking.

Research on carbonaceous deposits of kerosene has primarily focused on pyrolytic deposition from liquid fuel in heated tube experiments for regenerative cooling applications [5–8]. These studies showed and reiterated that carbon deposit build up results in increased thermal resistance and is important for heat transfer considerations. However, in contrast little open literature is available on soot deposits on the hot side wall in kerosene engines at high pressures.

Therefore, designing efficient cooling schemes for future advanced kerosene engines, requires an understanding of the fluid dynamics, chemistry and prediction of wall soot build-up. This project aims to investigate soot build-up at a variety of pressure conditions in order to develop a fundamental understanding of the governing mechanisms leading to this deposit in order to aid an engine designer with development of future reusable liquid booster engines.

1.2 Research Objectives

The major objectives of this research study can be summarized as follows:

1.) Develop a 2-D reacting flow simulation to understand the flow field inside a turbulent fuel rich reacting flow environment at rocket conditions.
2.) Investigate current volumetric soot formation models that could be incorporated in CFD such that the model is computationally inexpensive but can provide accurate trend prediction.
3.) Develop a simplified one-dimensional model that incorporates the main physics and chemistry of soot formation and deposit.
4.) Design an experiment to isolate and independently measure effects of pressure, residence times and flow conditions on the soot buildup.
5.) Verify and validate the global model, and the dependent sub models, with experimental results of wall soot from this project and from volumetric soot data from literature.
6.) Identify the key mechanisms and parameters in soot deposit at rocket conditions.

1.3 Dissertation Outline

This dissertation provides an overview of the numerical and experimental approach towards understanding the mechanisms of soot deposition and the outcomes of this research. The modeling simultaneously informed and was guided by the experimental design, and vice versa. It was difficult to separate the numerical work from the experimental as I had usually worked on both at the same time or occasionally shifted my focus to the other when debugging the obscure bugs became too frustrating or when taking a break from debugging to bend tubes became too tedious. But both efforts were split into separate chapters, with some back and forth discussion in the relevant sections.

This dissertation describes how I approached trying to understand soot deposition along with the justification or assumptions for certain decisions. The intent is to serve as a guide for potential future work related to either this topic or to provide a starting point for numerically or experimentally analyzing similar types of propulsion systems. The thesis is organized into the following chapters:

- Chapter 2 provides an overview of previous research on carbon deposition. It also discusses the main conclusion
- Chapter 3 discuss the numerical approach to understanding soot formation including an initial plug flow reactor and 2-D axisymmetric reacting CFD approach to understand the fuel rich flow field. It also discusses a reduced order soot plug flow reactor model for predicting soot formation and deposition in a numerically economical approach.
- Chapter 4 discusses the experimental approach and analysis that went into designing and fabricating an experiment and a propellant feed system to obtain soot measurement
- Chapter 5 provides the main numerical results from the initial plug flow reactor modeling, the reacting CFD, the sooty plug flow reactor model and compares the predictions with the experimentally measured chamber pressure and soot deposit thickness
- Chapter 6 summarizes the important findings from this research project. It also provides avenues of future research, both numerical and computational, towards understanding soot deposition in more depth.

2. BACKGROUND

Soot formation and deposition on chamber walls can occur in engines burning kerosene or hydrocarbons. As discussed in the motivation, understanding the deposition is important to predict heat transfer in a combustion – especially at rocket conditions. Despite this problem, literature on carbon deposition in rocket engines is lacking in open literature. There is little understanding of the physics and chemistry tackling the deposits – this is something this dissertation is attempting to improve.

2.1 Relevant Soot Deposit Research

Research on carbonaceous deposits of kerosene has primarily focused on pyrolytic deposition from liquid fuel in heated tube experiments for regenerative cooling applications [5–8]. These studies showed and reiterated that carbon deposit build up results in increased thermal resistance and is important for heat transfer considerations. However, little open literature is available on soot deposits in kerosene engines at high pressures. Previous work included a Zucrow Laboratory experimental and numerical study of chamber deposition in a low pressure 150-250 psia kerosene/hydrogen peroxide combustor where a simplified model of carbon wall growth was developed [9]. Hernandez et al. also experimentally studied carbon deposit of RP-1, propane and methane with liquid oxygen at fuel rich mixture ratios between 0.2 to 0.6 inside a torch ignited combustor tube [10]. The bulk deposits were quantified via pressure drop across the tube. Additionally, soot deposits have been studied and modelled in exhaust gas recirculation coolers [11,12]. The EGR models provide a physics-based understanding of the soot deposition dynamics and show the importance of thermophoresis on deposit mechanics but contained little focus on the chemistry of the soot formation process (soot volume fraction was an input parameter and the overall soot amount was conserved with no reaction source terms in the flow to generate additional soot particles). The models were also run at close to ambient pressure conditions, which is the typical operating range of EGR coolers, whereas rocket combustors operate at 1-2 orders of magnitude higher pressure conditions.

2.2 Fuel Rich Combustion

The focus of this work was on fuel rich combustion at a mixture ratio of unity, where the soot formation and deposition are high. At these fuel rich conditions, the gas composition requires long residence times to approach equilibrium and hence require solving for the reaction kinetics. Calculating the composition via equilibrium analysis, such as with NASA CEA [13] would produce erroneous gas properties. As Figure 2.1 shows for the gas temperature in a well stirred reactor calculated using the HyChem POSF5433 reaction mechanism [14,15], as the mixture ratio is reduced from stoichiometric – Stochiometric Mixture ratio is ~3.4 - to fuel rich conditions, the blow out limit increases. This can be seen by the sudden drop off in temperature due to not enough time to sustain the combustion reactions. The residence time to reach equilibrium (dashed line) also increases. The residence time to reach equilibrium temperature conditions increases by orders of magnitude with decrease in mixture ratio and is more than six orders of magnitude higher at a mixture ratio of unity compared to stoichiometric conditions. Compared to equilibrium temperature, some species may also require a long residence time to reach equilibrium conditions, even at stoichiometric conditions. The radical OH requires little residence time to approach equilibrium for the higher mixture ratios but requires much longer times for acetylene. The equilibrium concentrations of acetylene though are several orders of magnitude smaller for the close to stoichiometric conditions compared to the lower mixture ratios. Additionally, an interesting behavior at fuel rich conditions, as seen in Figure 2, is that the endothermic reactions are slower than exothermic reactions which results in a gas temperature overshoot over equilibrium conditions with increasing residence time before decaying down to equilibrium [16,17].

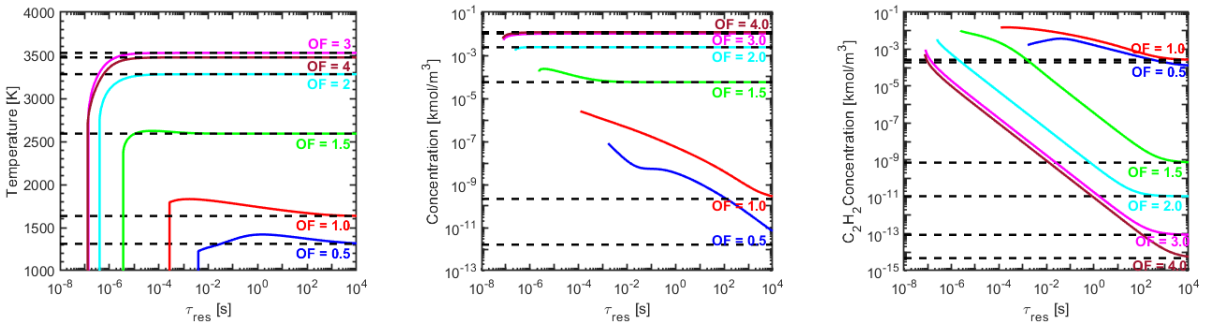

Figure 2.1 Reacting Gas Temperature [Left], OH Concentration [Middle], and C_2H_2 concentration [Right] in a Well Stirred Reactor for RP-2/GOx combustion at 17.2 bar as a function of mixture ratio and residence time using the HyChem POSF5433 Detailed Mechanism [14,18]. The dashed line is the corresponding equilibrium condition.

Consideration of the slower endothermic reactions in kerosene combustion is particularly important in a mixture ratio range of 0.5-1.5, as the temperatures could be higher than equilibrium, as shown in Figure 2.2. Designing an experiment with equilibrium assumption could result in hardware damage.

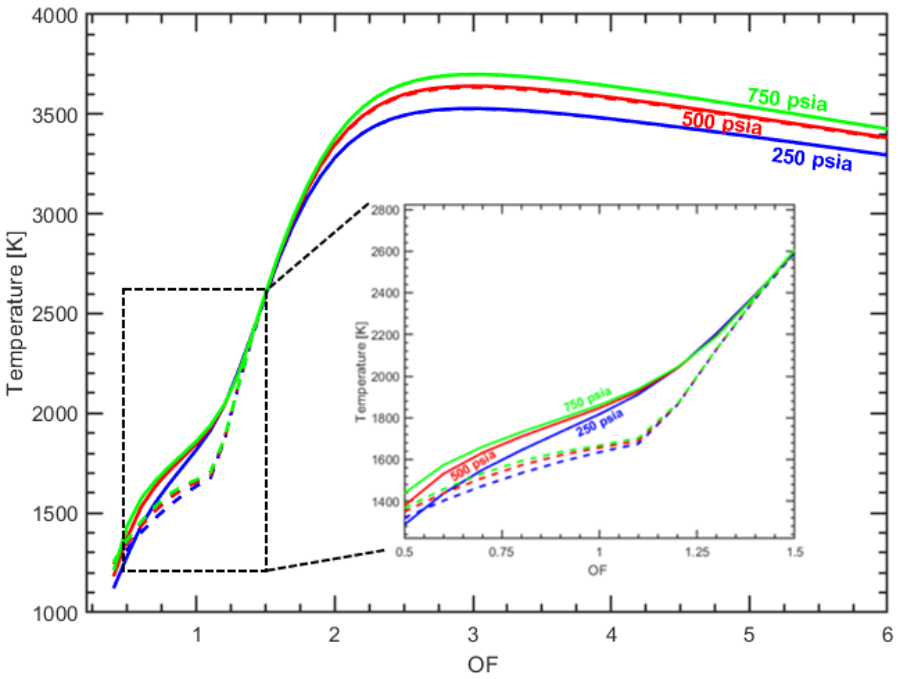

Figure 2.2. Bulk Gas Temperature of RP-2/GOx combustion in a well stirred reactor as a function of mixture ratio and comparison with equilibrium predictions. Solid lines are well stirred reactor calculations and dashed lines are equilibrium predictions. The calculation is done with the HyChem POSF5433 Reaction Mechanism and Thermodynamic Properties

Research in soot formation from gas phase combustion products to formation of solid soot is still on-going. It known though that incomplete combustion produces polycyclic aromatic hydrocarbons (PAH) [19]. The PAHs are the basic building blocks of soot and act as nucleate site for soot formation [20]. The surface of solid soot also resembles the structure of PAHs and it is thought there is chemical similarity in the growth processes of soot and gaseous PAHs. Growth is then thought to occur predominately via the hydrogen abstraction and acetylene addition (HACA) mechanism, with acetylene being the predominant species in surface growth [21,22]. As a result, most soot formation occurs at chemical non-equilibrium regime, where acetylene concentrations are high. Calculation of soot growth with a well stirred reactor, which was done in this work and will be discussed in more detail in Chapter3, predicts this behaviour as shown in Figure 2.3.

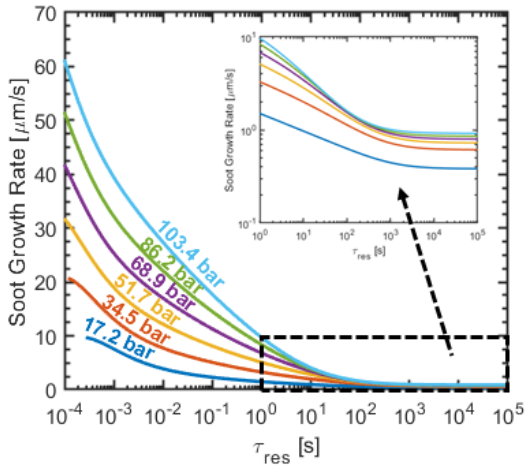

Figure 2.3. Soot growth rates in a fuel-rich (Mixture Ratio = 1) kerosene/GOx Well Stirred Reactor. We use the HACA mechanism to predict soot deposit growth rates, which is described later in this paper. Equilibrium is approached at large residence times

2.3 Soot Deposition

In trying to understand the process leading to wall soot growth, the overall soot deposit flux can be thought to be affected by three main drivers: chemical growth via the HACA mechanism, physisorption of soot in core flow at the wall, and removal of soot:

$$\dot{m}''_{soot} = \dot{m}''_{rxn} + \dot{m}''_{diffusion} - \dot{m}''_{removal} \qquad 2.1$$

Where the first term is surface growth of the chamber deposited soot. Soot formation in the flow and physisorption at the chamber surface is another potential contributor to the bulk soot wall deposit. The second term expresses this effect. Finally, the last term in equation 1 is soot removal due to effects such as shear forces stripping surface soot particles or removal due to particle impact [23]. The last term is more complex to model and can conflate overall soot deposit predictions when comparing with experiment if it is not accurately accounted for. Additionally, trying to model all terms simultaneously could result in tuning to experimental conditions and hence may not relate to accurate physics. However, research in exhaust gas recirculation cooler deposits has shown that the net removal decreases to a small amount, while simultaneously the soot particle sticking probability increases, as the bulk flow velocity decreases [12,23]. Hence, to simplify the problem and get an understanding of the deposit mechanisms at high pressure, this work focused on relatively low bulk velocities below 50 m/s (significantly lower than found in actual rocket combustors) where the removal term is thought to have negligible effect.

2.4 Soot Formation and Growth

Soot is a by-product of hydrocarbon combustion that consists of mostly carbon, with up to 15% mole fraction of hydrogen and several trace species [24]. It is formed in various quantities for a variety of hydrocarbon fuels, but the formation process is still not well understood. Significant progress however has been made through experimental and theoretical studies to understand the key soot formation processes. It is generally agreed that soot formation consists of four main processes: homogenous inception of soot particles, soot particle growth by coagulation, soot particle growth (and oxidation) via surface reactions, and soot particle agglomeration [25–27]. The formation process, from the initial pyrolysis of the propellants is illustrated in Figure 2.4.

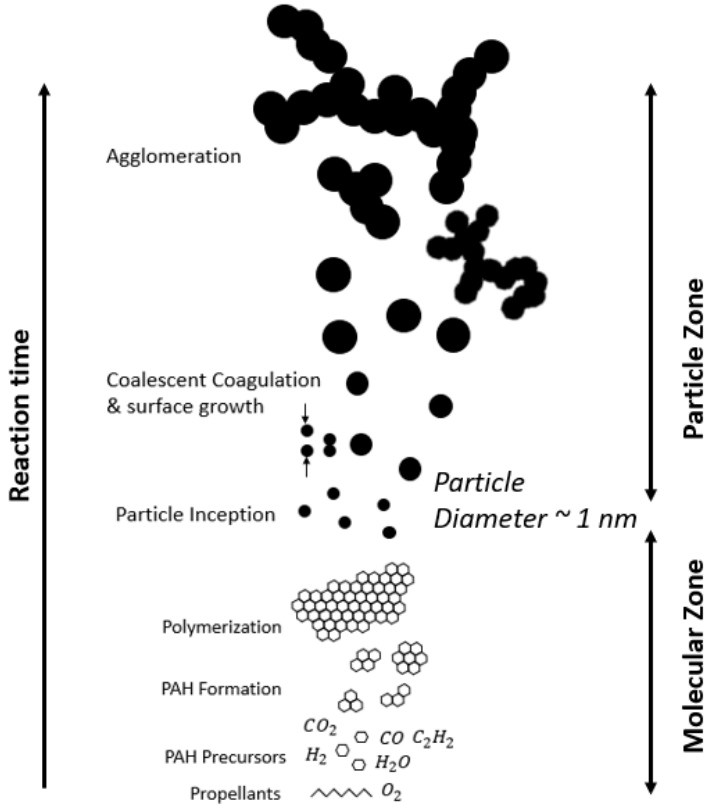

Figure 2.4 Volumetric Soot Formation Mechanism

The mechanism responsible for soot nucleation has been a subject of debate for a long time [25,26]. However, it is now widely accepted that the gas phase polycyclic aromatic hydrocarbons (PAH) are the main precursors of soot [21,28]. Furthermore, the formation of benzene (C_6H_6), the smallest aromatic ring, from straight-chained aliphatic molecules is thought to be the rate limiting

step in the reactions leading formation of larger aromatics [26,29,30]. The formation of the first ring occurs through a series of chemical reactions beginning with the pyrolysis of the propellants. Pyrolysis of all hydrocarbons essentially produce in some amounts PAH, polyacetylenes, unsaturated hydrocarbons and acetylene [31]. Once the first ring is formed, the molecule can further grow into PAH from the gaseous pyrolyzed species. Frenklach and Wang proposed that this growth occurs due to Hydrogen-Abstraction-Acetylene-Addition (HACA) mechanism [22,26]. As the name implies, the two major steps involve abstraction of hydrogen atom from the reacting surface by a gaseous radical which creates an active radical site, followed by addition of gaseous acetylene species to the radical site. Other growth mechanisms have also been postulated such as the addition of methyl, vinyl and proparyl [22,32,33]. However, Frenklach et al. studied the influence of fuel molecules on the chemical pathway to soot and found that regardless of what the initial pathway is for formation of small PAH's, all the pathways eventually relaxed to the HACA mechanism because acetylene exists in much larger concentrations compared to the other reactants- therefore HACA growth rates overshadowed the other mechanisms [34]. Oxidation of PAH can also occur via O_2 and OH. However, oxidation has two competing effects on the size of the PAH molecule. Oxidation decreases the amount of carbon - which contributes to growth, but at high temperatures the total number of radicals is increased due to production of molecular oxygen - which promotes soot formation via the HACA mechanism. The net effect is determined by a balance of the two processes.

Despite significant research over several decades, the transition of the gas-phase PAH species to solid particles is still one of the least understood soot processes. Early modeling attempts defined soot as the mass accumulated in PAH species above a certain size and that transition occurs solely via chemical growth, however this underpredicted the soot volume. Frenklach and Wang later proposed that after some size, the PAH species coalesce to form dimers, which then collide with other PAH molecules to form trimers, tetramers… all while the individual PAH species continue growing via chemical reactions [21,35]. The coalescence of the large PAH's and formation of the dimers is then assumed to be the incipient solid soot particle, with a spherical geometry and diameter of about 1 nm containing about 100 carbon atoms [22,36].

In recent work from Sandia National Laboratory, Johansson et al., show that a clustering of hydrocarbons by radical-chain reactions (CHRCR) mechanism seems to provide another route to particle formation. [37] In their approach, the PAH dimers may be stabilized into covalently

bound clusters at high temperatures via a rapid radical driven hydrocarbon clustering mechanism, which can then lead to formation of soot particles. However, the detailed rates for the radical chain propagation steps still need to be worked out before the mechanism can be tested to assess the predictability of soot formation.

Once the smallest soot particles are formed, they can increase in size via collision and coagulation with other particles. Initially, growth of the nascent soot particles have been observed to produce closely spherical geometries with diameters in the range of 1-40 nm [26,27]. However, as the particles grow larger they start agglomerating and forming fractal chain like structures [38], which can grow to be several micrometers in size. These two growth regimes are typically classified as coalescent growth and agglomeration, respectively. The point of transition from coalescent growth to agglomeration is not clear but seems to depend on the soot size and surface growth rate [27,39]. For small particle sizes, surface growth via heterogenous reactions on the surface are quick enough to smoothen the surface of the particles. As the particles get larger however, surface growth is not fast enough to smoothen the shape and the particles grow into fractal like agglomerates. In both processes, coagulation reduces the number density of soot particles but conserves the total mass of the system.

The soot particles can also grow further via heterogenous surface reactions with the gas-phase species. The exact reaction pathways are not well understood but it is generally accepted that acetylene is the main gas-phase species involved in soot growth [21]. It was hypothesized that the surface of soot particles resemble the edge of a large PAH molecule and hence surface growth reactions of soot are chemically similar to the corresponding reactions for the PAH [21,35]. Hydrogen abstraction creates surface radical sites, which then react with the gas phase species. This is similar to the HACA mechanism in PAH growth and termed by Frenklach as surface-HACA [22]. This description is consistent with the observed soot surface growth rates in laminar premixed and diffusion flames [40–43] Furthermore, the surface growth rates of soot particle have been observed to decrease over time due to soot surface aging [27,40]. This is a result of a decrease in H radical concentrations and a decrease in the surface reactivity of the soot particle due to a decrease in the number of active surface sites [21]. In modeling the soot particle growth for this project, the surface-HACA mechanism was assumed with aging considered as will be discussed.

The soot particles can also grow due to condensation of PAH molecules on the soot surface [44]. This process resembles coagulation, where collision with PAH molecules results in a larger

soot particle. However in a parametric soot model study, Mehta showed that the overall contribution of PAH condensation is small compared to surface reactions for diffusion flames, and even smaller for premixed flames [45].

3. NUMERICAL MODELING

3.1 Overview

The driving mechanisms of soot deposition were explored via several modeling approaches. As described in the previous chapter and illustrated in Figure 3.1, soot deposition was thought to be driven by surface reactions, and thermophoretic and mass driven diffusion.

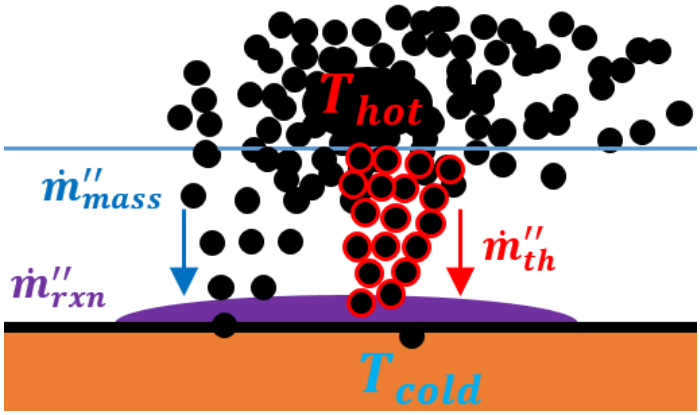

Figure 3.1 Hypothesized soot deposition and growth mechanisms

Soot removal can also strip away particles from the deposit, but it was assumed negligible for the operating conditions explored in this work. The modeling was performed with the experiment in mind. As discussed in the background, and will be discussed in more detail in section 4.3 , the experiment was sized for a low bulk velocity so that removal is small. The soot deposit mass growth flux was then thought to be a sum of the surface growth reactions, and mass and thermophoretic diffusion:

$$\dot{m}''_{soot} = \dot{m}''_{rxn} + \dot{m}''_{diffusion} + \dot{m}''_{thermophoretic} \quad 3.1$$

Predicting these mechanisms in a combustor first requires modeling the chamber gas properties and bulk soot – which in fuel rich combustion requires consideration of finite reaction rates. Since the gas can require a long residence time to reach equilibrium in fuel rich combustion, the mixture properties can significantly differ from equilibrium predictions. In particular, the species concentrations that are involved in soot growth - such as acetylene - can be orders of

magnitude higher. As a result, consideration of chemical kinetics is important in predicting soot formation and growth rates.

The surface growth and diffusion terms in equation 3.1 were explored with both reduced order reactor type modeling and 2-D axisymmetric reacting CFD. The goal of the modeling effort was to understand the influence and overall magnitude of the deposit mechanisms, rather than predict the exact details. For this reason, reduced order reactor modeling was preferred and primarily employed in this work. As Figure 3.2 shows, an approach consisting of 0-D Continuously Stirred Reactors (CSTR) – also referred to in literature and in this dissertation as Well Stirred Reactors (WSR) – and a 1-D plug flow reactor (PFR) can be used to model a reacting environment. The approach is significantly less expensive than reacting CFD and can be used to quickly iterate through parametric cases with reasonable accuracy, as the results in Chapter 5 will show.

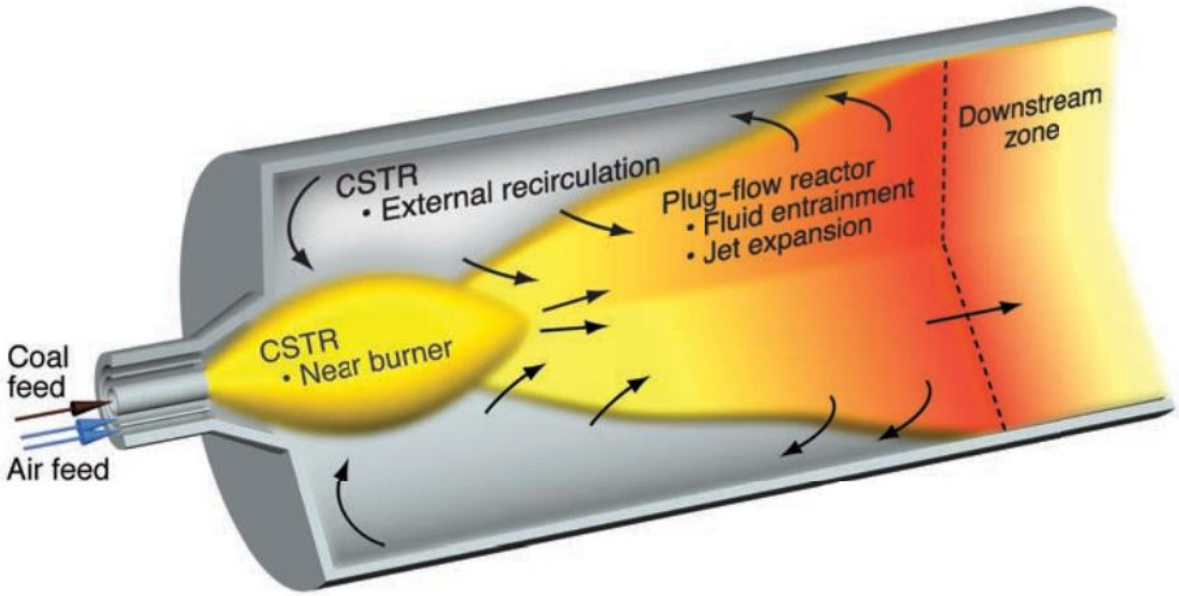

Figure 3.2 Swirling pulverized-coal combustor modeled with low order reactor network. Flow is like soot deposit experiment combustor. Figure taken from Kee's Chemically Reacting Flow Textbook [46]

The models developed in this project were primarily for the geometry and operating conditions of the experiment discussed in chapter 4. However, they could be readily adaptable to any other sooty, or non-sooty, condition.

The modeling effort started with building 0-D WSR and 1-D PFR models for predicting the bulk chamber conditions. Afterwards, higher fidelity 2-D reacting flow CFD simulations were run to verify these predictions and get a better idea of the near wall gas properties. These simulations were run without soot in the flow, but the gas solution was used to calculate the heterogenous soot growth term in equation 3.1. These simulations were also used to guide the design of the experiment.

The next step in the modeling effort involved predicting volumetric soot in the core flow. This was done with the Method of Moments with Interpolative Closure (MOMIC) model. The MOMIC model provided statistics of the soot particle distribution and was able to predict the bulk soot properties. This soot model was then coupled to the PFR model to create a reduced order 1-D soot prediction model. The last two terms in equation 3.1 were then calculated with this coupled 1-D soot PFR model. The soot model predictions were first validated with other simulations and experimental soot measurements in literature – however at different conditions than those focused on in this work as there was little open literature found on kerosene soot measurements. The experimental effort, discussed in chapter 4, was done to get soot deposit measurements at higher pressures from kerosene combustion. Soot deposit predictions were verified with measurements from this experiment and will be discussed in chapter 5.

Most of the calculations in the plug flow reactor model were run with the detailed HyChem POSF5433 RP-2 112 species- 841 reaction mechanism [14,15]. This mechanism was designed to model the reaction kinetics of the same batch of RP-2 fuel (POSF5433) that was burned in the experiments in this work. Other mechanisms were investigated as well for comparison including the detailed San Diego Mechanism [47], JetSurf Version 1.1 and 2.0 [48,49], and the skeletal 10 species 14 step kerosene reaction mechanism of Ten-See Wang [50]. The Ten-See Wang mechanism was numerically preferable for CFD; however, it was found to over-predict gas temperatures at fuel rich conditions because of a lack of endothermic reactions and generally had poorer agreement in WSR simulations compared to the other mechanisms. The well-established GRI-Mech 3.0 mechanism [51] containing 53 species and 325 reactions for natural gas combustion was also used for initial debugging and qualitive comparison with the other mechanisms of fuel rich combustion characteristics.

3.2 Well Stirred Reactor Model

The well stirred reactor (WSR) is an idealized zero-dimensional chemical reactor concept that is often used to investigate gas phase kinetics of a system [46]. This model was used as the foundation for the 1-D plug flow reactor model as will be discussed in sections 3.3 and 3.8.

An inherent assumption in the model is perfect instantaneous mixing within the control volume - with no spatial variation in the gas properties. The unburned inlet gas is assumed to instantaneously mix with burned gas in the reactor. In turn, reactions are assumed to occur homogenously within the control volume, with rates calculated with a single point for temperature, pressure and species composition. The reactor temperature, pressure and species composition in the model are calculated from the mass, energy and species conservation equations.

For all the reactor calculations in this work, the ideal gas equation of state was used, where the density of the gas mixture, ρ_g, is defined as:

$$\rho(p_g, T_g) = \frac{p_g M_{\mathrm{W,mix}}}{R_u T_g} \tag{3.2}$$

Where p is the gas pressure, $M_{w,mix}$ is the mean molecular weight of the gas mixture, R_u is the universal gas constant and T_g is the gas temperature.

With the ideal gas EOS, the governing equations for the WSR can be written as:

Mass Conservation

$$\frac{dm_g}{dt} = \frac{d(\rho_g V)}{dt} = \dot{m}_{g,in} - \dot{m}_{g,out} - V\sum_{k=n}^{N} \boldsymbol{\omega_{s,k}} M_{W,k} \tag{3.3}$$

Species conservation:

$$\rho_g V \frac{dY_{g,k}}{dt} = \dot{m}_{g,in}(Y_{g,in,k} - Y_{g,k}) + V(\dot{\omega}_{g,k} + \boldsymbol{\dot{\omega}_{s,k}}) M_{\mathrm{W,k}} - Y_{g,k} V \sum_{k=1}^{n} \boldsymbol{\dot{\omega}_{s,k}} M_{\mathrm{W,k}} \tag{3.4}$$

Energy Conservation

CV

$$\rho_g c_{v,g} V \frac{dT_g}{dt} = \dot{m}_{in}\left(h_{in} - \sum_{k=1}^{n} \frac{u_k(T_g) Y_{g,in,k}}{M_{W,k}}\right) - \frac{p_g}{\rho_g}\dot{m}_{out} - V\sum_{i=k}^{n} u_k(T_g)\left(\omega_{g,k} + \boldsymbol{\omega_{s,k}}\right) M_{W,k} + \boldsymbol{N_s} V\left(\boldsymbol{\dot{Q}_s} + \frac{\sum_{k=1}^{n} u_k(T_s)\boldsymbol{\omega_{s,k}}}{\boldsymbol{N_s}}\right) + \dot{Q}_{source} \tag{3.5}$$

CP

$$\rho_g c_{p,g} V \frac{dT_g}{dt} = \dot{m}_{in}\left(h_{in} - \sum_{k=1}^{n} \frac{h_k(T_g) Y_{g,in,k}}{M_{W,k}}\right) - V \sum_{i=k}^{n} h_k(T_g)\left(\omega_{g,k} + \boldsymbol{\omega_{s,k}}\right) + \boldsymbol{N_s} V\left(\boldsymbol{\dot{Q}_s} + \frac{\sum_{k=1}^{n} h_k(T_s)\boldsymbol{\omega_{s,k}}}{\boldsymbol{N_s}}\right) + \dot{Q}_{source} \quad 3.6$$

The bolded terms in the equations are soot-related and calculated from the soot model, which is discussed later in this chapter.

The mass conservation equation 3.3 relates the rate of change reactor gas mass to the inflow and outflow of mass across the control surfaces, as well as mass exchange during soot production. In these equations, V is the reactor volume; $\dot{m}$ is the gaseous mass flow rate, with the subscripts referring to inlet and outlet; $\omega_{s,k}$ is the soot source term and accounts for consumption or production of the kth gas species, and $M_{W,k}$ is its molecular weight. The soot source term is calculated from the Method of Moments with Interpolative Closure soot model, which is discussed in sections 3.6 and 3.8.

In the mass conservation equation, the inlet mass flow is an input to the model. The outlet mass flow however is calculated by either imposing a constant pressure in the reactor and calculating the necessary mass flow to maintain this pressure, or via the compressible mass flow relation as shown:

$$\dot{m}_{g,out} = \dot{m}_{g,in} + 10^{-5}\left(P_g - P_{set}\right) \quad 3.7$$

$$\dot{m}_{g,out} = \mathrm{AP_g}\sqrt{\frac{\gamma M_W}{RT_g}}\mathrm{M}\left(1 + \frac{\gamma - 1}{2}\mathrm{M}^2\right)^{-\frac{\gamma+1}{2(\gamma-1)}} \quad 3.8$$

If a constant pressure is imposed in the reactor, then the outlet mass flow is calculated with 3.7. This setup is like the approach used in Cantera [52] and sets the outlet mass flow rate equal to the inlet flow rate as well as a correction term that depends on the difference between the current reactor gas pressure, P_g, and a desired setpoint pressure for the reactor, P_{set}. During integration of the governing equations, if the reactor gas pressure was to increase above the setpoint pressure then the outlet mass flow would increase in order to lower the pressure, and vice versa. At steady state, the reactor gas pressure should be equal to the set pressure and in turn the correction term would be zero.

Alternatively, if a flow outlet area is defined, then the mass flow rate can be calculated with this compressible mass flow rate relation as written in 3.8. This is more representative of the experimental reactor discussed in Chapter 4, where the mass flow rate is restricted by a choke plate. The mass flow rate is a function of the outlet area, A; the gas specific heat ratio, γ; the Mach number at the outlet; and the gas temperature, pressure, molecular weight. The Mach number at the outlet area is dependent on the exit pressure and calculated as:

$$M = \begin{cases} 0 & if\ P_g \leq P_e \\ \min\left(1, \sqrt{\frac{2}{\gamma-1}\left(\left(\frac{P_e}{P_g}\right)^{-\frac{\gamma-1}{\gamma}} - 1\right)}\right) & if \quad P_g > P_e \end{cases} \tag{3.9}$$

If the chamber pressure is less than the outlet pressure, then the outlet flow is set to 0. Backflow is not considered in this model. Otherwise, the Mach number is calculated with the isentropic compressible pressure relation. The Mach number at the minimum outlet area can range from zero up to unity, where the flow becomes choked, and the mass flow becomes independent of downstream conditions.

The species conservation, equations 3.4, describe the evolution of gas species within the well stirred reactor due to convective transport through the control surface and species generation due to both homogenous gas-phase reactions and heterogenous soot reactions. The last term in the convective transport equation is required to satisfy continuity in the case where species are consumed or produced by the soot reactions. Discussion of the soot model, from which the source terms are calculated, is deferred to sections 3.6 and 3.8. In the equations, Y_k and $\omega_{g,k}$ are the mass fraction and net production rate of the k^{th} species, respectively. The amount of species equations solved is equal to the amount of species considered. The net production rate in the equations is calculated from the reaction mechanism as:

$$\dot{\omega}_{g,k} = \sum_{n=1}^{N} v_{k,n} q_n \tag{3.10}$$

Where $v_{k,n}$ is the matrix of net stoichiometric coefficients for species k in reaction n, and q_n is the rate of progress for reaction n. The rate of progress is calculated as:

$$q_n = \frac{1}{MW_{mix}}\left(k_{f,n}\prod_k [MW_k Y_k]^{v_{k,f}} - k_{r,n}\prod_k [MW_k Y_k]^{v_{k,r}}\right) \tag{3.11}$$

Where $k_{f,n}$ and $k_{r,n}$ are the forward and reverse reaction rate coefficients; and $v_{k,f}$ and $v_{k,r}$ are the forward and reverse stoichiometric coefficients for the reaction The forward rate coefficient is calculated from the reaction mechanism via pressure dependent Arrhenius rate expressions, falloff reactions, or possibly another expression depending on the type of reaction. If the reaction is reversible, the reverse rate is calculated from equilibrium constant, otherwise it's set to zero.

Finally, the energy conservation equation is derived from the 1st law of thermodynamics for an open system by neglecting kinetic and gravitational potential energy. The energy equation can be written in constant volume form as in equation 3.5, or constant pressure as shown in equation 3.6. With the ideal gas assumption, the total internal energy and enthalpy of the mixture can be calculated as the mass average of the components as shown in equations 3.12 and 3.13 respectively.

$$U(T) = m_g \sum_k Y_k u_k(T) \tag{3.12}$$

$$H(T) = m_g \sum_k Y_k h_k(T) \tag{3.13}$$

Where the enthalpy, h_k, and internal energy, u_k, of the k[th] gas species are calculated as:

$$h_k(P,T) = h_{ref,k}\left(P, T_{ref}\right) + \int_{T_{ref}}^{T} C_p(T)\, dT \tag{3.14}$$

$$u_k(P,T) = h_k\left(P, T_{ref}\right) - \frac{P_g}{\rho_g} \tag{3.15}$$

Where C_p is the specific heat at constant pressure and calculated with the Chemkin polynomial with coefficients from an input thermodynamic database [52,53].

Taking the derivative of the total internal energy and enthalpy, and substituting the result into the 1st law, along with $\frac{dm_g}{dt}$ and $\frac{dY_g}{dt}$ terms from the continuity and species relations, results in the two different energy equations depending on which assumption are made for the resulting terms – constant pressure or constant volume. The physical significance of the terms in the equations is the rate of energy stored in the ideal gas reactor, a function of reactor temperature, is equal to the energy transferred by mass at the control surfaces; energy released in homogenous gas-phase reactions and heterogenous soot reactions; energy transferred to the soot particles; and heat transfer across the reactor surfaces. Calculation of the soot related source terms are discussed

later in the dissertation, in sections 3.6 and 3.8. The heat transfer term, $\dot{Q}_{source}$ is calculated as shown in equation 3.16.

$$\dot{Q}_{source} = \sum_{in,liquid} \dot{m} h_{vap} + h_{conv} A_w \left(T_g - T_w\right) + \epsilon \sigma A_w \left(T_g^4 - T_w^4\right) \tag{3.16}$$

Where the terms include energy loss due to vaporization of liquid propellants, calculated based on the propellant enthalpy of vaporization, h_{vap}; convective heat transfer across the reactor wall surface, calculated based on the bulk convective coefficient, h_{conv}, reactor wall surface area, A_w, and temperature difference between the reactor and gas walls; and radiative heat transfer calculated with the Stefan-Boltzmann law with a specific emissivity, ϵ. The convection coefficient is calculated with the Dittus-Boelter, which provides an estimate of heat flux in fully developed turbulent flow in smooth circular tubes for moderate temperature difference between the gas and wall and for Prandtl number of $0.6 \leq Pr \leq 160$ and Reynolds number $R_{e_D} \geq 10000$ [54,55], and calculated as:

$$h_g = 0.023 R_{e_d}^{\frac{4}{5}} P_r^n \left(\frac{k_g}{D}\right) \tag{3.17}$$

Where k_g is the gas conductivity, D is the chamber diameter the and the n exponent is 0.3 for the case of cooling or 0.4 for heating.

In solving the well-stirred reactor, the constant pressure reactor formulation was used for all constant pressure cases and the constant volume formulation for all other cases. The constant volume formulation can also be solved with a constant pressure, by using the exit mass flow condition shown in equation 3.7. Both approaches were verified to provide the same result for a constant pressure reactor, however the constant pressure reactor formulation simplifies the code and results in easier convergence in some cases.

The well-stirred reactor model, without any soot source terms, was initially solved directly with the Cantera framework, which incorporates the Sundials ODE solver [52,56]. However, modifying Cantera code to include source terms seemed to be more challenging. So instead the governing equations were written in a python function and then integrated with SciPy ODE [57,58] with an implicit solver based on backward-differentiation formulas [59].

3.3 Plug Flow Reactor Model

3.3.1 Overview

One of the approaches to model the bulk gas properties in the experiment, which is discussed in chapter 4, was with a plug-flow reactor (PFR). A plug flow reactor is an idealized one-dimensional steady-state reactor, where gas composition is assumed to be perfectly homogenous in the radial direction but can vary axially. The governing mass, species, energy and momentum equations for a plug flow reactor can be derived by considering a differential control volume, and details provided by Kee and Turns [46,60]. The resulting governing equations for an ideal gas, with soot source terms (**bolded**), are the following:

Mass Conservation

$$\frac{d(\dot{m}_g)}{dz} = -V\sum_{k=n}^{N} \boldsymbol{\omega_{s,k}} M_{W,k} \tag{3.18}$$

Species Conservation

$$\rho u \frac{dY_k}{dz} = A_c(\omega_k + \omega_{s,k})W_k - Y_k V\sum_{k=n}^{N} \boldsymbol{\omega_{s,k}} MW_k + \frac{d}{dz}\left(\rho D_k \frac{dY_k}{dz}\right) \tag{3.19}$$

Energy Conservation

$$\dot{m}_g c_p \frac{dT_g}{dz} = -A_c\sum_{k} h_k\ (\omega_k + \boldsymbol{\omega_{s,k}})M_{W,k} - V\sum_{k=n}^{N} h_k \boldsymbol{\omega_{s,k}} M_{W,k} + \boldsymbol{N_s} V\left(\boldsymbol{\dot{Q}_s} + \frac{\sum_{k=1}^{n} h_k \boldsymbol{\omega_{s,k}} M_{W,k}}{\boldsymbol{N_s}}\right) + \dot{Q}_{source} \tag{3.20}$$

Momentum Conservation

$$\dot{m}\frac{d(u_z)}{dz} = -u_z V\sum_{k=n}^{N} \boldsymbol{\omega_{s,k}} M_{W,k} - \frac{d(pA)}{dz} - \tau_w P' \tag{3.21}$$

The mass conservation equation describes the change in gas mass in the axial direction to gas mass exchange with soot. This equation is coupled with the soot model, which is discussed in section 3.8. The species conservation equations relate change in axial gas mass fraction to gas-phase reactions, consumption or production in heterogenous soot reactions, and diffusion of species – D_k is the mass diffusivity. The energy conservation equation, written in constant pressure form, relates the change in gas temperature - with the same ideal gas assumption employed in the

WSR model discussed in section 3.2 - to homogenous gas-phase reactions, heterogenous soot reactions, energy exchange with the soot particle phase, and heat source term. The heat source term is the same as shown in equation 3.16. Finally, the momentum equation relates the change in axial gas momentum to momentum loss in forming soot particles, pressure, and shear stress at the wall from friction. The term P' is the perimeter of the reactor, which for a cylindrical reactor is equal to πD_c.

The second order diffusion term in the species equation necessitates solving the plug flow reactor as a boundary value problem, with a discretized mesh. However, since the Peclet number, which is the ratio of advective to diffusive transport, is >> 1 for most combustors – including the experiment being modeled, advection overshadows diffusion. This is especially true at higher pressures, since mass diffusion decreases with increasing pressure. As a result, the diffusion term can be assumed to be negligible. Eliminating the 2nd order diffusion term significantly simplifies solving the plug flow reactor since the equations now have flow properties change one-way and could be solved as a simpler initial value problem. In fact, the PFR could be modeled as a chain of WSR's, with each WSR sequentially integrated to steady state. Molin et al. showed that if the number of WSR's is large enough then the solution approaches that of a plug flow reactor [61]. This was the approach taken to model the PFR, as shown in Figure 3.3. The necessary number of reactors was determined by resolving the system with increasing number of reactors until temperature and species mass fractions converged.

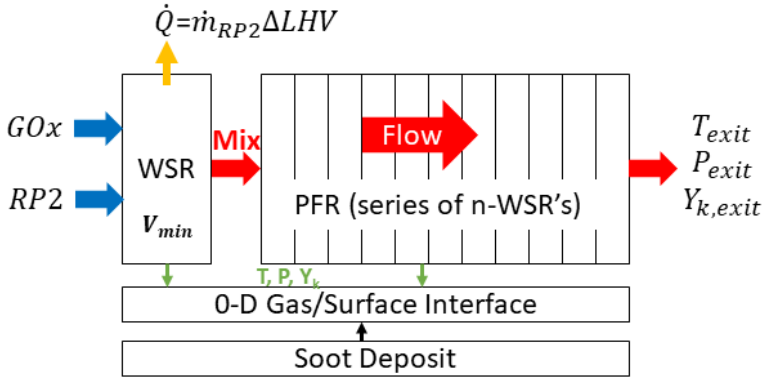

Figure 3.3 Plug Flow Reactor Model Overview

The PFR model was assumed to be at constant pressure for the entire domain and frictionless. A chain of WSR's modeled the PFR, with the WSR model described in section 3.2.

The PFR pressure was either imposed or iterated based on the calculated outlet mass flow from the last WSR in the series, as will be described.

RP-2 fuel and gaseous oxygen oxidizer were introduced into the first well stirred reactor at a specific mixture composition, with the inherent pre-mixed assumption. The reactor equations can only handle gaseous propellants. The liquid RP-2 was modeled with two approaches. First, it was assumed to be entirely in gas state, and the enthalpy of vaporization accounted for in the energy equation, as described in section 3.2. A more realistic approach was to model vaporization with the D^2 law and only introduce vaporized portion of RP-2 into the reactors. Since not all the fuel is instantaneously vaporized, this approach predicted a higher mixture ratio near the inlet, and hence a higher temperature in the experiment. This approach is discussed in section 3.3.2.

In order to have an ignited solution, the residence time in the first reactor needs to be long enough for the chemistry to react. Otherwise, the reactor would blowout, and since information doesn't propagate upstream in the model, the inlet to all subsequent reactors would just be cold propellants – resulting in a trivial solution. The residence time is controlled via the volume of the first reactor, which was iterated via a bisection algorithm to find the minimum that results in an ignited solution. Additionally, the initial condition for the first reactor was arbitrarily set to the equilibrium composition and the reactor integrated to steady state. The ignited steady state solution is independent of the initial condition.

Once the first WSR was solved, the WSR's in the sequence were sequentially integrated to steady state using the upstream reactor solution as the inlet condition. The volume of each of these reactors was equal and were determined by subdividing the total plug flow reactor volume by the number of constituent WSR's. An arbitrary 50 number of WSR's were initially used to model the PFR and calculate the gas property distribution within the domain. The number was then sequentially increased by 1.5, and the overall system re-solved until the relative and absolute difference for all the scalars between the current and previous solution were less than 1e-5.

All the WSRs in the PFR were modeled with the constant volume formulation, so that the volume of each WSR could be explicitly set, but used the constant pressure mass flow condition, as described by equation 3.7, for all except the last WSR. If a constant pressure was imposed for the PFR, then the last WSR was also solved with the constant pressure mass flow condition. Otherwise, the outlet mass flow rate for the last WSR was calculated with compressible mass flow rate relation, described by equation 3.8, with an input outlet area and outlet pressure. The PFR

pressure was then iterated until the calculated outlet mass flow rate matched the inlet mass flow rate to within 0.01%. This second approach was used to model the experimental conditions described in section 4.3.

The solution in each WSR was then extracted and used in a accompanying surface reactor to calculate the soot deposit growth rates due to heterogenous surface reactions. The heterogenous soot surface reactor is described in section 3.5.

3.3.2 Liquid injection and Droplet Burning

Droplet vaporization requires some finite amount of time and as droplets vaporize, the gas mixture ratio decreases. In fuel rich combustion with liquid kerosene, there can be a hotspot near the injector because of an initially larger gas mixture ratio. This hot-spot provides energy to drive the gas-phase reactions and vaporize the remainder of the propellants. Not capturing the finite droplet vaporization and assuming the injected propellants are all in gas phase can affect the temperature and species predictions – and possibly produce incorrect predictions. As an example, fuel rich kerosene gas generators typically operate at a mixture ratio less than 0.5 and have a hot region near the injector that drives the chemical kinetics. Modeling this with a WSR by assuming the propellants are instantaneously vaporized would result in a gas temperature that is too low to sustain combustion and in turn would result in blowout - unless there is an artificial higher temperature defined to drive the chemical kinetics [62–64]. Including droplet vaporization in a PFR model though produces the correct behavior, as described in section 3.3.3.

The PFR and WSR models calculate reactions and properties in the gas phase - modeling injection or vaporization requires supplementary equations. The injector droplet diameters in this work were calculated with the Ingebo correlation [65] and then vaporization was modeled with D^2 law, using the fuel properties of RP-1 from National Institute of Standards and Technology [66].

The droplet vaporization calculation assumed uniform droplets with a certain mean droplet diameter. In the soot experiment, a Fuel-Oxidizer-Fuel injector was employed to inject and atomize the kerosene propellant. As discussed in section 4.4.2, the injector configuration had two liquid RP2 impinging jets through a GOx core flow. The mean droplet diameter for this specific injector configuration was calculated with the Ingebo correlation, which was developed for impinging sprays in an airstream [65]:

$$\frac{D_j}{D_{30}} = 2.64\sqrt{D_j V_j} + 0.97 D_j \Delta V \quad (3.22)$$

The parameters in the correlation are the orifice diameters (D_j), the volume number mean drop diameter (D_{30}), the liquid-jet velocity (V_j), and the velocity difference between the airstream and the liquid jet (ΔV), which in this case is the difference between the kerosene and gaseous oxygen velocities.

Afterwards, the droplet vaporization was calculated via the D^2 droplet burning model as described in Lefebvre's Atomization and Sprays textbook [67], assuming droplets are all uniform, independent, and consist of only a single fuel species. This is a significant simplification for modeling droplet evaporation and burning of heavy multicomponent fuels, including RP-2, since it consists of many constituents with a large variation in physical and chemical properties. The evaporation process also consists of lower boiling point volatile components evaporating first, along with thermal decomposition within the drop producing heavy tars followed by slower heterogenous combustion of the residue, and potential for explosive ejection of smaller drops from the initial drop [67,68]. Additionally, a soot shell can form in between the droplet and flame [69], which can affect both droplet vaporization and initial soot formation. These effects were not included in the interest of developing a simpler model and since droplet vaporization was not thought to significantly impact soot deposition, which was the primarily focus of this work.

The droplet evaporation model employed assumed steady state evaporation, with a uniform droplet temperature equal to the surface boiling temperature. Additionally, the heat supplied to vaporize the droplet was from gas phase combustion. With these assumptions, the droplet diameter can be described with the following relation:

$$\frac{dD_{drop}}{dt} = \frac{4k_g \ln(1+B)}{\rho_l C_{p,g} D_{drop}} \quad (3.23)$$

Where D_{drop} is the instantaneous droplet diameter, k_g is the gas conductivity, B is the heat transfer number, ρ_l is the liquid density, and $C_{p,g}$ is the gas specific heat capacity. The heat transfer number compares the enthalpy of the surrounding gas to what is required to vaporize the liquid and can be written as:

$$B = \frac{c_{p,g}(T_g - T_b)}{LHV} \quad (3.24)$$

Where T_g is the gas temperature, T_b is the liquid boiling temperature, and LHV is the latent heat of vaporization.

Then assuming the droplet maintains a spherical shape as it evaporates, the rate of gas produced from liquid vaporization can be expressed as:

$$\dot{m}_{vap} = 2\pi D \left(\frac{k}{c_p}\right)_g \ln(1 + \frac{c_{p,g}(T_f - T_b)}{L}) \quad 3.25$$

This relation is true for quiescent droplet vaporization, but convection can greatly enhance droplet vaporization. Ranz and Marshall studied heat transfer and evaporation of droplets developed a correlation to predict droplet evaporation rates due to convection [70]. The enhanced rate of gas produced from liquid vaporization can then be written as [67]:

$$\dot{m}_{vap,conv} = \dot{m}_{conv} * (1 + 0.3 * R_e^{0.5} P_r^{0.33}) \quad 3.26$$

Where $\dot{m}_g$ is the quiescent gas vaporization rate, R_e is the Reynolds number with respect to the droplet, and P_r is the Prandtl number.

Both the quiescent and convective vaporization rate models were incorporated in the PFR model. To couple these to the PFR, the liquid droplet diameter was first calculated with equation 3.22 – with all droplets assumed to be of uniform diameters. The number of liquid droplets was also determined by dividing the total liquid mass by the mass of each droplet as:

$$N_{drops} = \frac{\dot{m}_{liq}}{\frac{\rho_{liq}}{6}\pi D^3} \quad 3.27$$

This established the initial droplet diameter and droplet mass. Afterwards, to start the calculation the propellants (both liquid and gas) in the first WSR of the PFR were assumed to be at equilibrium and WSR integrated to steady state. The residence time in the first reactor was then calculated based on the WSR properties and total gas outlet mass flow rate as:

$$\tau_{res} = \frac{\rho_{gas} V_{WSR}}{\dot{m}_{gas}} \quad 3.28$$

With the gas properties and residence time, the total vaporized droplet mass was calculated by integrating either equation 3.25 or 3.26 from zero to τ_{res} and multiplying by the total number of drops from equation 3.27. If the total vaporized mass equaled the initial liquid mass, then that meant all the liquid was vaporized within the first WSR, and the WSR droplet model was converged. Otherwise, if only a portion of the liquid mass was vaporized then the WSR gas inlet

was updated to only include the vaporized partition. The WSR was then resolved to steady state and the new vaporized amount of liquid calculated with the updated WSR gas properties. The WSR was then iterated until the vaporized mass was within 1e-5 of the previous calculation. Once the WSR was converged, the final droplet diameter was calculated by integrating equation 3.23 from 0 to τ_{res} and using the initial droplet diameter as the initial condition. The total gas mass and remaining liquid mass was also calculated. An overview of the WSR droplet solution approach is shown in Figure 3.4.

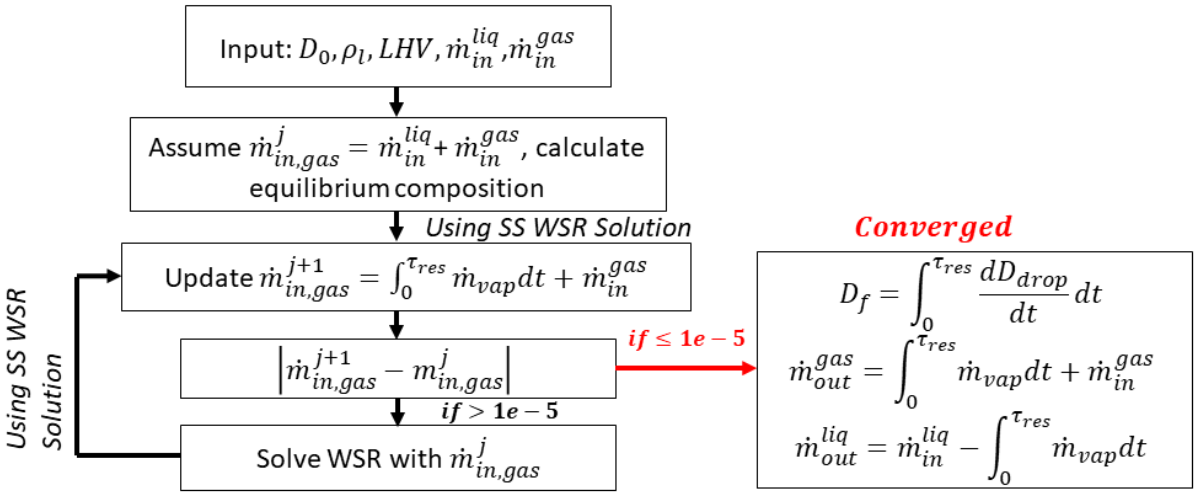

Figure 3.4 PFR/WSR solution approach with consideration of droplet vaporization

In the PFR model, the WSR was solved with the approach shown in Figure 3.4 if there was any liquid fuel remaining at the inlet. Otherwise, if all fuel was vaporized then the PFR was simply solved as discussed in section 3.3.1.

It should be also noted that the first approach was to solve the droplet equations directly coupled with the WSR equations where the gas inlet was a function of the integrated vaporized mass, without iteration. These were incorporated in a python function that was integrated with the SciPy backward-differentiation formulas ODE solver [57–59], which used a numerically calculated Jacobian at every time step. Droplet vaporization in some cases, especially when soot was included, was very sensitive to changes in WSR gas properties, which in turn increased the stiffness of the overall system and resulted in a long computation time. The iterative approach allowed for faster computation time by having constant gas inlet properties during every iterative step.

3.3.3 Validation

The plug flow reactor predictions were compared with high pressure kerosene preburner testing discussed by Lawver and Schoenman [71,72]. Several liquid oxygen and liquid RP-1 pre-burner configurations were studied for a high-pressure staged combustion application. The conditions examined included fuel-rich pre-burners in the mixture ratio of 0.2-0.4. Though this mixture ratio range is predicted to produce little soot because the gas temperatures are small, the measured bulk chamber pressure and C^* from the testing provided good data to compare the PFR bulk gas predictions and verify trend predictability. Specifically, the test conditions that were modeled with the PFR are shown in Table 3.1.

Table 3.1 Fuel Rich Kerosene Preburner testing conditions [71,72] that were modeled with PFR

Propellants	Liquid Oxygen, Liquid RP-1
Chamber Pressure (**Assumed Constant**)	2200 psia
Mixture Ratio	0.2-0.4
Total Propellant Flow	16.8 kg/s
Combustion Length	31 in
RP-1 Droplet Size (**Assumed**)	70 μm

The propellants burned in the pre-burner testing were liquid oxygen and liquid RP-1. As a simplification, the oxygen was assumed to be injected as gas since it has a much lower vapor pressure. RP-1 vaporization was calculated with the droplet vaporization model described in section 3.3.2. The chamber pressure conditions in the testing varied from ~1700-2200 psia but a constant pressure of 2200 psia was assumed in all the PFR parametric simulations discussed in the section. The effect of pressure on gas temperature and species fraction was verified to be minimal in this range. Additionally, the PFR model assumes ideal gas whereas at these high pressures and lower temperatures real gas effects would become important. The predicted trends though would still be consistent – the main goal of the PFR was to validate trend predictability.

A total propellant flow rate of 16.8 kg/s was flown and the fuel rich preburner operated at a mixture ratio in the range of 0.2-0.4. Several combustion chamber lengths were also tested but the data showed minimal effect on gas temperature and C^*. In the PFR model, a constant chamber length of 31 in was used. Finally, the droplet size for the RP-1 depends on the relative difference between the liquid and gas streams, which in turn depends on mixture ratio and chamber

conditions. For simplicity, the initial RP-1 droplet size was assumed to be 70 μm for all conditions, which is about what was calculated by Lawver [71]. This assumption affects prediction of the absolute values, but the trends with mixture ratio should still be consistent.

The PFR model was then setup for the conditions shown in Table 3.1. The detailed HyChem RP-2 POSF5433 [14,15] containing 112 species and 841 reactions was used to calculate reaction rates. The RP-1 fuel was modeled as RP-2, which has similar properties. The preburner gas temperature data and comparison with the PFR model are shown in Figure 3.5. The measured *C** data from the pre-burner predicted *C** and comparison with the data are also as shown in Figure 3.6. The data points from the model comparison were extracted from the plots in Lawver's report with WebPlotDigitizer [73]. The *C** was calculated from the PFR solution as:

$$C^* = \sqrt{\frac{R_u T}{\gamma M_{w,mix}}} \left(\frac{\gamma+1}{2}\right)^{\frac{\gamma+1}{2(\gamma-1)}} \tag{3.29}$$

Where the properties from the last WSR in the PFR chain were used to calculate *C**, and γ is the specific heat ratio calculated as $\frac{c_p}{c_p - R}$.

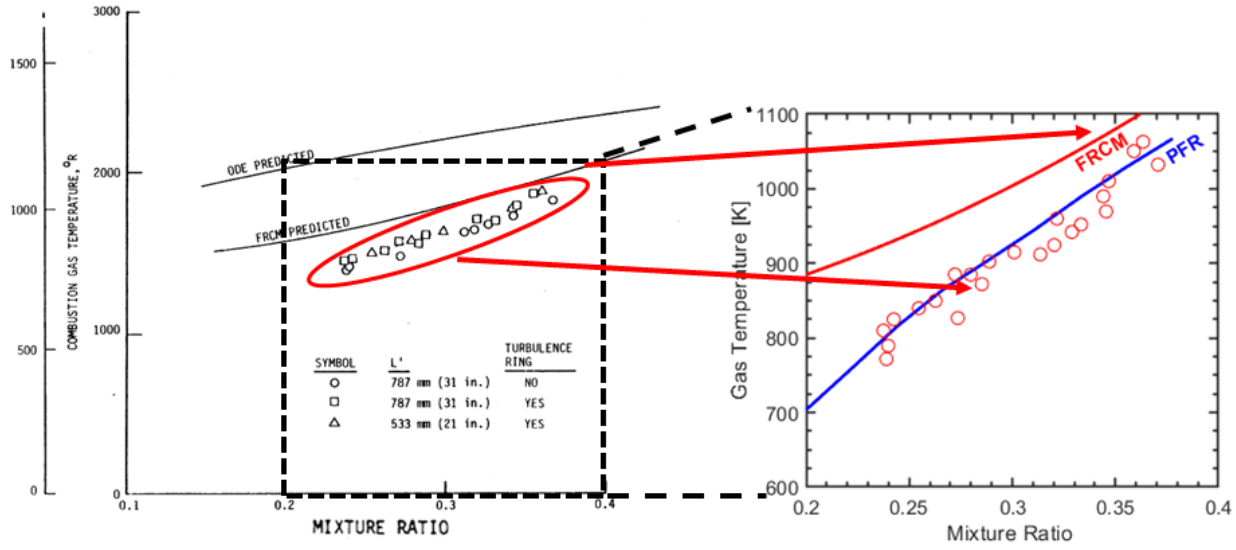

Figure 3.5 Measured gas temperature from fuel rich pre-burner testing [71] [Left] and comparison with PFR predictions [Right]

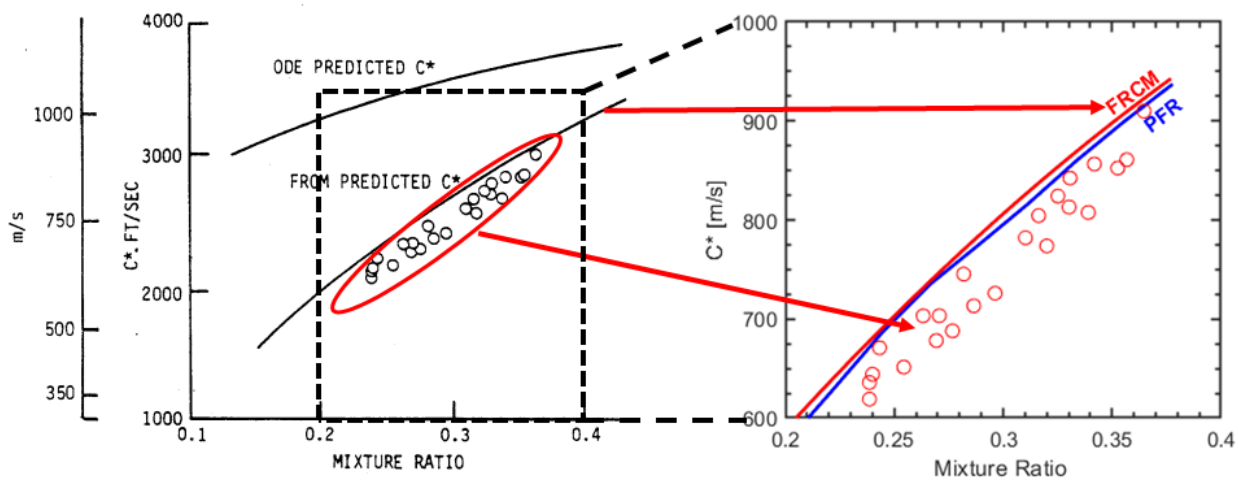

Figure 3.6 Measured *C** from fuel rich pre-burner testing [71] [Left] and comparison with PFR predictions [Right]

Lawver compared the fuel-rich pre-burner data with equilibrium prediction, as well as from a fuel rich combustion model developed during the program. As the left plot in Figure 3.5 and Figure 3.6 show, the equilibrium predictions had similar trend but resulted in higher temperature and *C** velocity predictions. This is consistent with the discussion provided in Chapter 2 on fuel rich combustion. The fuel rich combustion model was developed to improve predictability by assuming that combustion happens in two steps. First all the oxygen is vaporized and is at equilibrium with a small amount of vaporized fuel, afterwards kinetics are taken into account to predict gas properties for the residence times at the different conditions [71,72]. This improved predictability with data. In the PFR, droplet vaporization was considered, and the amount of gaseous fuel propellant added in each reactor dependent on the amount of the fuel that was vaporized. The PFR approach predictions were consistent with the fuel rich combustion model, and provided slightly improved predictability of gas temperature in the 0.2-0.4 mixture ratio range as shown on the right of Figure 3.5. The predicted *C** velocity with the PFR was also within 10 m/s of the fuel rich combustion model and provided good agreement with the pre-burner data.

Though the conditions provided in these pre-burner results were outside the range of interest for this work, these were the closest found in open literature. These results provided confidence in the plug flow reactor model formulation before moving forward with the modeling effort.

3.4 Reacting Flow CFD

3.4.1 Overview

Two-dimensional axisymmetric reacting flow simulations were run to verify the bulk 1-D PFR predictions and to investigate the effect that boundary layers could have on near-wall soot growth rates. The simulations were run with the General Equations and Mesh Solver (GEMS), which is a Fortran CFD code that has been developed over a 20-year period by Professor Merkle's research group at UTSI and Purdue University [74,75]. GEMS is a finite volume density-based solver for the multi-species reacting Favre averaged conservation equations. GEMS has previously been used to study a variety of problems including combustion instability, hypergolic propellant modelling and rotating detonation engines [74,76,77].

In this work, GEMS was used to solve the discretized reacting flow conservation equations with second order spatial and temporal accuracy. The code employs pseudo-time stepping to temporally step through the conservation equations while handling the added stiffness from reaction kinetics. Wilcox's k-ω turbulence model was used for turbulent closure, with the original parameters from [78]. Ideal gas was assumed for the equation of state in this work. Furthermore, the thermodynamic and transport properties for each species were calculated based on the NASA piecewise polynomial functions, as described by [79]. Viscosity and thermal conductivity curves were generated for each species as a function of temperature via kinetic theory, as described in the Chemkin manual [53], using the HyChem thermodynamic and transport data. These curves were then fit by least squares to the NASA polynomial function, and the function used in GEMS calculations. Mixture properties for viscosity, thermal conductivity, and mass diffusivity were calculated via the mixing rules of Bird and Mathur [80,81].

GEMS can handle several types of boundary conditions. In this work, a mass flow inlet, no-slip wall, and supersonic outlet pressure boundaries were employed. The boundary conditions are implemented via a ghost cell approach. The mass flow inlet required defining: massflow rate, temperature, species fraction. The velocity and pressure are then calculated from these inputs. The wall boundary conditions assumed no flow normal to the boundary and zero velocity on the boundary. Finally, the supersonic outlet pressure boundary required defining a pressure that was lower than the pressure upstream to choke the flow. If this was met, then the flow would only flow in one way, with no information propagating upstream. The Roe flux scheme was used at the cell

interface. The conservation equations, along with the source terms, were then solved implicitly via the line Gauss-Seidel algorithm. Further details about the numerical schemes are provided in [74,82].

3.4.2 Model Setup

The fuel rich reacting flow-field was modeled via a two-part approach, with several simplifying assumptions. First, a plug flow reactor calculation was run for a specific mass flow rate and chamber pressure condition. Afterwards, the solution at a point in the PFR where the reaction rates had decayed below a certain value was extracted and used as a uniform inlet condition in a two-dimensional axisymmetric reacting CFD model. Though this likely produces a nonphysical velocity condition at the boundary, the domain was set up to be long enough to allow for the flow to achieve full development. All results discussed in this dissertation primarily focus on the fully developed region, which should be mostly independent of the inlet velocity profile. The near-wall flow solution in this region was then extracted and used in a zero-dimensional soot surface reactor to estimate soot surface growth rates at the chamber wall. The soot surface reactor is discussed in section 3.5. This approach reduced the computational cost of solving for the near-wall flow properties in the fully developed region by at least a factor of a hundred compared to running a full 2-D axisymmetric simulation with ignition kinetics - as will be described.

Detailed modeling of ignition and droplet vaporization involves a large range of spatial and temporal scales, and possibly requires solving for two-phase flow. In particular, the ignition kinetics are very stiff, and this requires solving the reacting equations with small time steps. Initial reacting CFD simulations showed that the time step required in GEMS to run a full reacting simulation would have needed to be less than 1e-8 s, as simulations were diverging after a couple hundred-time steps with this time step. However, since these effects are not particularly important for modeling the near wall environment – the main interest of this work, these were modeled with the relatively inexpensive PFR. Details of the PFR are described in section 3.3. The kinetics in the PFR were calculated with the detailed 112 species-841 reaction HyChem POSF5433 RP-2 mechanism [14,15].

The PFR solution was then used to generate the inlet boundary conditions for the reacting CFD and then solved until steady state convergence. The computational approach is shown in Figure 3.7 and the parametric cases that were run in this study summarized in Table 3.2. These

cases included low flow, small bulk velocity conditions, that were representative of the experimental conditions; and higher flow, higher bulk velocity cases, for comparison of boundary layer effects in these two different flow regimes. The low flow conditions were all at a constant mass flow rate of 0.03 kg/s and the bulk pressure regulated via a choke plate (with throat area calculated based on 1-D equilibrium calculation for a specific pressure). The high flow cases were at constant contraction ratio of 3 and the mass flow set for a specific bulk chamber pressure (also calculated via a 1-D equilibrium calculation).

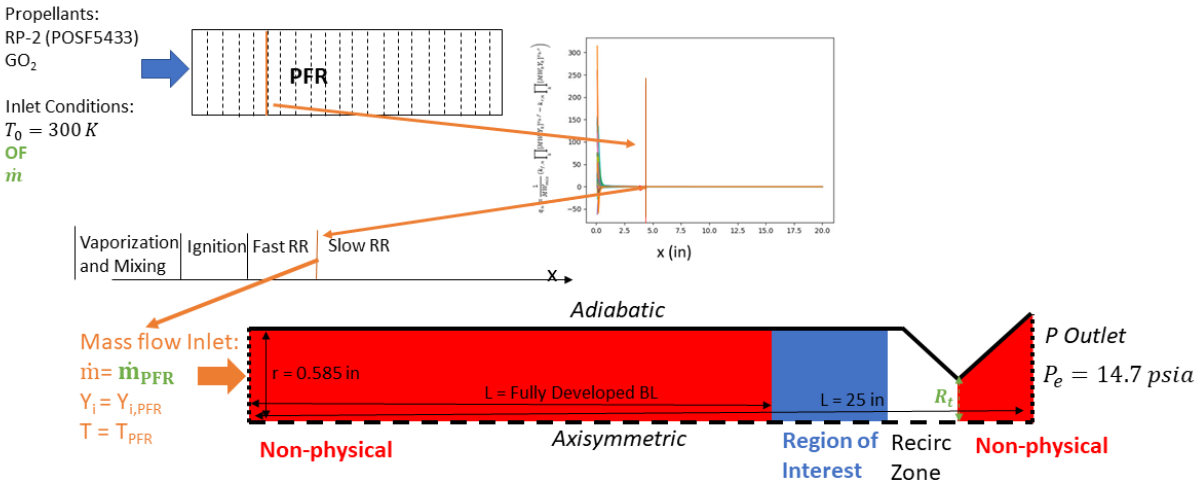

Figure 3.7 Two part reacting flow model combining a plug flow reactor with 2-D reacting CFD

Table 3.2 Reacting Flow Parametric Study Conditions. Headings in orange are model inputs and bolded values correspond to the experimental conditions. The *italic* conditions are the low flow conditions, and the rest are high flow conditions.

Throat Diameter [inch]	Bulk Pressure (psia)	Bulk Mass Flow [g/s]	Bulk Velocity [m/s]
0.308	***250***	***60***	***~ 50***
0.338	250	144	~ 200
0.218	***500***	***60***	***~ 20***
0.338	500	286	~ 200
0.179	***750***	***60***	***~ 15***
0.338	750	430	~ 200
0.155	***1000***	***60***	***~ 12***
0.139	*1250*	*60*	*~ 10*
0.127	*500*	*60*	*~ 8*

The model domain in the reacting flow CFD is a simplification of the soot deposit experiment, which will be discussed in the next chapter. The domain contains a diverging nozzle section to ensure that flow becomes supersonic and choked at the throat, whereas the experiment only has a converging section as seen in Figure 4.1. The flow in the diverging section is fictious but since the flow is choked at the throat, it does not affect the upstream solution. The diverging section was added because the flow was not choking without it in about two or three cells near the exit boundary and this was causing convergence issues. The cross-sectional radius of the constant area was set to the soot experiment cross sectional radius of 0.585 inch. The throat radius was calculated for a specific chamber pressure based on equilibrium one-dimensional isentropic flow:

$$r_t = \left(\frac{\dot{m}}{\pi P_c}\right)^{\frac{1}{2}} \left(\frac{T_t R}{\gamma MW}\right)^{\frac{1}{4}} \left(\frac{\gamma+1}{2}\right)^{\frac{\gamma+1}{4(\gamma-1)}} \quad 3.30$$

As mentioned, the inlet boundary condition was determined from the PFR solution. The PFR model was solved to get the bulk gas distribution within the combustor. The rates of each reaction and rates of radical production in each WSR that comprise the PFR were also calculated. The solution at the location where the reaction rates decayed below a certain value and the rates of radical production were monotonically decreasing with axial length was used as the inlet condition. It was found that the chemistry was less stiff after this region and the reacting flow CFD could be run with a larger time step. For all the cases in Table 3.2 this was within 2.5 - 3.5 inches. For consistency, the plug flow temperature and species mass fraction solution at 4 inches was used for generating the inlet boundary condition. A mass flow boundary condition with uniform velocity (calculated based on mass flow, cross sectional area and density) was then imposed at the inlet. The uniform velocity profile is likely a non-physical boundary condition for the soot deposit experiment and instead depends on injection parameters, droplet vaporization, kinetics, etc. This in turn could affect how the boundary layer develops. However, for simplification, the details of boundary layer development were ignored and instead the domain was set up to be longer than the estimated turbulent entrance length (estimated based on correlation in Fundamentals of Fluid Mechanics textbook [83]) so the flow can become fully developed. Though the initial developing region is non-physical, the fully developed solution should not be substantially affected. As will be discussed in the next chapter, the experiment was initially designed to be long enough for the boundary to fully develop so the measured soot deposit results could be consistently compared with these model predictions. Later modeling though showed a long experiment was not

necessarily, and the experimental combustion chamber was shortened. The outlet was set to a pressure boundary with a pressure of 14.7 psia (arbitrary pressure below choking limit that does not affect the choked solution in the constant area section) and an axisymmetric boundary condition was used at the centerline with no-slip at the walls.

Furthermore, the thermal boundary condition of the wall has an impact on solution of the flow-field energy equation, which in turn affects the kinetics rates. This effect was estimated for RP-2 and GOx combustion in a 0-D WSR. Simulations were run at a mixture ratio of 1 for a range of pressures and residence times with adiabatic and isothermal chamber wall conditions. The heat flux for the isothermal case was determined with a convection coefficient calculated from the turbulent Dittus-Boelter correlation [54] with a wall temperature of 300 K (corresponding to the initial wall temperature in the soot deposit experiment). The detailed POSF5433 HyChem Mechanism was used for the calculation [14,15]. The gas properties at the different conditions were determined by integrating the WSR to steady state. Afterwards, the solution was also used to compute soot growth rates via the HACA mechanism, which will be discussed in section 3.5. The results of the calculation are shown in Figure 3.8.

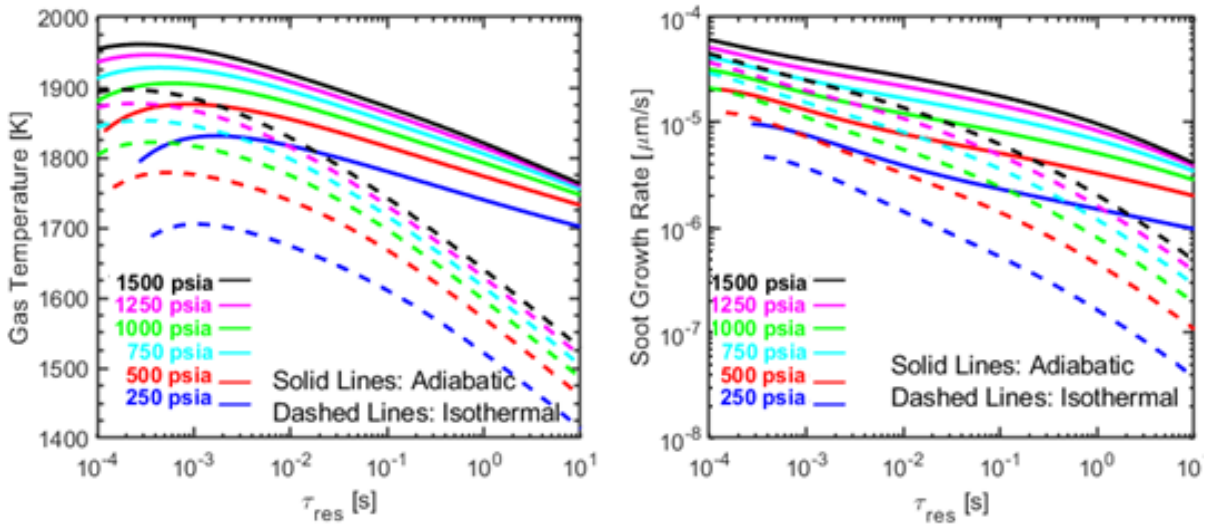

Figure 3.8 Comparison of Adiabatic and Isothermal (T=300 K) wall temperatures on gas temperature [Left] and predicted soot growth rates [Right].

The 0-D WSR results show a 300K isothermal wall boundary condition can produce a temperature drop of about 200 K compared to adiabatic for WSR residence times in between 1e-3 to 1e-2 seconds – approximately the residence time of the gas in the soot deposit experiment. Not shown, but this drop in temperature affects kinetic rates of the bulk gas and produces lower concentrations of radicals and acetylene. As a result, the predicted soot growth rates are lower as shown on the right of Figure 3.8. However, the trends in the temperature and growth rates are consistent at both the isothermal and adiabatic conditions. In the experiment being modeled, the isothermal boundary condition would represent the initial boundary condition during propellant ignition whereas the adiabatic condition would be the upper limit as the walls heat up and soot deposits on the wall. Hence in the experiment, the gas conditions would likely sweep in between the dashed lines and solid lines at the different conditions shown in Figure 3.8. Additionally, fuel rich combustion produces lower chamber heat flux, in contrast with stoichiometric combustion, which also decreases with run-time as the walls heat up and soot deposit accumulates on the surface. Therefore, an adiabatic boundary condition was employed in the CFD model as an approximation of the heat transfer at close to steady state conditions. The predicted magnitude of soot growth rates was also larger, and since the trends are consistent at the different conditions, it was thought it would make it easier to differentiate the results in the CFD.

The reacting CFD simulations used the reduced POSF5433 HyChem mechanism containing 38 species and 192 reactions.[18,84] to calculate the reaction source terms. The PFR calculations were performed with the detailed HyChem mechanism and in order to accurately balance the mass fractions at the inlet boundary conditions (to ensure they sum to unity and the species mass fraction ratio stays consistent), the mass fractions from the detailed mechanism were normalized by the sum of the mass fractions of the species present in the reduced mechanism.

The simulations were initially run to steady state as non-reacting to verify proper convergence of the numerical solution. This case was first run with the steady state solver, and then with the unsteady solver with a time step of 1e-6 seconds for at least 3 flow through times to ensure steady state conditions (the flow through time was estimated for each case based on bulk velocity and domain length). The initial conditions in all cells were arbitrarily set to the inlet conditions. Twenty-eight point probes were set up to output the temperature, pressure, species, and velocity at every time step situated at the centerline and wall at 1 inch axial spacing location, from

10 inch to 24 inch. The final bulk averaged steady state solutions were all within 5% of isentropic pressure and velocity predictions.

Afterwards this solution was used as the initial condition for a reacting flow case and run as unsteady with a time step of 1e-6 seconds for the low bulk velocity case, and a time step of 5e-7 seconds for the higher bulk velocity case. By not modeling the stiff ignition kinetics, the simulation could be run with this larger time step. As mentioned earlier, the initial CFD effort tried to model ignition directly for the low flow conditions, however the minimum time step required for numerical stability was less than ~1e-8 seconds, which would have resulted in at least two orders of magnitude extra computational time. All the cases were run on Purdue's Rosen Center for Advanced Computing Brown Cluster on the shared community cluster using 15 nodes with 24 Intel Xeon Gold 6126 cpu's. Each case took about one week to compute.

3.4.3 Spatial and Temporal Convergence Study

Mesh and time step convergence studies were performed for the 500 psia case prior to running the remainder of the simulations in the parametric study. Three structured mesh's of varied refinement were generated: coarse, nominal and fine. All the mesh's were generated with Ansys ICEM CFD via blocking approach [85]. The nominal mesh was created by first estimating the near-wall cell height for a y+ value of 1 for isentropic flow. This is critical for properly modeling the laminar sublayer and shear stress at the wall with the $k-\omega$ turbulence model. The first cell was then set to this value and 30 radials cells were created with a bigeometric distribution with a growth rate of 1.3. The axial cells in the constant area section were uniformly spaced with 800 cells, corresponding to about a spacing of 0.0275 in. The mesh spacing was further refined at the nozzle corner and in the nozzle where the flow velocity has larger gradients. The total number of cells was 27240 cells, and the mesh overview shown in Figure 3.9. A course mesh was then created by decreasing the radial cells to 25, increasing the growth rate to 1.4, and decreasing the axial cells to 700. This resulted in 19825 cells. Furthermore, a finer mesh was also created by increasing the number of radial cells to 35, decreasing the growth rate to 1.2, and increasing the number of axial cells to 900. The corresponding cell count was 33880. These mesh's were then partitioned with METIS in order to be solvable by parallel computing with message passing interface. [86]

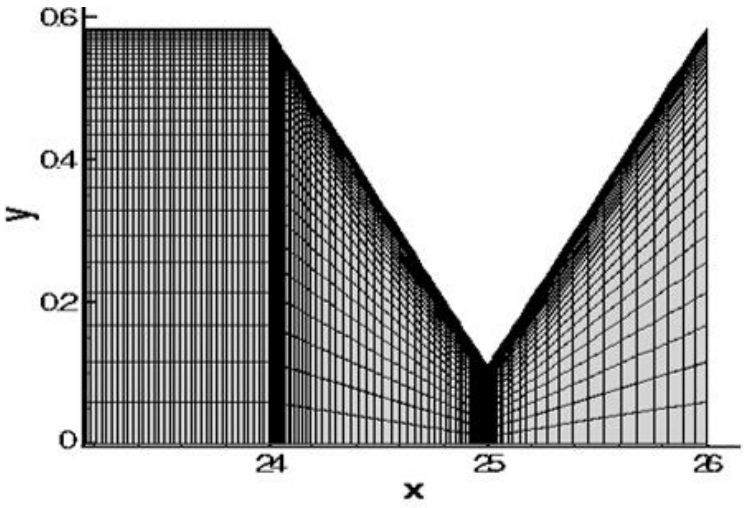

Figure 3.9 Nominal mesh (27240 cells) overview, truncated to the end of the domain. The x and y spatial coordinates are in inches.

All three meshes were run via the same reacting flow model approach as described in section 3.4.2, with a time step of 1e-6 s. The convergence of the non-reacting solution was first verified and compared with isentropic flow theory. Afterwards, reactions were turned on and the simulations run until steady state convergence. As will be discussed, reactions introduce some unsteadiness into the solution so in order to compare the average solutions from the three grids, the results were averaged for 1 flow through time. Subsequently, a temporal convergence study was performed with three different time steps for both the 500 psia low and high bulk velocity cases. The low flow case used time steps of 5e-7s, 1e-6 s, and 5e-6 s. The high flow case, due to a larger bulk velocity, used smaller time steps of 1e-7s, 5e-7s and 1e-6s.

The goal of the CFD was to assess the effect of near wall gas on wall soot growth rates. As such, the calculated soot growth rates were used to assess convergence for the different mesh and time steps. The soot growth rate was calculated by extracting the CFD solution near the wall and using it in a separate 0-D soot surface growth reactor. The soot reactor will be discussed in section 3.5. The calculated soot growth rates for the different meshes, and for the different time steps, are shown in Figure 3.10.

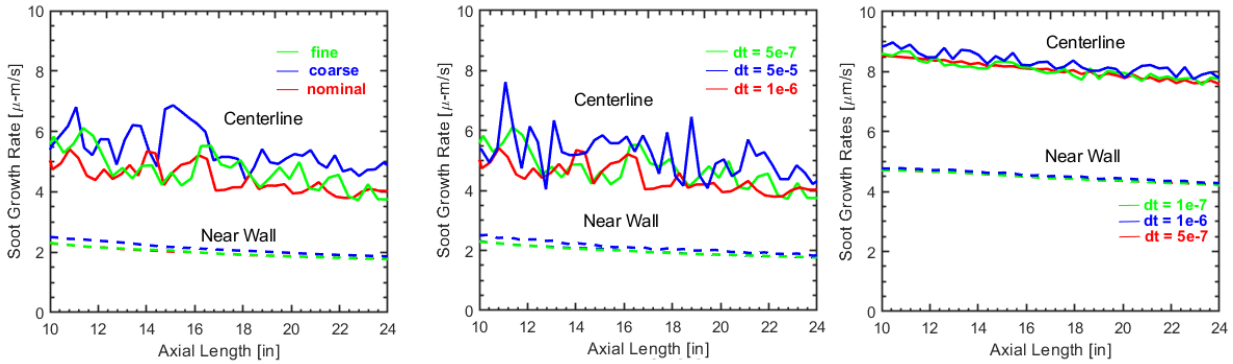

Figure 3.10 Mesh convergence (Left) and time step convergence for low bulk velocity (Middle) and high bulk velocity (Right) studies for CFD calculated soot growth rates for centerline (solid line) and near wall (dashed line).

3.5 Soot Surface Growth Reactor

The 1-D PFR model and 2-D Axisymmetric CFD models that were discussed in sections 3.3 and 3.4, respectively, were used to determine the bulk and near-wall gas solution. The soot surface growth rates were then calculated with a 0-D heterogenous surface reactor using the gas solution.

The wall surface growth rates due to heterogenous reactions with the gas were calculated by assuming the wall surface was initially covered with a thin layer of benzene rings, the smallest of the polycyclic aromatic. Additionally, a common assumption in literature for modeling soot growth is assuming chemical similarity between the surface of the soot molecule and the carbon-hydrogen edge of PAH molecule [22,45,87]. Moreover, the soot surface growth in the post flame region - where the soot deposit is measured in the experiment, is thought to predominately occur via the hydrogen abstraction and acetylene addition (HACA) mechanism [21,22,35]. Other growth mechanisms have also been postulated such as the addition of methyl, vinyl and proparyl [22,32,33]. However, Frenklach et al. studied the influence of fuel molecules on the chemical pathway to soot and found that regardless of what the initial pathway is followed for the formation of small PAH's, all the pathways relaxed to the HACA mechanism because of much smaller relative concentrations of other reactants downstream of a flame, and hence much smaller growth rates in comparison [34].

The soot surface growth was assumed to occur via the HACA mechanism. The HACA soot growth mechanism shown in Table 3.3, with the reactions and kinetic parameters from Appel et al. [87], was used to calculate to calculate the soot growth rates due to reactions with the gas phase.

Table 3.3 Soot Surface Growth Mechanism for soot growth prediction in the Plug Flow Reactor Model with kinetic parameters taken from [87]

Reaction	$A\ (\frac{cm^3}{mol-s})$	N	E $\left(\frac{kcal}{mol}\right)$
$C_{soot} - H + H \leftrightarrow C_{soot^*} + H_2$	$4.17e13$		13.0
$C_{soot} - H + OH \leftrightarrow C_{soot^*} + H_2O$	$1.0e10$	0.734	1.43
$C_{soot^*} + H \rightarrow C_{soot} - H$	$2.0e13$		
$C_{soot^*} + C_2H_2 \rightarrow C_{soot} - H + H + 2\ CB - CB3$	$8.0e7$	1.56	3.8
$C_{soot^*} + O_2 + 2\ CB - CB3 \rightarrow 2CO + products$	$2.2e12$		7.5
$C_{soot} - H + OH + CB - CB3 \rightarrow CO + products$	reaction probability = 0.13		

In modeling the surface chemistry, the total number of surface sites per unit area was set to 2.5e15 cm^{-2} as estimated by Wang and Frenklach [29], corresponding to the number of carbon-carbon rings of benzene per unit area. Growth was then assumed to occur via hydrogen abstraction acetylene addition at the active surface sites. The bulk soot growth rates corresponded to the net production rates of CB-CB3 in the mechanism.

The gas temperature and mass fractions from either the PFR or boundary values in the reacting CFD were extracted and used in a 0-D surface reactor. The surface coverage equation was then advanced to steady state, and is as shown below:

$$\frac{d\theta_k}{dt} = \frac{\dot{s}_k \sigma_k}{\rho_s} \tag{3.31}$$

Where θ_k is the coverage of species *k*, or the moles of species *k* per site density, $\dot{s}_k$ is the surface reaction rate of species *k*, σ_k is the total number of surface sites, and ρ_s is the site density. The thickness growth rate of the soot layer was then calculated as:

$$\dot{t} = \frac{d[CB - CB3]}{dt}\left(\frac{M_{W,c}}{\rho_{soot}}\right) \tag{3.32}$$

Where the molecular weight of Carbon ($M_{W,c}$) is 12.01 kg/kmol and the density of soot (ρ_{soot}) was set to 1.8 g/cm^3, which is a typical value used in soot formation models and represents the density of condensed phase carbon black [88,89].

The thickness growth rates were assumed to be steady and constant. This model provided initial insight of the soot growth behavior at various pressure and mass flow conditions and was used to guide the design of the soot deposition experiment, as will be discussed in the next chapter.

3.6 Volumetric Soot Modeling

3.6.1 Modeling Approaches Overview

The previous modeling discussion focused solely on trying to predict soot growth rates due to heterogenous surface reactions on the soot deposit surface. However as discussed at the beginning of this chapter, a major source of soot deposit is volumetric soot that is formed in the core flow and is transported to the chamber wall surfaces. Modeling this deposit process first requires modeling volumetric soot formation and growth.

At present, soot modeling is a challenging task because of the limited understanding of the chemistry and physics governing the formation and growth processes, as briefly described in the background chapter. Further complicating the task is soot in real flames encompasses a large range of particle sizes and number densities with different properties (mass, composition, surface area, …). Present models must make several significant assumptions about the soot particles that can't be easily verified experimentally, such as treating the soot particles as an amalgamation of pure carbon atoms with constant density or approximating a surface area for surface reaction calculations.

However, despite the limitations, several approaches with different levels of sophistication have been proposed to model soot. The models can be broadly classified into: empirical, semi-empirical, and detailed [25].

Empirical models are essentially experimental correlations. Typically, these attempt to predict the threshold equivalence ratio for premixed flame (equivalence ratio of when soot is observed), and threshold sooting height for diffusion flames (height at which soot emission is observed) [25,90]. These correlations depend on the fuel used, which can have different sooting tendencies. The threshold sooting index (TSI) was defined as an attempt to correlate flame and fuel properties to the threshold equivalence ratio from the measured sooting tendency [91]. In general, empirical models lack physical insight and may lack reliability outside of the experimental conditions where the data was collected.

Semi-empirical soot models attempt to describe some of the chemistry and physics behind soot formation and growth usually via 1 or 2 coupled differential equations, which describe soot number density and soot mass fraction [25,92,93]. This includes the 2 equation model proposed by Leung et al [93] and later modified by Guo et al. [94], which attempts to describe soot inception and evolution in terms of C_2H_2 concentration. The model assumes simplified soot nucleation and surface growth and oxidation reaction steps in calculating the soot number density and mass fraction. In these models, the reaction rate expressions are typically tuned to match experimental soot profiles and hence although they are more detailed than empirical models while also relatively cheap to solve, they may also lack reliability outside of the experimental conditions where they were calibrated.

Detailed models attempt to describe the soot particle size distribution (PSD) with more detailed physics and chemistry to describe the formation and growth of the sub-processes that occur in the gas phase, solid phase, and surface of the soot particles. These models can predict soot properties for a larger range of operating conditions but are more expensive and numerically difficult than the semi-empirical models. Detailed models of varying complexity have been proposed in soot related literature. Two of the widely used deterministic approaches in modeling the soot particle dynamics are the discrete-sectional method [30], and the method of moments [21,95]. The discrete sectional method can describe the soot particle size distribution by dividing it into several particle size bins and solving coupled differential equations for each bin that describe the evolution of each particle size. It can directly describe the PSD with good accuracy, however the amount of sections (and hence the amount of coupled equations that need to be solved) can get expensive. The method of moments approach attempts to model the evolution of the statistical moments of the PSD, rather than the PSD itself, from which the average properties of the PSD can be obtained. As a result, the number of moment equations that need to be are significantly cheaper than discrete sectional method while still maintaining good accuracy. Other models of even higher detail include a stochastic model to solve for the PSD [96], and molecular dynamics [20,97] that can provide a detailed description of the soot processes at the molecular level. However, these models are very expensive and can only be applicable to simplified flow-fields.

After an extensive literature review and discussion with soot modeling experts at CFD Research Corporation, the Method of Moments with Interpolative Closure (MOMIC) [95] approach seemed to offer sufficient accuracy for a high pressure fuel rich condition while being

numerically economical (especially since one of the initial ideas in the project was to incorporate it in a CFD framework).

3.6.2 Method of Moments with Interpolative Closure (MOMIC)

The main idea behind the method of moments is that the properties of particle size distribution function can be described by statistical moments, and knowledge of all moments is equivalent to knowledge of the distribution function [98].

The starting point for describing the particle size distribution are the Smoluchowksi master equations [99,100] which model Brownian collisions between aerosol particles (essentially non-reacting soot particles):

$$\frac{dN_i}{dt} = -\sum_{j=1}^{\infty} \beta_{i,j}\, N_i N_j \quad i = 1 \tag{3.33}$$

$$\frac{dN_i}{dt} = \frac{1}{2}\sum_{j=1}^{i-1} \beta_{j,i-j} N_j N_{i-j} - \sum_{j=1}^{\infty} \beta_{i,j}\, N_i N_j \quad i = 2,3,\dots,\infty \tag{3.34}$$

Where N_i is the number density of particle size i, $\beta_{i,j}$ is the collision coefficient between particle sizes i and j. The negative term represents the decrease in the ith particle size number density due to collisions with other particle sizes and the positive term represents the gain in the ith particle size due to collisions with smaller particles. These terms are dependent on the collision coefficient which in general is a function of $\beta_{i,j}(N_i, N_j, m_i, m_j)$ where m_i are the mass of particle size i.

In the method of moments, the particle size distribution is solved for by taking the moments of the Smoluchowski equation (along with additional reacting source terms which are not present in the equations). The concentration moment of the particle number densities is defined as:

$$M_r = \sum_{i=1}^{\infty} m_i^r N_i \tag{3.35}$$

Where m_i is the particle mass of the ith size class. In this formulation, the 0th moment is $M_0 = \sum_{i=1}^{\infty} N_i$ and corresponds to the total particle number density. The 1st moment is $M_1 = \sum_{i=1}^{\infty} m_i N_i$ and corresponds to the total particle mass density. From this the volume fraction can be calculated as $f_v = \frac{M_1}{\rho_{soot}}$. Higher order moments correspond to the variance, skewness, kurtosis and

other statistical properties of the distribution. By knowing all integer moments ($r = 0,1,2, \dots, \infty$), the particle size distribution is known. However, most of the properties of particle size distribution can be determined with accuracy for just a few moments. Hence this approach results in a significantly reduced numerical cost to calculating soot distribution properties.

Differential equations can be written to describe the evolution of each moment as follows:

$$\frac{dM_r}{dt} = R_r + G_r + W_r \tag{3.36}$$

Where R, G and W are the nucleation, coagulation and surface growth terms, respectively.

The nucleation term accounts for the creation of the smallest soot particle and contributes to the mass and number density of the particle side distribution. This is modeled with the simplified acetylene based nucleation model of Lindstedt et al. [101]. Typically, other MOMIC implementations base the nucleation term on the gas phase PAH, which requires using a large gas phase mechanism that includes details of PAH growth. However Mehta showed there is good accuracy in using the Lindstedt acetylene model compared to the PAH based nucleation model [45], and thus this model used the simplified approach. Also, the RP-2 HyChem Mechanism did not have PAH formation and would have required incorporating PAH steps from a larger mechanism – this would then have needed validation. The acetylene-based nucleation mechanism in contrast was much simpler.

Coagulation models the collision of smaller soot particles to form larger particles and depends on the Knudsen number. It also conserves the mass of the particle size distribution but decreases the number density.

Finally, surface growth contributes to an increase in mass of the particle size distribution, while conserving the number density. The surface growth rates are modeled with the Hydrogen-Abastraction-Acetylene-Addition mechanism.

The formulation of the sources is the same as discussed by Frenklach [95,102]. Details of the source term formulation are provided in Appendix A.

Furthermore, at higher pressures and increased residence times, the soot growth transitions from coalescent coagulation to agglomeration regime, as shown in Figure 2.4. As section 2.4 describes, in this regime the soot geometry starts to become fractal-like. This fractal geometry can be described via the fractal relationship [103]:

$$n = k_f \left(\frac{2R_g}{d_p} \right)^{D_f} \tag{3.37}$$

Kazakov et al. developed an extension to MOMIC to describe this agglomeration regime by writing additional moments to describe the number of primary particles in an aggregate soot particle [104]:

$$P_r = \sum_{i=1}^{\infty} n_i^r N_i \tag{3.38}$$

The evolution of these moments is described via additional differential equations:

$$\frac{dP_r}{dt} = R_0 + H_r \tag{3.39}$$

Where the terms on the right-hand side are the aggregate nucleation and growth terms. Additionally, the coalescent surface growth and coagulation terms are also modified to account for the change in the soot particle shape. The solution of the coagulate and aggregate moment equations can then provide the evolution of the soot PSD in the flow. Details of the aggregate terms are provided in Appendix A.

3.6.3 Soot Property Calculation

From knowledge of the moments, the average properties of the soot particle size distribution can be determined. These properties are derived and summarized in Table 3.4.

Table 3.4 Method of Moments Via Interpolative Closure Average Soot Quantities

Average PSD Properties:	Calculation:
Number Density	$\frac{n}{V} = M_0, P_0$
Average Diameter	$d_p = \left(\frac{6m_c M_1}{\pi \rho_{soot} M_0}\right)^{\frac{1}{3}} = \left(\frac{6m_c}{\pi \rho_{soot}}\right)^{\frac{1}{3}} \mu^{\frac{1}{3}}$
Surface Area	$S^{Spherical} = \left(\frac{6m_c}{\rho_{soot}}\right)^{\frac{2}{3}} \mu_{\frac{2}{3}}$ $S^{Aggregate} = \left(\frac{6m_c}{\rho_{soot}}\right)^{\frac{2}{3}} \mu_{\frac{2}{3}} \pi^{\frac{1}{3}}$
Volume Fraction	$f_v = \frac{m_c M_1}{\rho_{soot}}$
Mass Fraction	$Y_{soot} = \frac{\rho_{soot} f_v}{\rho_{soot} f_v + \rho_{gas}(1 - f_v)} = \frac{m_c M_1}{m_c M_1 + \rho_{gas}(1 - f_v)}$
Surface Area Density	$\frac{S}{A} = \pi \mu_{\frac{2}{3}} M_0 \left(\frac{6m_c}{\pi \rho_{soot}}\right)^{\frac{2}{3}}$

3.6.4 Solving the MOMIC equations

The method of moments with interpolative closure was written in Fortran 90 for performance reasons, since it is was initially intended to be incorporated into the GEMS code to perform reacting flow soot CFD calculation. However, it was later found that this would require significant effort and the PFR solution showed good agreement with the bulk solution in the CFD. As a result, the MOMIC model was only incorporated with the reduced order WSR and PFR models. The outline of the code is shown in Figure 3.11. Not pictured is the effort in developing this code, which writing it was about 10% and debugging 90% of the work.

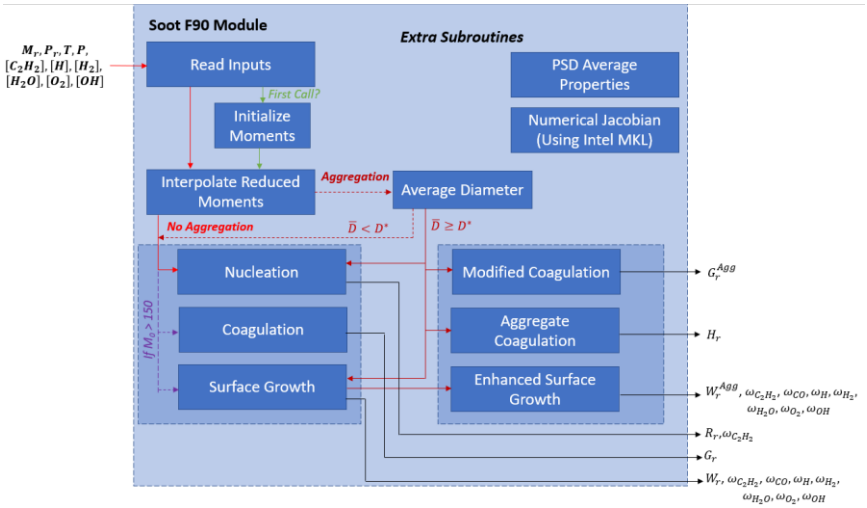

Figure 3.11 Method of Moments via Interpolative Closure Code Outline

The first attempt at predicting soot with the MOMIC model was with a WSR, using the WSR model discussed in section 3.2. These were first solved in a decoupled approach, where the WSR was first solved to predict the gas solution and then this solution was used to predict the steady state moments. The moment conservation equations for the WSR were initially solved as:

$$\frac{dM_{r,WSR}}{dt} = \frac{M_{in} - M_{r,WSR}}{\tau_{res}} - S_{M_r}(M, P, T, P, Y_i) \tag{3.40}$$

$$\frac{dP_{r,WSR}}{dt} = \frac{P_{in} - P_{r,WSR}}{\tau_{res}} - S_{P_r}(M, P, T, P, Y_i) \tag{3.41}$$

Where the rate of change of the M and P moments in the WSR are equal to the moments entering the WSR; moments in the WSR; and M and R moment source terms, S_{M_r} and S_{P_r}, which are calculated from equations 3.36 and 3.39, respectively. The WSR residence time, τ_{res}, was determined based on the gas solution. Steady state was determined when the rate of change of the M and P moments was zero. However, it was impossible to get convergence with this formulation of the equation unless the moments were somehow guessed to be close to the steady state moments. The moment equations are nonlinear and moment scalars can each range on the order of 1 to 1e200 or higher. The computational round off error with dealing with scalars of these large and different magnitudes made convergence impossible. From discussion with Dr. Mehta from CFD Research Corporation, it was suggested to solve for $\ln(M)$ and $\ln(P)$ instead, which reduces the range of possible values. Equations 3.40 and 3.41 were then rewritten as:

$$\frac{dln\left(M_{r,WSR}\right)}{dt} = \frac{1}{\tau_{res}}\left(\frac{M_{in}}{M_{r,WSR}} - 1\right) - \frac{S_{M_r}(M, P, T, P, Y_i)}{M_{r,WSR}} \tag{3.42}$$

$$\frac{d\ln\left(P_{r,WSR}\right)}{dt} = \frac{1}{\tau_{res}}\left(\frac{P_{in}}{P_{r,WSR}} - 1\right) - \frac{S_{P_r}(M, P, T, P, Y_i)}{P_{r,WSR}} \tag{3.43}$$

This reformulated approach worked and resulted in stable convergence regardless of the initial condition. Furthermore, to speed up convergence for the steady state moment solution, the moment conservation equations were first integrated for some time and then switched to an iterative Newton solver for a few steps and then cycled through both solvers until the residuals decreased below 1e-5. The Newton solver required computing a numerical Jacobian which was done using the Intel Math Kernel Library [105]. This approach was based on the scheme discussed by Adhikari et al [106].

A series of WSR's, with the MOMIC equations, was then used to construct a PFR, exactly as described in section 3.3 – with addition of the extra MOMIC equations. This provided predictions of the volumetric soot distribution within the PFR. From this distribution, soot particle deposition on the wall could be calculated. Soot particle deposition is discussed in the next section. Afterwards, the MOMIC soot model was directly coupled with the PFR gas equations to predict the effect of soot formation on gas phase chemistry, and vice versa. The coupled model is discussed in section 3.8.

3.7 Soot Particle Deposition

Soot particles were assumed to deposit on the walls via thermophoretic and Brownian diffusion. Aerosol and exhaust gas recirculation literature show that thermophoresis and Brownian diffusion are the predominant deposition mechanisms of submicron particles, such as soot. [12,23,107–109] Other mechanisms such as turbophoresis or electrostatic attraction may also be present but are several orders of magnitude smaller [109]. The particle deposit flux was calculated with these two mechanisms as:

$$\dot{m}''_{soot}(x) = C_{soot}(x)(V_{th} + V_{br}) \quad 3.44$$

This flux was calculated based on the concentration of the soot at an axial location, C_{soot}; and the thermophoretic and Brownian deposition velocities calculated via the models discussed in this section. The soot concentration was calculated from the moment solution of the Method of Moments with Interpolative Closure model, described in the previous section. The concentration was simply equal to the first moment multiplied by the mass of a carbon atom - $M_1 m_c$.

When particles are near the wall, they can then stick because of the Van der Waals forces [110]. In this model, it was assumed that all particles had perfect sticking. As Reza et al. has shown, the sticking probability of particles in an EGR cooler increases as bulk velocity decreases [12]. For this project, the bulk flow velocity in both the experiment and the model was minimized in order make this assumption applicable.

3.7.1 Thermophoretic Diffusion

A temperature gradient in a flow-field can induce movement of a soot particle towards the cooler direction via thermophoresis, as shown in Figure 3.12. This is a result of the hotter gas

molecules having a higher kinetic energy compared to the colder molecules. In turn the collisional force of the gas molecules is higher on the hotter side of the particles, which induces a net force towards the colder molecules.

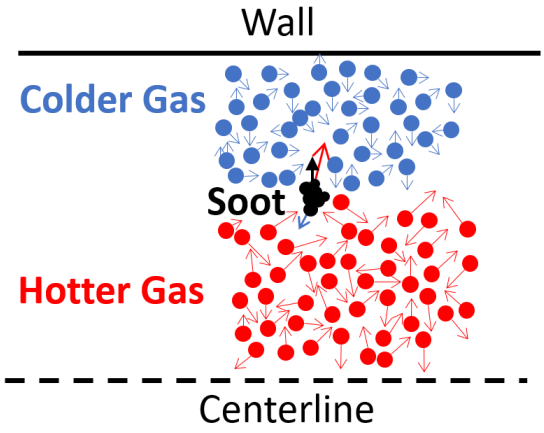

Figure 3.12 Overview of Thermophoretic Force

The Talbot model [111,112] has been empirically derived to predict this phenomena in the continuum and free-molecular cases and has been successfully employed in EGR soot deposit models [11,23,108,109]. With this model, a thermophoretic drift velocity can be determined by balancing the thermophoretic force and drag, with the resulting expression as shown:

$$V_{th} = -\frac{K_{th}\nu}{T}\nabla T \tag{3.45}$$

Where ν is the gas kinematic viscosity and K_{th} is the thermophoretic coefficient that is defined as:

$$K_{th} = \frac{2C_sC_c\left(\left(\frac{k_g}{k_p}\right) + C_tKn\right)}{(1+3C_mKn)\left(1+2\frac{k_g}{k_p}+2C_tKn\right)} \tag{3.46}$$

Where C_s, C_t and C_m are the thermal slip, temperature jump and momentum exchange coefficients and have values of 1.147, 2.20 and 1.146 respectively [113]. Cc is the Cunningham correction factor and can be expressed as $C_c = 1 + 1.257Kn$ [114]. Kn is the Knudsen number and defined as $Kn = \frac{2\lambda}{D_p}$ where λ is the mean free path of the bulk gas and D_p is the soot particle diameter, which is calculated from the MOMIC model as described in the previous section. k_g is

the gas thermal conductivity and k_p is the particle thermal conductivity, assumed to have a value of $0.68\frac{W}{m-K}$ based on experimental measurement by Nishiwaki [115].

The temperature gradient at the wall was evaluated via a Nusselt number correlation, similarly to the exhaust gas recirculation cooler deposit model of Abarham [109]:

$$\nabla T = \frac{\partial T}{\partial r}\Big|_{r=\frac{D}{2}} = \frac{N_u\left(T_w - T_g\right)}{D_c} \tag{3.47}$$

Where N_u is the Nusselt number, T_w is the wall temperature, T_g is the gas temperature and D_c is the chamber diameter. The turbulent Nusselt number was calculated via the Gnieliski correlation for smooth tubes [54,116]:

$$N_u = \frac{\left(\frac{f}{8}\right)\left(R_{e_D} - 1000\right)P_r}{1 + 12.7\left(\frac{f}{8}\right)^{\frac{1}{2}}\left(P_r^{\frac{2}{3}} - 1\right)} \tag{3.48}$$

Where $R_{e,D}$ is the Reynolds number with respect to the chamber diameter, P_r is the Prandtl number and f is the friction factor. The friction factor was calculated via the Petukhov correlation [54,117] as:

$$f = (0.790\, ln\, R_{e_D} - 1.64)^{-2} \tag{3.49}$$

3.7.2 Fickian Diffusion

The submicron soot particles can also be transported from regions of high concentration to lower concentration via eddy motion. This diffusive flux can be described via Fick's law [60]:

$$J = -\rho_g D_b \nabla Y \tag{3.50}$$

With the diffusion velocity defined as:

$$V_{br} = -D_b \nabla Y \tag{3.51}$$

Where ρ_g is the gas density, D_b is the particle diffusion coefficient and the last term is the concentration gradient. The particle diffusion coefficient in this paper was calculated from the Stokes-Einstein equation [118]

$$D_b = \frac{k_b T C_c}{3\pi\mu d_p} \tag{3.52}$$

Where k_b is the Boltzmann constant, T is the temperature, C_c is the Cunningham correction factor, μ is the gas viscosity and d_p is the soot particle diameter. The soot particle diameter is calculated from the MOMIC model, just like in the thermophoretic diffusion calculation.

The concentration gradient at the wall was evaluated via a Sh, Sherwood number, correlation, similarly to the exhaust gas recirculation cooler deposit model of Abarham [109]:

$$\nabla Y = \frac{\partial Y}{\partial r}\Big|_{r=\frac{D}{2}} = \frac{Sh(Y_{wall} - Y_{core})}{D_c} = -\frac{ShY_{core}}{D_c} \quad 3.53$$

Where the subscript core refers to soot concentration at the core and wall refers to concentration at the wall - which is set to zero assuming the soot sticks once it reaches the wall. The correlation of Berger and Hau [119] for turbulent mass transfer in pipe flows was used to estimate the Sherwood number:

$$Sh = 0.0165 R_e^{0.86} Sc^{\frac{1}{3}} \quad 3.54$$

Where Sc is the Schmidt number and defined as $Sc = \frac{\nu}{D_b}$.

The thermophoretic and Brownian diffusion velocities were calculated with the bulk solution in each WSR of the PFR and then soot deposit mass calculated with equation 3.44. The deposit calculation was decoupled from the bulk solution for all the calculations in this work. The total predicted soot deposit mass was less than 0.1% of the bulk soot mass in all the calculations and hence it was not thought to cause significant error.

3.8 Coupled Soot Solver

3.8.1 Incorporating MOMIC with PFR

The last part in the modeling effort was coupling the MOMIC model discussed in section 3.6 to the PFR model discussed in section 3.3. Soot formation depletes gas-phase soot precursors in the flow and accounting for this is important to more accurate predict soot volume fractions at fuel rich and high-pressure conditions. As the results in section **Error! Reference source not found.** show, the decoupled approach can produce an order of magnitude higher prediction of soot volume fraction because precursor depletion is not considered. In addition, coupling is important

to account for the consumption of gas-phase moles to form solid phase soot – which can contribute to substantial pressure drop as soot volume fractions get large.

The coupled soot PFR model was setup just like the non-sooty PFR – as a series of 0-D WSRs. An overview of the approach is shown in Figure 3.13. Soot was assumed to be perfectly mixed in each WSR. The particles were assumed to be spherical –the aggregate soot particles were also treated as spherical with equal volume as the aggregate particle. A thin boundary layer was assumed to surround the particles and energy exchange with the gas phase assumed to be mainly via convection. The soot particles could also radiate energy, and it was assumed that radiation transfer between the particle and wall was dominant. A numerical and experimental study of coal gasification, which is similar but an opposite process to soot formation, has shown that particle radiation is several orders of magnitude higher than for bulk gas [120]. Hence bulk gas radiation was assumed negligible. In addition, mass, species and energy could be transferred between the gas and particle phase via energy release or absorption during surface reactions on the soot surface.

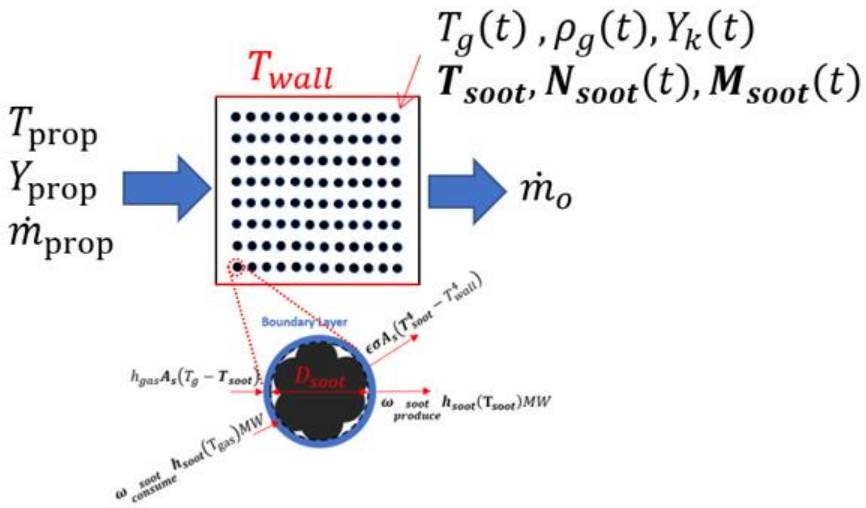

Figure 3.13 Overview of WSR coupled to soot

The governing equations for the gas phase are the same as those discussed in section 3.2, except now the soot source terms are nonzero:

Mass Conservation

$$\frac{dm_g}{dt} = \frac{d(\rho_g V)}{dt} = \dot{m}_{g,in} - \dot{m}_{g,out} - V\sum_{k=n}^{N} \boldsymbol{\omega_{s,k}} M_{W,k} \quad 3.55$$

Species conservation:

$$\rho_g V \frac{dY_{g,k}}{dt} = \dot{m}_{g,in}(Y_{g,in,k} - Y_{g,k}) + V(\dot{\omega}_{g,k} + \boldsymbol{\dot{\omega}_{s,k}})M_{\mathrm{W,k}} - Y_{g,k}V\sum_{k=1}^{n} \boldsymbol{\dot{\omega}_{s,k}}\, M_{\mathrm{W,k}} \quad 3.56$$

Energy Conservation

$$\rho_g c_{v,g} V \frac{dT_g}{dt} = \dot{m}_{in}\left(h_{in} - \sum_{k=1}^{n} \frac{u_k(T_g)Y_{g,in,k}}{M_{W,k}}\right) - \frac{p_g}{\rho_g}\dot{m}_{out} - V\sum_{i=k}^{n} u_k(T_g)\left(\omega_{g,k} + \boldsymbol{\omega_{s,k}}\right)M_{W,k} + \boldsymbol{N_s} V\left(\boldsymbol{\dot{Q}_s} + \frac{\sum_{k=1}^{n} u_k(T_s)\boldsymbol{\omega_{s,k}}}{\boldsymbol{N_s}}\right) + \dot{Q}_{source} \quad 3.57$$

These are solved simultaneously with the particle phase equations, that include the moment and energy equations:

Moment Conservation

$$\frac{dln(M_{r,WSR})}{dt} = \frac{1}{\tau_{res}}\left(\frac{M_{in}}{M_{r,WSR}} - 1\right) - \frac{S_{M_r}(M,P,T,P,Y_i)}{M_{r,WSR}} \quad 3.58$$

$$\frac{d\ln(P_{r,WSR})}{dt} = \frac{1}{\tau_{res}}\left(\frac{P_{in}}{P_{r,WSR}} - 1\right) - \frac{S_{P_r}(M,P,T,P,Y_i)}{P_{r,WSR}} \quad 3.59$$

Energy Conservation

$$\rho_s V_s c_{p,s} \frac{dT_{soot}}{dt} = \left(-\boldsymbol{\dot{Q}_s} - \frac{\sum_{k=1}^{n} u_k(T)\boldsymbol{\omega_{s,k}}}{N_{tot}} + \epsilon\sigma A_s(T_{soot}^4 - T_{wall}^4)\right) \quad 3.60$$

In these equations, $\omega_{s,k}$ is the gas-phase species consumption or production rate in forming soot particles. This term accounts for consumption of consumption of acetylene during soot nucleation, as well as consumption and production of several species in soot growth. For small soot volume fractions, this term is small and there is little error if it assumed to be zero in the gas-phase equations – i.e. decoupling soot from gas-phase equations. However, as the soot volume fractions get larger, like for the conditions in this work, then this term becomes important because a significant number of gas-phases gets consumed. The consumption term depends on the total

surface area of the soot particles – which is calculated from the Moment solutions, as well as gas phase properties. The details of this calculation are provided in appendix A. The effect of this term on mass conservation is to decrease gas mass and in turn gas density – leading to pressure loss. It also removes species from gas-phase and can affect some reaction pathways if it becomes significant. In addition, species consumption or production results in energy exchange between the gas and particle phase due to heterogenous surface reactions. Additionally, energy could be exchanged with the soot particle phase via convection and depends on the total number of soot particles – which is calculated as the number density times volume of the WSR: $N_s V$. The energy transfer between the soot particle phase and gas phase was assumed to occur solely via convection as:

$$\dot{Q}_s = -hA_s\left(T_g - T_{soot}\right) \tag{3.61}$$

This is like how Qiao et al. had modeled coal gasification – a similar but opposite process of soot formation – which showed good experimental comparison [121,122]. In their work, the heat transfer coefficient between carbon particle and gas phase was calculated using the correlation developed by Guo et al. [123]:

$$h = \frac{N_u k_g}{d_{soot}} \frac{B}{\exp(B) - 1}, \quad B = \frac{\dot{m}_{soot} C_{p,g}}{\pi d_{soot} N_u k_g} \tag{3.62}$$

Since the processes were thought to be similar, the same heat flux correlation was used in the model. A Nusselt number of 2 was also assumed for simplicity, consistent with Qiao et al. [121,122].

The particle equations consisted of the moment conservation equations to describe the particle size distribution and energy conservation. Mass conservation is inherent in the moment equations. The energy equation makes a lumped mass assumption and assumes all the soot particles are at the same temperature. The energy is assumed to transfer between the bulk gas phase and soot via convection, heterogenous surface reactions and radiation to the wall.

These governing equations described a sooty WSR and were written in a python function and then integrated with the SciPy backward-differentiation formulas ODE solver [57–59]. The PFR model was setup as a series of these WSR and sequentially integrated to steady state, exactly like described in section 3.3, except with the extra particle phase equations. The calculated soot volume fractions and properties in each WSR were then used to calculate soot deposition rates as described in section 3.7.

This model was also coupled to the droplet vaporization model discussed in section 3.3.2 and solved in an identical approach as shown in Figure 3.4. The WSR soot model was solved to steady state, then the droplet estimates updated, and then the model resolved… until steady state convergence.

3.8.2 Initial Validation

There was little open literature found that discusses soot deposition during fuel rich combustion and none found with deposit measurements. The experimental effort, described in chapter 4, was done to obtain soot deposit thickness measurements at a variety of conditions. The deposit predictions could not be validated without these measurements and this validation is discussed in chapter 5. However, several studies have been run with either numerical or experimental results of soot volume fractions in well stirred reactor, or high-pressure flames. These studies were used to validate the bulk soot predictions in the coupled PFR.

Comparison with WSR simulations of Brown et al. [124]

The implementation of the coupled soot model was verified with simulations of Brown et al. which coupled method of moments with interpolative closure to a well stirred reactor model. [124]. The simulations Brown et al. focused on soot formation in ethylene/air combustion at a variety of residence time, reactor temperatures and pressure conditions. Their calculations of soot volume fraction at a reactor temperature of 1750 K and equivalence ratio of 2.5 at pressure of 1 and 10 bar were compared with the predictions from coupled model. The coupled soot model simulations were run with the same gas-phase mechanisms of Wang and Frenklach [29] that Brown et. al used [124]. Brown et. al also used the surface growth mechanism of Kazakov et al. [125], which includes a term to account for the fraction of surface sites available for chemical reactions which depends on soot particle morphology and in turn the temperature. The same growth mechanism was used in the coupled soot model but the term for fraction of surface sites was different based on updated temperature dependent value of Appel et al. [126]. Additionally, the nucleation mechanism between the two simulations were different. Brown et. al used a PAH nucleation step based on the concentration of pyrene in the flow. However, the coupled soot model employed an acetylene-based mechanism. The remainder of the parameters were consistent

between the two models. The energy equations in the WSR, equations 3.57 and 3.60 were also not solved and instead the reactor and soot temperature assumed to be at a constant temperature of 1750 K to be consistent with the simulations of Brown et al.

The calculation with the coupled soot model and comparison with the results of Brown et al. are shown in Figure 3.14. The results from paper of Brown et al. [124] were digitized with WebPlotDigitizer [73].

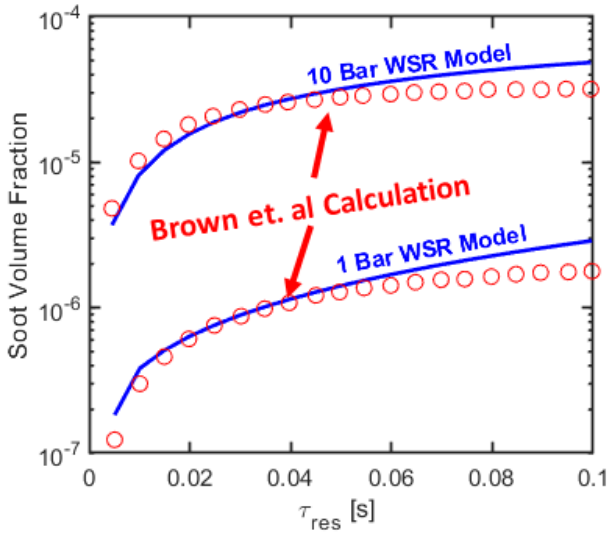

Figure 3.14 Comparison of soot volume fraction in ethylene/air combustion as a function of residence time at 1750 K, $\phi = 2.5$ between calculation of Brown et. al [124] and the model in this work

The predicted soot volume fractions from the sooty WSR model in this work matches the calculations of Brown et. al relatively well at lower residence times and the difference is within a factor of 1.5 at larger residence times. The trends with pressure and residence times also agree well and are as expected – higher residence time provides longer time for soot to form and higher pressures increase both coagulation rates as well as surface growth kinetics. The differences between the model in this work and the simulations of Brown et. al. are likely primarily due to difference in soot nucleation model as well as different estimate of the fraction of soot surface sites available for reaction. Nucleation is important initially as soot particles are small. Brown et. al assumed a nucleation rate based on gas-phase Pyrene PAH, whereas the soot model for this work based it on acetylene – since it was designed for the HyChem POSF5433 mechanism which did not have PAH reactions. The difference in the soot volume fractions at small residence times is

likely due to this difference – though it's rather small. As particles get larger, surface growth rates become important since the surface area increases. Differences in volume fractions at the larger residence times are likely due to a difference in how surface growth rates are calculated between the two models. The soot growth mechanism was identical, however the calculation for the fraction of soot surface sites was different. The model by Brown et. al calculated it via the model of Kazakov [125] as shown in equation 3.63, which only depends on gas temperature. However, the model in this work calculated this factor via equation 3.64, which depends on both gas temperature and the reduced moment of the soot particle size distribution. It was found that this factor was larger in the model in this work compared to Brown et.al for most of the range of residence times and hence this was likely why there was larger difference at higher residence times – where the soot surface growth mechanism was dominant.

$$\alpha = \frac{1}{2}\left(\tanh\left(\frac{8168}{T} - 4.57\right) + 1\right) \tag{3.63}$$

$$\alpha = \tanh\left(\frac{a(T)}{log\,\mu_1} + b(T)\right) \tag{3.64}$$

Additionally, the model of Brown et. al used Chemkin to solve the WSR with the moments. However, the sooty WSR in this work was written in a python function and integrated with Scipy ODE solver [58]. This might also account for some numerical difference but is likely small.

Comparison with Jet Stirred Reactor Experiments of Vaughn [127]

Another source of comparison for the coupled soot solver was with experimental soot volume fraction measurements of Vaughn [127]. These measurements were taken for ethylene and air combustion in a jet stirred reactor at a range of equivalence ratio and at ambient pressure. The reactor temperature in the measurements was constant at 1628 K and controlled via nitrogen purge. The residence time was calculated to be 5 ms. The experiment was modeled using the 1bar C2 hydrocarbon mechanism of Appel et al. [126]. The mass flow rate was adjusted to provide a residence time of 5ms in the reactor at the different equivalence ratio conditions and calculated based on chamber volume and steady state gas density as:

$$\dot{m} = \frac{\rho_{gas} V}{\tau_{res}} \tag{3.65}$$

In addition, nitrogen gas was introduced into the simulation to provide a reactor temperature of 1628 K – the mass flow of the gas was dependent on the equivalence ratio. The simulation was then run at reactor pressure of 1 atmosphere and equivalence ratio range of 1.9 to 2.6. Comparison of the predicted soot volume fraction with Vaughn's measurements at the different conditions are shown in Figure 3.15. The results from Vaughn's [124] dissertation were digitized with WebPlotDigitizer [73].

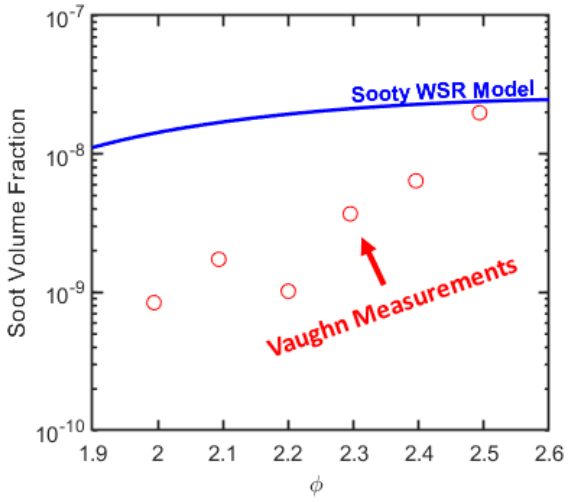

Figure 3.15 Comparison of soot volume fraction as a function of residence time at 1750 K, $\phi = 2.5$ between calculation of Brown et. al [124] and the model in this work

As Figure 3.15 shows, the predicted soot volume fractions were within an order of magnitude of the experimental measurements. The predicted trend of increase in soot volume fraction with higher equivalence ratio generally agrees with the measurements. The drop in the measured volume fraction at equivalence ratio of 2.2 is likely just an experimental error as this behavior was not specifically discussed [127]. If the last measurement point is also assumed to be a high outlier, then the slope of the measurements generally seems to agree with the predicted behavior. Overall though the goal of the reduced order modeling effort was to correctly match soot volume fractions at different conditions and these results seemed to validate the predicted trends.

Comparison with High Pressure Premixed Flame of Heidermann et al. [128]

A third source of model comparison was with the experimental soot measurements of Heidermann et. al. in premixed acetylene-air flames at high pressures [128]. Laser-scattering and

molar absorptivity measurements were used to determine soot properties including number density and volume fractions for premixed flames at a variety of pressure conditions – the model comparison focused on the 35 and 70 bar flames. Unlike the previous model validation cases, modeling the premixed flame was a bit more involved since a well stirred reactor was not necessarily appropriate. The flame was instead modeled with an initial well stirred reactor connected to a constant pressure reactor, as shown in Figure 3.16.

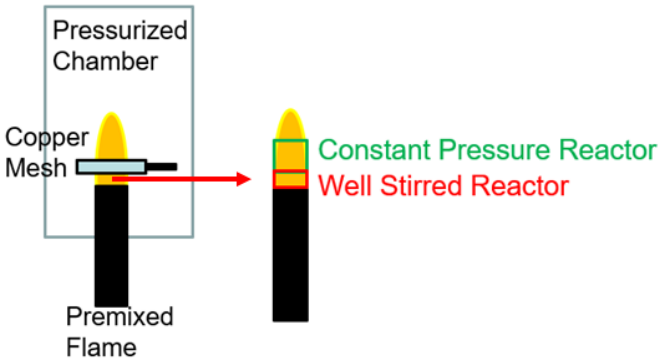

Figure 3.16 Approach to modeling the premixed flame of Heidermann et al. [128] using a well stirred reactor connected to a constant pressure reactor.

The sooty well stirred reactor in the model was modeled as described in section 3.8.1. The well stirred reactor solution was then integrated in a constant pressure reactor. This reactor was used to solve for the evolution of gas and soot in a closed system. The equations were like those described in section 3.8.1, except without the inlet and outlet terms. These equations for gas mass, gas species, gas energy and the moment equations could be written as:

$$\frac{dm_g}{dt} = \frac{d(\rho_g V)}{dt} = -V \sum_{k=n}^{N} \boldsymbol{\omega_{s,k}} M_{W,k}$$

$$\rho_g V \frac{dY_{g,k}}{dt} = V(\dot{\omega}_{g,k} + \boldsymbol{\dot{\omega}_{s,k}}) M_{\mathrm{W,k}} - Y_{g,k} V \sum_{k=1}^{n} \boldsymbol{\dot{\omega}_{s,k}} M_{\mathrm{W,k}} \quad 3.66$$

$$\rho_g c_{v,g} V \frac{dT_g}{dt} = -V \sum_{i=k}^{n} u_k(T_g)\,(\omega_{g,k} + \boldsymbol{\omega_{s,k}}) M_{W,k} + \boldsymbol{N_s} V \left(\boldsymbol{\dot{Q}_s} + \frac{\sum_{k=1}^{n} u_k(T_s) \boldsymbol{\omega_{s,k}}}{\boldsymbol{N_s}} \right) \quad 3.67$$

$$\frac{dln(M_r)}{dt} = -\frac{S_{M_r}(M, P, T, P, Y_i)}{M_r} \quad 3.68$$

$$\frac{d\ln(P_r)}{dt} = -\frac{S_{P_r}(M,P,T,P,Y_i)}{P_r} \quad 3.69$$

Additionally, these equations were solved differently from the 1D soot model discussed in section 3.8.1, where the equations were integrated to steady state. Instead, the equations were integrated for the reaction time of the gas molecules using a Lagrangian reference, where the time was calculated based on the height in the flame where the measurements were taken and the velocity of the flame. This was calculated as:

$$t = \frac{h}{u_z} \quad 3.70$$

This model was then run at pressures of 35 and 70 bar and for carbon to oxygen ratios of 0.6 to 0.72 – consistent with the experiments of Heidermann et al [128]. The results are shown in figure Figure 3.17.

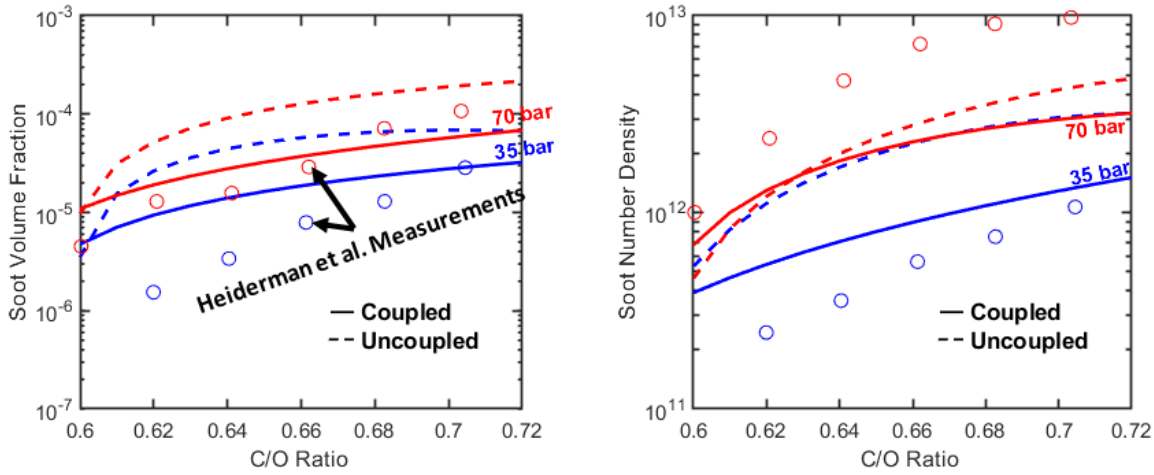

Figure 3.17 Comparison of predicted soot volume fraction [Left] and number density [Right] in ethylene/air premixed flames at high pressure as a function C/O ratio with measurements of Heidermann et. al [128]

4. EXPERIMENTAL DESIGN AND SETUP

4.1 Overview

An experiment was designed and operated to get soot deposit measurements at a variety of pressure and residence time conditions for model validation. The experiment consisted of a torch ignited RP-2 and gaseous oxygen (GOx) combustor as shown in Figure 4.1. Propellants were combusted at fuel rich conditions within the stainless-steel combustion chamber and product gases flown through the copper sample chamber out through the pressure controlling choke plate. Soot deposits were collected on the thin sample liner tube. Thermocouples were also used to measure the back-wall temperature of the sample tube, from which the sample surface temperature and heat flux could be estimated. Post-test, the sample tube was removed, cut, and imaged with an optical profilometer to measure the deposit thickness. This thickness measurement was directly compared with the 1-D model discussed in section 3.8.

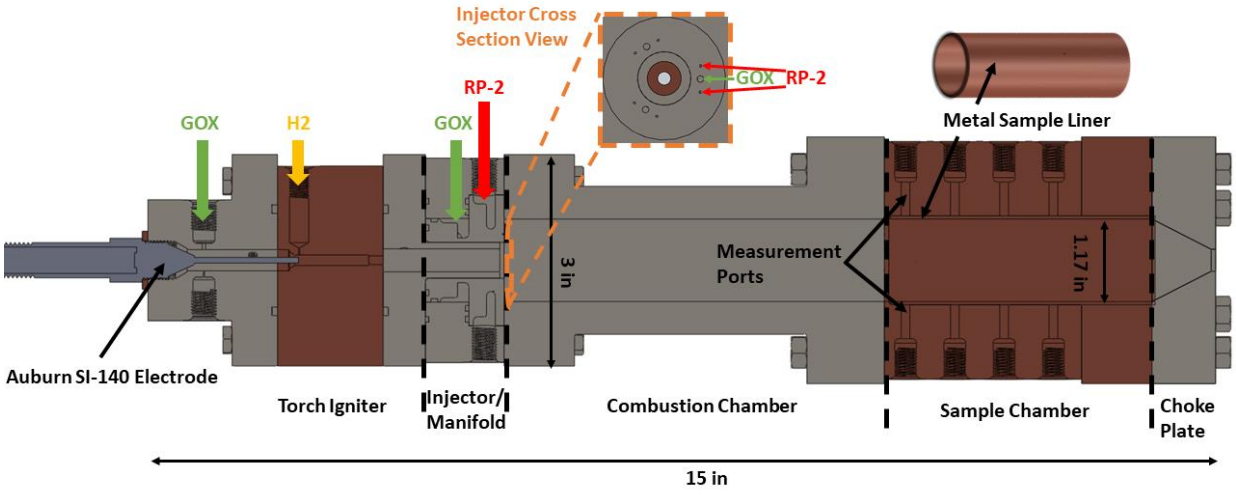

Figure 4.1. Soot Deposit Experiment Overview.

The design of the experiment and the model development was done in conjunction. The modeling effort informed the experimental design. The experimental design in turn guided the modeling approach and conditions. As such, this chapter contains a lot of back and forth discussion with the previous chapter. The experiment underwent significant amount of iteration based on continuously updated modeling capability, machinability issues, or budget limitations as this

section discusses. One of these included sizing the combustion chamber for flow to become fully developed within the copper heat sink chamber, because the reacting CFD results showed that the boundary layer had a significant impact on local gas chemistry and in turn soot deposit surface reactions. However, later modeling showed that surface reaction contributions to soot deposit layer growth is overshadowed by thermophoretic driven deposition and surface reaction contribution would not be measurable in the current experiment. As a result, the experiment was updated again to a shorter chamber. Additionally, the torch igniter had undergone significant iteration based on initial failures in the experiment. The experiment was also originally intended to be axisymmetric to aid with computational comparison. However, the experiment operating conditions were designed for a low bulk velocity (in order to reduce effects of soot removal mechanisms) and this required operating at small flowrates, which in turn made it impossible to design a machinable axisymmetric injector. Instead, the injector employed was changed to a Fuel-Oxidizer-Fuel impinging triplet which seemed to provide the closest injection conditions to axisymmetric.

This chapter describes the experimental effort involved to obtain soot deposit measurements at fuel rich conditions. The effort included developing tools to assist with the design and analysis of the experiment, sizing the operating conditions to provide good comparison with the modeling effort, developing the hardware and propellant feed system, and determining the run sequence for safe successful ignition.

4.2 Design Tools

Several analysis tools were written to analyze and iterate the design of the soot deposit experiment. This section provides an overview of the codes. These codes, along with the coupled 0-D/1-D well stirred reactor models are freely available on the GitHub repository included with this dissertation.

4.2.1 Matlab 2-D Heat Diffusion Model

A 2-D axisymmetric heat transfer code was written in Matlab using the Partial Differential Equations Toolbox [129] to perform the thermal analysis for design of the soot experiment. The PDE toolbox can solve partial differential equations in the form of:

$$m\frac{\partial^2 u}{\partial t^2} + d\frac{\partial u}{\partial t} - \nabla(c\nabla u) + au = f \tag{4.1}$$

The radial heat diffusion equation, assuming no internal heat generation and axisymmetric can be expressed in the acceptable form as:

$$\frac{1}{r}\frac{\partial}{\partial r}\left(k(T)r\frac{\partial T}{\partial r}\right) + \frac{\partial}{\partial z}\left(k\frac{\partial T}{\partial z}\right) = \rho c_p(T)\frac{\partial T}{\partial t} \tag{4.2}$$

With either time-dependent temperature specified at a boundary with a Dirichlet boundary condition:

$$T(x,t) = T \tag{4.3}$$

Or time-dependent heat flux specified at a boundary with a Neumann boundary condition:

$$k\frac{\partial T}{\partial r}|_{r=x} = h_{conv}\big(T(x,t) - T_{ref}\big) + \epsilon\sigma\big(T(x,t)^4 - T_{ref}^4\big) \tag{4.4}$$

The thermal properties in the code can be specified as either a constant, or a function of temperature. For the soot experiment thermal analysis, the temperature dependent thermal properties were used. The temperature dependent specific heat for copper was determined by interpolating the data reported by White and Collocott [130], and the thermal conductivity calculated from correlation provided by Eishah [131]; the specific heat and thermal conductivity for stainless steel 316 was determined using the Stainless Steel property fit in Eurocode [132]; and for GRCOP-84, the the property measurements of Ellis [133] were used.

In the analysis three different heat flux correlations were used. These included the Bartz correlation, which is an empirical correlation that accounts for boundary layer temperature gradient effects on rocket combustion gas properties [3,134]:

$$h_g = \frac{0.026}{D^{0.2}}\left(\frac{c_p\mu^{0.2}}{\mathrm{Pr}^{0.6}}\right)(\rho v)^{0.8}\left(\frac{\rho_m}{\rho'}\right)\left(\frac{\mu_m}{\mu_0}\right)^{0.2} \tag{4.5}$$

Where D is the local flow diameter, $c_p$is the gas specific heat, μ is the gas viscosity, Pr is the Prandtl number and calculated as: $P_r = \frac{c_p\mu}{k}$ where k is the gas conductivity, ρ is the gas density and v the local velocity. The m subscripts refer to property calculation at the arithmetic mean temperature of the local free-stream static temperature and wall temperature. The 0 subscript refers to property calculation at stagnation conditions. The $'$ superscript refers to the local free stream value.

The Gnieliski correlation was the second heat flux correlation calculated, which provides an estimate of heat flux in turbulent flow for smooth tubes for a Prandtl number of $0.5 \leq P_r \leq 2000$ and Reynolds numbers of $3000 \leq R_{e_D} \leq 5e6$ [54,116], and calculated as:

$$h_g = \frac{\left(\frac{f}{8}\right)\left(R_{e_D} - 1000\right)P_r}{1 + 12.7\left(\frac{f}{8}\right)^{\frac{1}{2}}\left(P_r^{\frac{2}{3}} - 1\right)}\left(\frac{k_g}{D}\right) \quad 4.6$$

In this correlation, all properties are evaluated at the mean temperature between the flow and wall. R_{e_D} is the Reynolds number with respect to flow diameter calculated as $R_{e_D} = \frac{\rho v D}{\mu}$; and f is the friction factor, which can be calculated via the Petukhov correlation [54,117], and is valid for Reynolds numbers of $3000 \leq R_{e_D} \leq 5e6$:

$$f = (0.790 \ln R_{e_D} - 1.64)^{-2} \quad 4.7$$

The Dittus Boelter equation was the third heat flux correlation calculated, which provides another estimate of heat flux in fully developed turbulent flow in smooth circular tubes for moderate temperature difference between the gas and wall and for Prandtl number of $0.6 \leq Pr \leq 160$ and Reynolds number $R_{e_D} \geq 10000$ [54,55], and calculated as:

$$h_g = 0.023 R_e{}_d^{\frac{4}{5}} P_r^n \left(\frac{k_g}{D}\right) \quad 4.8$$

Where the n exponent is 0.3 for the case of cooling and 0.4 for heating.

The three heat flux terms all have different ranges of applicability and accuracy in predicting heat transfer for the soot experiment. Since it was not a major importance to optimize the thermal design of the experiment, as a conservative estimate the highest of the three correlations was used for calculating the heat transfer coefficient (which in turn would result in a conservative high heat flux estimate).

The geometry, and boundary edges, in the code are specified as a set of r,z coordinates. Multiple domains can be specified, with different thermal properties, but with the assumption that the materials are in perfect contact. Afterwards, the Matlab partial differential equation toolbox generates an automatic mesh for the specified geometry domain. The PDE toolbox can generate either linear triangular mesh or quadratic element, with a specified mesh element size and growth rate. The time stepping is done internally in the toolbox and the results output at specific time intervals.

The heat transfer was solved for the initial mesh and then it was decreased in size by half and resolved. If the error was below a specified tolerance then the solution was decided to be converged - otherwise the mesh size was decreased, and the solver rerun until convergence.

All the thermal analysis discussed in this chapter was performed using this analysis code.

4.2.2 Transient Fluid System Model

A model of the propellant feed system was made to guide the design of the torch plumbing, injection and purge sequence, and later the main ignition sequences. The model consisted of a coupled network of 0-D reactor control volumes to understand the bulk gas behavior in the torch igniter, experiment chamber and various sections of the feed line. It was written in an object-oriented framework to be modular and allow for quickly changing and predicting feed system pressures or interactions with the main chambers, if the injection becomes unchoked. Various aspects from the code were used for designing the experimental components and timing sequences, which the component design discussion in section 4.4 discusses further. The reactors in the network were modeled as zero-dimensional well stirred reactor using the Cantera toolbox [52]. An overview of the model is shown in Figure 4.2

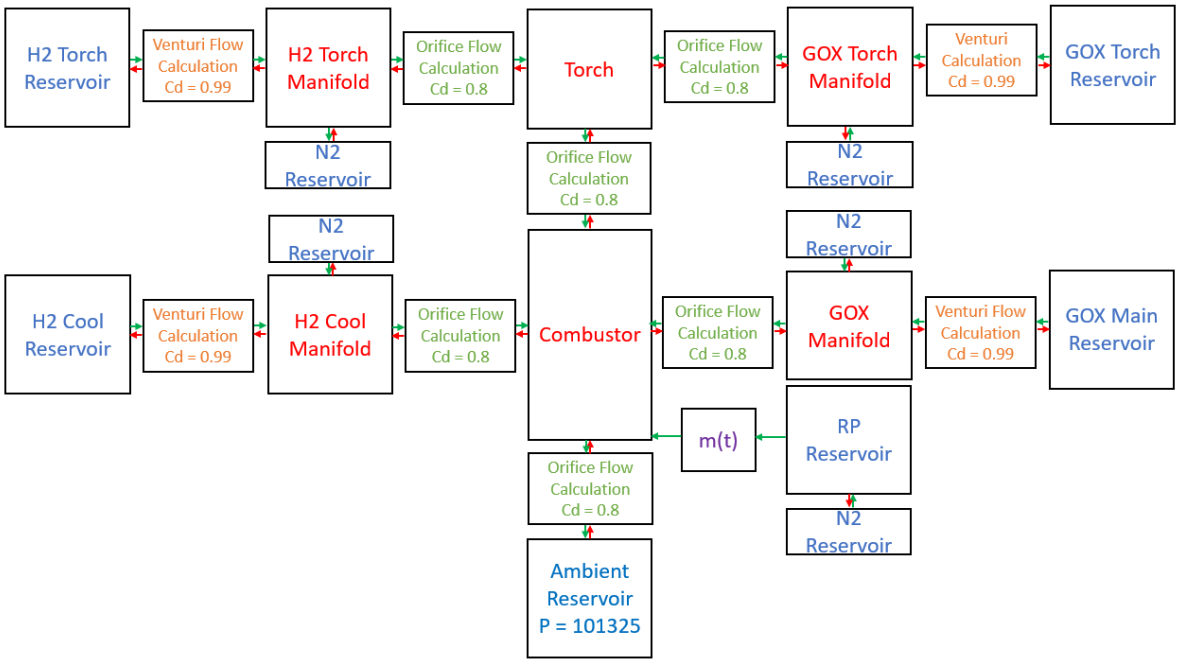

Figure 4.2 Reacting Engine Systems Model Overview. Red components are well stirred reactors, where transient temperature, pressure and species mass fractions are solved; blue components are reservoirs, where temperature, pressure and species fractions are static; and green and orange are mass flow controllers that govern mass flow between the reactors. The green arrows are upstream flow and red are downstream flow.

The fluid system model has well stirred reactor nodes connected to other well stirred reactors or a reservoir. A reservoir is reactor where the gas composition and thermodynamic properties are constant. Each reactor is modeled as an ideal gas reactor, where the density is calculated from the ideal gas equation of state. The flow in between the reactors is controlled via a Cantera Mass Flow Controller object. This object calculates the mass flow from the upstream to downstream reactor based on an input mass flow function if the upstream pressure is larger than downstream, otherwise mass flow is 0. To simulate backflow (for example if there is overpressure in one of the reactors due to a very rapid reaction event), a backwards mass flow controller object was added in the model setup. The forward flow is calculated with the upstream gas properties and downstream pressure, and vice versa with the backwards flow calculation. Hence two mass-flow values are calculated at every transient time step, with one always zero if the other is non-zero. The properties in each reactor can calculated as frozen, where the composition stays the same, or with chemistry enabled, where reaction rates can be solved to calculate gas composition. However, depending on the number of reactors and reaction mechanism this can get very expensive (for example the

HyChem POSF5433 mechanism has 841 reactions and 112 species and requires this combined number of equations to be solved at every time step in the reacting case). To simplify the numerics, the manifolds and feed line sections are modeled with a constant gas composition - assuming no backflow of hot combustion products, there shouldn't be any reactions occurring in the feed lines. If back-flow is detected, then reactions can be solved to investigate the effect that the backflow can have on the manifold chemistry - but from an engineering standpoint the conditions should be redesigned because backflow is undesirable!

The governing equations for each well stirred reactor that are solved with Cantera can be written as, with the variables equivalent to those defined in section 3.3:

Continuity

$$\frac{dm}{dt} = V\frac{d\rho_g}{dt} = \sum_{in,inj} \dot{m}_{in,inj}(t) + \sum_{in,WSR} \dot{m}_{in,WSR} - \sum_{out,WSR} \dot{m}_{out} \tag{4.9}$$

Energy

$$mc_V \frac{dT}{dt} = -\dot{Q} + \sum_{in} \dot{m}_{in}\left(h_{in} - \sum_k u_k Y_{k,in}\right) - \frac{P_g}{\rho_g}\sum_{out} \dot{m}_{out} - V\sum_k \dot{\omega}_k W_k u_k \tag{4.10}$$

Species Conservation

$$m\frac{dY_k}{dt} = \sum_{in} \dot{m}_{in}\left(Y_{k,in} - Y_k\right) + V\dot{\omega}_k MW_k \tag{4.11}$$

Where the continuity equation expresses that for a constant volume reactor, the rate of density change is equal to the inlet and outlet mass flow rates. The inlet mass flow consists of fluid injected into the reactor from a reservoir, which can be transient, and from all the connected well stirred reactors. In the code, the injected mass flow can either be specified as a numerical value that's a function of time or calculated as a function of reactor pressures. Flow through the orifice and venturi are calculated with the equations described in 4.5.1. Furthermore, events such as purge valve opening can be modeled by specifying the mass flow as 0 for times before the valve opening and then full flow after some opening time (or as a function of the valve transient opening time). The mass flow between two connected reactors m and n are calculated via the compressible mass flow relation as:

$$\dot{m}^n_{in\,\&\,out} = \sum_{A_i} C_{d_i} A_i P_t^n \sqrt{\frac{\gamma^n MW^n_{gas}}{RT^n}} M_n \left(1 + \frac{\gamma - 1}{2} M_n^2\right)^{-\frac{\gamma^n + 1}{2(\gamma^n - 1)}} \tag{4.12}$$

$$M_n = \begin{cases} 0 & if\ P_t^n \le P^m \\ \min\left(1, \sqrt{\frac{2}{\gamma^n - 1}\left(\left(\frac{P^m}{P_t^n}\right)^{-\frac{\gamma^n - 1}{\gamma^n}} - 1\right)}\right) & if \quad P_t^n > P_m \end{cases} \tag{4.13}$$

In the relation, the mass flow into the well stirred reactor is positive if the upstream reactor pressure is higher, or zero otherwise. Both the inflow and outflow mass between the reactors m and n are calculated with the same equations, except with reverse m and n indices. If the inlet mass flow rate from the upstream reactor is positive then the outlet mass flow is zero, and vice versa. Also, these relations assume the flow in the reactors is relatively slow, where the total properties are approximately equal to the local properties. If the bulk flow velocity approaches high Mach numbers, then the total properties in the relations can be calculated from the local properties and Mach number.

The energy equation describes the rate of reactor temperature change due to flow work, convective energy transfer and heat transfer across the reactor control surfaces, and from reactions within the control volume. The inflow masses include the injected propellants into the control volume and the flow from the connected reactors.

The enthalpy and internal energy for the inlet propellants are evaluated at the inlet temperature. The heat source term accounts for vaporization of liquid fuel and heat transfer through the walls of the reactor and is calculated as follows:

$$\dot{Q} = \sum_{in,liquid} \dot{m}\Delta h_{vap} + A_s^n q(t) \tag{4.14}$$

$$q(t) = h(gas\ properties)\left(T_{gas} - T_{wall}\right) \tag{4.15}$$

Where Δh_{vap} is the vaporization enthalpy of the liquid propellants, A_s^n is the surface area of the nth reactor, calculated as $A_s = \pi DL$, and the heat flux term q(t) can either be specified as a function of time or calculated for a convection condition, where the convection coefficient h used is one of the three discussed in the previous section.

The last term in the energy equation accounts for the reaction energy, with the species production rate, $\dot{\omega}$, calculated from a specified gas phase chemistry mechanism.

The species conservation equations are the same as discussed in the plug flow reactor model, except the wall source term has been omitted since for most of the combusting flow cases it doesn't affect the bulk properties significantly but requires slightly longer computational time. The species conservation equations describe the rate of change of species mass fraction due to convective mass transfer and reactions, with the number of equations solved for each well stirred reactor equivalent to the number of species in the gas phase reaction mechanism.

For this work, the detailed HyChem POSF5433 mechanism [14,15] was used to calculate the species production source terms in all of the calculations. The reactions were integrated in time using the Sundials ODE solver [56] with Cantera calculation for gas properties. The code, with reactions enabled, took about 1-2 minutes to run on a Pentium Core i7 Gen 8 processor with five connected and coupled reactors.

Finally, the soot model that was discussed in section 3.8 was not included in the formulation as it had not been written yet. This was written as a quick engineering model for analyzing the fluid system within the Cantera framework, which did not allow for including the reactor formulation as described in section 3.8. However, this model approach can be adapted in future work to include soot formulation, which can account for considerable pressure drop at high pressure conditions.

4.3 Operating Conditions

The operating conditions were continuously iterated and updated from the beginning of the project based on updated analysis, modeling goals and primarily on budgetary considerations. This section provides a brief overview of the evolution of the operating conditions and concludes with the final conditions that were run in the soot experiment.

As a starting point, the Air Force Phase I STTR experiment guided the initial operating condition considerations for the soot experiment. The propellants burned in the soot experiment were RP-2 and Gaseous Oxygen, whereas the Phase I combustor were RP-2 and 90% hydrogen peroxide. However, to start the initial mass flow rate and chamber pressure parameters in the soot experiment, along with chamber geometries were equivalent. The target mixture ratio considered for the gaseous oxygen and RP-2 propellants was between two and three in order to investigate soot deposit at conditions closer to actual rocket combustors. However, this presented challenges

in cooling the combustor wall. Since, the goal of this work was to understand the mechanisms of soot deposit from the core flow, there were no plans to use wall film cooling because otherwise it would complicate measurements by introducing an additional source of carbon deposit. Furthermore, with the Phase I mass flow rate, the heat flux to the walls was extremely high and would have required high flow rate, high pressure regenerative water cooling in a calorimetric type chamber in order to adequately cool the inner chamber walls. In addition, a literature review at the start of the project showed the volumetric soot volume fraction for hydrocarbon fuels is either very small or non-measurable at these mixture ratios but increase with decreasing mixture ratio [135–137]. Later modeling with the MOMIC model as discussed in the previous section, confirmed this result. The soot growth rates predicted with the HACA [87] mechanism were also at or close to oxidative regime, meaning the wall soot growth rates would be small. In turn, this would have required operating the soot experiment for a long time to get any measurable deposit. A preliminary calorimetric copper chamber design was explored to operate at steady state operation at these conditions; however, the estimated machining costs were considerably higher than the budgetary allowance of the project, especially if parts were needed to be repaired or re-machined.

Based on further discussion with NASA Marshall ER32 Branch, along with additional thermal analysis and updated soot prediction capability, the target mixture ratio was iteratively lowered to a value of 1. Initial calculations showed the deposit rates at the Phase I STTR chamber pressure of 150 psia were on the order of micrometers per second, and measurable with a profilometer. As a result, the experiment could have a short run duration to get adequate soot deposit. Since the run duration could be short, the experiment could then be designed to utilize much simpler and cheaper heat-sink cooling. The combustion temperature is also lower at the lower mixture ratio and cooling becomes less of a concern. However, reaction kinetics become important at this low mixture ratio since the gas composition requires long residence times to approach equilibrium. The gas temperature calculated in a Cantera well stirred reactor, at a pressure of 250 psia and residence time corresponding to the final soot experiment operating conditions, and comparison with equilibrium predictions is shown in Figure 4.3. The bulk gas temperatures start deviating from equilibrium predictions below a mixture ratio of 1.5. The temperatures are higher than equilibrium because the rates of the exothermic reactions are faster than endothermic. The species predictions also show a significant deviation from equilibrium near this mixture ratio, and some species require long residence times to reach equilibrium, even at

stoichiometric conditions, as section 2.2 in the background section describes. Therefore, despite the fuel rich gas temperature being lower than during stoichiometric combustion, consideration of non-equilibrium gas behavior is still important for safely designing an experiment at these conditions. All the heat transfer analysis for the experimental components in the soot experiment were done using these Cantera predictions.

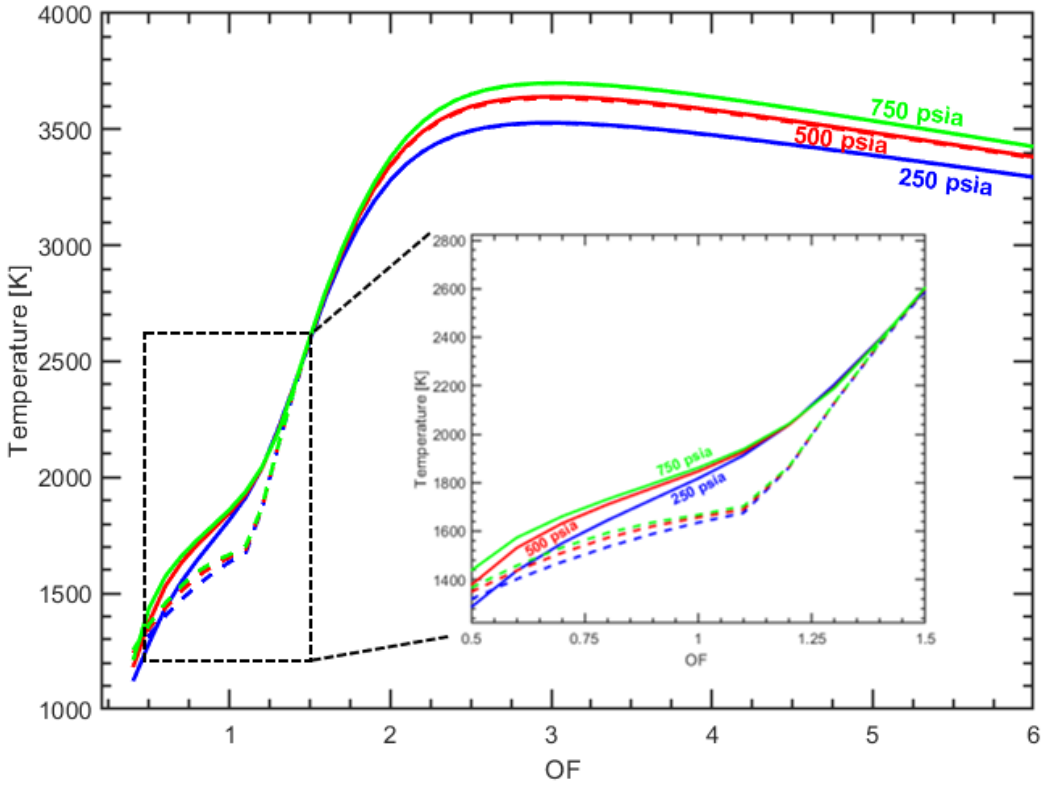

Figure 4.3. Bulk Gas Temperature of RP-2/GOx combustion in a well stirred reactor as a function of mixture ratio and comparison with equilibrium predictions. Solid lines are well stirred reactor calculations and dashed lines are equilibrium predictions. The calculation is done with the HyChem POSF5433 Reaction Mechanism and Thermodynamic Properties

The operating chamber pressures were sized with the experimental goal in mind of understanding the pressure effect on soot deposit. Pressure generally increases reaction rates in the kinetics limited regime and was thought to produce higher soot deposit rates with increasing pressure. The diffusion rate of gas species and particles however exhibits the opposite trend and at some point, the reactions can become diffusion limited, where the kinetic rates are limited by rate of diffusion of species [138]. Once this limit is reached, the soot deposit rate should taper off and no longer increase with increase in pressure. This type of behavior for volumetric soot has been

observed experimentally for methane, ethane and propane in pressurized laminar diffusion flames, as shown in Figure 4.4 [139]. Furthermore, the mean free path of the combustion gas products with the hard-sphere model at ~1600-1800K is on the order of 1e-8 m at 500 psia and on the order of 1e-9 m at 1000 psia. An initial literature review conducted at the start of the experimental design phase showed that average primary soot particle diameters are 1-30 nm [140,141] (though these were at lower pressures and not quite as fuel rich conditions, calculations with the MOMIC model, which hadn't been written at the time of design phase, show the soot particles can be larger). Therefore, it was thought that the increase of soot deposit with pressure should drop off in the 500-1000 psia range because the mean free path becomes smaller than the soot particle size. The original target pressures for the experiment were then set to include this range and go to 1500 psia (for verification that soot deposit amounts are constant with pressure). The experiment was designed and fabricated for the 1500 psia max operating pressure condition. However, later modeling work (discussed in the results section) suggested that soot deposit rates should drop off in the 500-750 psia range and there would be little scientific reason to operate at higher pressures, so the operating conditions were updated by reducing maximum operating pressure to 750 psia.

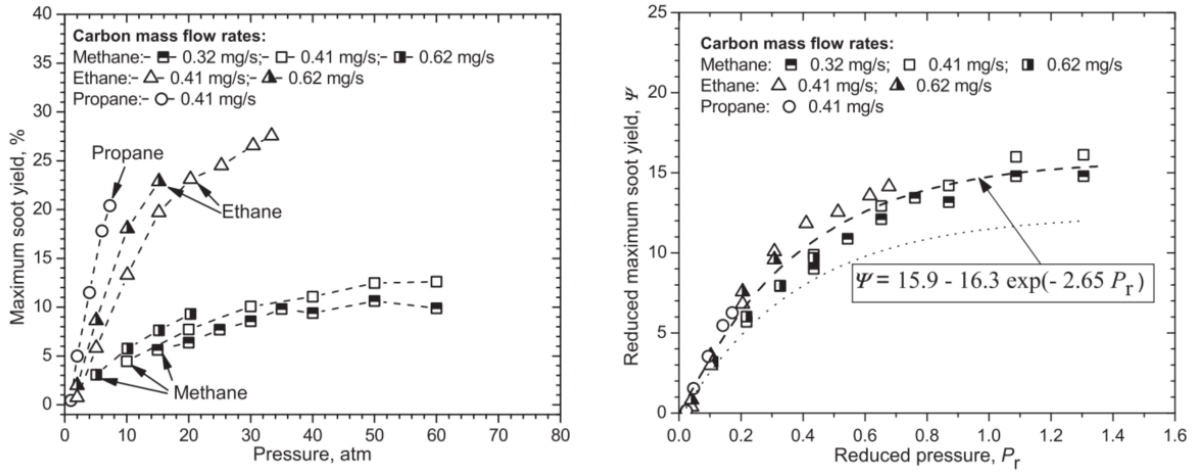

Figure 4.4. Maximum soot yields of methane, ethane, and propane diffusion flames as functions of pressure [Left] and variations scaled with reduced pressures. The soot yield percent and scaling's are discussed in the paper by Gülder et al. The figures are taken from [139]

The testing was performed in the ZL1-108A test cell and used the existing nitrogen fluid system. Additional components were purchased, and test cell plumbed for the other system fluids to handle this range of pressures. However, as will be discussed in the later fluid systems section, the existing nitrogen purge regulators were limited to 500 psia output pressure. In the experiment,

nitrogen purges were required to be on for the entire duration of the test after the torch is turned off to prevent potential hazardous backflow into torch hydrogen and oxygen lines. This required having the purge pressures be higher than chamber pressure, with some safety margin. As a result, the experiment could not be operated safely above ~400 psia (considering pressure drop and safety margins). This issue was discovered during the test readiness review, and the project budget did not allow for purchasing replacement regulator. Because of this oversight, the maximum pressure of the experiment was limited to 400 psia. The final target pressures were then 150 psia, 250 psia, and 350 psia. This range of pressures encompassed the kinetics limited regime and provided good model comparison.

Finally, another goal in the experiment was to understand the effect of residence time on soot formation and deposition. The residence is directly dependent on the bulk mass flow rate. As a start, the nominal flow rate and run time considered for designing the soot experiment were originally equivalent to the Phase I experimental conditions of around 95 g/s (0.21 lbm/s) and 5 seconds. However, when the experiment was being designed for the original high-pressure 1500 psia condition, this flowrate resulted in a very high calculated heat flux. This in turn would have limited the run time for the heat-sink cooled experiment to ~2 seconds, and it was thought this would decrease the potential measurable soot deposit. Though later modeling showed this would have probably produced significant deposit. Furthermore, the mass flow rate is directly proportional to bulk gas velocity and a literature review of soot deposit in EGR coolers showed that the sticking probability decrease and soot removal effects increase with increasing bulk velocity [12,23], as Figure 4.5 shows. It was thought soot removal could conflate the understanding of the deposit mechanisms if it is not accounted for properly. Modeling soot removal would also have introduced additional complication towards understanding the deposit mechanisms. Therefore, to prevent soot removal from conflating the deposit measurements, it was decided to reduce the flow rates to a value that results in bulk velocities below 50 m/s, where soot removal effects could be assumed to be negligible. Reducing the bulk velocity also helped with decreasing heat flux to the chamber. Though the later CFD and 1-D modeling showed that the predicted wall soot growth rates may actually be higher at larger bulk velocities [142,143]. But soot removal at higher velocity case might be more pronounced, which is not accounted for in the models and this would affect interpretation of the soot measurements.

.

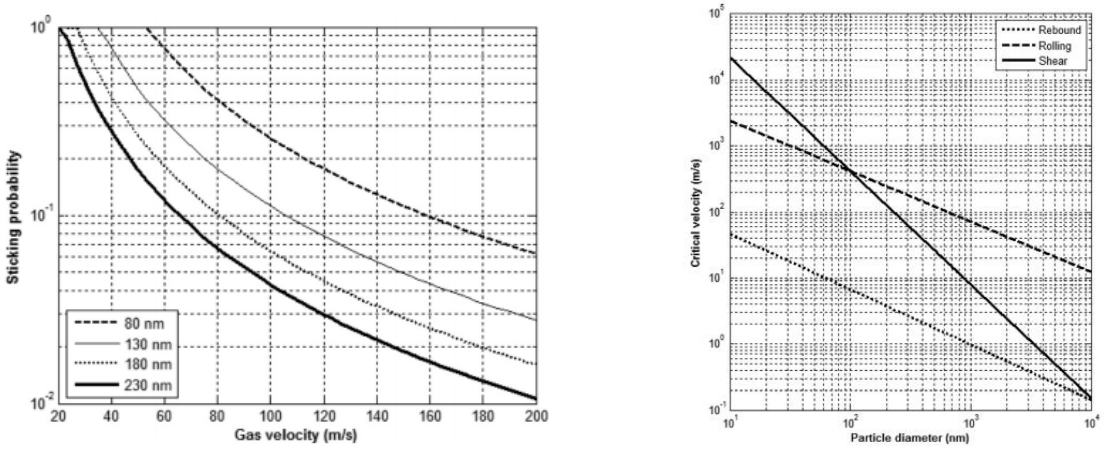

Figure 4.5. Sticking Probability of soot particles of various diameters colliding with a clean surface as a function of bulk gas velocity [LEFT] and critical velocity required for removal of surface soot particles [RIGHT]. Both figures are taken from [12]

The flow rate in the experiment was then sized with consideration of limiting the bulk velocity to 50 m/s to reduce soot removal effects and machining considerations of the injectors. As will be discussed, good injector performance requires a certain pressure drop and this pressure drop $\Delta P \sim \dot{m}^2$. The pressure drop can be increased by decreasing the injector hole diameter, however at some point manufacturing small diameter holes can become impractical, at least from a budgetary perspective. Thus, the injectors provided a constraint on the possible lower bounds of the mass flow.

The lower and upper bound constraints were then used to determine a nominal, a low and a high flow rate for a specific chamber pressure condition. These flowrates were iterated on simultaneously with the injector design. The range of flowrates in turn directly translated to a range of residence times for a specific pressure condition, from which the effect of residence time could be determined. Furthermore, as will be discussed, the pressure in the chamber was set via a choke plate. If the choke plate remains the same, the chamber pressure then becomes directly proportional to the mass flow rate while the bulk velocity and residence time remains roughly the same. The residence time is actually not quite the same because the gas properties (molecular weight, temperature, species) change with pressure but for the operating conditions of the soot experiment

the difference is small. Hence, to compare the effect of pressure on soot deposition, the same choke plate was used to ensure roughly the same residence time in all the cases. Initial plug flow reactor calculations suggested these conditions should produce enough measurable deposit for a five second operation. After designing the ignition sequence, an extra second was added in order to reduce the effect of ignition transient and allow for at least a full five seconds of steady state operation.

With all the considerations discussed, the operating conditions were reduced to three chamber pressures with three mass flow conditions each. This allowed for studying both the effect of pressure and residence time on carbon deposition. However due to time constraint in test cell availability, the test matrix was reduced to three chamber pressures and three different mass flow conditions at just the 250 psia test. This reduced test schedule still met all the test objectives. The overall operating conditions for the tests that were run are summarized in Table 4.1. As previously mentioned, these conditions have been significantly updated from the start of the project until the experiment was finally run. The soot modeling papers that were presented at the following AIAA SciTech and JPC conferences [142–145] showed the previous iterations of the operating conditions and the experiment design. The updates to the experimental conditions have been partly informed by those results.

Table 4.1. Soot Deposit Operating Conditions

Design Pc (psia)	**RP-2 Flow Rate (g/s)**	**GO2 Flow Rate (g/s)**	**Residence Time (ms)**	**Condition**
150	18	18	6.1	Lower Pressure
250	25	25	7.3	Higher Residence Time
	30	30	6.1	Nominal
	42	42	4.2	Lower Residence Time
350	42.5	42.5	6.1	Higher Pressure

Furthermore, as discussed in the background, the Phase I SBIR effort showed that metal composition may have a catalytic effect on carbon deposition [9]. To investigate whether metal composition has a catalytic effect on soot deposition, experimental samples were machined from Copper 101, stainless steel 316. Sample of GrCop-84, a copper and steel alloy that was developed at NASA Glenn Research Center for potential use in future booster engines [146], were also partially machined but the budget allowance made it difficult to complete the fabrication. However, as will be discussed in the results section, the metal composition did not seem to have any

significant catalytic effect and thus there was little justification to test a different metal. The major driver of soot deposit seemed to be thermophoresis and differences in deposit between copper and stainless seemed to be only due to different wall temperatures because of different thermal conductivities. Testing with GrCOP-84 would likely just change the wall temperature and affect thermophoretic deposit but not significantly affect the soot deposit composition.

4.4 Soot Experiment Component Design

Once the initial operating conditions were determined, the experiment was designed to meet the requirements with consideration of budget and modeling goals. The goal of the design was to design the experiment as close to axisymmetric as possible (to reduce sources of error with comparison of axisymmetric modeling work). This section provides a discussion of the analysis and justification of the design decisions in the development of the soot deposit experiment. The machine drawings of all the final components are provided in Appendix B.

4.4.1 Torch Igniter

Several ignition sources were investigated for igniting the fuel rich kerosene and gaseous oxygen propellant mixture in the soot experiment. Glow plugs were initially examined because of their relatively simplicity. However a literature review showed glow plugs have unreliable ignition in diesel engines when the mixture is very rich or at the very least long ignition times are required [147]. Since the target conditions for the soot experiment are fuel rich, a glow plug igniter did not seem optimal. An e-match igniter was considered next due to relatively simplicity in igniting propellants. However, a survey of commercially available e-matches showed they largely consist of carbon containing compounds and it was uncertain how the burned e-match composition would affect the soot chemistry during the ignition transient. So, to limit their potential effect on soot deposit, this idea was discarded. In retrospect, the soot modeling (which I had not started or even thought about for another 1-2 years in my PhD) showed that the initial transients likely only have a small impact on soot deposits and hence e-match ignition may have been a viable approach. Laser ignition methods were also examined due to the promise of simplifying the ignition system and minimally affecting the flow-field. However, they have not been demonstrated for fuel rich

applications, and generally have a lower energy output compared to spark igniters [148], which could be a problem for fuel rich ignition. Still, laser ignition should be considered for any future work based on this project as it offers a promising approach to simplify the ignition system and does not require any additional propellant or purge flows, which as will be discussed can provide some unanticipated headaches.

Spark plug ignition was subsequently investigated as it is a developed and proven ignition system that has been extensively used in many engine applications with high reliability. However, a literature review failed to find spark plug application in high pressure fuel rich kerosene engines. A review of UAV and engine research found that spark ignition suffers from cold start issues with hydrocarbon fuels, where there is not enough energy in the spark to vaporize and ignite cold propellants [149–151]. This could be particularly troublesome for the soot experiment because the injected propellants are at significantly higher mixture ratios compared to these studies. Further literature review found that hydrogen-oxygen torch augmented spark igniters have been successfully used to ignite various rocket propellants including kerosene [152]. In this igniter configuration, hydrogen and oxygen gas is first ignited with a spark plug and then the combusted gases are used to ignite the main propellants. Based on my initial survey of igniters, a torch igniter seemed to be the most practical for igniting the liquid kerosene and gaseous oxygen propellants in the soot experiment and it was ultimately chosen.

This section describes the design work that went into developing a gaseous hydrogen and oxygen augmented spark igniter for the soot experiment. The design was initially based on previous igniter configurations and roughly designed with a 0-D approach. However, testing resulted in significant hardware damage which required re-evaluation of the design. Post-test CFD showed that the 0-D assumption was erroneous because the flow was very non-homogenous. Additional CFD was then used to inform a redesign of the igniter, which was tested reliably without any noticeable problems. This section discusses the design and flaws in the initial design approach and the effort leading to a successful redesign.

Initial Design

Little discussion has been found in literature to guide torch design. Repas [152] and Helderman [153,154] describe gaseous hydrogen and gaseous oxygen torch designs that have been

successfully tested experimentally but lack discussion of design analysis or approach for flow-rate sizing, determining ignition properties or discussion of applicability to other flow conditions. Their designs provided a good starting point though for approaching the design of a hydrogen and oxygen torch igniter for fuel rich kerosene ignition in the soot experiment.

Both the Repas and Helderman designs, shown in Figure 4.6, consist of a main uncooled torch combustion chamber, and a regeneratively cooled torch tube. Gaseous hydrogen and oxygen propellants are burned at a high oxygen-rich mixture ratio within the torch chamber in order to limit the gas temperature. The product gases then exit through the torch tube into the main chamber. Hydrogen coolant gas simultaneously flows around the torch tube, which then mixes with the oxygen rich torch core flow at the exit and reduces the overall mixture ratio closer to stoichiometric. This produces a flame which Repas describes as hot enough to vaporize and ignite cold propellants [152]. The main difference between the two designs is Repas uses a Champion N19 surface gap sparkplug, whereas the Helderman design employs a Champion CH31887 electrode igniter. Both igniters however are aerospace grade and quite expensive, Helderman mentioned the champion spark plugs cost on the order of $1000 and required a minimum quantity of 20 per order [154]. As an alternative, Helderman also tested with much more affordable Auburn SI-140 furnace igniters which cost about $30 but he noted that due to their lower quality, they would sometimes fail if the pressure exceeded 700 psia. Additionally, another difference between the two torch designs is the injection scheme, with the Repas injection scheme being simpler and containing both the hydrogen and oxygen inlets within the main chamber. The Helderman design on the other hand requires machining a more complicated igniter insert with a hydrogen inlet hole that taps off from the coolant flow, as shown in Figure 4.6. Helderman also noted the igniter requires metal seals, which can be significantly more expensive than rubber seals, and requires proper compression otherwise there is a high risk of hardware damage.

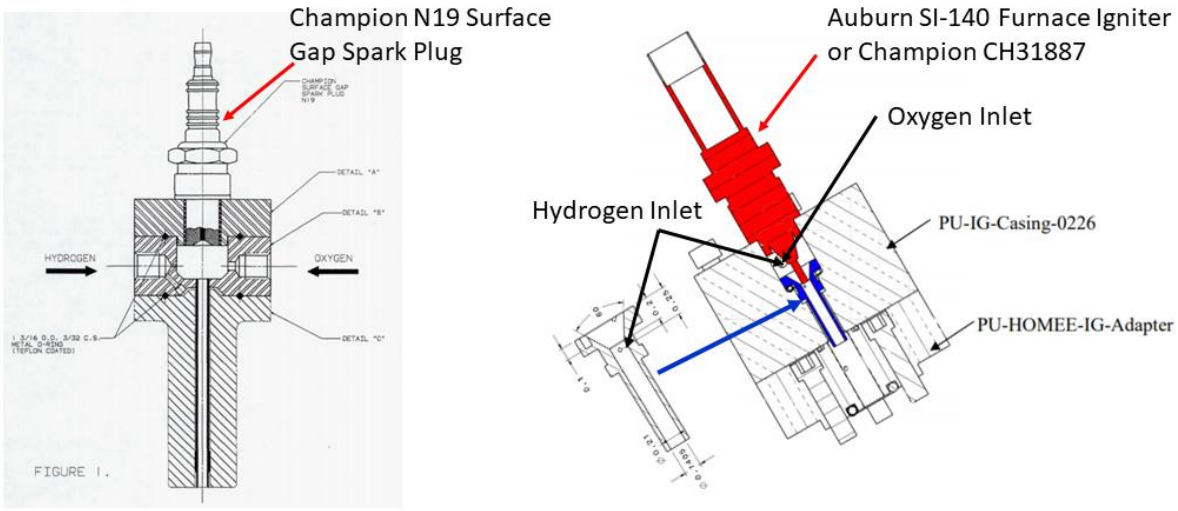

Figure 4.6 Comparison of Repas [Left] and Helderman Hydrogen and Oxygen Augmented Spark Igniters [Right] [152–154]

The initial design of the igniter for the soot experiment, shown in Figure 4.7, used the same configuration as both the Repas and Helderman designs with a main chamber and coolant flow. It was a hybrid of both designs and borrowed features that reduced cost in order to stay within the limited budget of this project. The main feature included using the significantly more affordable Auburn SI-140 furnace igniter. Despite Helderman encountering issues at high pressure with this igniter, it has been reliably used by other research groups at the Zucrow laboratories [155,156]**.** If the Auburn igniter would also need to be replaced after every test in the soot experiment it would still be significantly cheaper than purchasing just one of the Champion sparks plugs. Additionally, the main torch chamber, tube and hydrogen coolant jacket were also designed to be simpler to machine and contain looser tolerances.

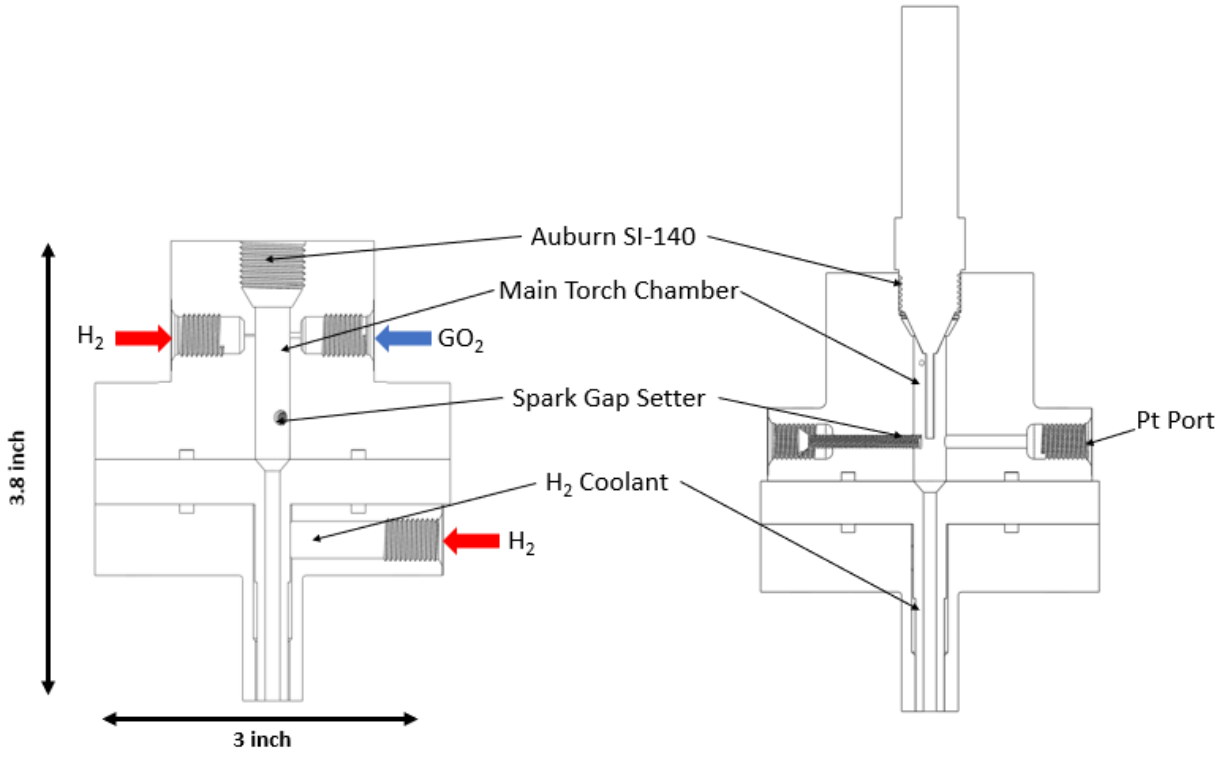

Figure 4.7. Initial Torch Igniter Design

As a starting point in the igniter design, the torch flow rates were first determined by estimating the ignition energy for the main propellants. From internal discussion at Zucrow, the Helderman torch with the original design flowrates would sometimes fail to ignite the main chamber in some experiments, especially if the mixture ratio was decreased. Ramping the main propellants or introducing some additives would sometimes be required to get ignition. Some combustion experiments also contained multiple torches to ignite the main chamber, which added extra complexity. A potential cause of no ignition may have been the energy provided by the torch was below the minimum ignition energy. Hence the first step in developing a suitable torch igniter for the soot experiment was estimating how much energy would be required to ignite the main propellants for the flow conditions shown in Table 4.1. As will be discussed, the approach taken was likely overly conservative and resulted in an estimate that was significantly higher than the minimum ignition energy. However, at least in the case of the soot experiment, optimizing ignition was not important and it was not an issue if the torch energy or torch flow rates were higher than necessary as long as the main propellants ignited. The torch would only be operating for a short

duration, and any effects such as higher heat fluxes due to a larger flow rate could be readily designed for.

The ignition energy for the propellant flow conditions was estimated with an adiabatic zero dimensional well stirred reactor model assuming perfect mixing. As will be explained, this results in the highest possible ignition energy estimate. The model was directly created using the Cantera IdealGasReactor object, with a premixed inlet mass flow corresponding to the soot deposit experiment conditions, shown in Table 4.1; and the outlet mass flow calculated from the compressible 1-D choked flow relations, exactly as described in section 3.2. The governing equations for this WSR control volume are described in section 3.2. The reaction rates and thermodynamic properties were evaluated with the detailed HyChem POSF5433 mechanism [14,15]. The initial condition in the reactor was set to Nitrogen gas at 101325 Pa (14.7 psi) and 300 K. To start the calculation, a pulse of energy was introduced at time zero with a delta function. Numerically, this was done by modifying the enthalpy of the initial inlet mixture and can analogously be described with the following WSR energy formulation:

$$mc_v\frac{dT}{dt} = -\dot{Q} - \sum_k u_k\left(\dot{\omega}_k V M_{w,k}\right) + \sum_{in}\dot{m}_{in}\left(\left(h_{in} + e_{ign}\delta(t)\right) - \sum_k u_k y_{k,in}\right) - \frac{pV}{m}\sum_{out}\dot{m}_{out} \tag{4.16}$$

Additionally, the heat loss in vaporizing the liquid RP-2 propellant was included in the heat term, as described in section 3.2 and as shown:

$$\dot{Q} = \dot{m}_{RP2}\Delta h_{vap} \tag{4.17}$$

The inlet gas enthalpy was increased by a certain amount of energy for the first-time step and then reverted to the original inlet conditions for all subsequent time steps. This produced the ignition energy pulse at the start of the calculation. The ignition energy pulse could have also been done introduced in the $\dot{Q}$ term, or potentially any other terms, but it was just easier to modify the inlet enthalpy in the code. The overall energy equation would have been equivalent and in turn the result would have been identical. After introducing the pulse in the first-time step, the model was integrated to steady state. If the input energy was too low, then the propellants would just increase in temperature but fail to ignite within the residence time of the soot experiment combustor and

instead blow out. At some point as energy is increased, there is enough energy to ignite the mixture, but the ignition delay could be long. If the energy is increased further, then the minimum residence time required to ignite the propellants decreases. In all the cases, the final steady state solution has been verified to be identical once the propellants have ignited. The minimum ignition energy with this approach was iteratively found with a bisection algorithm by varying the initial energy and checking to see if the steady state solution was ignited.

The calculated energy value likely significantly overpredicts the minimum ignition energy for several important reasons. First, it assumes the propellant injection is initially premixed at the design mixture ratio. However, unless specifically adjusted for each condition, the fill time of the RP-2 and GOx in the feed lines and manifolds is different, which in turn affects the amount of propellant injected into the chamber and the transient mixture ratio. If the GOx fill time is faster, then the chamber mixture ratio would start high and drop, which in turn would decrease minimum ignition energy. Non-uniform injection would also create localized regions where the mixture ratio could be closer to stoichiometric and require less energy to ignite. Additionally, the fuel droplet vaporization is finite and, not instantaneous like this calculation assumes. As such, as some initial portion vaporizes, the transient gas mixture ratio could be high and drop off as more fuel is vaporized. In turn this initial transient mixture ratio would be easier to ignite and once lit, it would provide additional energy to vaporize and ignite the remaining droplets. In fact, in very fuel rich liquid combustion there is likely a zone where the propellants burn at close to stoichiometric proportions which then provides energy to vaporize and burn the remainder of the fuel, as section 3.3 and the work on fuel rich pre-burners discusses [71,72]. Therefore, the required ignition energy would be lower. Some of the injection and droplet vaporization effects could be included in the model to get a more accurate minimum ignition energy prediction. A plug-flow reactor model with droplet vaporization calculation could also be written to capture the effect of the initial hot zone. More accurate estimates of minimum ignition energy may be determined from experimental data in literature, though none were available for our operating conditions, or via an approach such as what is described in Turns combustion textbook for calculating minimum flame kernel radius to produce ignition [60]. However as previously mentioned, optimizing the ignition energy was not important for this project but rather only ensuring successful ignition. Hence, this calculation provides a estimate of the highest possible energy that could be needed to ignite the propellants.

Once the ignition energy is determined, the torch flow rates for any combination of torch propellants could be estimated by balancing the total minimum energy required to ignite a certain mass flow of propellants with the reaction energy of the torch, which depends on the torch mixture ratio:

$$\dot{m}_{torch} = \frac{\dot{m}_{in} \mathrm{e}_{\mathrm{ign}}}{\Delta \mathrm{h}_{\mathrm{rxn,OF}}} \tag{4.18}$$

To determine the minimum hydrogen/oxygen torch flow rate required to ignite the RP2 and GOx propellant, the flow rate was optimized with the Distributed Evolutionary Algorithm in Python (DEAP) [157]. In the optimization, the objective functions for minimization were the flow rate and ignition delay (it was desired that ignition delay should be less than 10% of the ignited residence time in order to prevent fuel and oxidizer from pooling up in the combustor and causing a hard start). Unsurprisingly, the minimum torch flow rate corresponded to a slightly higher mixture ratio than stoichiometric. However, the hydrogen and gaseous oxygen flame temperature was very high and heat transfer analysis for flow that is slightly more oxygen rich than stoichiometric showed risk of thermal damage near the torch tip after ignition (the operating mixture ratio is fuel rich and oxygen rich torch flow would increase the overall mixture ratio). A torch mixture ratio of five (at the torch exit plane) though seemed satisfactory.

The main chamber mixture ratio was similarly set via a heat transfer analysis of the torch tube and Auburn SI-140 electrode tip. However, this analysis erroneously assumed that the hydrogen and oxygen propellants in main chamber are perfectly premixed. As will be discussed, our test results and later post-test CFD analysis showed that the oxygen-rich conditions within the chamber was very nonhomogeneous. The analysis as a result was invalid. This was not initially realized though, and adiabatic equilibrium gas properties calculated with NASA CEA Code [13] were used for the thermal analysis. A mixture ratio of 50 was calculated to be conservative enough and allow for the torch to operate for several seconds before encountering thermal problems. With these mixture ratios, the combined torch flow rate was set to 15 g/s (this was about 56% higher than the minimum calculated ignition energy and even more conservative). The breakdown of the chamber and coolant flow rates for the initial torch design are summarized in Figure 4.2.

Table 4.2. Initial Torch Igniter Flow Rates.

Flow	Mixture Ratio	Flow Rate [g/s]
Torch O_2	50	12.5
Torch H_2		0.25
Coolant H_2	0	2.25
Combined Flow	5	15

Once the torch flow rates were determined, the next part in the design was considering the main chamber pressure, feed system setup and the torch operating sequence for starting and safely shutting off the torch flow after ignition of the main propellants. The transient fluid system model discussed in section 4.2.2 was used to guide the design of the torch operating sequence. An initial feed system approach considered was having the torch hydrogen and oxygen feed pressures be below the ignited main chamber pressure, with check valves at the manifold inlets to prevent backflow into the feed lines. Torch propellants would flow normally and then the rise in back pressure during the main chamber ignition pressure spike would effectively shut off the flow within a few milliseconds. The model showed that ignition was probable with this approach, even if the torch flow was instantaneously turned off a millisecond before ignition. However, after extensive internal discussion it was deemed that check valves are not a reliable enough engineering control and if they fail during any test then there would be dangerous backflow of the hot fuel rich chamber gas into the high-pressure torch oxygen lines. Instead, it was decided to have the torch feed pressures be set above the maximum chamber pressure. Torch flow would then only be shut off once the torch propellant run valves are closed. To prevent backflow and keep the propellent lines clean, a nitrogen purge would be on during the entire test sequence with a set pressure that is above the maximum chamber pressure but below the torch hydrogen and oxygen feed pressures. Check valves downstream of the purge run valve would prevent propellant gases from flowing into the purge lines. The purge run valves would also be open during the entire test duration and nitrogen ready to flow in case of abort. As a result, after the torch is shut off, there would be a trickle flow of nitrogen into the main chamber. An overview of this plumbing setup for the torch feed is shown in Figure 4.8, with more detailed plumbing and instrumentation diagrams provided in the appendix.

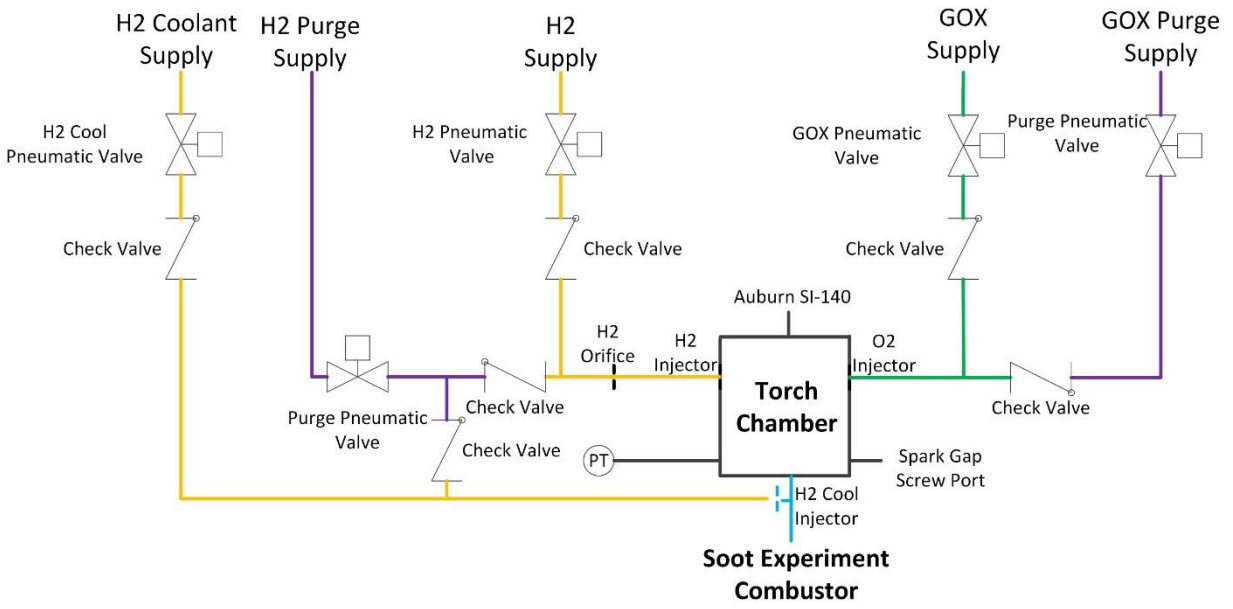

Figure 4.8. Torch Plumbing and Instrumentation Diagram (Subset of the Experiment P&ID diagram that is shown in Figure C.1)

A potential issue with the torch operation, is the purge flow can contribute to a considerable amount of total combustor flow and potentially affect combustion performance or participate in high temperature reactions to produce products such as NOx. The torch hydrogen and GOx injector areas were partly sized with this consideration in mind. The nitrogen purge flow in the feed system was restricted only at the injectors and hence it was desirable to have a smaller injector hole diameter in order to limit the amount of purge flow into the combustor. However, at the same time, a smaller injector hole requires a larger propellant feed pressure in order to deliver the design mass flow rate. Sizing the injector holes required some iteration to ensure that the propellant feed pressures would be viable, and the amount of nitrogen wouldn't significantly affect the soot formation rates or numerical comparison with the experimental results. Discussion of this issue is provided in Chapter 0 but ultimately it was found that the effect of excess nitrogen likely only resulted in higher chamber pressure, and in turn slightly higher soot formation rates, but this could be accounted for in the numerical modeling. Ultimately, a GOx injector hole diameter of 0.05 inch was settled on as a compromise between minimizing the required upstream propellant pressure and purge pressure. For hydrogen, even though the density is 16 times smaller than GOx, the design flowrate was smaller by a factor of 50 and this allowed for machining an even smaller injection hole. However, the smallest hole that could be machined affordably was 0.02 inch. This

was larger than ideal primarily because the required hydrogen feed pressure for the design mass flow rate with this hole diameter was near or below the soot experiment ignited main chamber pressure for some of the operating conditions, and hence there could be risk of backflow into the hydrogen lines. To restrict the flow even further, a smaller diameter orifice was installed into the torch chamber, as shown in Figure 4.8, in order to have a high enough upstream pressure at the design mass flow rate. The hydrogen coolant mass flow rate, which was significantly higher than the main chamber hydrogen, was controlled with a restriction near the torch tip.

Once the injector areas were sized, the rest of the torch geometry was designed. The torch was designed to be coaxial with the main experiment injector insert, discussed in section 4.4.2 which placed a constraint on the torch tube coolant jacket outer diameter. Furthermore, the outlet of the torch tube was designed to be on the same plane as the outlet of the main injectors, which set the length of the coolant jacket and the torch tube. The torch tube inner diameter set the torch chamber pressure; however, the torch chamber pressure was not important for ignition of main propellants. It was only important that propellant supply pressure was higher than chamber pressure to prevent backflow into the lines, but it was not an issue if there was backflow into the torch chamber. Calculations with the transient fluid system model showed ignition was still possible if the torch pressure was turned off a millisecond before ignition, such as in the case of if the torch pressure was below the ignited chamber pressure. The torch tube inner diameter was mainly set because of machining considerations. Specifically, I tried drilling the hole with a 7/64-inch drill bit, because it was already set up on the machine, but the bit broke halfway into the hole. Fortunately, it was a high-speed-steel drill bit and I was able to purchase a stronger carbide 1/8-inch drill, the next larger size, and drill out the hole. This then set the torch tube diameter and in turn the chamber pressure of 270 psi, assuming equilibrium conditions. The main torch chamber length was primarily set by the constraint of the AS5202-2 ports. The torch chamber had two AS5202-2 ports for the propellant and two AS5202-2 ports in the flange section for a threaded rod and pressure measurement. In order to ensure the fittings were able to be installed in the port, the propellent ports needed to have some clearance in between the flange. Finally, a #5-40 threaded rod set the spark gap distance between the chamber and electrode and the maximum depth that could be threaded with the existing tools corresponded to a chamber diameter of about 0.30 inch.

In this initial torch igniter, ignition of the GH_2 and GOx propellants was designed to occur within the main chamber with the Auburn SI-140 electrode igniter. An electrode igniter is

electrically insulated from the chamber body and spark discharge occurs between the electrode and closest chamber surface. In this design, the #5-40 threaded rod set the minimum distance. The voltage required to generate the spark discharge, at a given spark gap distance and pressure, was calculated from the Paschen law [158] as:

$$V_b = \frac{Bpd}{\ln(Apd) - \ln\left(\left(ln1 + \frac{1}{\gamma_{se}}\right)\right)} \tag{4.19}$$

Where V_b is the required breakdown voltage (in volts), p is the pressure (in pascals), d is the electrode distance (in meters), γ_{se} is the secondary-electron-emission coefficient and A and B are constants accounting for the ionization saturation in gas and the excitation and ionization energies. The spark gap distance and pressure at the minimum required voltage for discharge can also be found by differentiating the relation which yields:

$$pd = \frac{\exp(1)\ln\left(1 + \frac{1}{\gamma_{se}}\right)}{A} \tag{4.20}$$

The parameters in the Paschen law calculation can be determined from Nugent's study of breakdown voltages of gaseous propellants for rocket applications, including oxygen [159]. For this project, a Allanson 1092 Type N furnace transformer was used which outputs 6000V at 60 hz, and which has been successfully used in Helderman's torch design [153,154].

Testing of Initial Design

The torch igniter was tested separately to verify proper operation before being integrated into the soot experiment. The testing was only done with GOx and torch chamber H_2 flow. Nitrogen was flown in the annular coolant jacket around the torch tube. The operating conditions for all the torch tests that were run for the initial design are shown in

Table 4.3. The GOx flow rate was set by the injector, as described in the previous section, and the H_2 flow was set by a McMaster orifice. The predicted ignited chamber pressure, assuming well mixed equilibrium flow, was 270 psia. However, as will be shown, the flow was very nonhomogeneous.

Table 4.3. Torch Test Operating Conditions

Flow	Mixture Ratio	Flow Rate (g/s)	Orifice Diameter (inch)	Propellant Supply Pressure (psia)	Purge Pressure (psia)
Torch O_2	50	~12.5	0.05	740	400
Torch H_2		~0.25	0.016	710	350

Before hot-fire testing, nitrogen was flown through the system to characterize the transient pressure response and to get a rough estimate of the discharge coefficients for: hydrogen, and oxygen injectors; the hydrogen orifice; and the torch tube. This involved measuring the propellant upstream pressure and the torch chamber pressure rise after separately opening each individual run valve at several supply pressures, followed by simultaneously opening the run lines together. In addition, the hydrogen orifice was temporarily removed, and this same process repeated. From this data, it was possible to back calculate the discharge coefficients of the GOx and H_2 injectors, as well as the H_2 orifice and the torch tube. It also provided a rough estimate of the valve opening time. These parameters were used in the well stirred reactor systems model discussed in section 4.2.2. This model was used to understand the test results and fluid fill times.

In the subsequent hot-fire tests, the spark was on for the entire duration, purge valves were initially open, and the GOx valve was opened with a 0.2 second lead before hydrogen in order to prevent the chamber mixture ratio from dropping below the design mixture ratio of 50 during startup. Since the purge valves were open initially, the run lines and chamber filled with nitrogen. As a result, after opening the run valves the propellant gases in the lines were initially dilute and required some time for the propellant mass fraction to build up. In turn, the gas composition in the torch chamber took some time to reach an ignitable mixture ratio, as calculated and shown on the right of Figure 4.9. The first tests had the GOx run valve open for a short duration, less than 0.3 second, but these failed to ignite because the torch gas composition had not yet reached an ignitable mixture ratio. However, after doubling the valve run duration, another issue was encountered where the igniter still did not ignite while the propellant run valves were open but produced a hard start about half a second after the valves were closed before being extinguished by the purge flow.

The chamber pressure reading on the left of Figure 4.9 shows this behavior during one of the tests. The cause of the issue was initially thought to be the transients in the fluid system. As mentioned, it takes some time for the nitrogen in the fluid lines to evacuate and to completely fill with the propellant gas; the calculations showed the time was likely longer than in the initial run sequence. At shutdown, the hydrogen run valve closed 0.1 second before the GOx valve. However, the hydrogen flowrate was significantly smaller than the oxygen flowrate and in turn the rate at which the residual hydrogen in the line would have emptied was smaller than GOx. As a result, the injected mixture ratio from the residual gas in the lines would have dropped. The transient well stirred reactor model calculations predict this, as shown on the right of Figure 4.9. The smaller residual gas mixture ratio would have then been easier to ignite and hence it was likely the cause of the hard start on shutdown.

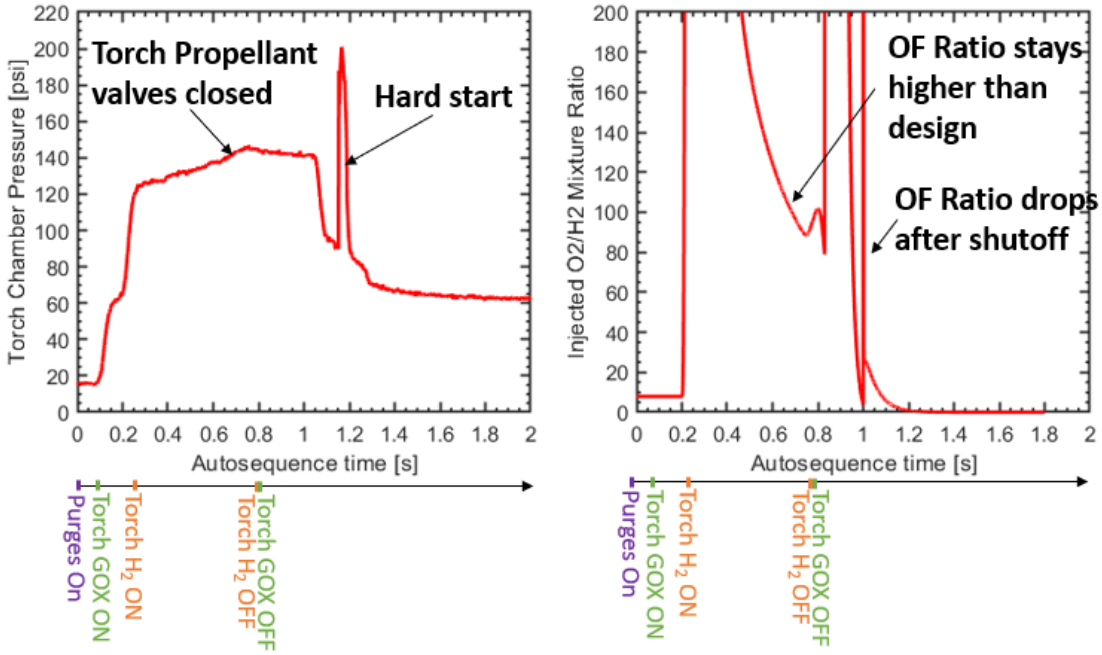

Figure 4.9. Measured Chamber Pressure [Left] and Calculated Chamber Mixture Ratio [Right] for a torch test that produced a hard-start ignition after run valves were closed

After tracing the initial problems to the run sequence, two additional tests were run in an attempt to get successful and smooth ignition. The first approach simply involved running the same sequence for a longer time and produced a relatively smooth ignition at start. However, there was still a pressure spike near shutdown and damage to the Auburn SI-140 ceramic, in addition to

partial melting of the electrode near the hydrogen injector as shown on the left of Figure 4.10. The initial thought was this problem was still due to mixture ratio near the hydrogen injector dropping during the shutdown transient and causing the observed damage. As a remedy, for the next test the GOx run valve was open for 2 full seconds to essentially purge the chamber with GOx after the hydrogen run valve was closed before finally kicking on the nitrogen purge. However, this test resulted in significant hardware damage. There was a smooth ignition at start, but the chamber pressure continued to rise after hydrogen was turned off. After nitrogen purges turned on, the chamber pressure reading was much smaller than nominal, indicating the torch tube outlet area had enlarged. In reality, the torch tube had completely burned up as the post inspection photos in Figure 4.11 show. The nickel electrode was also mostly vaporized, except for about a quarter of an inch from the top, as shown on the right of Figure 4.10. The main chamber though was intact with little signs of thermal damage. The coolant jacket had some metal deposits on the inside walls from the melting of the torch tube, as shown in Figure 4.11, but it was salvageable and likely saved from additional hardware damage by the purge flow that was running. No further testing was done with this torch configuration, as the results clearly showed a problem with this initial torch configuration.

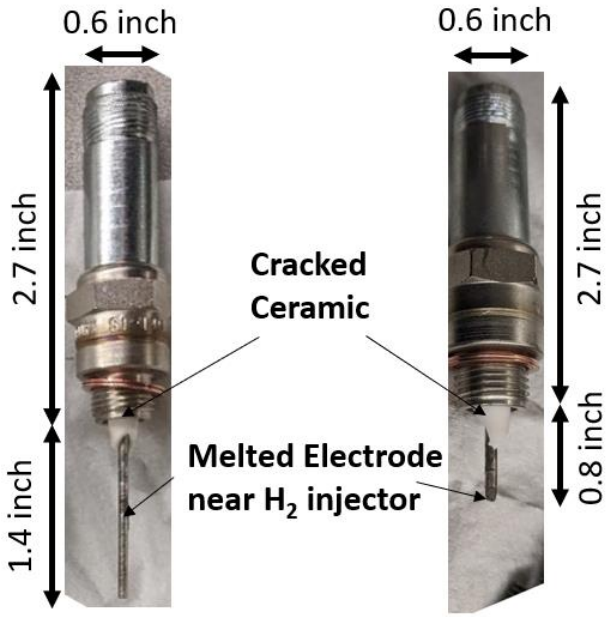

Figure 4.10. Post-test inspection of the Auburn SI-140 electrode for the second to last test [Left] and the last test [Right]

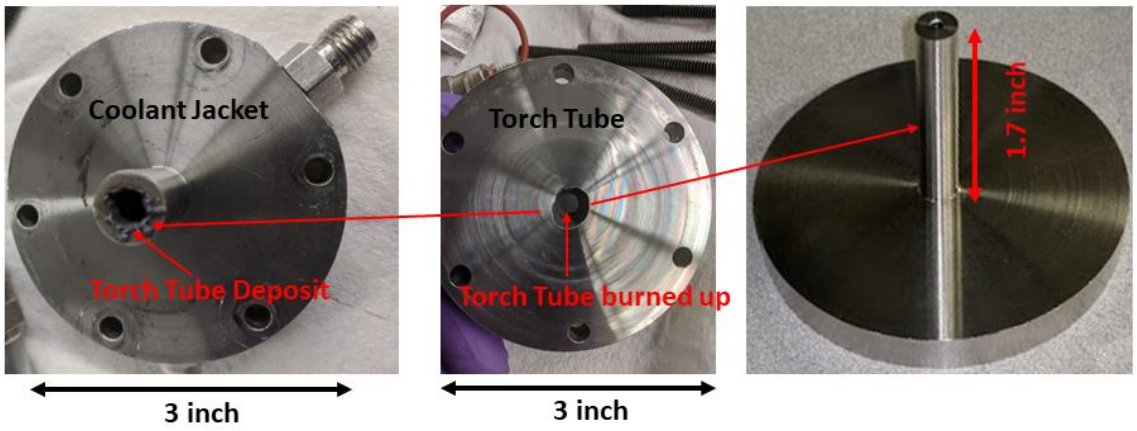

Figure 4.11 Post-test inspection showing hardware damage of the coolant jacket [Left] and torch tube [Center, Right].

Troubleshooting

The test results showed there was an issue with the torch design. However, it was not entirely clear from the test data and the 0-D fluid and thermal models what the cause of the hard-start was and what lead to experimental hardware damage. The nickel electrode was almost completely vaporized so this suggested that the temperatures in the torch chamber were significantly higher than predicted. It was originally thought the issue might have been due to the shutdown transient, but the last test seemed to confirm that this was not the case. From the posttest inspection, a local hotspot was suspected near the hydrogen which could have led to some initial melting of the electrode. Afterwards, the hot nickel metal likely burned itself and during the last test was supported by the oxygen rich environment. However, this behavior could not be captured with the 0-D models and was not considered in designing the initial igniter. To understand this in more detail, I ran non-reacting 3-D CFD simulation of the torch chamber to get an idea of the conditions near the hydrogen injector.

The CFD calculations were done with the GEMS CFD code, which was discussed in section 3.4. The domain modeled and boundary conditions are shown in Figure 4.12 and is simplified from the actual geometry. The injector geometry was not modeled and instead a constant steady uniform mass flow at the hydrogen and oxygen inlets was assumed corresponding to the torch test conditions shown in Table 4.3. The torch tube was also not modeled and instead the torch exit area was set to an ambient pressure condition. The simulation had roughly 5 million

computational cells. The mesh was generated with IcemCFD and the easiest/fastest approach in the software to have a fine cell resolution near the hydrogen injector in order to accurately capture maxing was to make the entire domain fine resolution. The simulation was run with two species using the HyChem [14,15] thermal and transport properties for O_2 and H_2. The time step was set to 10^{-5} seconds. No mesh or time step sensitivity studies were done the goal was to capture the trough qualitative behavior of the mixing near the hydrogen injector, the mesh was also likely overkill. Turbulence was captured with the *k-ω* model and the y+ value at all the wall boundaries was in the range of 0.75-1.5.

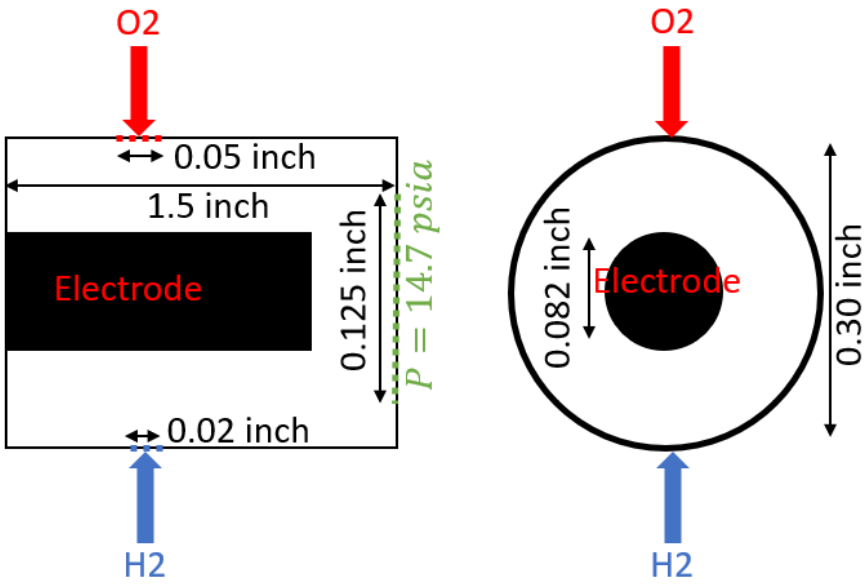

Figure 4.12. Non-reacting 3-D CFD model setup of the torch igniter chamber. The torch tube was not modeled and instead a uniform outlet pressure assumed at the exit.

The resulting simulations were run until steady state. Mass flow convergence between the inlets and exits was not possible because of a large amount of recirculation within the domain. However, the simulations were run until the temperature, pressure and mass fraction solution at several point probes within the domain reached a limit cycle. The averaged results of the simulation are shown in Figure 4.13

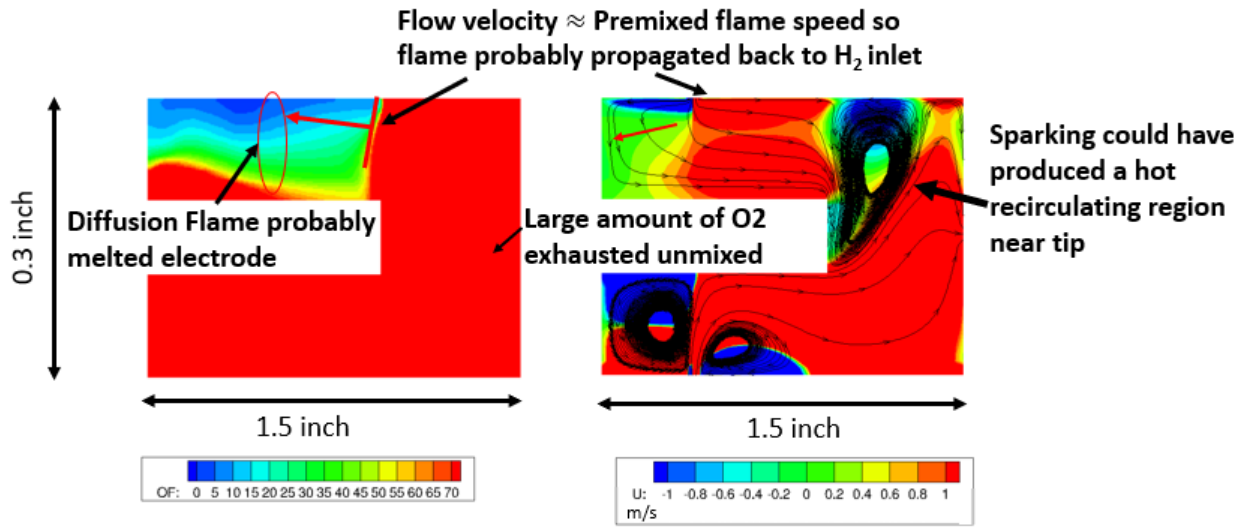

Figure 4.13. Non-reacting CFD results O_2/H_2 Mixture Ratio [Left] and Velocity [Right] for the initial torch igniter

The non-reacting CFD results suggest what may have led to the failure of the torch and show several clear pitfalls with the initial torch design. The zero-dimensional analysis approach, that was used to design the torch, assumed perfect mixing within the torch chamber with a uniform mixture ratio within the torch chamber. However, as the left of Figure 4.13 shows, this was an extremely poor assumption. The large oxygen to hydrogen flow rates, at a mixture ratio of 50, essentially resulted in oxygen filling the chamber. The injected hydrogen velocity in this design is also small, and hence the injected hydrogen momentum is small, which essentially resulted in hydrogen being pushed closer to the injector. Mixing occurred primarily via diffusion, not very efficiently, and the results show this would have produced a very nonhomogeneous mixture in the chamber. There was also a large amount of oxygen that was exhausted unmixed. About 70% of the cells near the outlet area had oxygen mass fraction of unity.

Furthermore, due to the large difference in the momentum ratio of the injected hydrogen to oxygen, the results predict a recirculating region near the electrode tip. The recirculation would have occurred near where the sparking was occurring. Sparking was not modeled, but it is probable that this region may have been substantially heated. As a result, when the mixture ratio became favorable for ignition, it likely would have ignited in this region. This could explain why ignition was observed about 0.5 second after the sparking and run valves were closed during the initial tests. As the residual hydrogen in the lines flowed out, the mixture ratio could have continued to

drop in this region and even though the spark was turned off, this recirculating region could have been hot enough to produce ignition. In addition, hydrogen could have also pooled up near the hydrogen injector, and since the gas velocity in this region was very small, a flame near the ignition region could have rapidly propagated upstream to the hydrogen injector. Rapid consumption of hydrogen in the region may have led to the observed pressure spikes in all, except the last, test conditions. During the last two test conditions, the hydrogen and oxygen valves were open for a longer period and hydrogen would have still been flowing after the flame propagated to the injector. Since the injection velocity was small a diffusion flame would have formed in the surrounding oxygen rich environment. The diffusion flame would have then impinged on the electrode surface causing it to melt, as observed in Figure 4.10. The last test was especially dangerous since now if the diffusion flame was melting and started burning the nickel electrode then the oxygen would have supported the combustion after hydrogen was turned off. The electrode burning would have resulted in significantly higher heat fluxes than what the torch was designed to handle and hence was probably responsible for observed hardware damage.

In summary, the experimental and CFD results suggested that a Repas-like torch igniter with a center electrode is an extremely poor design choice. The original Repas igniter uses a surface sparkplug, with no center rod onto which a potential diffusion flame could impinge. Hence, the Repas igniter would likely have worked with the same operating conditions if a surface sparkplug was used instead. However, it's not mentioned in the Repas paper, but since the flow in the torch chamber is also relatively stagnant, there might still be a risk of a hard-start if the hydrogen gas was to build up and then suddenly ignite. The Repas igniter used an aerospace grade Champion spark-plug which could likely tolerate the hard-start but the cost is an order of magnitude higher than the Auburn SI-140's.

Redesign

The initial torch igniter design had several clear design flaws as the post-test troubleshooting analysis showed and would not be workable for the soot experiment. A redesign was required. However, several tens of hours were already spent machining the original torch components on a CNC-lathe and thus to reduce both additional re-machining time and cost the focus of the redesign was on developing retrofitted solution and reusing salvageable components.

As a first step, several hydrogen injection strategies were explored, including changing the torch operation from oxygen rich to fuel rich. Non-reacting CFD simulations were run for all the cases, via the same approach as discussed in the previous section. The CFD for most of the cases however showed similar poor mixing as in the original torch design for the same reason, the small injected hydrogen momentum impedes adequate mixing. The same was true for injected oxygen in the fuel-rich torch cases. It appeared that one of the difficulties in operating an extremely oxygen rich or fuel rich torch configuration is poor mixing. The small local gas velocity near the hydrogen injector is also unavoidable and as a result it is likely difficult to prevent a hot diffusion flame from forming at the inlet. Increasing the injected gas momentum is difficult, as the injected gas velocity is sonic limited with a straight port and increasing it further would require an infeasible converging-diverging injector. Increasing the mass flow would increase the gas momentum but would also bring the mixture ratio closer to stoichiometric and hence even if the mixing is improved, the higher gas temperature would become a concern.

With the limitations of the low hydrogen inlet momentum and poor mixing within the torch igniter in mind, several approaches were conceptualized for modifying the original torch igniter that would still be workable for the soot experiment. The most viable redesign options thought of are shown in Figure 4.14.

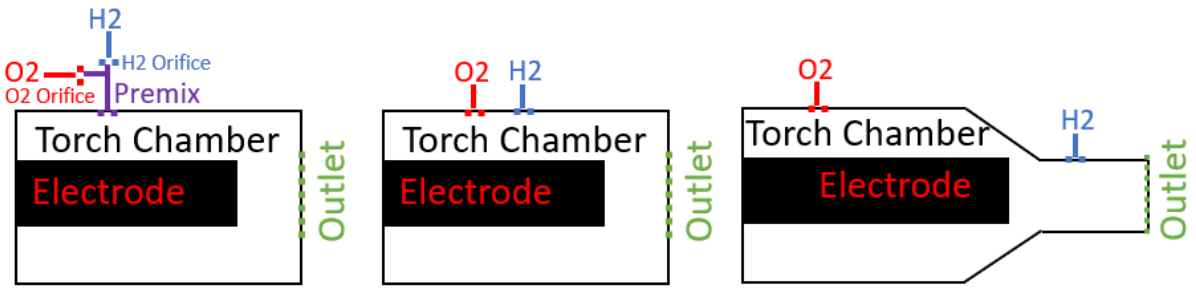

Figure 4.14. Torch Redesign Concepts: Premixing Hydrogen and Oxygen in the feed lines [Left], Injecting Hydrogen below Oxygen [Center], Injecting Hydrogen below the electrode [Right]

The first solution considered was premixing the oxygen and hydrogen directly in the feed-system setup before injecting the mixture into the chamber, as shown on the left of Figure 4.14. This would require essentially no modification to the original torch design. GH_2 and GOx would flow from the supply through an orifice and would mix in a fluid line before being injected into the torch chamber. The injection pressure would be sized so that it provides sonic flow into the

torch chamber in order to prevent any potential for flashback into the lines. However, based on internal discussion, it was thought there might be some risk with this approach when the torch is integrated into the soot experiment. During the experiment, the torch chamber becomes unchoked after ignition in the main chamber and the torch chamber pressure was predicted to rise as a result. See section 4.6 for how the torch behavior was predicted when integrated in the soot experiment. It was thought that if the pressure rise occurs more rapidly than predicted then there is potential to unchoke the injector and cause the flame in the torch to flashback into the feed-system. Increasing the injection pressure so that it is always higher than the torch chamber pressure would mitigate this, but there is a limit on the supply pressure and some of the original conditions in the soot experiment would have required extremely high injection pressures. Also, it was thought that any potential backflow in this situation would be serious. At the very least it would require re-plumbing and re-oxygen cleaning portions of the oxygen feed-system. After installing and cleaning the entire GOx and GH_2 feed system in the ZL1 test cell, replumbing and re-cleaning is something that I strongly wanted to avoid even if the risk was tiny.

A solution explored to avoid premixing the propellants was injecting the hydrogen on the same side as oxygen but lower, as shown in center of Figure 4.14. The approach is like the original design and mixing would still be primarily via diffusion but now there is a shorter distance between the inlets to slightly improve mixing. The oxygen would still push up against the hydrogen, but now the local mixture near the hydrogen inlet would be more oxygen rich. However, since velocity in chamber remains small, there is still a risk of creating diffusion flame that could cause similar problems as in the initial torch design. This could be verified by running a reacting flow 3D CFD simulation, but the computational expense would have required a significant amount of time. There was also still the risk of the electrode burning and being supported via the excess oxygen.

An alternate approach subsequently explored to prevent a straight diffusion flame from forming at the hydrogen inlet was to use a jet in crossflow configuration by injecting GOx like in the initial design but hydrogen downstream in the torch tube near the electrode tip, as shown on the right of Figure 4.14. This is the same injection strategy employed in the Helderman torch design, as shown Figure 4.6. Since there is a reduction in area, GOx would accelerate and have some axial velocity near the hydrogen inlet. If the bulk velocity is larger than the diffusion rate of hydrogen, there would be no flame propagation above the hydrogen inlet and hence little risk of damaging the electrode. Also, if the annular gap between the electrode and torch tube produces the minimum

area for GOx flow then the GOx would be sonic at that point and any pressure spike during ignition would be damped upstream of the torch tip. Hence, the risk of mechanically damaging the electrode is further reduced. Additionally, in this approach, sparking occurs between the electrode and the closest chamber wall with no setscrew, with the minimum required gap distance calculated with the Paschen law as discussed in the initial design section. This configuration is what was ultimately decided for the redesign based on additional reacting flow CFD analysis and from valuable discussion with Robin Osburne from NASA Marshall Space Flight Center.

Furthermore, as previously mentioned, the goal of the redesign was to reduce new machining by salvaging the components from the initial torch igniter testing. The torch chamber and the hydrogen coolant jacket were fixable and only the center torch tube would have to be replaced. The center torch tube required about ten hours of machining time and in the interest of reducing extra machining time alternate solutions were explored. As an initial thought, the possibility of igniting the kerosene with just the main oxygen rich torch flow was explored, without relying on additional hydrogen from the coolant flow. The original minimum ignition energy calculation required the coolant flow to mix with the main torch flow in order to provide a hot enough torch flame to vaporize the main RP-2 propellant and ignite the main propellant mixture at the experimental operating conditions, shown in Table 4.1. The main assumption in this calculation was that propellants are all perfectly premixed at the design mixture ratio, which as previously mentioned was likely an overly conservative estimate. Non-homogeneity due to the injectors, and differences in the manifold fill times would affect the transient mixture ratio and potentially require less energy to ignite. Additionally, the original calculation did not consider the effect of torch flow on the main mixture composition. An oxygen-rich torch would increase the fuel-rich mixture ratio of the main propellants, bringing it closer to stoichiometric, and in turn decrease the ignition energy. For the torch operating conditions shown in Table 4.2, the oxygen rich torch raises the mixture ratio in the main chamber from unity to a value in range of 1.28-1.67 depending on the main propellant flow condition, shown in Table 4.1. In fact, after running the WSR system model with the HyChem RP-2 POSF5433 reaction mechanism [14,15]; and with just the oxygen-rich torch composition, with the flowrates in Table 4.2; and the soot experiment RP-2 and GOx flowrates of 30 g/s, the model predicted successful ignition. Hence the calculations showed that the additional hydrogen from the coolant flow was not required, which greatly simplified the torch re-design. To address potential thermal issues by not having convective

hydrogen coolant, heat sink cooling was employed by replacing the original torch tube with a larger 3-inch copper chamber. This copper chamber was sandwiched between the original torch chamber and torch coolant jacket. The redesigned torch and comparison with the initial design is shown in Figure 4.15; and integration in the main soot experiment is shown on the bottom of Figure 4.1. The redesign had no coolant hydrogen flow. Instead the torch GH_2 and GOx are ignited in the torch chamber and the hot gas products are flown through the coolant jacket into the main chamber. The hydrogen coolant injection port was plugged. The only new machining required was the redesigned copper torch tube, which required less machining time in comparison to the original torch tube.

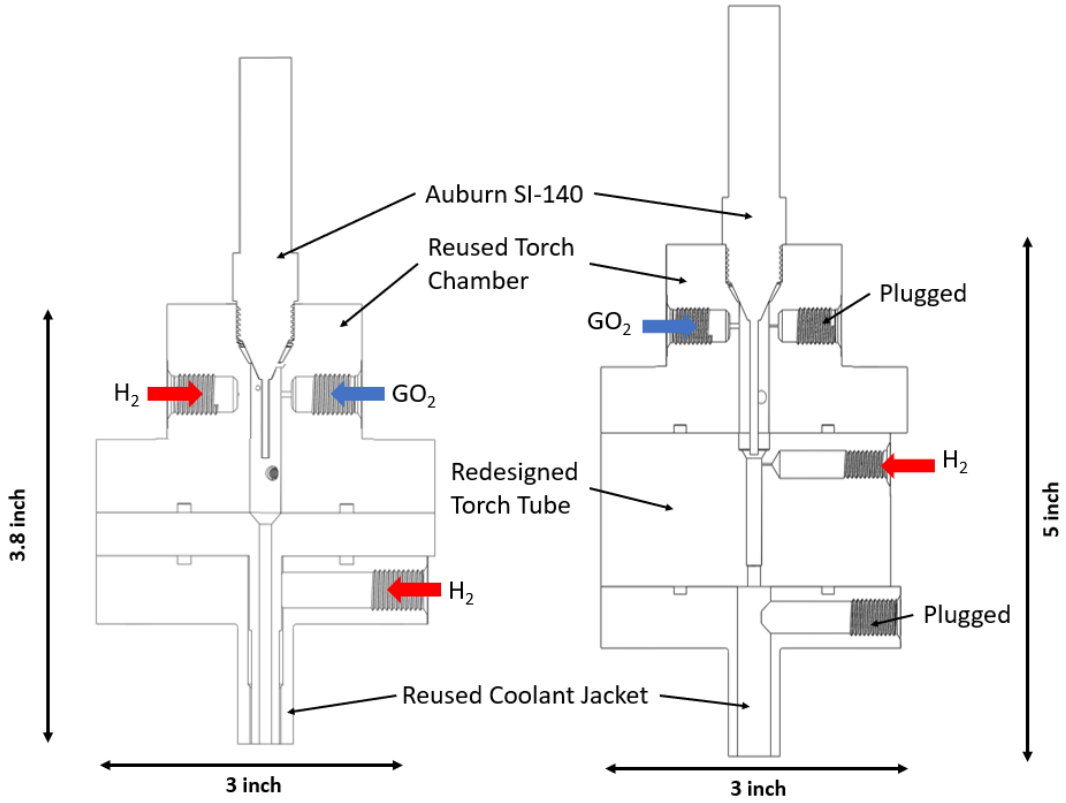

Figure 4.15. Initial Torch Design [Left] and redesigned Torch Igniter Configuration [Right].

The redesign of the torch igniter was also guided via additional non-reacting and reacting 2-D axisymmetric CFD simulations using the same GEMS code. The torch igniter is not necessarily axisymmetric because the hydrogen and GOx injectors are not axisymmetric, but it was assumed in order to reduce computational cost and quickly iterate through several design ideas. The injector was transformed to a circumferential disc in the 2-D model, with the total injector

flow area staying consistent. A circumferential length for each injector was calculated from the diameter of the chamber and the area of the original injector. The flow rates for GH_2 and GOx were the same as in the original design and corresponded to values shown in Table 4.2. The model domain and mesh for the final torch igniter redesign is shown in Figure 4.16. The torch igniter was modeled as integrated in the soot deposit experiment with two inlet mass flow conditions and an outlet pressure condition of 14.7 psia. Initially the torch igniter was modeled separately, up to just the coolant jacket, and an outlet pressure condition of 14.7 psia imposed at the exit. However, the solution was unstable and resulted in large unphysical backflow when reactions were turned on. This was because the uniform outlet pressure boundary condition at the coolant jacket exit was not correct. Modeling the torch correctly would require significantly extending the domain outside the torch tube and modeling the boundaries with a far-field boundary condition, which can be expensive. Instead to reduce computational cost, the entire soot deposit experiment was modeled instead since the outlet of the experiment is choked and the amount of required computational cells was thought to be less. Modeling the experiment domain was also useful to understand the torch flow field within the chamber. All the 2-D axisymmetric simulations discussed in this section were done with this approach. The reacting simulations were run with the Lawrence Livermore National Laboratory 2004 Hydrogen reaction mechanism [160]. Continuous spark discharge was not modeled. Instead, to ignite the propellants a small 0.01 in by 0.01 in region near the hydrogen injector was set to a temperature of 2500 K as the initial condition for the simulation, as shown in Figure 4.16. All the 2-D axisymmetric cases were run with roughly 200,000 cells and a time step of 10^{-5} s for non-reacting and 10^{-6} s for reacting cases. No mesh or time convergence studies were done, as the goal was to qualitatively evaluate and iterate through several redesign options.

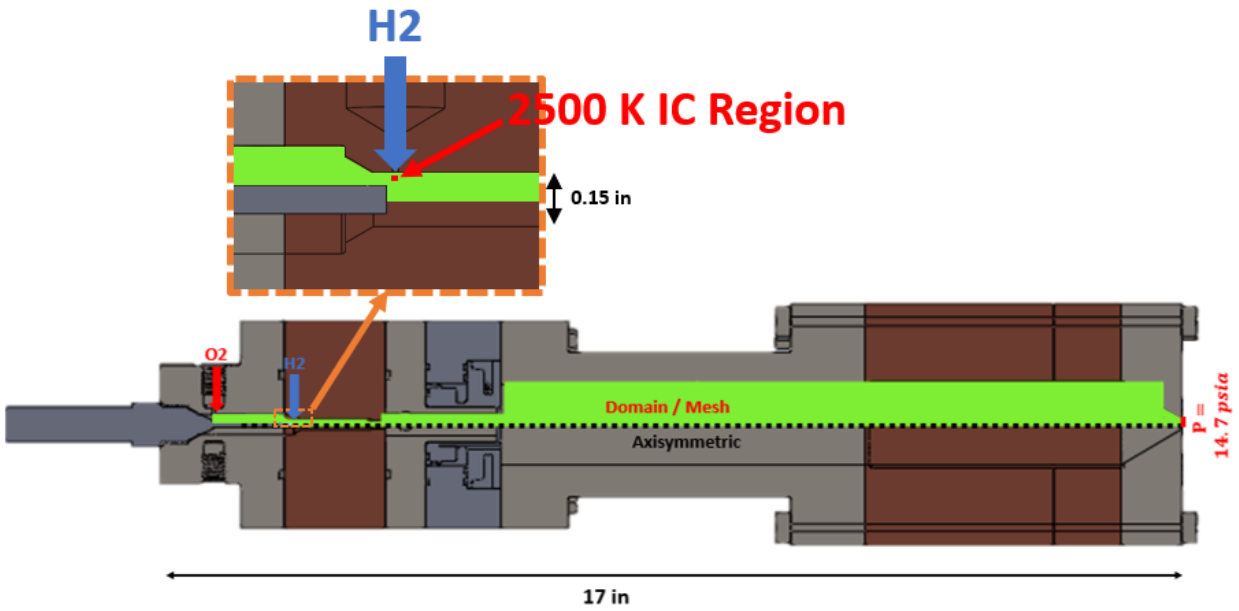

Figure 4.16. Redesigned Torch Igniter Reacting Flow Axisymmetric CFD Setup

Non-reacting simulations were first run for several redesign ideas to ensure the model was setup correctly, the mesh was numerically stable, and the predicted solution appeared physical. These simulations were run to steady state conditions. Steady state was determined when the integrated mass flow rate at the choke plate throat was within 1% of the inlet mass flow rate, and the temperature, pressure and species residuals were less than 1e-3. The non-reacting solution for the final torch igniter redesign is shown in Figure 4.17.

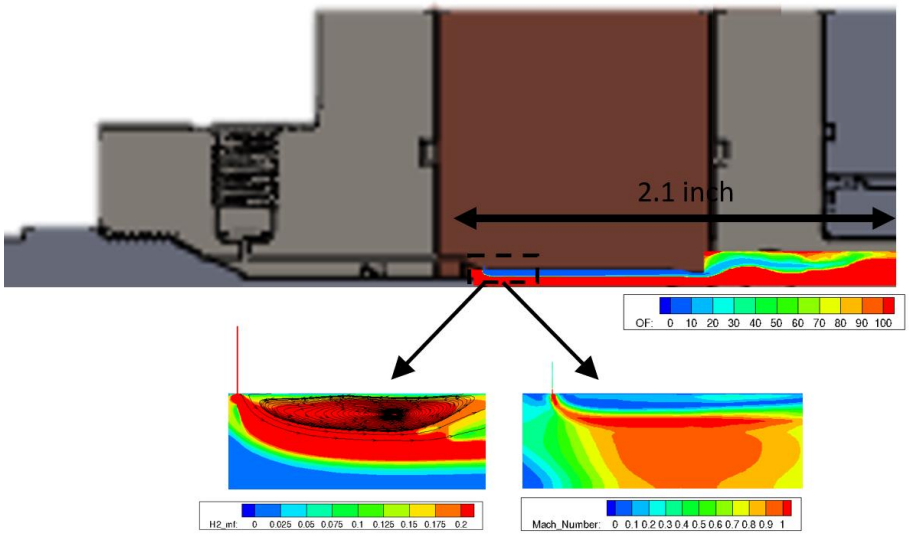

Figure 4.17. Redesigned Torch Igniter Nonreacting CFD Results at Steady State Conditions

The non-reacting solution predicted that in this updated jet in crossflow torch configuration the hydrogen gas remains poorly mixed. Like the original design, the momentum of the hydrogen jet is small because the mass flow rate is small. The injection velocity also cannot be increased above sonic without machining a converging-diverging injector, which is infeasible. As a result, the hydrogen jet does not fully penetrate into the main flow and instead flows along the inner walls of the torch tube. An idea that was looked at to increase the penetration was to inject hydrogen in the short converging section, right before the straight tube section, to add a ramp effect. However, at the current torch operating conditions this provided only a little additional hydrogen jet penetration, at the cost of requiring more expensive machining. Another idea that was explored was increasing the torch tube diameter in order to decrease the bulk velocity and hence increase the jet to crossflow momentum ratio. This provided some additional mixing but there was a limit to how large the diameter could be. In the redesign it was desirable for the GOx flow to enter the torch tube section at close to sonic conditions in order to reduce pressure spikes from propagating upstream and mechanically damaging the electrode, such as from a potential hard start. If the tube was too large, then the torch chamber conditions would be like the initial torch igniter. No good approach was found to improve mixing within the torch chamber, however as will be discussed, the reacting solution showed that poor mixing is not necessarily a problem since the flame produced would be hot enough to vaporize and ignite the kerosene propellants in the main soot experiment.

Reacting simulations were run afterwards to steady state convergence. The setup was the same, except hydrogen and oxygen reaction calculations were turned on and a 0.01 inch x 0.01 inch region near the injector was set to 2500 K as the initial conditions. Additionally, the walls in this simulation were modeled as adiabatic. Steady state was determined when the integrated mass flow rate at the choke plate throat was within 1% of the inlet mass flow rate, and the temperature, pressure and species residuals were less than 1e-3. The reacting flow results are shown in Figure 4.18.

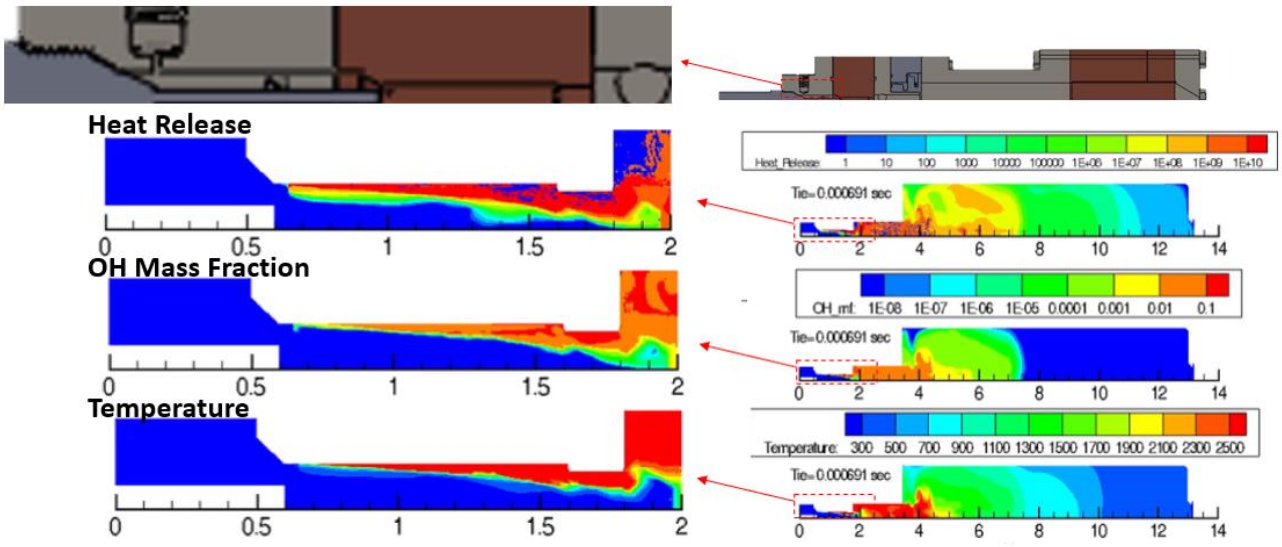

Figure 4.18. Steady state reacting flow CFD results of the redesigned torch igniter

From the reacting flow results, it was apparent that because of the low injected hydrogen momentum, most of the heat release within the torch tube occurs near the wall at an off-design mixture ratio. For this reason, the torch tube in the redesign was replaced with a copper heat sink cylinder to withstand the higher heat fluxes. The predicted core-flow in the torch tube consists of relatively cool unmixed oxygen. However, mixing is improved downstream of the torch tube and the flow is more uniform in the combustion chamber section. There is also some recirculation of the hot torch products near the main injector in the combustion chamber, which should provide enough energy and residence time to ignite the propellants, as calculated via the zero-dimensional Cantera WSR calculation. No detailed CFD simulations were run for main propellant ignition as that would be very computationally expensive.

Moreover, a small step at the torch tube exit was added in the redesign to choke the propellant flow and have subsonic flow upstream. Otherwise, the flow would be sonic in the torch section. The reacting CFD showed that ignition and flame holding in the torch was more difficult with a sonic flow for the same torch propellant flow conditions. The results predicted the flame would blow out within a few milliseconds after ignition. The initial conditions simulated a single spark by setting a small region to 2500 K, so it's possible that continuous sparking would keep the torch lit. It was also possible in the CFD to stabilize the flame downstream by incorporating a

cavity flame-holder, like what is used in scramjet combustors [161]. However, the choked subsonic torch approach was the simplest to machine and experimentally test.

Additionally, the reacting flow CFD showed that the electrode is surrounded by cold oxygen and remains cool throughout the test. As such, this should prolong the life of the electrode and allow for significantly more test firings.

Simultaneously with the CFD simulations, heat transfer calculations were done to evaluate the viability of various redesign options. These were run with the model discussed in section 4.2.1 as the latest version of GEMS did not have an ability to calculate conjugate heat transfer. The CFD solution was used to calculate the wall heat flux. The gas properties were assumed constant and hence the heat transfer coefficient assumed constant. Since the CFD used adiabatic boundary conditions with no heat loss to the wall (which would be significant for copper), the calculated wall heat fluxes were conservative in the calculation. The transient heat transfer predictions for the final redesign option are shown in Figure 4.19. In this calculation, the model was simplified by truncating the copper part and applying adiabatic boundary conditions on the other walls.

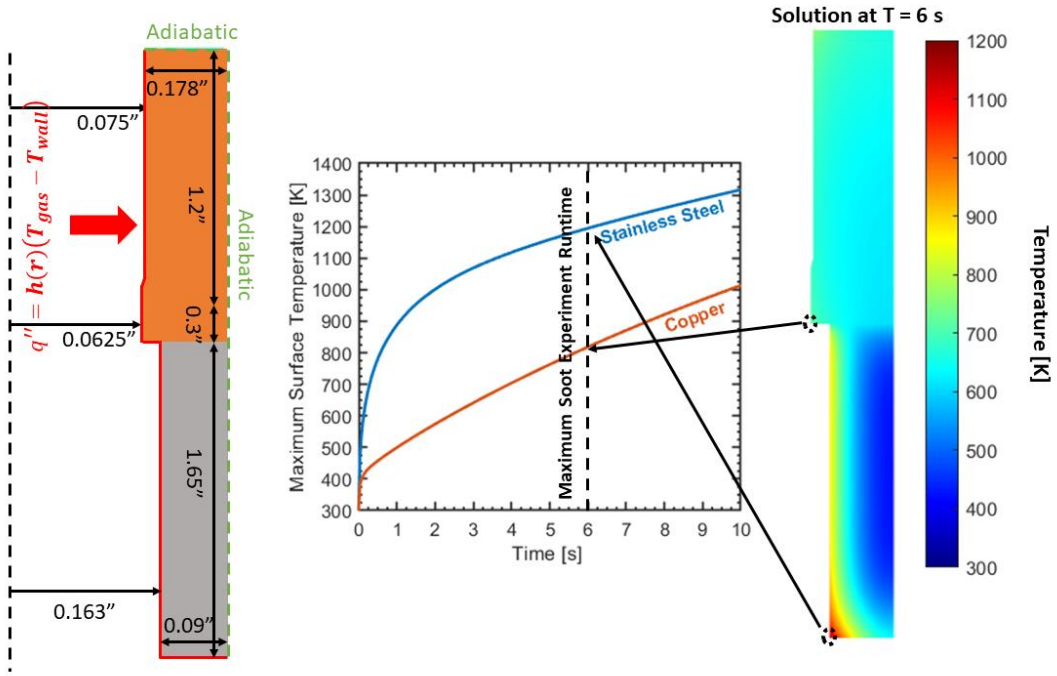

Figure 4.19 2-D transient heat transfer predictions for redesigned torch igniter with the reused stainless steel coolant jacket.

The maximum run time that was envisioned for the soot experiment was six seconds, as discussed in section 4.3. The thermal results showed that it would be safe to operate the redesigned torch igniter for the entire test duration if needed. Due to a large copper mass of the redesigned torch tube (which is much larger than what was used in the thermal analysis) and high thermal conductivity, the part can operate for an extended amount of time before encountering any thermal related issues. The limitation on the redesigned igniter is the reused stainless-steel coolant jacket, which has a much smaller thermal conductivity but can withstand higher temperatures before encountering thermal problems. Nonetheless, the thermal analysis showed it was satisfactory for the soot experiment.

Testing

After machining the copper torch tube and repurposing the initial stainless-steel torch chamber, the redesigned torch tube was tested. All the flow parameters were the same as in the original torch design and the feed system remained the same, as shown in Figure 4.8. Initially, testing was done without the repurposed coolant jacket and the run time slowly increased up to 2 seconds to ensure no damage of the components. Afterwards, the same testing was done but with the coolant jacket installed. As shown in Figure 4.15, the coolant jacket port was plugged, and it was basically just a straight tube extension. The coolant jacket served no purpose in the torch tube operation anymore, but the outside diameter is what set the position for the main soot experiment injector, as discussed in section 4.4.2. Torch testing was done with the coolant jacket to check if it could present any potential unforeseen issues for running the main experiment. The torch was fired several times and showed successful ignition without any noticeable damage to any hardware components after a post-test visual inspection. Figure 4.20 shows the torch firing from two of the tests. The yellow plume that's visible was likely due to dust particles in the air.

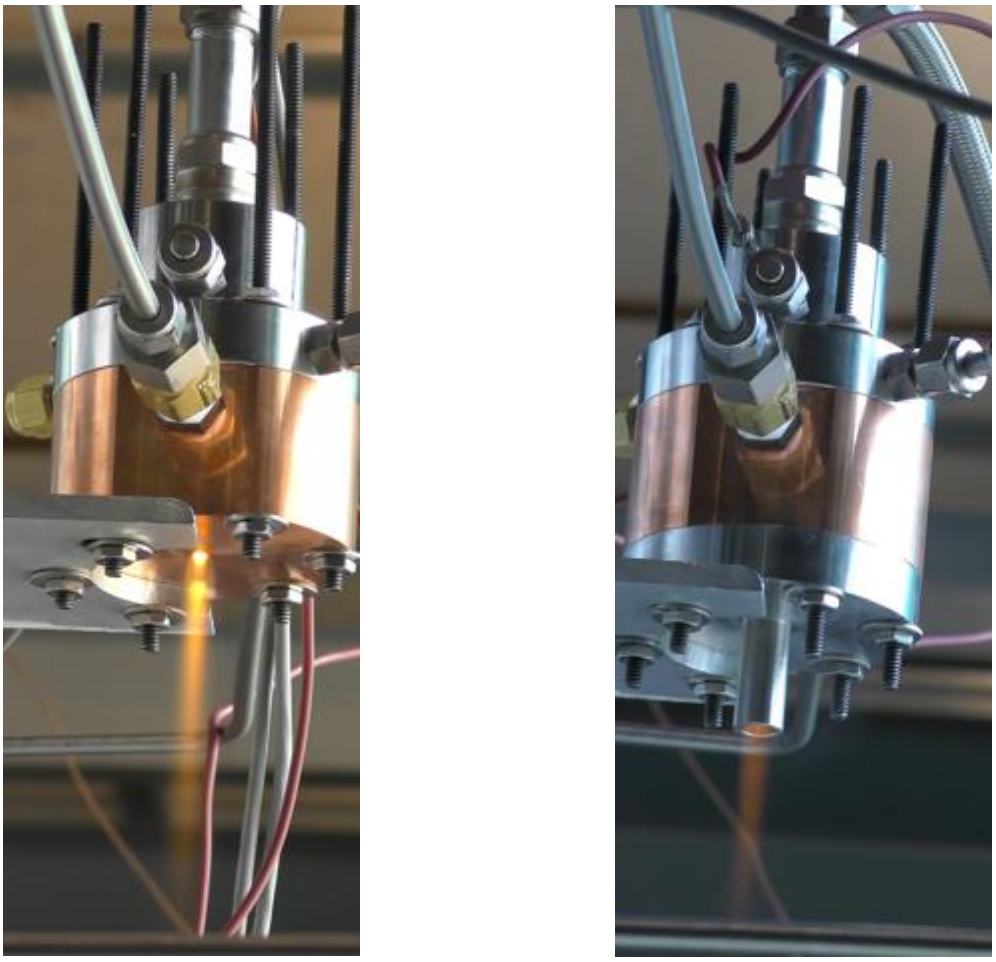

Figure 4.20. Torch igniter test fire without torch tube [Left] and with the torch tube reused from the original design [Right].

The torch chamber pressure reading showed smooth ignition as predicted by CFD, as shown in Figure 4.21. The transient pressure prediction with the well stirred reactor model also showed reasonable agreement with the experiment despite being a 0-D calculation. Differences between the experiment and model are probably mostly due to the nonhomogeneous flow.

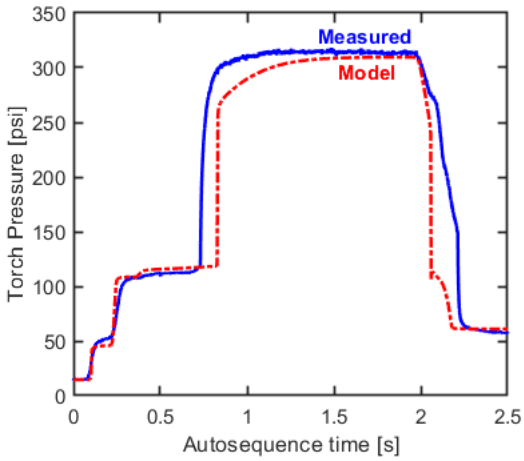

Figure 4.21. Torch Chamber Pressure compared to model prediction. The differences in the transient pressure rise and fall are probably largely due to the perfectly mixed assumption in the WSR model

The torch igniter worked flawlessly during torch testing. However, there was an issue with repeatability after it was integrated into the soot experiment. In some tests the igniter ignition was repeatable. Testing on another day resulted in ignition failure and required several run attempts to ignite, as shown on the left of Figure 4.22. The mixture ratio being close to ignition limit was suspect but after lowering the ratio and testing again, similar inconsistent behavior was still observed. Removing and cleaning the electrode seemed to improve ignition for several attempts, but then ignition was unreliable. The data also showed the regulators feeding the torch exhibited droop by 40-80 psia. Attempts to correct for this by raising the supply pressure still resulted in ignition inconsistency. After a lot of head scratching, inconsistent spark location was suspected.

In the igniter, the electrode tip is right at the entrance to the torch tube, as shown in Figure 4.15, however the electrode is not perfectly concentric. Repeated operation of the torch might result in some slight deformation of the electrode and in turn the minimum distance between the electrode and torch chamber body shifting to a different location. If the spark location happened to shift upstream, then this could have prevented ignition. As a potential solution to increase ignition reliability, the electrode length was increased so that it partially stuck into the torch tube and spark would occur within the tube. This approach seemed to fix the inconsistency and all the igniter runs for the remainder of the testing in this project ignited successfully, as shown on the right of Figure 4.22 for some of the checkout tests. Note the pressure is slightly higher than

previously because adjustment to the drooping regulators resulted in slight increase of propellant mass flow.

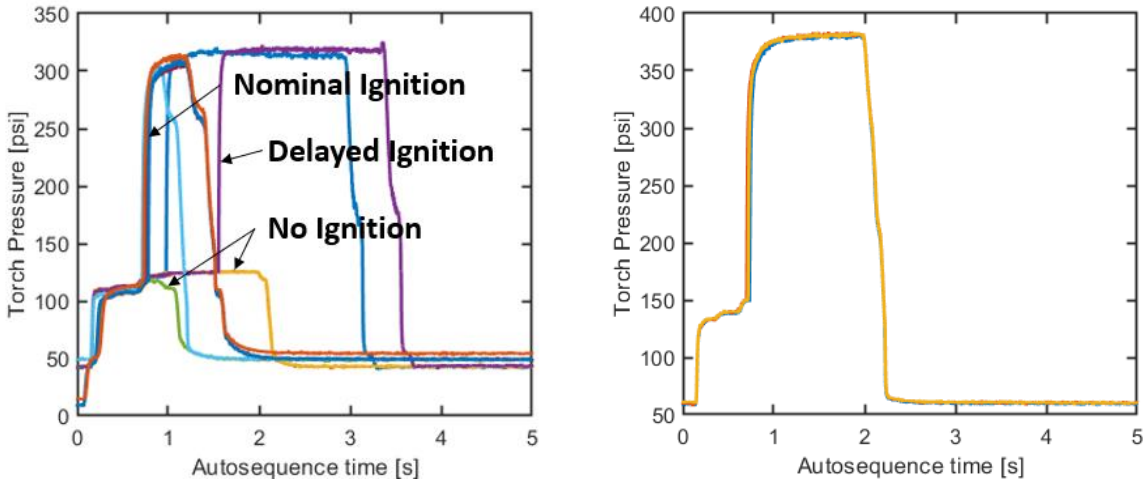

Figure 4.22. Inconsistent ignition during initial testing, with ~30% cases igniting [Left] and consistent ignition after increasing the electrode length [Right]

Another torch concept from CFD

Reacting flow CFD was run for several various igniter concepts to help guide the torch igniter redesign. Some of the concepts were either not viable to machine or didn't ignite or if they did then they would blowout unless some recirculating steps or cavities were used to stabilize the flame. The redesigned torch was ultimately chosen as the safe option. However, the CFD also suggested an interesting Bunsen-burner like approach as an alternative to operating the torch igniter which could allow for extended run times or operation at close to stoichiometric conditions. The reacting flow results showed that if the igniter is ignited normally and then the mass-flow is increased above the blowout limit, the torch will blowout but will stabilize at a recirculating step at the outlet of the torch, as shown in Figure 4.23. Since, the flame now lies outside of the of the torch, this could allow for operating the torch at a mixture ratio close to stoichiometric without risk of thermal damage to the torch components. Other torch designs such as the Repas and Helderman [162,163] utilize a coolant flow on the outside of the torch tube, which mixes at the exit plane to produce a near-stoichiometric flame. This approach could simplify the torch design if a hot torch exhaust is required by utilizing just one main torch chamber. The main hydrogen torch flow can be ramped up after ignition to produce this blowout and stabilization. Alternatively,

another injection port can be added to the torch to inject additional hydrogen. The redesigned torch hardware can be operated this way and the only changes that would need to be made are plumbing related. This design however was only numerically simulated and not developed or tested. As a future investigation, it may be interesting to test this idea to verify the practicality of such operation.

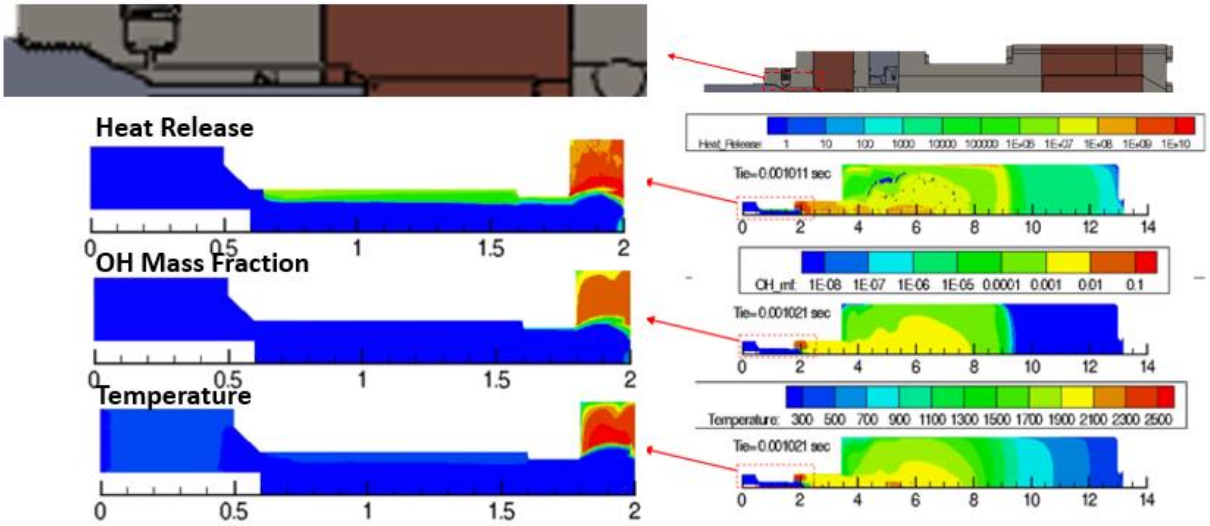

Figure 4.23 Steady state reacting flow CFD results of a Bunsen Burner like torch igniter

4.4.2 Injector and Manifold

As described in the experimental overview, the experiment was intended to provide axisymmetric flow in order to facilitate experimental comparison with the 0-D, 1-D and 2-D axisymmetric models (modeling the injection and reacting flow-field as three-dimensional was beyond the scope of available computational resources and was not thought to provide much scientific usefulness for understanding soot deposition). Therefore, it was very desirable to have an axisymmetric injector with good atomization. Additionally, the torch igniter was designed with the same axisymmetric considerations which constrained it to be at the center of the combustor. This in turn constrained the injector design to wrap around the torch. Several injector types were surveyed for liquid kerosene and gaseous oxygen injection that could satisfy this constraint.

Initially, a coaxial counter swirl injector was investigated and designed based on both the guidelines provided by Bazarov and scaling to experimental data in literature [164–167]. In the design, the liquid kerosene and gaseous oxygen were injected through two annular injectors around

the torch tube with the swirl from each sized to cancel out the overall angular momentum. However, after later discussion with researchers at NASA Marshall Space Flight Center ER32 Branch, it was advised to avoid this design because of potential instabilities (and hence non-axisymmetric flow phenomena) in fuel rich kerosene mixtures unless the injector was properly designed with detailed CFD and machined with exact tolerance and good surface finish. This would have likely been beyond the scope and budget of this work, and as such alternative injector designs were explored.

A shear coaxial injector design was subsequently investigated as another axisymmetric injector. For this design, two alternative configurations were explored. One design involved using the same center-port torch for GOX flow and flowing liquid kerosene from an annular coaxial port. A second design investigated two annular coaxial injectors wrapped around the center-port torch, just like in the initial counter swirl injector concept. Both injectors were sized based on the guidelines and scaling to experimental data provided by Davis [168]. However due to the small operating flow rates of liquid kerosene in the experiment, and with a higher comparative density to gaseous oxygen, the required size and tolerance of the kerosene injector was too small to feasibly machine within the budget of the project. This was also true for the counter-swirl injector design. If the flow rates were an order of magnitude higher, then this would probably have been a decent axisymmetric injector design choice.

Other injector designs were briefly investigated for small flow rates, but no other types were found that were axisymmetric. Ultimately the final injector design decided upon was an impinging Fuel-Oxidizer-Fuel (FOF) triplet injector. This injector configuration, as used in the soot deposit experiment, is shown in Figure 4.24.

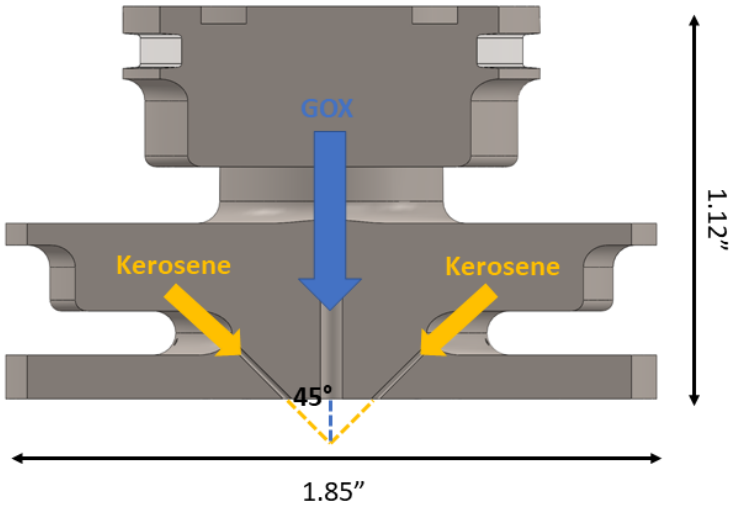

Figure 4.24. Kerosene and Gaseous Oxygen Fuel-Oxidizer-Fuel (FOF) Triplet Injector

Compared to other impinging injectors, such as the like and unlike doublet impinging injectors, literature shows that FOF injectors have higher mixing efficiency and less of mixing performance drop due to misalignment of the holes during machining [169,170], which was a very important consideration since I was originally planning to machine the entire part. The FOF injector has also been successfully used in other fuel rich kerosene experiments [10].

The design of the injector was guided based on the experimental results from prior Rockwell (at the time) Rocketdyne studies on gas-augmented injectors [169,171]. The studies included a triplet Fuel-Oxidizer-Fuel injector investigation of liquid oxygen and gaseous hydrogen. Though this propellant combination was different from my experiment conditions, the key results from the study were used for designing the liquid kerosene and gaseous oxygen triplet injectors for the soot experiment, as no other literature or guidelines for kerosene triplet injector design were found at the time of the design phase.

In the gas-augmented injector report [169], the triplet injector performance data from [171] was empirically correlated with several injector parameters. One of these correlations was for the ratio of total injected hydrogen gas momentum (M_g) to liquid oxygen flow rate ($\dot{m}_0$) as $\frac{M_g}{\dot{m}_o}$, as shown in Figure 4.25. It was thought this was a measure of the potential capability of gas to atomize and mix with the liquid oxidizer. The trend showed that this parameter significantly impacts performance if it is too low but performance asymptotes above a value of 600 ft/sec (183 m/sec).

For the design of the triplet injectors in the soot deposit experiment, the injected gaseous oxygen momentum to the liquid kerosene flow rate ratio was designed to be over 600 ft/sec (183 m/sec), in accord with these results.

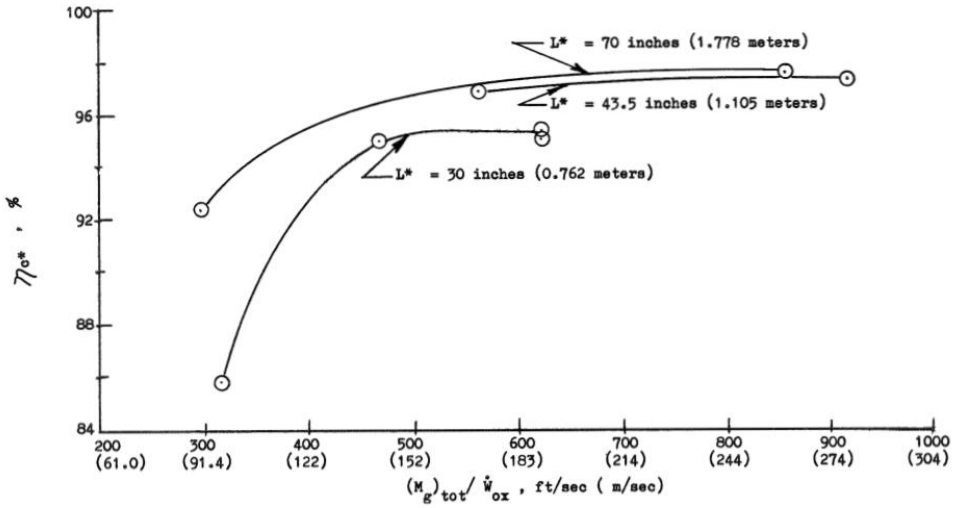

Figure 4.25.Gas Momentum Effects on Fuel-Oxidizer-Fuel Injector Performance. Figure taken from [169].

Furthermore, results on the effect of chamber L* showed that even though spray vaporization approaches 100% with increasing L*, the propellant mixing changes slowly from what is established near the injector [169]. All the modeling discussed in Chapter 3 assumed pre-mixed inlet conditions and hence designing the injector to have good mixing was important to reduce error in the comparison of results. In the report, it was mentioned that previous experience at the company has shown a significant correlation between penetration of the liquid stream into the gas flow and propellant mixing, including distribution uniformity. The penetration was assessed by the penetration parameter, which was defined as:

$$\frac{x_p}{D_g} = 2.5\left(\frac{M_l}{M_g}\cos^2\theta\right)^{\frac{1}{2}} \qquad 4.21$$

Where x_p is the penetration length, D_g is the center port diameter, M_l is the liquid jet momentum (for an individual jet), M_g is the gas jet momentum (through the center port) and θ is the complement of the impingement angle between the liquid and gas jets.

The penetration parameter was calculated for a long L* hot fire test and mixing efficiency values were compared against this parameter and plotted, as shown in Figure 4.26. From these results, the optimum value of the penetration parameter was found to be between 0.5 and 0.8. Other testing also showed a similar trend. This range was targeted for the design of the soot experiment triplet injectors.

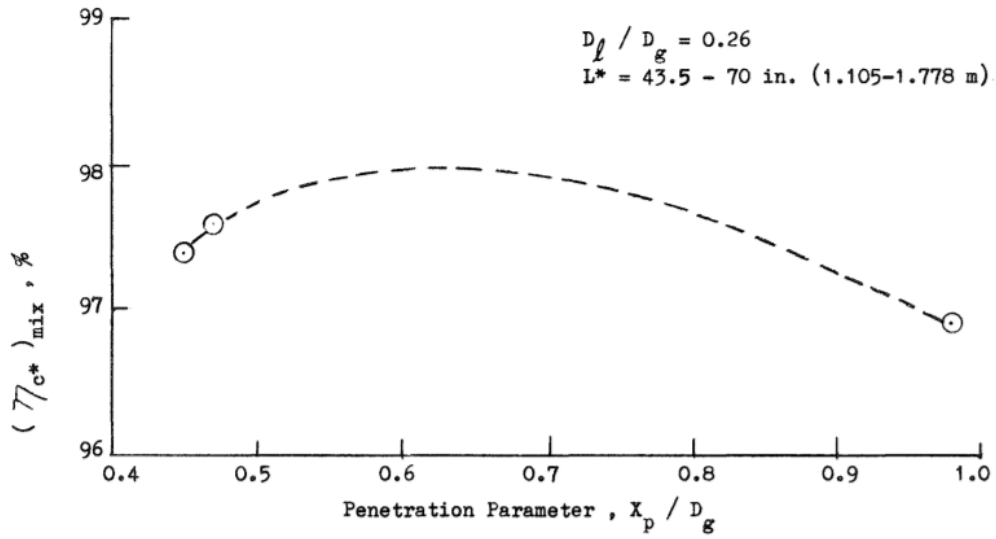

Figure 4.26. Mixing Efficiency of Gas Augmented Impinging Jet vs Penetration Parameter. Figure taken from [169]

The effect of the liquid and gas injection diameter ratios on mixing efficiency was also assessed with cold flow testing. Mixing efficiency was determined by assuming the gas was well mixed and measuring the liquid dispersal. The cold flow results showed that the liquid to gas orifice diameter ratio $\frac{D_l}{D_g}$, has a strong influence on spray distribution uniformity and is in fact independent of penetration parameter (penetration parameters in the optimum range of 0.5-0.8 still result in higher performance compared to outside this range) as Figure 4.27. shows. The optimal diameter ratio from the study was found to be above 0.3, and similarly this was the target for the soot deposit experiment injector design.

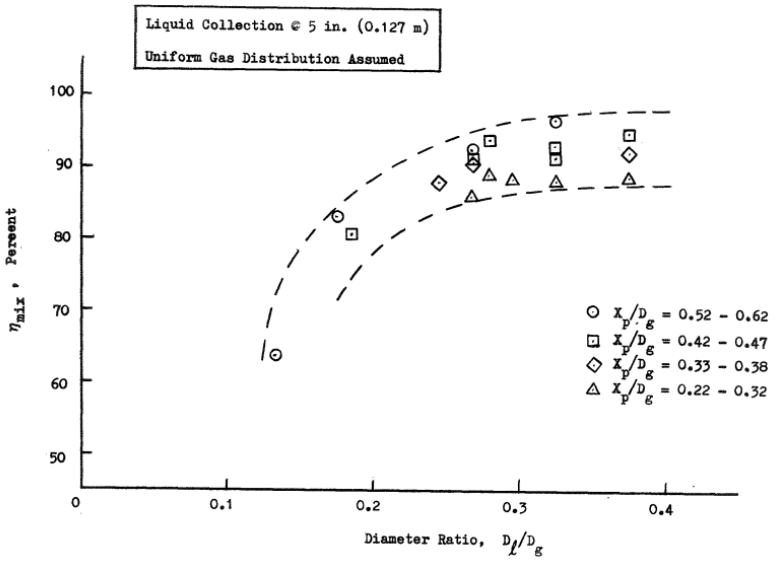

Figure 4.27. Diameter Ratio Influence on Mixing Efficiency. Figure taken from [169]

Additionally, vaporization efficiency versus injection droplet size was examined. Droplet sizes were estimated with the empirical Ingebo correlation [65]:

$$D_{30} = \frac{1}{2.64\sqrt{\frac{V_j}{D_j}} + 0.97(\Delta V)} \qquad 4.22$$

Where V_j is the liquid injection velocity, D_j is the liquid orifice diameter and ΔV is the difference between the gas and liquid velocities. The vaporization efficiency was then modeled and the efficiency versus droplet size plotted as shown in Figure 4.28. The predicted vaporization efficiency is close to 100% for all cases but drops when the droplet size gets above 50 microns. In the soot deposit experiment, the FOF injectors were designed to have a droplet size below this value, as calculated with the same Ingebo correlation.

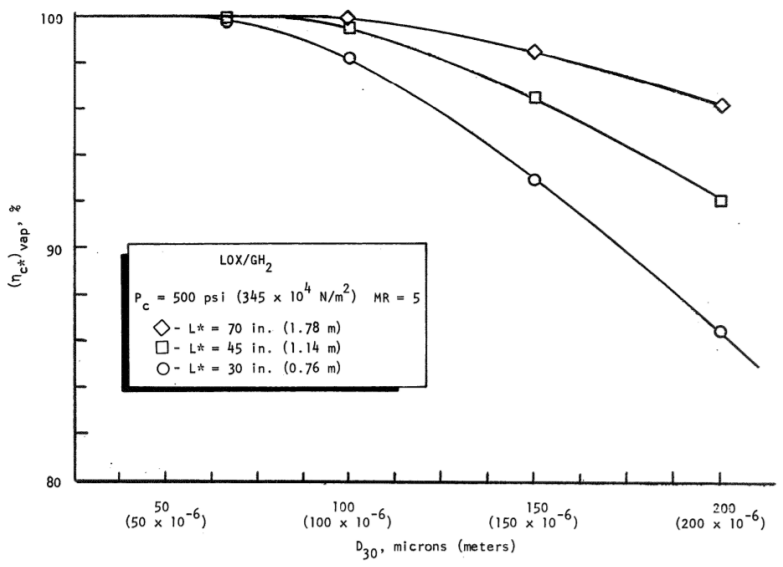

Figure 4.28. Droplet Vaporization Efficiency versus mean droplet size. Figure taken from [169]

Additional consideration in sizing the injectors included sizing them to produce a pressure drop of 20% of the steady chamber pressure in order prevent blockage or instability due to potential pressure spikes in the combustion chamber, as suggested in NASA SP-125 [172]. The pressure drop across the kerosene injector was calculated via the Bernoulli equation assuming incompressible flow:

$$\Delta P = \frac{1}{2}\rho_{RP-2}V_{inj}^2 \tag{4.23}$$

Where V_{inj} is the injection velocity and calculated from the 1-D mass flow equation as:

$$V_{inj} = \frac{4\dot{m}_{RP-2}}{C_d\rho_{RP-2}n_{holes,RP-2}\pi d_{hole,RP-2}^2} \tag{4.24}$$

Where n_{holes} are the number of injector holes, d_{hole} are the injector hole diameters and C_d is the discharge coefficient for the injector. The discharge coefficient depends on the dimensions and type of the injector inlet. It can be determined through a CFD calculation or via a waterflow test. However as an initial estimate in the design, a value of 0.9 was used based on the discharge coefficient provided in Sutton for a short-tube with rounded entrance and length to diameter greater than 3 [3]. The final injector designs all had a length to diameter ratio greater than 3.

For the gaseous oxygen injector, the density depends on pressure and compressibility effects need to be considered. The 1-D mass flow equation, assuming ideal gas, can be expressed for isentropic flow in terms of total properties as:

$$\dot{m} = \frac{C_D \pi n_{holes,GOX} d_{hole,GOX}^2 P_t}{4} \sqrt{\frac{\gamma R}{T_t MW}} M_{inj} \left(1 + \frac{\gamma - 1}{2} M_{inj}^2\right)^{-\frac{\gamma+1}{2(\gamma-1)}} \quad 4.25$$

Where the injector Mach number depends on the downstream chamber pressure and has a maximum value of unity at choked conditions:

$$M = \begin{cases} \sqrt{\frac{2}{\gamma - 1}\left(\left(\frac{P}{P_t}\right)^{-\frac{\gamma-1}{\gamma}} - 1\right)} & if \quad \frac{P}{P_t} > \left(\frac{\gamma+1}{2}\right)^{\frac{\gamma}{\gamma-1}} \\ 1 & if \quad \frac{P}{P_t} \leq \left(\frac{\gamma+1}{2}\right)^{\frac{\gamma}{\gamma-1}} \end{cases} \quad 4.26$$

These two relations can be solved iteratively to find the total upstream pressure, as well as determine whether the gaseous injector is choked. The pressure drop is then simply the difference between the total and static chamber pressure at the exit. Once this is known, the injection velocity for isentropic flow can be calculated as:

$$V_{inj} = \sqrt{2 c_p T_0 \left(\left(\frac{P}{P_t}\right)^{-\frac{\gamma-1}{\gamma}} - 1\right)} \quad 4.27$$

The final, but probably the most important consideration in the design of the injector was machinability. Due to the small flow-rates in the experiment, the required injection holes were generally smaller than what could be drilled, at least by me at the BIDC. From discussion with Jeff Huddleston at BIDC, electrical discharge machining (EDM) was advised for making the injectors since it could produce small tight tolerance holes. Furthermore, from discussion with the EDM shop Wire Cut Technologies, it was recommended to keep hole sizes above 0.012" since that was generally the smallest hole tool in stock and would not require additional custom tooling, and hence would be more affordable. Having larger holes was also preferable in the experiment to prevent soot from clogging the injection ports. Additionally, hole angles of 0°, 30°, 45°, and 60° were also preferable for cost considerations, though any angle was technically possible but would be more expensive due to tool-setup.

In summary, the design of the FOF injectors were guided based on several injector design guidelines and machining considerations, which are listed in Table 4.4.

Table 4.4. Fuel-Oxidizer-Fuel Injector Design Parameters

Description	**Design Parameter**	**Target**
Gas Momentum to Liquid Flow Rate	$\frac{M_{GOX}}{\dot{m}_{RP-2}} = OF * V_{GOX}$	$> 183 \frac{m}{s}$
Penetration Parameter	$\frac{x_p}{D_g} = 2.5\left(\frac{M_{RP-2}}{M_{GOX}}\cos^2\theta\right)^{\frac{1}{2}}$ $= 2.5\cos\theta\left(\frac{1}{4OF}\right)\left(\frac{D_g}{D_l}\right)\left(\frac{\rho_{GOX}}{\rho_{RP-2}}\right)^{\frac{1}{2}}$	$0.5 < \frac{x_p}{D_g} < 0.8$
Liquid to Gas Orifice Area	$\frac{D_l}{D_g}$	> 0.3
Mean Droplet Size	$D_{30} = \frac{1}{2.64\sqrt{\frac{V_j}{D_j}} + 0.97(\Delta V)}$	$< 50\ \mu m$
Injector Pressure Drop	ΔP	$> 0.1\ P_c$
Injector Hole Size	d_{hole}	$> 0.012\ inch$
Injector angle	θ	$0°, 30°, 45°, 60°$

Based on the parameter targets listed in Table 4.4 , three FOF triplet injectors were designed to cover the original range of operating pressures in the soot experiment (as discussed in the operating conditions section, the conditions were updated a year later based on additional modeling results, and then updated again to lower pressure conditions during the test readiness review because one of the regulators was not able to output the required pressures). These injector configurations are listed in Table 4.5. Only the first injector was used in the entirety of the testing for this project. The configuration of 3 FOF triplets for each injector also set the uniformly spaced design of the injector face, which is shown in Figure 4.29.

Table 4.5. Fuel-Oxidizer-Fuel (FOF) Injectors

Injector	Pressure Range (psia)	#FOF Triplets	Fuel Port Diameter (in)	Oxidizer Port Diameter (in)
1	250-500	3	0.02	0.06
2	500-1000	3	0.017	0.042
3	1000-1500	3	0.015	0.034

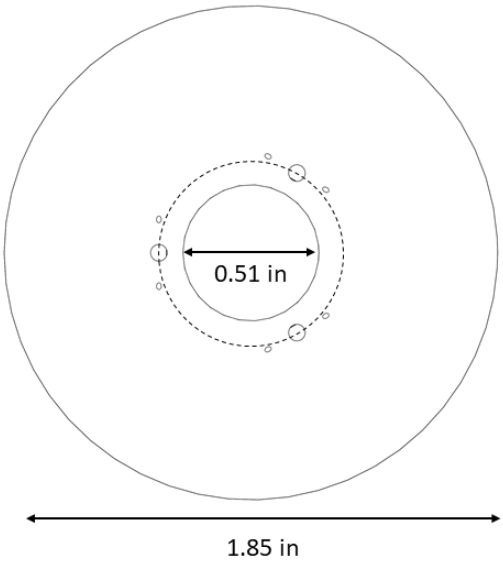

Figure 4.29. Soot Experiment Fuel-Oxidizer-Fuel Injector Hole Pattern.

The geometry of the injector piece itself was designed based on the constraint that it must wrap around the center torch. Furthermore, based on additional machining considerations the liquid kerosene and gaseous oxygen manifolds were designed into the injector piece. The manifolds were sized based on guidelines suggested in NASA SP-125 [172]. This included sizing the manifold passage such that it is at least four times the flow area of the group of injectors that are fed by it. Also, the "1% rule" was applied, where the velocity head of the manifold inlet was sized to be at most 1% of the local static pressure. This condition can be written as:

$$\frac{1}{2}\rho V_{in}^2 = \frac{8}{\rho D_{in}^4}\left(\frac{\dot{m}}{n_{in}\pi}\right)^2 < 0.01 P_{manifold} \quad 4.28$$

Where V_{in} is the inlet velocity to the manifold, which can be calculated and expressed in terms of the mass flow into the manifold, $\dot{m}$; the inlet diameter, D_{in}; and the number of inlets, n_{in}.

In order to satisfy this guideline for all the pressure conditions defined in the operating conditions, the manifold was designed to contain two AS5202-4 ports. The final design of the injector assembly for the soot deposit experiment is shown in Figure 4.30 and the manifold properties listed in Table 4.6.

Both the oxidizer and fuel manifolds were designed with a step that reduced the manifold height from 0.3125 inch to 0.125 inch in order to reduce the volume and hence the fill time of the manifolds. The initial 0.3125-inch height was set to match the AS5202-4 port dimensions to prevent blockage of the port. The 0.125-inch height was set by machine tooling considerations. This part was partially machined on a lathe at the Purdue BIDC machine shop and the smallest grooving tool available at the time that could machine the flow passage was 0.125 inch. After machining the other body, the injector holes were made via electrical discharge machining at Wire Cut Technologies in Indianapolis, IN.

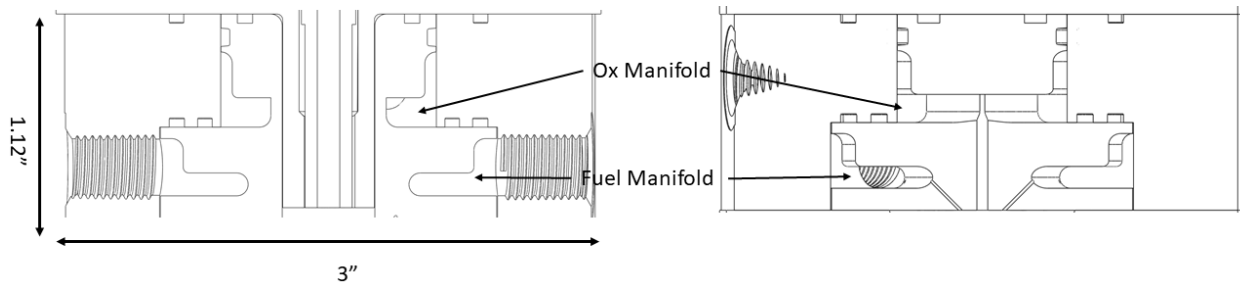

Figure 4.30. Soot Experiment Injector Assembly

Table 4.6. Soot Deposit Experiment Manifold Design

Manifold	**Volume (cm^3)**	**Inlet Ports**	**Fill time (s)**
Fuel	4.99	2x AS5202-4	0.14
Oxidizer	3.04	2x AS5202-4	< 0.01

4.4.3 Combustion Chamber

The combustion chamber was the simplest part in the soot deposit experiment - it was basically just a thick tube, as shown in Figure 4.31. It connected the torch and injector/manifold assembly to the sample chamber and was designed with two primary considerations:

First, the combustion chamber needed to withstand the heat fluxes for the duration of the test without any film cooling, as the goal of the project was to study soot formation and deposition resulting from just the bulk gaseous core flow. As mentioned in the intro of this chapter and in section 4.3 on the operating conditions, a calorimetric water cooled chamber was initially considered to allow for steady state operation. However, the preliminary design showed that both the machining and the necessary high pressure and high flow valves would exceed the budget of this project – thus not a viable option. Thermal barrier coatings were also considered but the cost was thought to be overbudget and not viable. Instead, the combustion chamber was designed for only short transient operation and the operating conditions discussed in section 4.3 were iterated in part based on this limitation.

Secondly, it was desirable to reduce heat loss of the gas to of the walls. The reason for this is soot was thought to primarily deposit via thermophoretic diffusion, which increases with the temperature difference between the particles and chamber wall. Since soot deposit was not measured in the combustion chamber, it was thought that reducing heat loss would increase the deposits where they are directly measured in the sample region. A detailed CFD approach was also being contemplated during this design stage to model soot particle deposition and assuming adiabatic boundary conditions, by reducing heat loss, is much easier than solving conjugate heat transfer. Though, after the experiment had already been machined and further thought put into the modeling, a 0-D/1-D reduced order approach was favored over CFD, as discussed in Chapter 3.

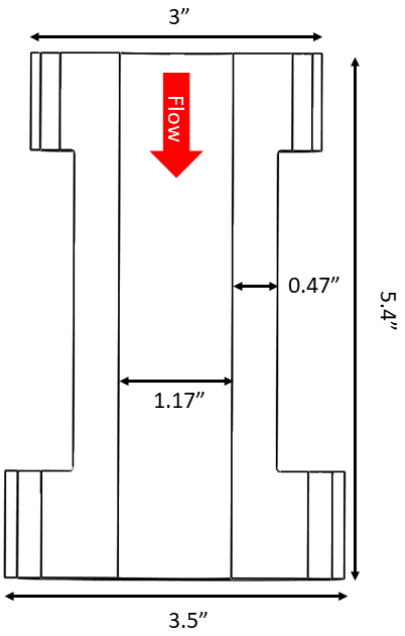

Figure 4.31 Soot Deposit Experiment Combustion Chamber

For these reasons, it was decided to make the combustion chamber of a low thermal conductivity metal with a large melting point such as stainless steel or Inconel. Stainless Steel 316 was ultimately selected as it was on sale when the material was being purchased and much cheaper.

The chamber inner diameter was set to 1.17 in - the same as the Phase I STTR combustor. The design analysis and initial modeling calculations didn't show any problems with this value, so it was used. A Phase II STTR fuel film combustor was also designed with this same dimension and having consistent chamber diameters helped facilitate comparison of results from both experiments. The wall thickness also had a large factor of safety with regards to mechanical failure – pretty much only because it was machined from a large round stock of stainless-316 and turning the outside diameter on the lathe at the BIDC takes a long time. Appendix D provides discussion on how machining considerations affected the experiment design.

The length of the combustion chamber was set to 5.4 inch - because the sale price was for a random non-standard sized length. The arbitrary length was not initially critical to the design - as long as it was larger than ~2 inches. The 1-D plug flow reactor model, discussed in section 3.3, predicted that all droplets would vaporize and most heat release reactions would occur within ~2 inches from the inlet, for for the operating conditions considered in section 4.3 and with the FOF injector discussed in section 4.4.2. A longer length would only just add extra margin for error.

Figure 4.32 shows this calculation for the 250 psia chamber pressure condition with a combined propellant flow rate of 0.06 kg/s. The calculation was performed assuming stagnant droplet vaporization, as well as convective vaporization due to bulk gas velocity. Both calculations predicted a hot-spot near the injector, due to droplet vaporization, with the stagnant case experiencing having a larger hot-spot because the droplet takes longer to vaporize. Additionally, there is higher heat release initially predicted in the stagnant case because the droplet vaporization takes longer, and the gas phase is at a higher mixture ratio. The convective vaporization case is more representative of the actual soot experiment. Also, the calculation was performed without the soot model, which would decrease the gas temperatures further.

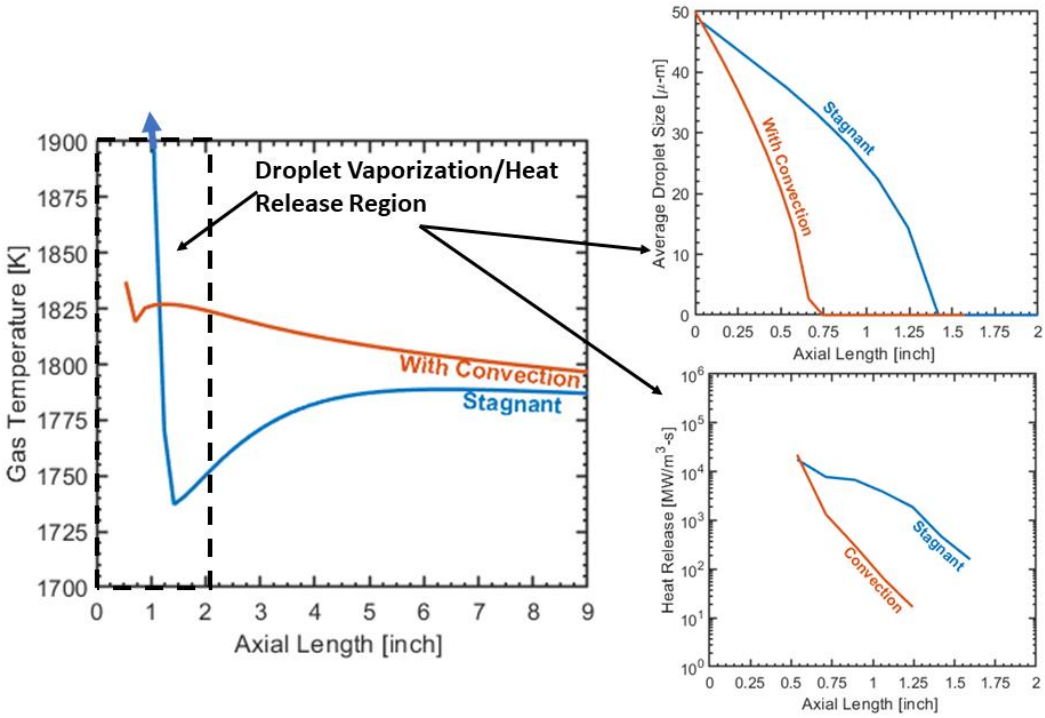

Figure 4.32 Plug Flow Reactor Simulation with Droplet Calculation Assuming both Stagnant and Convective Vaporization

The combustion chamber was machined with this 5.4-inch stock length. However, later CFD modeling, with the approach discussed in section 3.4, showed that boundary layers affect the near wall reacting gas chemistry and in turn soot surface growth rates via surface reactions. To ensure measurements at different conditions could be compared consistently, the experiment was

updated by increasing the combustor length so that the boundary layer would be fully developed flow at the sample section. A second combustion chamber extension was then machined to extend the overall chamber length. Even later modeling though showed that the contribution of surface reactions to overall soot deposit growth is overshadowed by transport of core flow soot particles to the wall - and would likely not be measurable in the experiment. A longer chamber would also increase heat loss to the wall. So, the experiment configuration was updated again back to the original condition with only one combustion chamber. One of the tests did use the combustion chamber extension though and there was higher soot deposition, but the gas residence time was larger at the same time and in turn so was the predicted soot volume fraction.

To ensure the operating conditions would not produce thermal problems, a 1-D axisymmetric thermal analysis was run for the stainless chamber. The analysis was initially done for the higher-pressure conditions, that were discussed in section 4.3, and did not show any problems for a six second run time. The analysis was then re-run for the updated – and safer – lower pressure conditions. The 1-D transient thermal analysis setup and wall temperature prediction for the stainless-steel chamber are shown in Figure 4.33. One of the calculations was run at 350 psia and 85 g/s propellant flow rate, the highest chamber and flow rate condition tested. The torch was assumed to turn off at 1 second and only the main propellant combustion occurring after. Additionally, one the conditions wanted to verify if soot deposited in the chamber at ambient pressures with an open chamber test. However, as discussed in section 4.6, the chamber was predicted to blowout because the residence time at ambient conditions would be too low to sustain combustion. To resolve this, the torch igniter would be on for the entire duration to supply energy to the propellants. This condition was also investigated for potential thermal issues, since the heat flux would be larger, and the thermal results are shown in Figure 4.33.

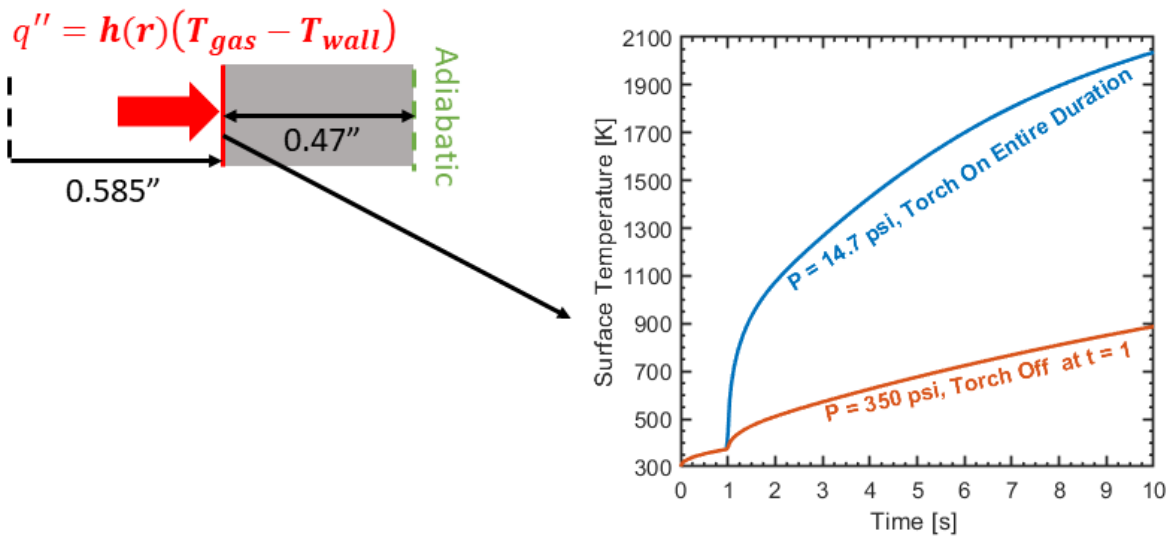

Figure 4.33 1-D transient heat transfer predictions for stainless steel combustion chamber with torch on for entire duration, or torch off at t = 1 second.

The 1-D calculation showed that the combustion chamber should not have any thermal issues during the normal operation: torch igniter on, main propellant ignition, propellant shutoff at 6 seconds. This is true despite all the thermal analysis that was run being very conservative by using the largest heat flux prediction and assuming the bulk gas doesn't lose heat to the walls, as discussed in section 4.2.1. The predicted stainless-steel surface temperature for even a 10 second test is well below the melting point. However, the analysis showed, due to the higher heat fluxes, the torch being be on for the entire duration has potential to damage the chamber. The surface temperature was predicted to reach the melting point of stainless for a six second test. This test condition was not necessarily critical for the overall of the experiment but was thought to provide an interesting data point though. For this reason, this condition was run at the end of the test campaign so all the necessary data could be collected first. The results did show a slight blue, green hue in the exhaust plume that was indicative of stainless steel. A post-test inspection also showed some melting of the walls - in agreement with the thermal analysis. The chamber was thick enough though that it did not cause any issues and could probably be re-used, just with worse inner aesthetics. Any effect on boundary layer would likely not be noticeable in the measurements since most of the soot deposit was found to occur from the bulk flow via thermophoresis.

4.4.4 Sample Chamber

The soot deposit sample geometry has evolved since the beginning of the project. A flat plate was initially considered since it would be easy to measure soot deposit thickness with a microscope or profilometer. However, it would not be axisymmetric, and the modeling effort would need to either simulate a more computationally expensive 3D domain or introduce another source of modeling error. Other flat sample geometries were also pondered to approximate an axisymmetric geometry, including making a hexagonal chamber with inserts on each side, but they were mostly thought to be complicated and costly to machine. A cylindrical chamber was ultimately decided on and a cylindrical sample made the most sense both in terms of machining cost and modeling consideration.

Additionally, as previously discussed, thermophoresis was thought to be the main driver of soot deposition and it is directly dependent on the wall surface temperature. A preliminary idea at the start of the experimental design was to make a water-cooled calorimetric chamber in order to study steady state deposition at a controlled wall surface temperature. This idea was however abandoned after the conceptual design showed that it would exceed the budget of the project. Not to mention, designing a water-cooled sample would be complicated and costly. The operating conditions were also changed to transient operation, as discussed in section 4.3. As a rough compromise to reduce cost, while maintaining an approximately constant surface temperature during the experiment run time, a thick heat sink copper chamber was designed. The design, as shown in Figure 4.34, consisted of a thin – 0.045-inch wall - cylindrical sample tube that was concentric with a thicker copper heatsink chamber. The heatsink chamber dissipated heat from the thin sample chamber and allowed it to withstand high chamber pressures - originally planned to be over 1000 psia as discussed in section 4.3. The sample tube was designed to extended outside the sample chamber into the extension section so that it could be removed easily post-test by removing the extension section and then pulling out the tube by grabbing onto the protruding outside wall. Otherwise, removing the tube would be more difficult or the sample would be disturbed if it needed to be removed by grabbing onto the inner surface. The sample chamber was also designed and machined with 16 ports to take thermal measurements on the outside sample wall. Heat flux measurements were originally considered with Medtherm coaxial thermocouple sensor, like what has previously been used in prior rocket combustion work at Purdue [173]. However, the heat flux sensors ended up being costly and had a lead time of over a year. So,

thermocouples were used instead to measure the sample outside wall temperature. One of the ports was also used for chamber pressure measurement.

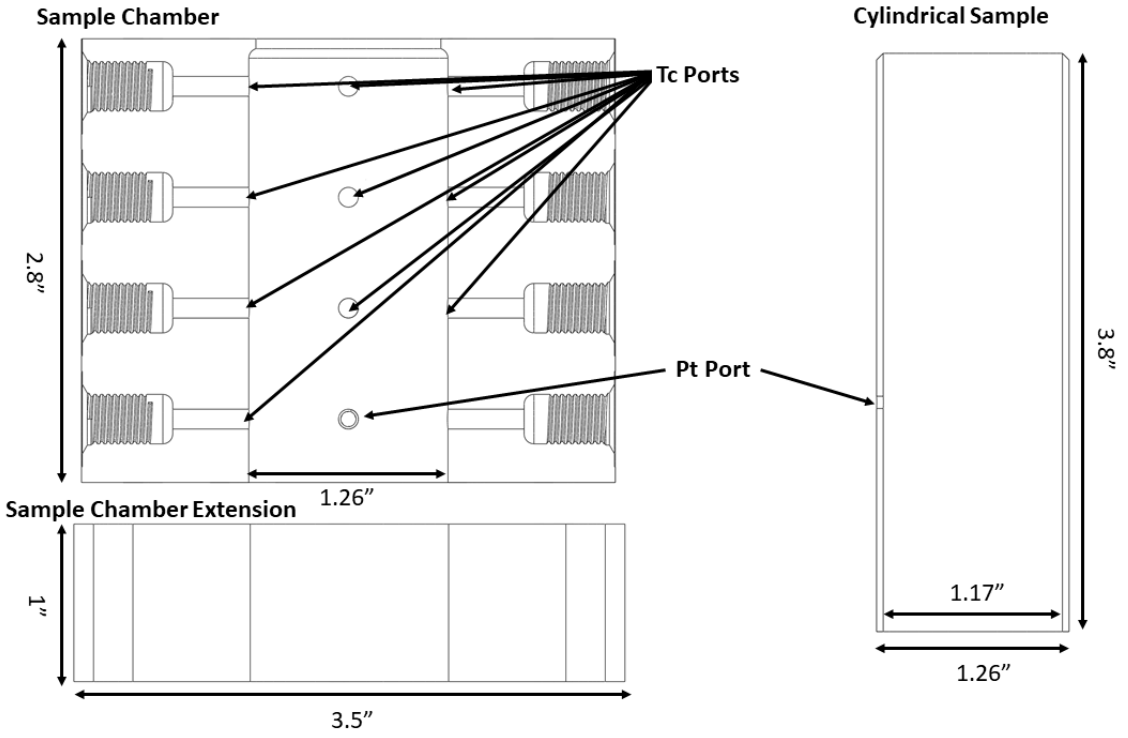

Figure 4.34 Sample and sample chamber overview

The design of the sample and sample chamber was informed by 2D thermal analysis, with the goal of keeping the sample surface temperature roughly constant during the duration of the experiment. The surface temperature is dependent on the rate of heat dissipation, which in turn depends on both the thermal conductivity and the temperature difference between the sample and sample chamber. The sample chamber mass affects how much energy it can absorb and as a result its transient temperature. Thus, a higher thermal conductivity of the sample material and a larger sample chamber would produce a smaller rate of temperature increase at the sample inner surface. Since copper has a high thermal conductivity, it was used as one of the sample materials. As for the chamber, the mass is proportional to the chamber (diameter)^2 – but unfortunately so was the cost. The heat transfer analysis was run for several standard stock diameters, to find the optimal for the price, including: 2, 2.5, 3, 3.5, and 4 inches. The calculations showed that a 3.5-inch diameter copper chamber would be able to keep the surface temperature to within 100 K for the duration of the test for all the planned test conditions and hence was chosen. The heat transfer

analysis setup and results for the 250 psia chamber pressure and 60 g/s combined flow rate condition are shown in Figure 4.35. In the analysis, the chamber heat flux was calculated for just torch flow for the first second and then for the combusted RP-2/GOx propellant flow. An adiabatic boundary condition was used for all the other walls. For this test condition, the copper inner wall was predicted to only rise by ~60 K for a 7 second test. Due to coppers high thermal conductivity, the inner wall temperature was also predicted to be roughly the same as the outer wall, where the thermocouple measurements were made.

Additionally, stainless steel samples were also made to allow for comparison of soot deposit at different wall temperatures. The thermal conductivity of the stainless is an order of magnitude lower, which reduces heat dissipation at the wall surface, and in turn results in higher temperatures. Figure 4.35 shows the thermal comparison of stainless steel with copper - the solution at t = 7s shows the much larger temperature gradient in the stainless sample compared to copper. The outside wall thermocouple measurements were also predicted to be roughly the same for both the copper and stainless.

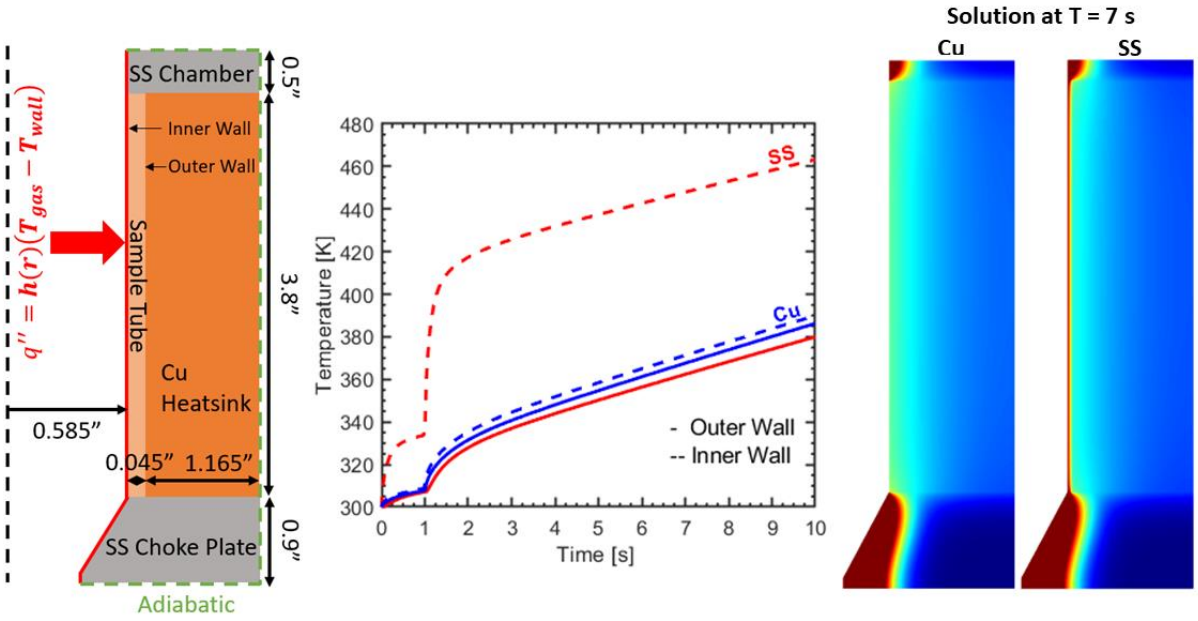

Figure 4.35 2-D transient heat transfer predictions for stainless steel and copper sample tubes. Outer walls are – and inner walls are --.

Thermal calculations were also done to estimate what effect soot deposit would have on the temperature measurement of the sample outer wall and if it would produce a measurable difference compared to a clean wall. This analysis was identical to the previous analysis, except

the inlet heat flux was modified to include effects of soot via thermal resistance concept. The overall heat transfer coefficient to the sample tube surface due to convection to the soot deposit and then conduction through it to the wall can be expressed with thermal resistors in series [54], as:

$$h_{conv,s} = \frac{1}{\left(\frac{1}{h_{conv,g}}\right) + \frac{D_c - 2t_s}{2\kappa_s} \ln\left(\frac{D_c}{D_c - 2t_s}\right)} \quad 4.29$$

Where $h_{conv,s}$ is the combined heat transfer coefficient and equivalent to the reciprocal of the sum of the thermal resistances due to gas convection and conduction through the cylindrical soot deposit layer. In the relation, $h_{conv,g}$ is the gas convection coefficient, D_c is the chamber diameter, t is the thickness of the soot, and κ_s is the soot deposit conductivity. The soot deposit thickness growth rate was roughly estimated to be $10\frac{\mu m}{s}$ and the soot thickness calculated at every time step – at the time of the design, the soot deposit model, that was discussed in section 3.7, was not started or even thought about yet. A constant value of $0.68\frac{W}{m-k}$ was used for the soot thermal conductivity, as determined by Nishiwaki for automative engine soot deposits [115].

The results of this heat transfer analysis for the 250 psia chamber pressure and 60 g/s combined flow rate condition are shown in Figure 4.36. The soot buildup was predicted to decrease the inner wall surface temperatures for the copper by a few Kelvin, and slightly more for the stainless. However, the difference is even smaller at the outer wall, where the temperature is measured. Hence discerning any difference due to soot with the experimental thermocouple measurements was thought to not be possible for the short run time of the experimental. Capturing the effect of soot deposit on heat transfer was thought to require a longer run time, or higher chamber heat flux, but these were not possible with the current combustor design. However, as the results in section 5.4.4 show, the measured soot deposit was porous, which produced a much smaller bulk thermal conductivity than used in this initial calculation, and made the effect of soot visible in the data!

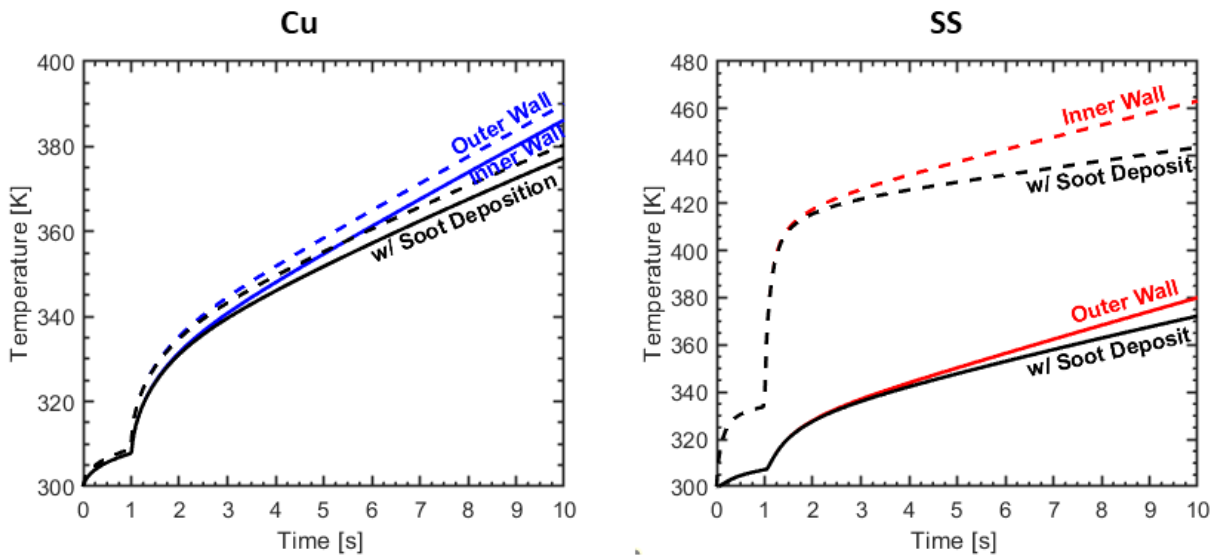

Figure 4.36 2-D transient heat predictions for stainless steel and copper sample tubes with soot deposition. Outer walls are – and inner walls are --.

4.4.5 **Choke Plate**

The pressure in the combustion chamber was set with a simple converging sonic choke plate. A graphite converging nozzle insert was considered at the beginning of this project, when the chamber pressures and mixture ratios being considered were higher. However, after the conditions were revised lower pressure fuel rich transient operation, the choke plate was changed to a stainless-steel 316 plate. This was mainly because machining stainless material is much easier, especially if multiple choke plate discs were required. I was also able to reduce cost by personally machining the stainless choke plates at BIDC and would have needed to send it out if they were graphite.

The throat cross sectional area for a specific mass flow and chamber pressure condition was calculated with the 1-D choked flow relation:

$$A_t = \frac{\dot{m}}{P_t}\sqrt{\frac{T_t R}{\gamma MW}}\left(1+\frac{\gamma-1}{2}\right)^{\frac{\gamma+1}{2(\gamma-1)}} \tag{4.30}$$

The gas properties (Temperature, specific heat and mixture molecular weight) at the specific chamber pressure were predicted assuming equilibrium conditions with the CEA code [13].

Several different diameter choke plates were made for the different test conditions discussed in section 4.3. A 2-D heat transfer analysis was done for each to check for any potential thermal related problems. The thermal analysis problem setup and prediction of the maximum surface temperature (found at the throat) for the 350 psia case, the largest operating pressure tested in the soot experiment, are shown in Figure 4.37. The analysis calculates the inner wall heat flux assuming purely torch flow for the first second, followed by combustion of the RP-2 and GOx propellants. The inner wall heat flux is calculated using the Bartz correlation [134] with chamber gas properties (which is a conservative estimate since it doesn't account for the drop in temperature and pressure due to gas acceleration in the converging section). The pressure on the lower outer surface is ambient and - as a very quick and rough conservative approximation - the heat flux was estimated by scaling the chamber heat flux calculated with Bartz by $P^{0.8}$ as $(14.7/350)^{0.8} = 0.079$.

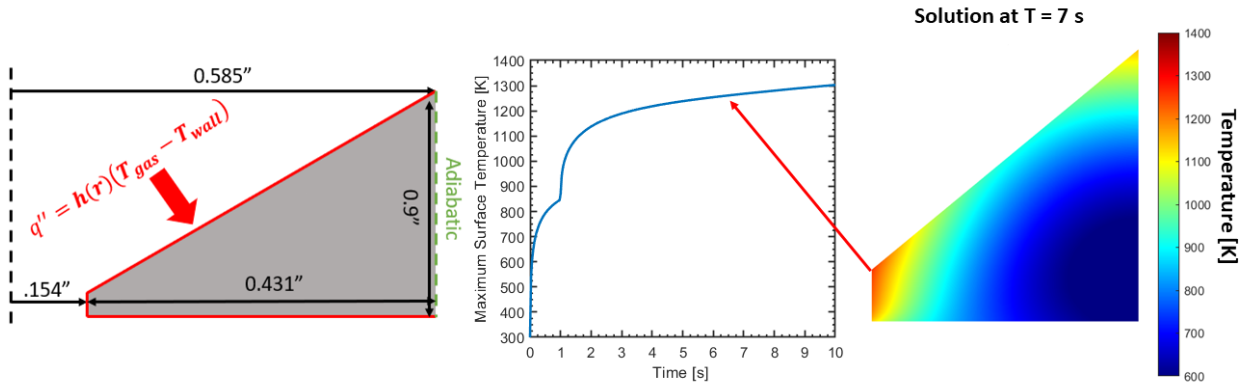

Figure 4.37. 2-D transient heat transfer predictions for stainless steel choke plate

The thermal results showed the maximum surface temperature of the 316 stainless steel choke plate can reach 1300 K at the highest soot experiment testing pressure of 350 psia. This is about 400 K below the melting point but this is higher than the typically recommended working temperatures of stainless materials because of oxidization and decrease in mechanical strength [174]. However, oxidation consideration was not a big problem since the choke plates would only be used for just a few tests and the design was very simple to re-machine if need be. The structural integrity of the stainless steel at high temperatures was considered further.

Structural analysis was performed with SolidWorks finite element analysis toolbox to check for potential mechanical issues at high temperature operation. In the analysis, the choke plate displacement was constrained on the bottom surface and a uniform pressure distribution, for

conservativeness, equal to the chamber pressure used as the inner boundary conditions. The outer boundaries were set to a uniform pressure distribution of 14.7 psia. Additionally, the high temperature structural properties of stainless steel 316 from [174] were used in the simulation. Data for tensile strength near 1300 K was not found and instead a value of 10 ksi was used by extrapolating the data in [174] and then rounding down. The results for all the conditions discussed in section 4.3 didn't show any structural problems at high temperature conditions. Figure 4.38 shows the calculated factor of safety distribution with regards to von mises stress for the 350 psia test condition, the highest pressure tested. The simulations were run as 3-D despite being axisymmetric simply because it was easier to quickly setup in the SolidWorks framework, and the computation time was faster than figuring out how to setup axisymmetric simulations. The minimum factor of safety for the 350 psia test was 13.

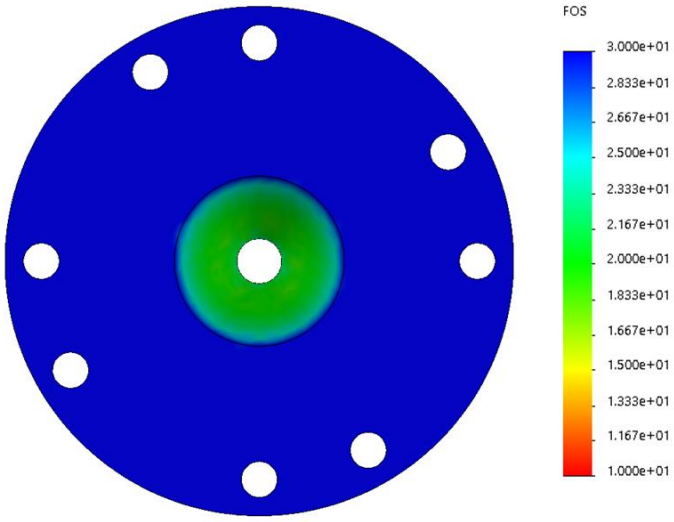

Figure 4.38 Factor of Safety with respect to Von Mises Stress for stainless steel choke plate at chamber pressure of 350 psia and tensile strength of 10 ksi, as predicted with the SolidWorks structural analysis simulation tool.

Several choke plates were machined for the original test conditions. The throat diameter was machined with a reamer and the converging surface with an inside turning tool. However, after the conditions were updated, as discussed in section 4.3, some of the smaller throat choke plates were modified by enlarging the diameter with a reamer to the new design point. The final choke plates that were used in the soot experiment are listed in Table 4.7:

Table 4.7 Choke Plate Throat Diameters used in soot experiment

Choke Plate Diameter [inch]	Pressure [psia]	Mass Flow Rate [g/s]
0.281	250	50
0.312	150, 250, 350	36, 60, 85
0.367	250	84

4.5 Fluid System

4.5.1 Flow Control

Gaseous Orifice Sizing

The orifice mass flow rate was calculated assuming ideal gas and isentropic flow with an empirical discharge coefficient accounting for losses. The 1-D mass flow equation for ideal gas in terms of total properties and velocity expressed in terms of throat Mach number can be written as:

$$\dot{m} = C_D A P_t \sqrt{\frac{\gamma R}{T_t MW}} M_t \left(1 + \frac{\gamma - 1}{2} M_t^2\right)^{-\frac{\gamma+1}{2(\gamma-1)}} \tag{4.31}$$

Where the terms are the same as previously defined. The throat Mach number for the orifice is a function of the upstream and downstream pressure. Since the orifice has solely a converging section, the flow can't accelerate past sonic conditions and as such the throat pressure is always equal to the downstream pressure. The throat Mach number can then be calculated from the pressure ratio as:

$$M_t = \begin{Bmatrix} \sqrt{\frac{2}{\gamma - 1}\left(\left(\frac{P}{P_t}\right)^{-\frac{\gamma-1}{\gamma}} - 1\right)} & if & \frac{P}{P_t} > \left(\frac{\gamma+1}{2}\right)^{\frac{\gamma}{\gamma-1}} \\ 1 & if & \frac{P}{P_t} \leq \left(\frac{\gamma+1}{2}\right)^{\frac{\gamma}{\gamma-1}} \end{Bmatrix} \tag{4.32}$$

The discharge coefficient for a small bore orifice was estimated from [175] as:

$$C_d = \left(0.5591 + \frac{0.0044}{D} + \left(0.3155 + \frac{0.0175}{D}\right)\left(\left(\frac{d}{D}\right)^4 + 2\left(\frac{d}{D}\right)^{16}\right)\right)\left(1 - \left(\frac{d}{D}\right)^4\right)^{\frac{1}{2}} \quad 4.33$$

$$+ \left(\frac{0.52}{D} - 0.192 + \left(16.48 - \frac{1.16}{D}\right)\left(\left(\frac{d}{D}\right)^4 + 4\left(\frac{d}{D}\right)^{16}\right)\left(\frac{1 - \left(\frac{d}{D}\right)^4}{R_e}\right)^{\frac{1}{2}}\right.$$

Where uppercase D is the tube inlet diameter, lowercase d is the orifice diameter, and R_e is the Reynolds number calculated as $R_e = \frac{4\dot{m}}{\pi D \mu}$. This correlation is valid for a diameter ratio of $0.1 \leq \frac{d}{D} \leq 0.8$ and Reynolds number $R_e \geq 1000$.

The gaseous orifice can be operated in two regimes, that depend on the upstream and downstream pressure ratio. If the ratio of the downstream pressure to total upstream pressure is equal or below the critical pressure ratio of $\left(\frac{\gamma+1}{2}\right)^{\frac{\gamma}{\gamma-1}}$, then the flow at the orifice throat is sonic and mass flow is choked. In this condition, the mass flow is only dependent on upstream pressure and pressure fluctuations downstream should not affect the mass flow (if the pressure fluctuations are not high enough to unchoke the throat). An orifice operating in this condition is typically referred to as a critical flow orifice.

If the ratio of the downstream pressure to total upstream pressure is above the critical pressure ratio, then the flow at the orifice is subsonic and the mass flow becomes dependent on the downstream pressure. The mass flow rate through the orifice in this operation can be calculated by first calculating the throat Mach number and then solving the compressible mass flow equation. In practice, using a subsonic orifice typically results in larger measurement uncertainty because it now requires two pressure measurements, upstream and downstream pressure, as opposed to a critical flow venturi where only the upstream pressure needs to be measured.

Gaseous Venturi Sizing

The gaseous mass flow rate through a venturi can be calculated from isentropic compressible flow theory. The 1-D mass flow equation with isentropic relations for total properties and velocity expressed in Mach is:

$$\dot{m} = C_D A P_t \sqrt{\frac{\gamma R}{T_t MW}} M_t \left(1 + \frac{\gamma - 1}{2} M_t^2\right)^{-\frac{\gamma+1}{2(\gamma-1)}} \quad 4.34$$

Choked flow is achieved when the throat is supersonic. Unlike an orifice, a venturi has a diverging pressure recovery region which can allow for lower upstream pressure to achieve choked flow. To determine whether a venturi is choked, two area ratios are first defined. The converging and diverging pressure ratios, which are calculated as:

$$AR_{conv} = \left(\frac{D_{in}}{D_t}\right)^2 \quad 4.35$$

$$AR_{div} = \left(\frac{D_e}{D_t}\right)^2 \quad 4.36$$

Assuming choked flow at the nozzle exit, the Area Mach equation can be iteratively solved to calculate the exit Mach number for the calculated diverging pressure ratio:

$$AR_{div} = \frac{\left(\frac{\gamma+1}{2}\right)^{-\frac{\gamma+1}{2(\gamma-1)}} \left(1 + \frac{\gamma-1}{2} M_e^2\right)^{\frac{\gamma+1}{2(\gamma-1)}}}{M_e} \quad 4.37$$

Two pressure ratios can then be defined, the critical pressure ratio that results in this Mach number (which can be calculated from isentropic pressure relation) and the actual pressure ratio based on the upstream and downstream pressures:

$$PR^* = \left(1 + \frac{\gamma - 1}{2} M_e^2\right)^{-\frac{\gamma}{(\gamma-1)}} \quad 4.38$$

$$PR = \frac{P_e}{P_u} \quad 4.39$$

If the actual pressure ratio is larger than the critical pressure ratio, then the flow cannot be expanded to supersonic conditions and is hence subsonic. In this case the venturi is not choked. To calculate the mass flow in the subsonic regime, the critical area ratio can be solved for a Mach number of 1.

$$AR^* = \frac{\left(\frac{\gamma+1}{2}\right)^{-\frac{\gamma+1}{2(\gamma-1)}} \left(1 + \frac{\gamma-1}{2} 1^2\right)^{\frac{\gamma+1}{2(\gamma-1)}}}{1} \quad 4.40$$

Afterwards, the ratio of the venturi throat to a sonic area can be calculated as:

$$\frac{A_t}{A^*} = \frac{AR^*}{AR_{div}} \tag{4.41}$$

The area-Mach relation can then be solved implicitly for the Mach number at this area ratio. Once the Mach number is calculated, the mass flow rate can be determined from equation 4.34

On the other hand, if the actual pressure ratio is equal or less than the critical pressure ratio, then the flow is sonic at the throat and the mass flow is choked. In this case, the mass flow relation can be solved at the throat with a sonic Mach number. If the pressure ratio is less than the critical pressure ratio, then the flow will further expand in the diverging section and experience a shock that brings the pressure up to the back pressure. Since the flow is choked, this effect would not affect the mass flow rate.

Cavitating Venturi Sizing

The operation of a cavitating venturi is like a critical flow gaseous venturi with the flow being choked at the throat. In the cavitating venturi, choking occurs when the liquid pressure drops below the vapor pressure and the fluid start to boil. The vapor bubbles that form block the throat and prevent any further increase in mass flow. An expression for the mass flow rate through the cavitating venturi can be derived from Bernoulli's equation and 1-D mass flow relation and expressed in the following form, with a discharge coefficient to account for non-ideal flow:

$$\dot{m} = C_D A\sqrt{2\rho g(P_u - P_v)} \tag{4.42}$$

Typically, a pressure drop greater than 20% across the cavitating venturi is enough to ensure cavitation at the throat [176].

4.5.2 Plumbing and Instrumentation

The soot deposit experiment was run at the Zucrow Laboratory ZL1 108A test cell. Prior to the soot deposit experiment, the cell was previously used to test several other combustors, including the Air Force Phase II STTR experiment, and had kerosene, as well as a high-pressure nitrogen system already plumbed. The test cell however was lacking a hydrogen and gaseous oxygen feed system that was required for this project and needed to be designed and plumbed.

The hydrogen and gaseous oxygen systems were planned out in conjunction with other projects in the test cell to reduce the purchasing cost of all the necessary plumbing (Valves/Regulators/Fittings…). Typically, valves and regulators are sized for a specific flow coefficient, which is a value that describes how much flow can pass through the device for a certain pressure drop. It is defined as:

$$C_V = \frac{\dot{m}}{\rho}\sqrt{\frac{SG}{\Delta P}} \tag{4.43}$$

The flow coefficient, C_V, combines the discharge coefficient and flow geometry effects of the device. The value is something that is provided by the manufacturer and is usually determined experimentally for a device by operating it at a range of flow rates and pressure conditions. The required C_V can be calculated for an operating condition and then the flow device selected such that the C_V is higher. If the device C_V is smaller than required, then the output flowrate would be smaller than required for a certain pressure drop. The upstream pressure can be increased to increase flow rate but there is a limit to the upstream pressure budget. In my experiment, the flow rate and pressure requirements were smaller compared to the other planned projects and so the feed system was sized primarily with consideration of the larger projects. All the feed system C_V's were higher than required for all the operating conditions in the experiment.

Along the same boat, all the new lines, except for the oxygen supply and main oxygen run lines, were constructed with 0.25-inch tube. This was the typical size used by the other projects in the lab and the pressure drop, estimated with fanno flow, for my experimental conditions was very insignificant. The oxygen supply and main run lines were made with 0.5-inch tubing to ensure the flow velocity remains below 100 ft/s, as recommended by the NASA safe oxygen handling guidelines [177].

During the time of this project, Zucrow Laboratories had a bulk supply of hydrogen at the ZL3 high pressure laboratory and a feed line that ran to ZL1. Several hydrogen lines were also already present from prior testing in the lab but were not used in a long time until this experiment. These lines were traced, visually inspected on the outside and repurposed for the hydrogen feed system. Furthermore, since hydrogen is a small molecule and leaks easier, all the new fittings that were used on the hydrogen side were primarily the more expensive Parker Seal-Lok to ensure leak-free connections - none of the Seal-Lok fittings leaked during nitrogen pressure testing even when

one of them was discovered to be finger-tight! The plumbing and instrumentation diagram (P&ID) for the entire hydrogen system is provided in Figure C.3. An image of the main hydrogen panel, as setup for the testing in this project, is shown in Figure 4.39. This system supplied hydrogen from the bulk hydrogen supply to the igniter in the experiment. As visible on the main panel, an isolation valve was present that isolated the rest of the hydrogen system from the supply – there was additional plumbing upstream and another isolation valve from the bulk supply of hydrogen to ZL1 as shown on the P&ID in Figure C.3. The panel also contained Swagelok spring regulators that were manually loaded prior to testing to set the required hydrogen pressures. For safety considerations, the hydrogen panel was installed on the opposite side of the test cell from the oxygen system to reduce the fire risk in case of leaks. Hydrogen sensors were also installed near the test stand and hydrogen panel to detect any potential leaks. These were calibrated with a 10% LEL hydrogen gas regulator prior to flowing hydrogen in the system. Additionally, a relief valve was installed in the hydrogen system to prevent overpressure. The hydrogen in the system was vented to the roof of ZL1 with a remotely controlled pneumatic actuated valve.

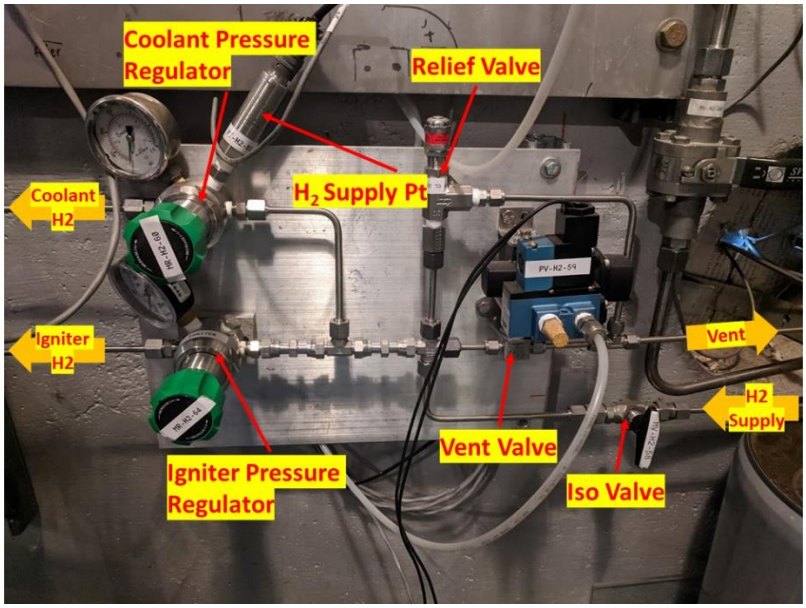

Figure 4.39 Hydrogen Panel

The GOx system in this experiment was new and was designed to run off a K-bottle. Extra precautions were taken, included following the NASA safe oxygen handling guidelines [177], to cleaning and install the system since GOx can be very flammable at high pressures. One of these

precautions included installing an inline Norman filter upstream of the GOx isolation valve to prevent any potential particulates in the K-bottle from propagating downstream and igniting the GOx. All the valves and regulators in the system were also purchased oxygen clean by the manufacturer. The plumbing and instrumentation diagram for the oxygen system is shown in Figure C.2 and image of the main GOx panel shown in Figure 4.40. This system supplied oxygen to both the igniter and the main propellant. As shown on the panel, remotely controlled pneumatic actuated valves were used to isolate the system from the gas cylinder and to vent GOx. Like the hydrogen system, the GOx was vented to the roof. The GOx torch pressure was set with a Tescom spring loaded regulator that was loaded prior to testing. The main GOX pressure was controlled by a TESCOM ER5000 dome loaded regulators that was loaded remotely. The ER regulator employed a Proportional-Integral-Derivative (PID) controller that adjusted the outlet flow to provide a constant pressure at some point in the system based on feedback from a pressure transducer. If the pressure downstream drops then the controller would increase flow, and vice versa. In order to have a smooth response, the PID values required manual tuning. These values were tuned with feedback from the upstream venturi pressure transducer so the main GOx flowrate would be constant. However, since the flow rates in the experiment were small, and smaller than the typical flowrates used with this ER regulator, the pressure feedback was very sensitive and a small change in pressure would result in large mass flow percent change. As a result, it took significant amount of time to tune the system to reduce the upstream venturi pressure overshoot or oscillatory ringing in the response. The PID controller was tuned via the TESCOM ERTune program by adjusting the PID values and then qualitatively checking the upstream venturi pressure response by flowing N_2 in the system. The final tuned response was damped but it took some time to reach the steady state pressure. Better tuning would have required significantly more time to manually tweak PID values or figuring out how to interface with the controller and writing a program to optimize the PID values for a certain response. As will be discussed in the next chapter, the tuning affected the transient GOx flowrate injected into the combustor and required some time to reach steady state operating conditions.

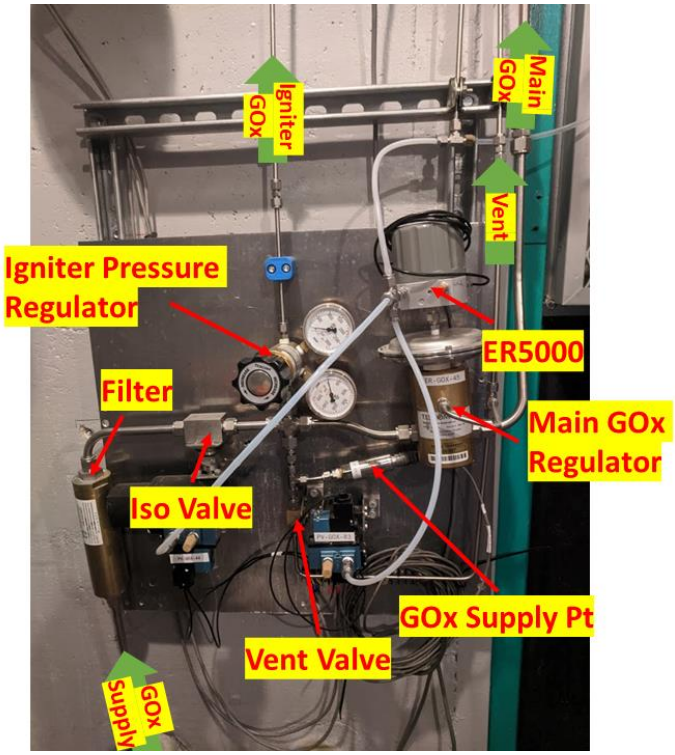

Figure 4.40 GOx Panel

Both the hydrogen and GOx system were plumbed all the way to the test stand. New nitrogen purge lines were also installed that tapped off the existing system to supply purge to the igniter and the main run lines. The nitrogen system was supplied by the bulk nitrogen from the ZL3 high pressure lab. The RP-2 line was mostly reused, except for a short tube that ran to the combustor. In the experiment, RP-2 was vacuum loaded into a stainless-steel tank and then it was pressure fed with nitrogen. The plumbing and instrumentation diagrams for all the fluid systems used in the experiment are provided in Appendix C.

An overview of the plumbing that fed the experiment is shown in Figure 4.41 and a subset of the instrumentations used listed in Table 4.8. More details are provided in Appendix C. Images of the fuel and oxidizer side on the test stand (installed on opposite sides to prevent fire from potential leaks) are shown in Figure 4.42 and Figure 4.43, respectively. All the run valves were pneumatic actuated ball valves. Check valves were installed just downstream of the run valves to prevent any potential backflow from propagating upstream. In the experiment, the hydrogen torch flow rate was set with a critical flow orifice and the torch GOx, along with the purges, via the injectors. The initial torch design used hydrogen coolant, but after redesigning it was no longer necessary and the line was capped off. A detailed discussion related to torch plumbing is provided

in section 4.4.1. The main RP-2 and GOx propellants were set via critical flow venturis. The venturi upstream pressure and temperature was recorded for back calculating the mass flow rates. Two pressure transducers were installed in the experiment to measure torch and chamber pressure. Thermocouples were also installed in the sample chamber to measure the back-wall sample temperature.

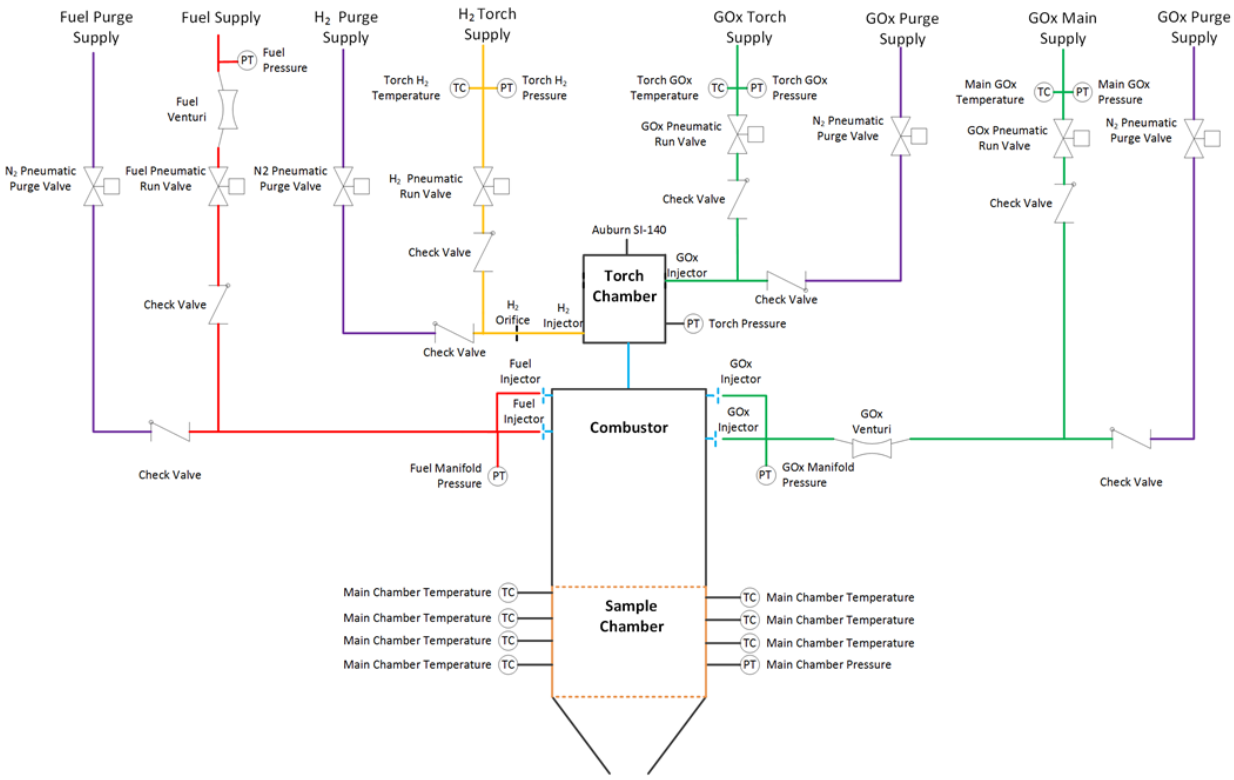

Figure 4.41 Experiment P&ID

Table 4.8 Soot Deposit Experiment Instrumentation

Measurement	**Instrument**	**Range**
Upstream RP Venturi Pressure Upstream GOx Main Venturi Pressure Upstream GOx Torch Pressure Upstream H_2 Torch Orifice Pressure RP Manifold Pressure Main GOx Manifold Pressure Torch Pressure Main Chamber Pressure	GE Druck Unik 5000	0-3000 psi
Upstream RP Venturi Temperature Upstream GOx Main Venturi Temperature Upstream GOx Torch Temperature Upstream H_2 Torch Orifice Temperature Sample Backwall Temperature	Omega KMQSS-062G-6	-200 – 1250 °C
Hydrogen Sensors	RKI 65-2450RK	0-100% LEL

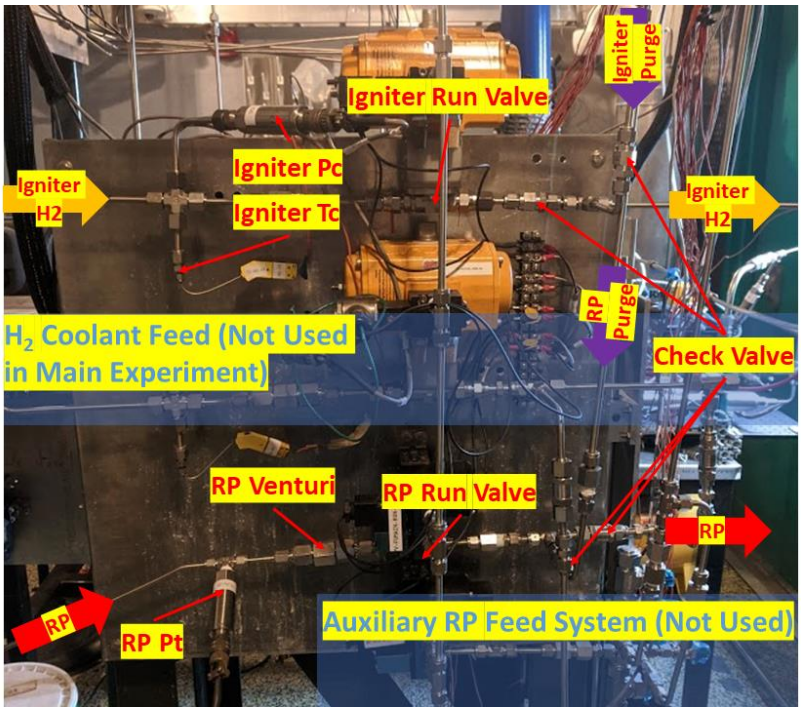

Figure 4.42 Fuel Side of Test Stand

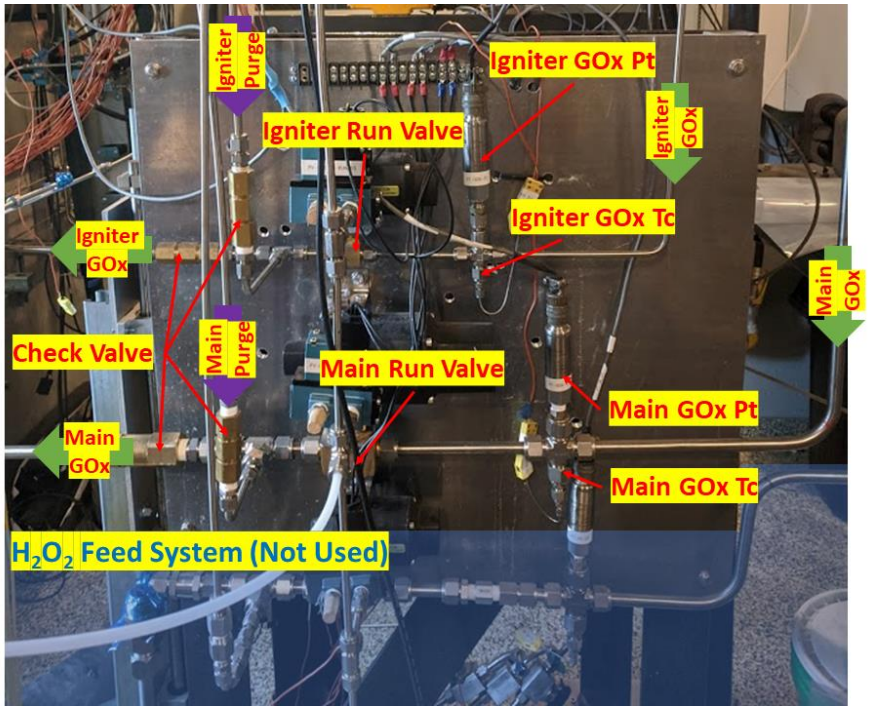

Figure 4.43 Oxidizer Side of the Test Stand

Several extensive weeks of long days and late nights were spent bending tubes for the feed system and oxygen cleaning the system. This included sonicating all small tubes and fittings with the NOC cleaner. The long tubes were cleaned with hot water, and then simple green flown through them for about 30 minutes with a pump, and then they were dried with nitrogen for 10 more minutes – a very thrilling process. Once the system was put together, there was some liquid found in the oxygen system and for safety reasons this required recleaning and rebuilding the system.

After the feed system was complete, all the electronic instruments including thermocouples, pressure transducers, valve actuators and the GOx ER regulator were wired to a patch panel in the ZL1 test cell. The patch panel connected all the instrumentation signals to a LabView SCXI-1001 Data Acquisition (DAQ) device. The valves were wired to a LabView cDAQ-9189 so more precise hardware timing could be used for auto sequencing. Appendix C includes a more detailed list of the electronic components used in the experiment. A LabView VI was then made to record and control the all the fluid systems in the experiment.

Once the plumbing and wiring was complete, the fluid system was leak checked with nitrogen gas. The nitrogen and RP systems were leak checked with bulk nitrogen supply. The GOx and Hydrogen systems on the other hand were leak checked with a nitrogen cylinder. It was connected in place of GOx in the GOx system, and for the hydrogen system connected to the supply line, just downstream of the hydrogen shutoff valve between the ZL3 high pressure lab and ZL1. The leak check procedure consisted of pressuring and isolating sections of the line, in between valves, by increments of 200 psia starting from 100 psia. If no pressure drop was detected in the line, then the pressure was increased until the full bottle pressure. Otherwise, the line was sprayed with soapy water to identify leak locations and the fittings tightened even more. There were some lines that leaked no matter how tight they were, and this required replacing the tube – the flaring or Swagelok ferrules might not have been properly made in these tubes. Once all the systems were leak checked, the experiment was ready to be mounted on the stand.

The experiment test article was mounted to the test stand via an angle bracket. Figure 4.44 shows the experiment in an open chamber configuration, with no choke plate or sample chamber, as it was mounted for the initial checkout test with the redesigned torch igniter. The setup is consistent with the P&ID shown in Figure 4.41. Not shown is an igniter cable that ran from the Allanson 1092 Type N furnace transformer to the Auburn SI-140 electrode. The grounding cable

in the image is also not connected to the torch chamber body. This cable ran from the body to a 6ft pole that was buried in the ground outside of the test cell. Section 4.4.1 discuss this further.

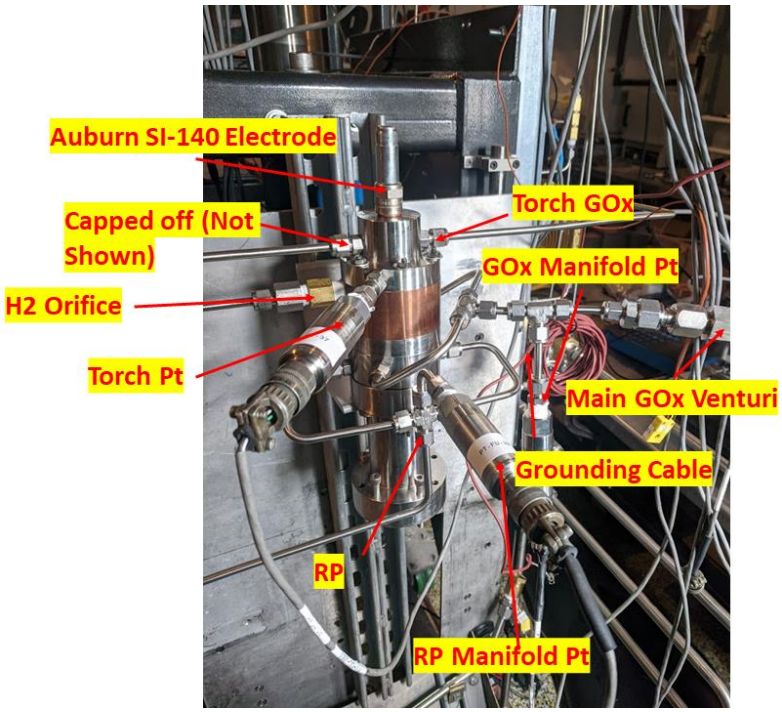

Figure 4.44 Experiment Mounted on test stand without sample chamber

This test stand configuration was used for all the testing in the project. Only the direct connections to the test article were removed between tests, all the components including orifice and venturis were the same. The fluid set pressures were changed to operate at the different conditions. The following section provides an overview of the installed orifice and venturi's and a calibration process for determining the discharge coefficients. Also, as noted in the experimental operating conditions section 4.3, the torch nitrogen purge regulators in the fluid system were repurposed from a different decommissioned system and it was thought the output pressure range of these were the same as the other regulators of 0 to 3000 psig. However, it was later realized during the test readiness review that these regulators can only output 500 psia. The torch igniter was designed to have a purge pressure higher than chamber pressure and as a result this oversight limited the maximum possible chamber pressure condition in the experiment. This required updating the conditions to workable range, as section 4.3 describes.

4.5.3 Discharge Coefficient Calibration

The discharge coefficient for all the flow limiting restrictions in the system, except for the main GOx Venturi, were calibrated prior to testing. The GOx Venturi discharge coefficient was assumed to be 0.985, as was suggested via internal discussion for an uncalibrated venturi. The discharge coefficients for the torch H_2 orifice and the flow limiting GOx injector were determined via the procedure described in section 4.4.1.

The main RP venturi was calibrated by flowing RP-2 for 30 seconds through it at several upstream pressures and measuring the weight of the fluid discharged into a beaker. An average mass flow was determined by weighing the beaker and assuming nominal flowtime of 30 seconds. The discharge coefficient could then be determined by comparing the average mass flow with ideal mass flow, calculated from equation 4.42 for $C_d = 1$.

The flow limiting restrictions used in the experiment and their discharge coefficients are shown in Table 4.9

Table 4.9 Discharge Coefficients of Flow Limiting Devices

Propellent	**Flow Restriction**	**Discharge Coefficient**	**Throat Diameter [inch]**
Torch H2	Orifice	0.64	0.018
Torch H_2 Purge	Injector	0.79	0.02
Torch GOx	Injector	0.8	0.05
Main GOx	Venturi	0.985*	0.088
RP	Cavitating Venturi	0.983-0.988	0.024

* Assumed Discharge Coefficient.

4.6 Run Sequence

The valve sequence timing in the experiment was designed with the transient fluid model discussed in section 4.2.2. The goal was to successfully ignite the main propellants with the torch igniter, safely shutoff the igniter and achieve steady state conditions without needing to do a bunch of trial and error to see what works. It was also desirable to have the same sequence for all the operating conditions for consistency. Investigating different valve sequence timings for the

experimental conditions to see if they would work or produce problems like hard-starts is much easier numerically since changing a variable in the code is simple but needing to rebuild an experiment is time-intensive, as the torch igniter design effort had shown.

The transient fluid model was run with the plumbing shown in Figure 4.41. All the lines downstream of the run valves were measured and input into the model. The mass flow rate through the flow limiting devices were also calculated with the parameters shown in Table 4.9. The manifold volumes for the main injector were as shown in Table 4.6, and the main injector discharge coefficient assumed to be 0.8. The run valve was assumed to have a discharge coefficient of 1 and take 0.1 seconds to open, with the flow area varying proportionally as it opens. The transient fluid model did not include liquid flow equations and so the liquid feed system was not modeled. Instead, as a rough approach, the mass flow injected into the chamber was assumed to proportionally increase from zero to full flow in a span of 0.2 seconds. Future development of this model can include a similar control volume approach for the fluid sections to calculate line fill time. A droplet vaporization model, like the D^2 model discussed in section 3.3.2, can also be added to calculate the gas addition to the well stirred reactor.

In determining the valve run sequence for the experiment, the initial sequence was the same same torch ignition sequence as discussed in section 4.4.1 since it seemed to provide good repeatable ignition. The main RP-2 and GOx valve timing was then explored, with the RP-2 run valve set to be open for 6 seconds. Several valve sequence timings were explored that would work for all the planned experiment operating conditions. These included: injecting the RP-2 and GOx simultaneously; injecting the RP-2 with a lead; or injecting GOx with a lead. In addition, the torch shutoff sequence order was examined.

All the cases that were examined with the GOx lead, or simultaneous RP-2 and GOx injection, showed either no ignition or a long ignition delay. The reason for this was that since the torch flow was very GOx rich, injecting the main GOx drives the mixture ratio further up. At the same time, since the injected GOx was colder than the torch flow and had a higher mass flow rate, the calculations showed it essentially quenched the torch flow. In addition, the model is 0-D with the assumption that the torch energy is distributed evenly throughout the control volume. Non-homogeneity and poor mixing in the experiment could still result in ignition. However, this injection timing was avoided. Injecting with RP lead showed successful ignition in most cases.

The mixture ratio did pass through the stoichiometric point on ignition, but this was only for a split second and was not predicted to cause any issues.

Furthermore, the torch shutoff timing was explored to find an optimal sequence that results in safe shutdown while successfully igniting the main propellants. If the torch is turned off too soon, then it can prevent ignition by not providing enough energy to vaporize and ignite the propellants. This is especially true at the lower pressure and higher main propellant flow conditions. The optimal shutdown could be optimized with the model for all the conditions but a run time of 0.5s after the GOx main propellant valve was opened was predicted to produce successful ignition for all the cases. This timing was used in the main experiment. As a safe approach, the hydrogen and spark igniter were turned off first, followed by the torch GOx 0.25 seconds later. If the GOx was shutoff first, the model predicted the mixture ratio in the torch region would drop and potentially produce a hotter flame. This was not necessarily an issue with the redesigned torch used in the experiment, but from internal discussion it was decided to shutoff hydrogen first just because it was tested and worked without issue during the torch component testing. Additionally, the simulations showed there might be some backflow into hydrogen manifold but only for a small amount and not enough to cause any issues. The manifold mixture would also be quickly diluted with the nitrogen purge. For the torch GOx, since injector was the flow limiting device in the line, and the purge pressure was higher than the chamber pressure, the manifold was predicted to remain clean.

After the torch is turned off, the model predicted it would take a short amount of time for the torch propellants to evacuate and the chamber pressure to drop to the steady state pressure. The final steady state chamber pressure was also predicted to be higher than the design pressure by a few percent because of torch purge flow, as discussed in section 4.4.1. This purge is accounted for in modeling the experiment.

Finally, the shutdown sequence was made to have the main GOx and RP valves close at the same time. From internal discussion with the senior test engineer in the group, it was thought that this approach was safest to prevent any potential backflow into the main propellant manifolds. However, one potential issue with this approach, is if the RP flow drops off faster than GOx then it would result in the mixture ratio rising above design and passing through stoichiometric point. This is exactly what the fluid systems model predicted for the feed system in the experiment. This would only be for a split second though and additional thermal analysis showed this should not be

a significant thermal issue for the experimental hardware. It might affect soot deposits by causing some oxidation, but the effect would be consistent in all the hot fire tests.

The final experimental run sequence that was iterated upon is shown in Table 4.10. The predictions of system pressure and bulk gas temperature for the duration of the experiment are shown in Figure 4.45 and Figure 4.46, respectively

Table 4.10 Soot Deposit Experiment Valve Run Sequence

Valve Event	**Time (s)**
Main RP-N_2 Purge Valve OPEN	0.00
Main GOx-N_2 Purge Valve OPEN	
Torch GOx-N_2 Purge Valve OPEN	
Torch H_2-N_2 Purge Valve OPEN	
Spark ON	
Torch GOx Run Valve OPEN	0.10
Torch H_2 Run Valve OPEN	0.30
Main RP Run Valve OPEN	1.00
Main GOx Run Valve OPEN	1.25
Torch H_2 Run Valve CLOSED	1.75
Spark OFF	
Torch GOx Run Valve CLOSED	2.00
Main RP Run Valve CLOSED	7.00
Main GOx Run Valve CLOSED	

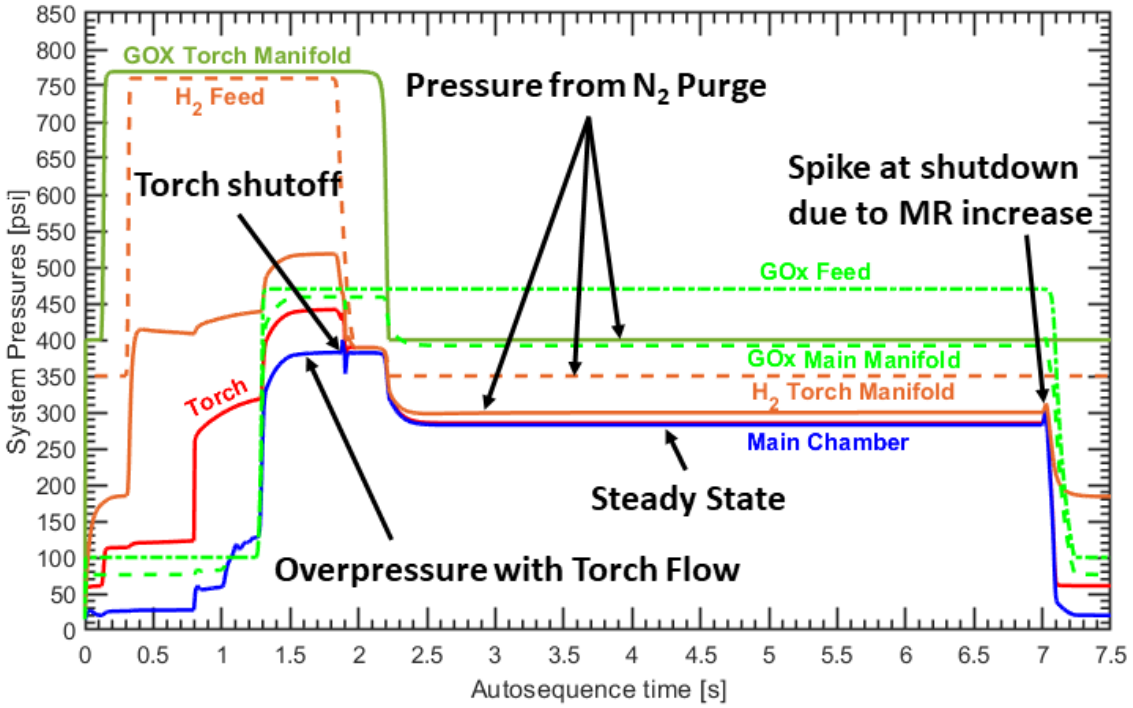

Figure 4.45 Predicted system pressures during experiment operation.

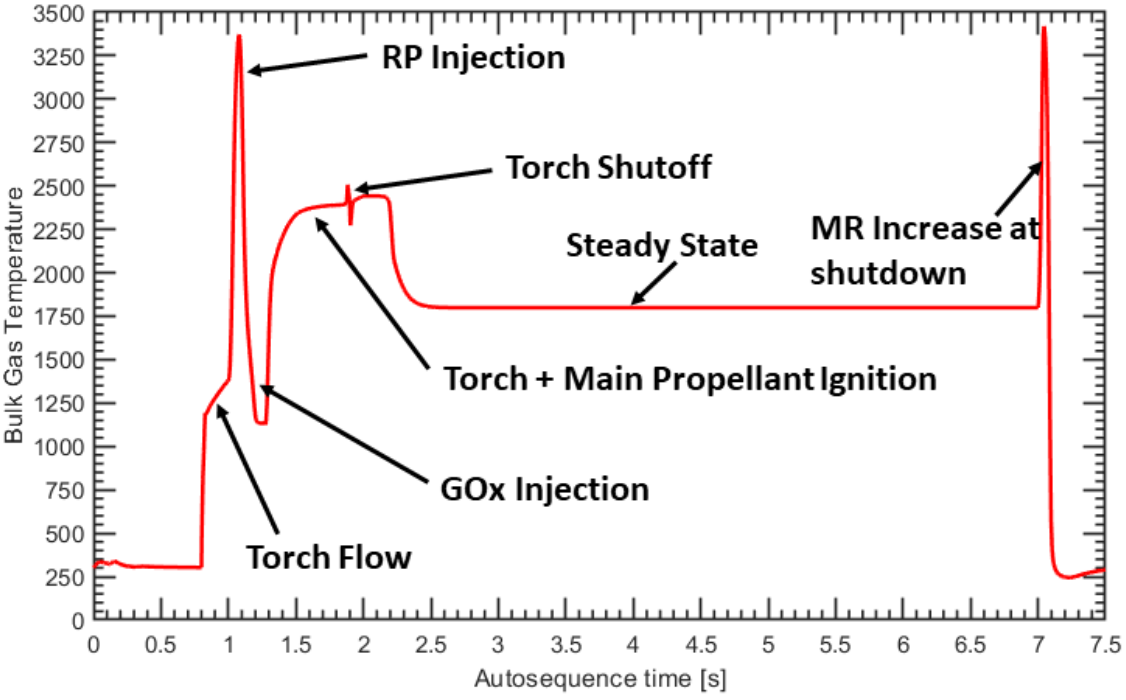

Figure 4.46 Predicted chamber temperature behavior during ignition and shutoff with the transient feed system model.

This same run sequence was used for all the experimental test conditions except for one no choke plate-open chamber test. The chamber was predicted to blow out in the open chamber test because the residence time would be too low. This was later verified during the initial checkout test; the combustor did blow out. So, the condition was run with the torch on for the entire duration of the test. As discussed in section 4.4.3, this case was predicted to potentially damage the hardware due to higher heat fluxes and so it was saved for one of the final tests in the campaign. The experiments also validated this prediction.

The measured chamber pressure in the experiment qualitatively agreed with these predictions. There was an over-pressure, just as predicted, before dropping down to close to the design pressure. However, as discussed in section 4.5.2, the ER5000 regulator tuning was difficult and it took some time for the delivered supply pressure to reach the target valve after the run valves were opened. In the experiment, it took some time for the propellant mass flow rates to reach the design point. Furthermore, there was a small spike in pressure when the torch hydrogen was turned off, as predicted. Also, as predicted, there was a pressure spike at shutdown due to increase in the mixture ratio. However, there also was some rough pressure oscillation at shutdown, which was likely due to vaporization and burning of the residual fuel drops.

5. RESULTS AND DISCUSSION

5.1 Initial Plug Flow Reactor Model

The first approach towards modeling the conditions in the soot experiment was with the plug flow reactor model – discussed in section 3.3. This model was run to predict bulk gas properties, without the soot model. Results from the soot coupled plug flow reactor model are discussed in section 5.3. This initial PFR was run for the conditions shown in Table 5.1. Results for the steady state reactor temperature and acetylene mass fractions distribution are shown in Figure 5.1. The bulk solution from the PFR was then used in the 0-D soot surface growth reactor, discussed in 3.5, to predict chamber wall soot growth rates via heterogenous surface reactions. The predicted soot growth rates are shown in Figure 5.2.

Table 5.1 Initial PFR Model Conditions

Fuel:	POSF5433 (RP2)	**Oxidizer:**	Gaseous O_2
Inlet Temperature:	298 K	**Inlet Temperature**	298 K
Mass Flow Rate:	0.03 kg/s	**Mixture Ratio:**	1
Chamber Pressures:	250 psia, 500 psia, 750 psia		

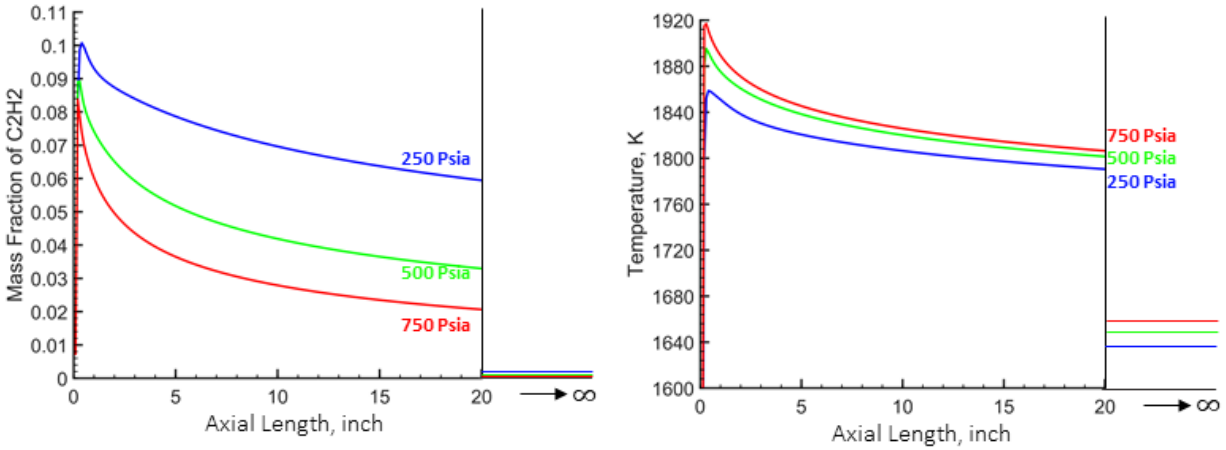

Figure 5.1 Cantera Plug Flow Reactor Temperature [Left] and C_2H_2 Mass Fraction [Right] predictions for length of soot deposition experiment chamber, and at equilibrium.

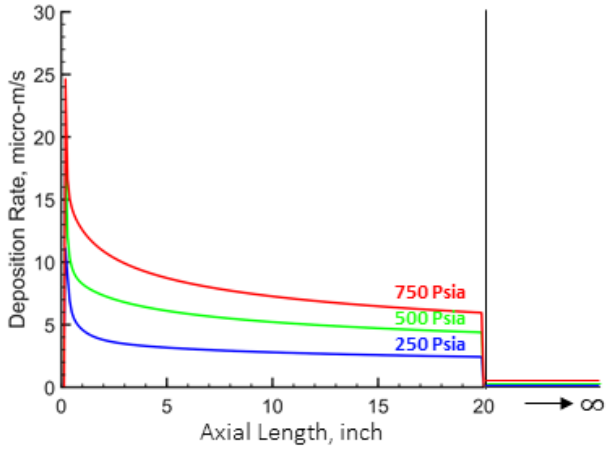

Figure 5.2 Soot Deposition Rate Predictions for the length of the soot deposition experiment chamber and at equilibrium, at 250, 500 and 750 psia.

It is apparent from the reactor results that the reactor is not at equilibrium. The predicted equilibrium temperatures with the Hychem POSF5433 mechanism for the 250 psia, 500 psia and 750 psia chamber pressures are 1636 K, 1646 K and 1667 K respectively. For comparison, the NASA CEA equilibrium temperature predictions are 1545 K, 1576 K, and 1599 K, respectively.[178] The roughly 5% difference is due to the different thermodynamic library in CEA compared to the HyChem mechanism, however the overall pressure trend matches. The residence time in the reactor would need to be ~100 times larger for an equilibrium state to be reached – and the reaction chamber would need to be longer by the same factor. The main reason for the higher than equilibrium temperature in a fuel rich mixture is that the endothermic reactions are slower than the heat release reactions, at least as modeled with the HyChem mechanism. Similarly, the acetylene mass fractions are far from equilibrium. Additionally, while the acetylene mass fraction decreases with pressure, the overall concentration of acetylene is higher.

According to the HACA mechanism, acetylene is the predominant species responsible for soot growth and hence higher concentrations of acetylene produces higher growth rates. This is confirmed by the carbon deposit model, as seen in Figure 5.2. The deposit is originally high at the beginning of the reactor because the temperature is high, and hence reaction rates are faster, and because there are higher concentrations of reactants contributing to HACA soot growth. However, as temperature tapers off, along with concentrations of radicals and acetylene, the deposit rate does too. The deposit rate is nearly constant but still monotonically decreasing with axial length. Ultimately the deposit approaches a steady equilibrium value, which is an order of magnitude

smaller than predicted in the chamber. The results show that carbon growth via surface growth reactions are primarily significant in nonequilibrium mixtures and not very substantial for equilibrium mixtures.

Finally, the simplified deposit model shows that pressure increases deposit rates because of higher concentrations of radicals and acetylene - in the kinetically limited pressure regime. As pressure increases, the mean free path of gas molecules decreases and in turn this results in lower diffusion rates. As a result, reactions would become diffusion limited and in turn HACA growth rates should plateau. Gülder et. al captured this behavior experimentally [179]. However, this effect is not capturable with the PFR model, since a key assumption in the model is premixed flow, and higher fidelity methods are necessary.

5.2 Reacting Flow CFD

Two-dimensional axisymmetric reacting CFD simulations were run after the initial PFR modeling in order to model the experimental flow-field with higher fidelity. This model was discussed in section 3.4 and the cases run shown in Table 3.2. As described in section 3.4, the conditions consisted of two general categories: low-flow cases where the mass-flow was constant and more representative of the conditions in the soot experiment and pressure was controlled via the outlet throat area; and high-flow cases that were more representative of actual combustor conditions with a constant contraction ratio of 3, bulk velocity of ~200 m/s and the pressure controlled by changing the mass flow rate.

Initially non-reacting simulations were run to steady state for each case. Steady state convergence was assessed by verifying that the inlet and throat mass flow rates matched within 5%, and the residuals of the conserved variables decayed to a steady value below 1e-4. In addition, twenty-eight point probes were set up at the centerline and near-wall cells in between 10-24 in region with a spacing of 1 inch. These were verified to be at a constant value $\pm$ 0.1% relative difference between time steps for the converged solution. The temperature and pressure were also compared with isentropic calculation and were verified to be within 5% of the isentropic predictions.

After verifying convergence of the non-reacting simulations, reactions were turned on and the simulations run to steady state. The reaction source term introduced some unsteadiness to the steady state solution and produced some small oscillation in the scalers. To assess convergence in

this case, the mass flow and residuals were first verified like before. The point probes were also examined but to account for unsteadiness, a moving average was calculated for all scalars based on the number of time steps required for 1 flow through time (based on average velocity in the 10-20 in domain), as shown in Figure 5.3 for the 250 psia case. The calculated moving average was then verified to be a constant value within $\pm$ 0.1% between time steps. Once all these conditions were met, the solution was determined to be converged. Furthermore, to account for the unsteadiness in the solutions in the parametric comparisons, the results described and shown in this section were averaged for 1 flow through time.

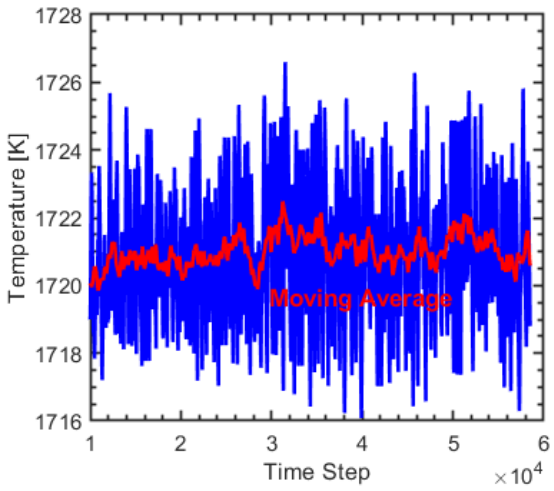

Figure 5.3 Centerline point probe for 250 psi reacting flow case. Point measurement moving average calculated for 1 flow through time (~1270 time steps).

The averaged CFD solution was used for calculating the soot growth rates. The scalars at the near-wall wall and centerline cells were extracted from this solution and used to integrate the HACA mechanism to steady state in the 0-D soot surface growth reactor discussed in section 3.5. The soot growth predictions for the low bulk velocity conditions are shown in Figure 5.4, and comparison with high flow conditions are shown in Figure 5.5. The results were plotted for an axial length of 10-24 inch, this is the region where the boundary layer becomes developed, which was determined by finding the location where the boundary layer ceased increasing with axial length. The boundary layer thickness was determined by finding where the axial velocity is 99% of the mean cross-sectional area averaged velocity. A radial profile of the calculated HACA soot growth rates at 20 in, where the boundary layer achieved fully developed conditions is plotted in Figure 5.5.

The calculated growth rates at the centerline are significantly higher than at the wall for all the conditions. The difference is even more pronounced at the high flow condition. In all the cases, the centerline soot growth rates are closer in agreement with the plug flow calculations, as can be seen by comparing the centerline soot growth rates in Figure 5.4 with the initial PFR results shown in Figure 5.2. Like the PFR predictions, higher pressure is predicted to produce higher soot growth rates. However, the near-wall rates increase with pressure only until about 500 psia and then drop off with further increase in pressure. This behavior can be seen more clearly in the radial profile of the HACA predicted soot growth rate, shown in Figure 5.5. The growth rates increase with pressure near the centerline but then decay near the wall. For the 250-1000 psia cases, the HACA growth rates are also mostly uniform near the centerline and only decrease near the vicinity of the boundary layer. However, for the 1250 psia and 1500 psia cases, the growth rates monotonically decrease towards the wall, except for a small region near the centerline. As will be discussed, this is due to the HACA reactions approaching diffusion limited conditions, where the rates of reaction are limited by the rate of diffusion of the reactant species. It can also be seen that the near-wall soot growth rate predictions are "smoother" compared to centerline cases at the lower pressures. This is due to the gas residence near the wall being higher and allowing for diffusion to produce a more well mixed mixture - whereas at the centerline, residence time is lower, and convection dominates over diffusion. Additionally, the higher-pressure cases also show smoother solution for the same reason. The higher-pressure cases, at a constant mass flow rate of 60 g/s, have a lower bulk velocity. This increases effects of diffusion and produces a more mixed flow. Hence, convection affects mixing which affects the calculated HACA rates and in turn produces the more erratic behavior seen in the centerline cases.

When comparing the high flow with the low flow conditions, for the same bulk pressure, the higher bulk velocity results in larger overall soot growth predictions, at both the wall and centerline. The trends with pressure are similar at both the wall and centerline for both flow conditions, however doubling the pressure from 250 psia to 500 psia results in significantly more soot growth rates for the high flow case. The 500 psia and 750 psia soot growth calculations are also close in comparison for both flow conditions.

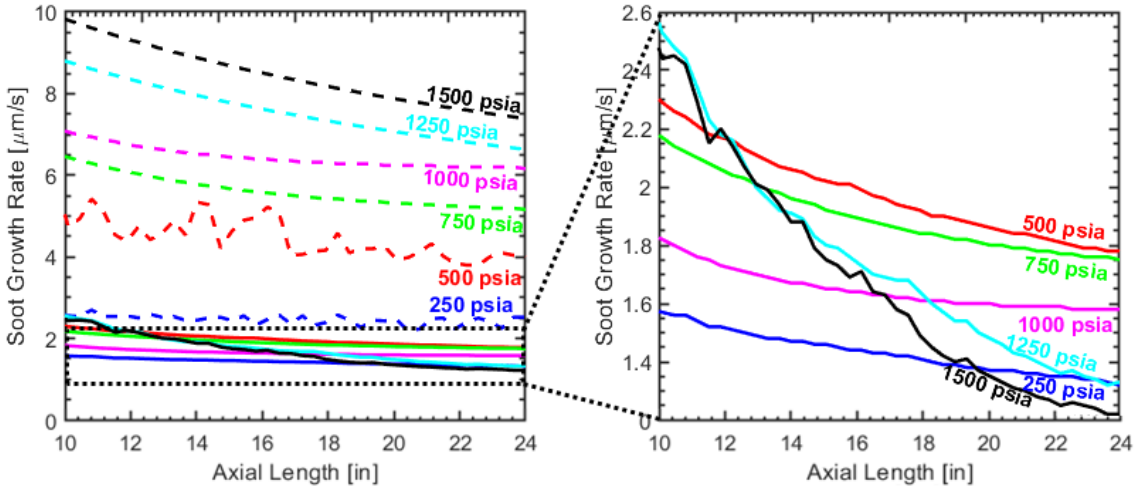

Figure 5.4 Soot Growth Prediction for low bulk velocity cases. The dashed lines are predicted soot growth centerline rates and solid lines are near-wall rates.

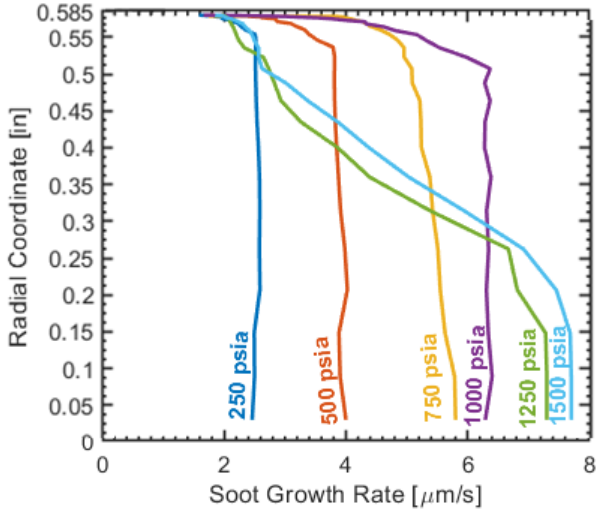

Figure 5.5 HACA Calculated Growth Rates for a radial slice at x = 20 in (fully developed boundary layer region)

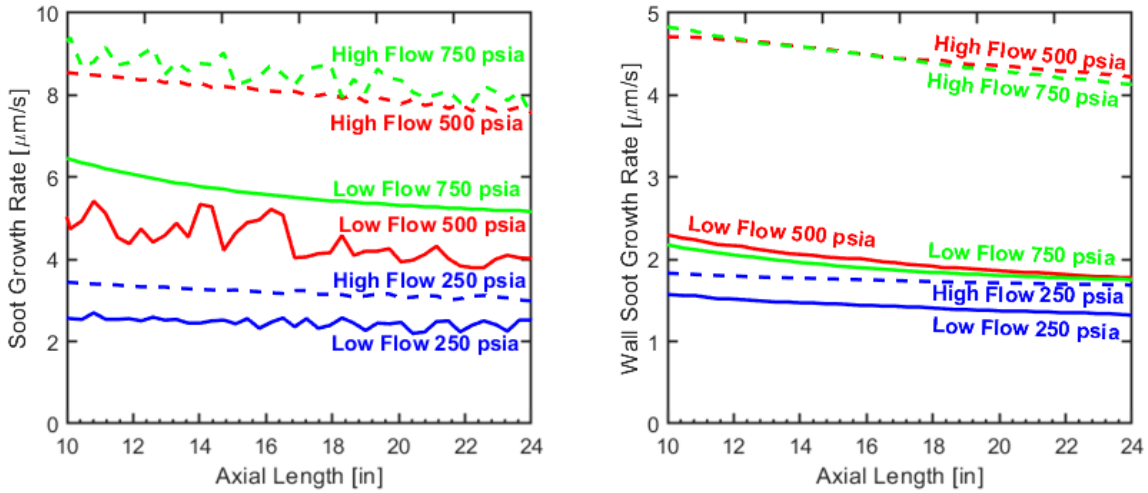

Figure 5.6. Comparison of Soot Growth Rates at the centerline [Left] and Wall [Right] between low flow (solid line) and high flow (dashed line) cases

Unlike the plug flow reactor model which assumed 1-D inviscid flow, the reacting CFD solved the 2D turbulent Favre averaged conservation equations - which with a no-slip boundary condition produces a boundary layer in the flow-field solution. The main disagreement between the plug flow reactor and CFD predicted soot growth rates was at the wall - suggesting that viscous effects in the boundary layer influence the soot reactions. To understand the influence of the boundary layer fluid effects on the chemistry, the local Damköhler number for each of the computational cells was computed as:

$$D_a = \frac{\tau_{res}}{\tau_{chem}} \quad 5.1$$

Where τ_{res} is the fluid time scale – taken as the local residence time of the fluid. τ_{chem} is the chemical time scale, which was estimated as the time for the local mixture composition to reach close to equilibrium soot rates (As shown in Figure 2.3 soot rates drop off as equilibrium is approached). The residence time of the fluid was based on a relative estimate of the advective time scale. It was estimated to be a function of local cell axial velocity and was computed using the local cell velocity and the chamber diameter for reference length as (the reference length is not important for comparison between the cases since all cases used the same chamber diameter):

$$\tau_{res} = \frac{r_{chamber}}{V_{axial}^{cell}} \quad 5.2$$

The chemical time scale was determined by extracting the gas solution in each computational cell and integrating it in time within a 0-D constant pressure reactor until equilibrium. The HACA soot growth rates were also calculated at every time-step. The time for when the rates were within 1% of the final equilibrium rate was assumed to be the chemical time.

The estimated residence time and characteristic chemical time for the low flow condition at an axial slice of 20 inch (where the boundary layer had become fully developed) are shown in Figure 5.7.

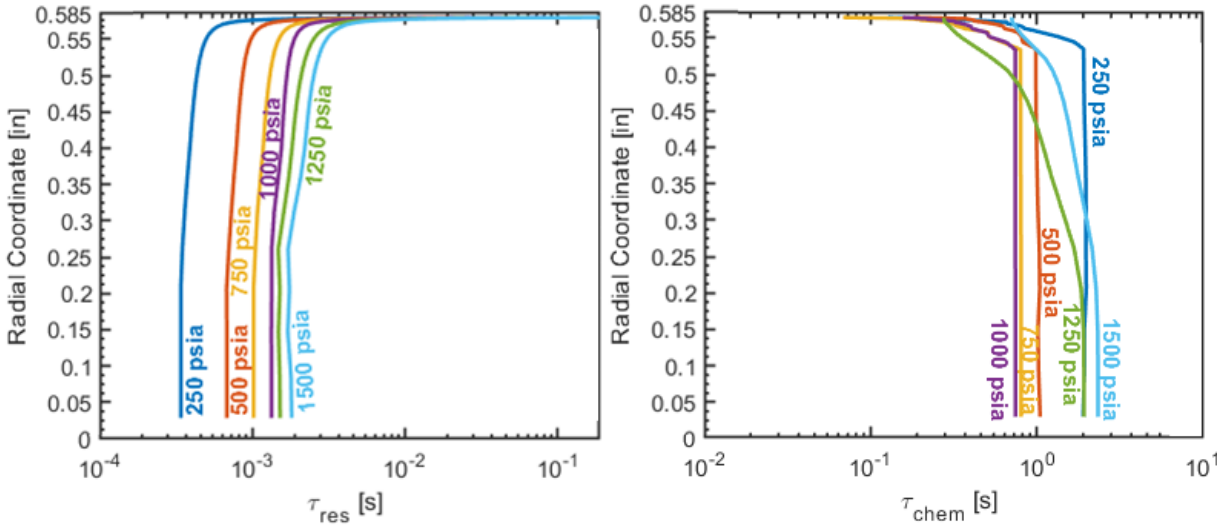

Figure 5.7. Estimate of local flow residence time [Left] and chemical time scale [Right] for the low flow case at x = 20 inch (fully developed boundary layer region)

The residence time estimate is a function of the velocity profile. For a constant mass flow rate in the low flow cases velocity decreases with pressure – which in turn results in higher residence time. Due to the no-slip boundary condition, the axial velocity in the boundary layer decreases towards the wall and hence the local residence time increases. The chemical time estimate is a function of the local gas chemistry and generally decreases towards the wall, as equilibrium conditions are approached. The higher residence times near the wall allows the chemistry to approach closer to equilibrium compared to the core. Additionally, in the kinetics limited condition, the chemical time decreases with pressure as pressure acts to increase the kinetic rates of reactions. This behavior is evident in the 250-1000 psia cases. However, as pressure is increased, the species diffusion rates decrease because the mean free path decreases, and reactions in turn can be limited by diffusion. This is true for the 1250 psia and 1500 psia cases - this regime will be discussed later in this section.

From calculation of these characteristics times, slices of Damköhler numbers were computed for both the high and low flow cases at the same corresponding axial coordinate of 20 inch, as shown in Figure 5.8.

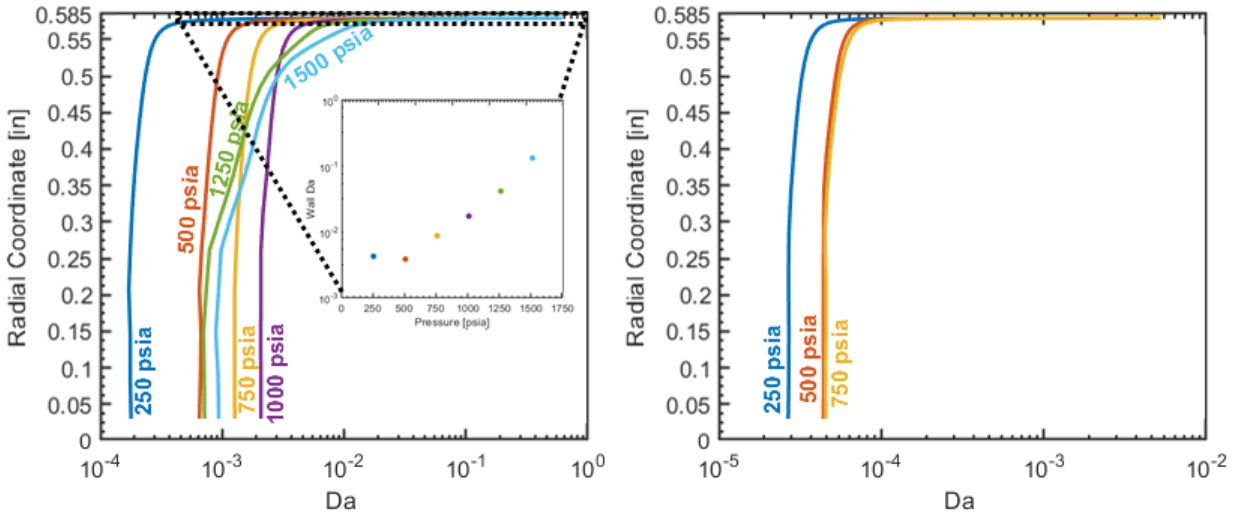

Figure 5.8 Estimated local Damköhler number for a radial slice at x = 20 inch (fully developed boundary layer region) for low flow [Left] and high flow [Right] cases. The inset plot shows the calculated wall Damköhler numbers.

The Damköhler plots provide insight into the interaction between chemistry and fluid mechanics. In all the cases, the Damköhler number is higher near the wall compared to the centerline. This is a result of both the relative flow residence time increasing, within the boundary layer, and the characteristic chemical time decreasing. The higher residence time within the boundary layer allows for the reactions to proceed closer to equilibrium conditions. As described in section 2.2, in the fuel rich regime the gas chemistry requires a long residence time to approach equilibrium conditions and hence a larger residence time significantly affect reaction completion. In this case, a higher residence time near the wall allows the gas-phase reactions to proceed further and this results in lower concentrations of soot growth reactants such as acetylene and radicals. As a result of lower concentrations in the reactants, the HACA predicted rates are lower. Hence, the soot growth rates are lower near the wall because the bulk chemistry is closer to equilibrium.

Comparing the low with high flow conditions, the high flow conditions at the same pressure have smaller Damköhler values. At the high flow conditions, the residence time is smaller which translates to a smaller reaction time and the local gas chemistry being further from equilibrium.

As a result, the concentrations of acetylene and radicals are higher, which explains why the predicted soot growth rates are larger for higher flow conditions.

Furthermore, the effect of pressure on the HACA rates has two competing effects on the soot growth predictions. On one hand it can produce higher HACA surface kinetic rates, due to higher overall concentrations of reactant species. However, on the other hand, pressure also increases the kinetics rate of the bulk gas-phase reactions and drives the bulk gas mixture towards equilibrium – which decreases the HACA reactant concentrations. In the low flow case, where the mass flow was constant, higher pressure resulted in higher residence time and hence provided extra time for the bulk gas-phase reactions to proceed.

The Damköhler number increases with pressure near the centerline for the 250-1000 psia cases for both the low and high flow conditions. Though this suggests that the gas chemistry is closer to equilibrium with increased pressure, pressure is still more dominant in increasing the HACA surface kinetics rates in this region. However, the ratio of the centerline soot rates at 1000 psia bar to 750 psia is smaller than 750 psia to 500 psia bar, as can be seen via visual inspection of Figure 5.4 or Figure 5.5. Pressure has a decreasing effect in the kinetics limited regime. At the wall, the Damköhler number decreases with pressure until 500 psia and then increases with increasing pressure - corresponding to the trend in the calculated wall soot growth rates. Pressure is more dominant in increasing HACA rates until 500 psia but afterwards it has a more dominant effect on driving the bulk gas chemistry to equilibrium and, with the higher residence time in the boundary layer, the resultant effect is a smaller HACA growth rate. The same trend is observed for the high flow conditions.

The 1250 psia and 1500 psia conditions show different behavior from the other pressure conditions. The rates at the centerline and wall follow the same trends as the other high-pressure cases, however the radial profile in between is different. The predicted soot growth is relatively uniform for the lower pressure cases in the core and then decrease within the vicinity of the boundary layer, however the rates in the higher-pressure cases monotonically decay towards the wall. The same behavior is observed in the calculated chemical time scale, in Figure 5.7, and in the Damköhler number, in Figure 5.8. This behavior is related to diffusion rates decreasing with pressure and at these high pressures, the decrease in diffusion rates affects reaction kinetics. To estimate change in diffusion with pressure, a mixture-averaged diffusion-coefficient was

calculated from the binary diffusion coefficients of each species via Cantera using the formulation described in [46]:

$$\frac{1}{D_{km}} = \sum_{j \neq k}^{K} \frac{X_j}{D_{kj}} + \frac{x_k}{1 - Y_k} \sum_{j \neq k}^{K} \frac{Y_j}{D_{kj}} \quad 5.3$$

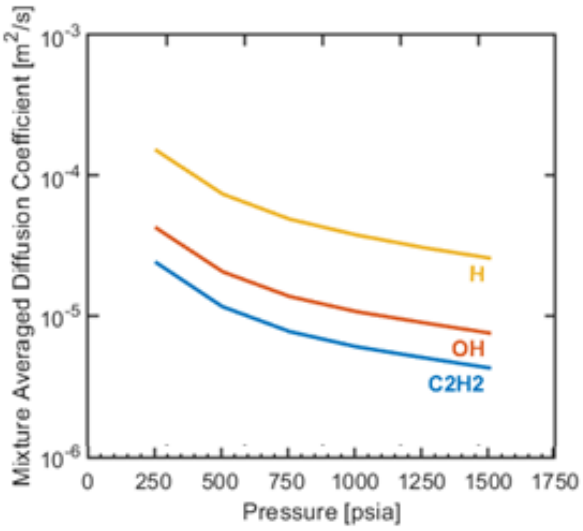

Figure 5.9 Mixture-Averaged Diffusion Coefficients for H, OH C2H2

The mixture-averaged diffusion coefficients decrease with increasing pressure and decrease by about 25% from 1000 to 1250 psia. The bulk gas reaction rates on the other hand generally increase with pressure (except for pressure independent reactions). When diffusion rates of species in a reaction are higher than the reaction rate, the bulk reaction rates are controlled via kinetics and hence are kinetically limited. However, as pressure is increased, the reactions at a certain point become limited by rate of diffusion of species to that point. In this regime, the reacting chemistry is diffusion limited. To compare the reaction with diffusion rates for the bulk gas at different pressure conditions, another Damköhler number was calculated as follows:

$$D_{a,k} = \frac{\omega_k * M_{W,k} * r_{chamber}^2}{\rho_{gas} * D_{km}} \quad 5.4$$

This Damköhler number compares the production (or consumption) rate of a certain gas species to the density and mixture averaged diffusivity. To nondimensionalize the ratio, the chamber radius was used for the length scale (and is the same for all the cases). The calculation

for a radial slice at 20 in for the hydrogen radical is plotted in Figure 5.10. The hydrogen radical is the lightest species involved in in the HACA mechanism and responsible for producing an active site on the soot surface, via abstraction, to which acetylene binds to. The other species in the reaction mixture follow the same general trend, though with differing profiles at the high-pressure conditions due to differing reaction rates and diffusion coefficients. For the hydrogen radical, the calculated Damköhler number with respect to diffusion for the 1250 and 1500 psia cases are larger by several factors compared to the 1000 psia and all the lower pressure conditions. Hence, at these high pressures, the diffusion rate of the hydrogen radical is much smaller than the consumption rate. This makes the gas phase reactions limited by diffusion and in turn limits the amount of hydrogen, along with the other reactants involved in soot growth, that can be consumed in the bulk core flow. As the gas diffuses towards the wall, hydrogen and acetylene get consumed and the concentration slowly drops, which in turn decreases the predicted HACA growth rates towards the wall and produces the decaying rate behavior observed in Figure 5.5. If the diffusion rate was higher, then the radial concentration gradients would be smaller and the profile would look more uniform, like for the other pressure conditions. Since the gas-phase reactions are diffusion limited at these higher pressure conditions, the residence time required to reach equilibrium conditions is also higher, as observed in the right plot of Figure 5.7. Since the gas is further from equilibrium, this results in higher soot growth rates at the core. Near the wall the chemistry is still limited by diffusion, but the higher pressure and residence time brings the local gas closer to equilibrium compared to lower pressure cases, as observed in the first Damköhler number calculation in Figure 5.8.

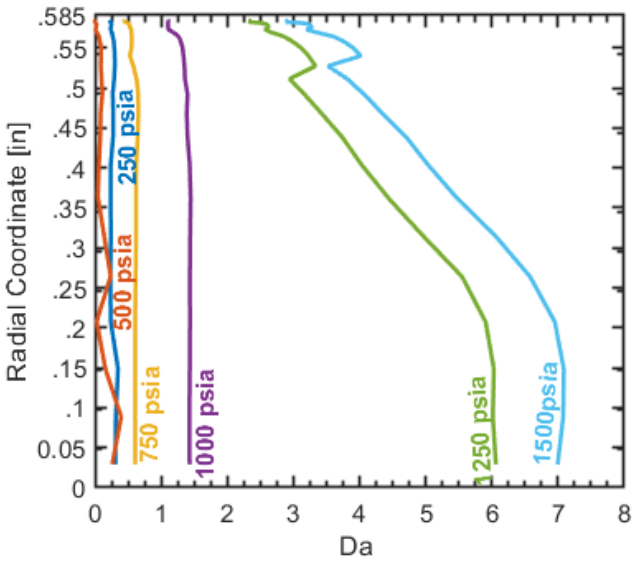

Figure 5.10 Damköhler number with respect to H* production and diffusion rates at a radial slice at x = 20 inch

5.2.1 Main Takeaways

The CFD results showed the effect of fluid dynamics on the fuel rich reacting flow field. This study was prompted when initial CFD calculation showed discrepancy in the wall soot growth rates between the simplified 1-D plug flow reactor approach, discussed in section 5.1. Based on the results, the study showed that at fuel rich conditions, the plug flow model provides a reasonable approximation of the bulk gas chemistry near the centerline of a reactor in a kinetics limited regime (below 1000 psia). However, prediction of near-wall chemistry requires resolving the boundary layer as higher residence times within the boundary layer significantly affect the reaction progress. The key takeaways from this study were:

1. Boundary layers increases gas residence time compared to the bulk core flow. At fuel rich conditions, the gas chemistry requires a long time to reach equilibrium and the extra residence time within the boundary layer brings the local gas closer to equilibrium. Soot growth is high at non-equilibrium conditions and drops off as equilibrium is approached due to decrease in the reactant species. As a result, the soot growth rates in the boundary layer region are lower than in the core
2. Higher velocity results in higher soot growth rates. As bulk velocity is increased, the residence time in all parts of the flow domain decrease, and the reaction progress towards

equilibrium is smaller - which results in higher concentrations of acetylene and hydrogen radical reactants and in turn higher soot growth rates.

3. Pressure has a variable effect on the overall soot growth rates in the fuel rich regime. At low pressures, increasing pressure increases the soot surface growth rates. However, as pressure is increased, it also increases the bulk gas reaction rates and drives gas closer to equilibrium. At relatively low local residence times, like in the centerline of a reactor, increasing pressure still results in increased soot surface growth rates. However, at higher residence times, like near the wall, pressure drives the bulk gas chemistry closer to equilibrium and results in less soot rates compared to lower pressure conditions. Furthermore, at even higher pressures, the diffusion rates of species become important since it can be lower than the rate of reactions. In this case, the chemistry is diffusion limited and properties in the bulk gas are less uniform compared to the lower pressure cases. This diffusion limited regime cannot be predicted with a plug flow reactor approach and requires CFD modeling.

5.3 Sooty Plug Flow Reactor Model

The CFD results showed that the PFR agrees with the bulk solution. Since most of the soot in the experiment is formed in the core, this suggested that modeling volumetric soot with a well stirred reactor or plug flow reactor would provide a good approximation of the bulk soot formed. This was done with the model discussed in section 3.8. All the simulations were run with the detailed HyChem POSF5433 RP-2 119 species-841 reaction mechanism [14,15]. The solutions used 6 coalescent moments and 4 aggregate moments based on a WSR convergence study. All the simulations were run for a range of conditions shown in Table 5.2.

Table 5.2 Reduced Order Soot Model Range of Conditions

Fuel	Oxidizer	Mixture Ratio	Pressure Range (psia)	Chamber Lengths (inch)	Reactor Heat Transfer
POSF5433 (RP2)	GOx	1	150-750	5 in – 13 in	Adiabatic, T_{wall} = 300 K

These simulations were run both with full coupling of the soot particle, gas equations and with the decoupled approach – where the gas solution was solved without soot and then this solution was used to calculate the soot formation rates.

This section discusses the effect of several parameters on soot formation and deposition. Comparison of the model predictions with the experimental data is deferred to section 5.5.

5.3.1 Effect of Pressure

The effect of pressure on soot formation was studied with the sooty PFR model. These simulations were run at a roughly constant residence time by varying the total PFR mass flow. The PFR outlet exit diameter was set to 0.312 in, corresponding to the nominal choke plate used in the experiment. The reactor was also run as adiabatic.

The pressure in the PFR was varied from 150-750 psia. The required mass flow for these pressures was found by scaling via the nominal 250 psia condition in the experiment as:

$$\dot{m}(\mathrm{P}) = \frac{P M_{w,mix,250psia} \mathrm{V_{PFR}}}{\tau_{res} R_u T_{250psia}} \approx \frac{P}{250} \dot{m}_{250psia} \qquad 5.5$$

The mixture molecular weight, and temperature can vary with pressure – which can affect the residence time. However, these were assumed to be small. The conditions that were run for the PFR model are shown in Table 5.3. The bolded values in the table were calculated assuming no soot formation. The corresponding residence time – accounting for differences in molecular weight and temperature are also shown for the no soot formation case. The PFR length was set to the length of the experimental chamber. The number of WSR's in the PFR chain was set to 200 based on a convergence study by increasing the WSR reactors and verifying the absolute and relative difference between all the scalars in the final WSR chain was less than 1e-5.

Table 5.3 Reduced Order Soot Model pressure conditions at a roughly constant residence time

Outlet choke Diameter (inch)	Chamber Length (inch)	**Gas Pressure without Soot (psia)**	**τ_{res} without soot (milliseconds)**	Total Mass Flow Rate (g/s)
0.312	9.2	150	5.7	36
		250	5.6	60
		350	5.6	84
		450	5.6	108
		550	5.5	132
		650	5.5	156
		750	5.5	180

The effect of coupling the MOMIC soot model to the PFR was first explored at a range of pressure conditions. The PFR bulk gas temperature and acetylene concentrations for both the coupled and uncoupled models are shown in Figure 5.11; and soot properties between both models shown in Figure 5.12.

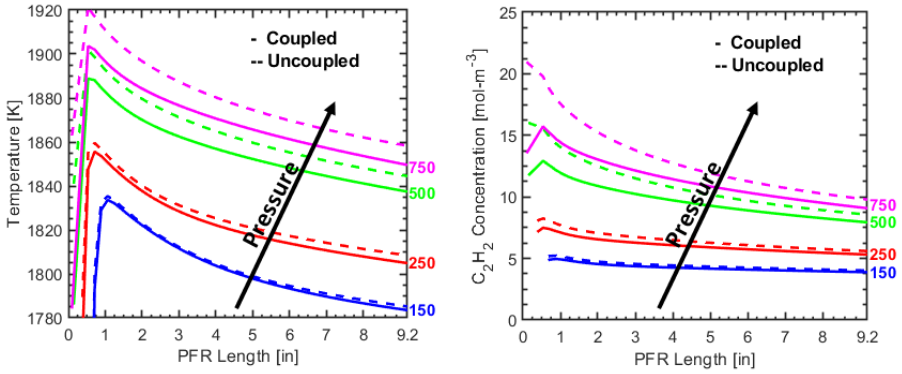

Figure 5.11 Effect of coupling soot to PFR on Temperature [Left] and C_2H_2 concentration [Right] at a roughly constant residence time and range of pressures.

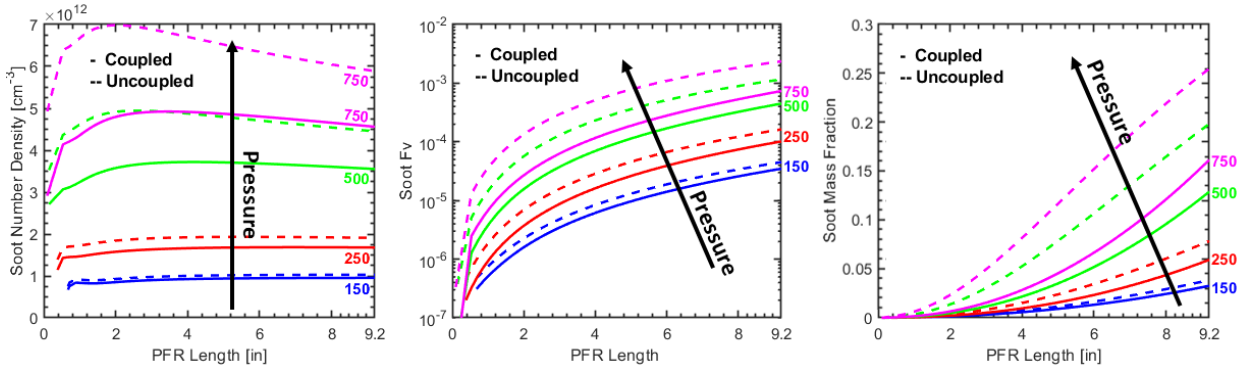

Figure 5.12 Effect of coupling soot to PFR on Soot Number Density [Left], Volume Fraction [Center] and Mass Fraction [Right] at a roughly constant residence time and range of pressures

The PFR solution shows little difference between the coupled and uncoupled models at a pressure of 150 psia. The trends also match between models – higher PFR pressure produces higher temperature and acetylene concentrations. However, the differences between the models increase with increasing pressure. These differences are due to two interrelated reasons. First soot formation physically consumes gas phase moles to form solid phase soot product. As Figure 5.12 shows, larger consumption of gas phase moles with increase in pressure produces larger soot volume fractions and mass fractions. Soot surface growth also consumes acetylene at a greater level with increased pressure due to soot particles becoming larger – and having a greater reaction surface area. The drop in the total amount of gas moles decrease the gas density, and in turn pressure. The drop in pressure in turn results in slightly slower heat release reactions. At the same time, soot formation produces an enthalpy loss in the gas phase. Heat transfer between soot particle and gas phase can further decreases gas temperatures. This calculation was run as adiabatic and the difference between coupled and uncoupled temperatures is not as significant. However, soot is an efficient radiator and if heat transfer to the wall was included then a large amount of energy would be transferred via radiation from the soot particles to the wall – leading to a higher gas temperature drop.

Coupling the soot equations to the gas phase WSR equations in the PFR also produces large differences in the predicted soot particles with increased pressure, as shown in Figure 5.12. The predicted number densities, volume fractions, and mass fractions are higher with the uncoupled model at the higher pressures – and the difference increases with increased PFR axial length. The reason for this is energy loss and species consumption of gas phase is not included in

the decoupled model, which results in higher soot nucleation and growth kinetic rates. The surface growth kinetic rates also increase with pressure and as a result there is increased species consumption at higher pressures. By neglecting this consumption, which increases with pressure, the surface growth rates in a decoupled approach are higher because of higher gas concentrations. Additionally, the soot particles grow as they flow along the PFR length. The differences between the uncoupled model and coupled models are initially small at the beginning of the PFR but become larger as the soot particle size distribution shifts to larger particles.

As mentioned, soot formation leads to pressure loss in a reactor because of a decrease in gas density due to consumption of gas phase moles. The higher the soot produced, the higher the pressure drop. The pressure loss due to soot formation with increased PFR pressure was calculated for the mass flow rates in Table 5.3 and shown in Figure 5.13. If soot calculations are turned off, then the predicted PFR pressures for the uncoupled PFR model are one-to-one with the no-soot pressure. However, soot formation at the same conditions is predicted to produce pressure loss. The difference is small at lower pressures but quickly increases with increased pressure as higher amounts of soot get formed – about 27% at 750 psia. Solely in terms of reactor, or engine performance, this result shows that soot formation is detrimental.

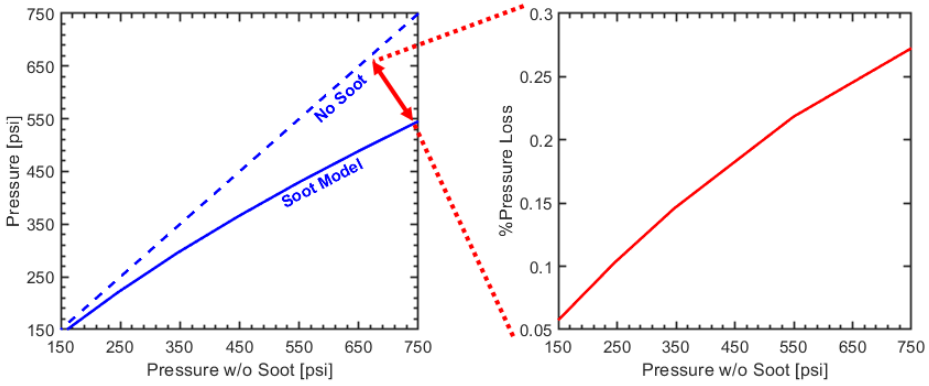

Figure 5.13 Effect of coupling soot to PFR on reactor pressure [Left] and percent pressure loss [Right] at a roughly constant residence time and range of pressures.

The effect of pressure for a larger number of conditions with the coupled model are shown in Figure 5.14 for the gas phase and Figure 5.15 for the soot particles. These were for the same conditions listed in Table 5.2. The pressure labels in the plot, correspond to the gas pressure if no soot was formed at that condition and is as listed in Table 5.2.

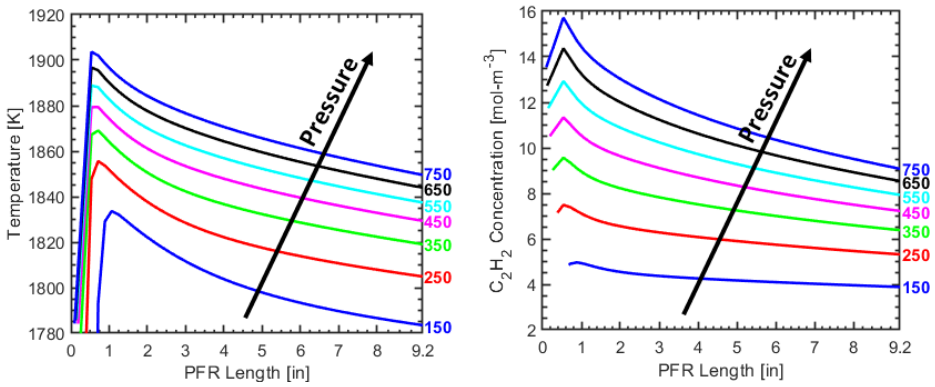

Figure 5.14 Predicted PFR Bulk Temperature [Left] and C_2H_2 [Right] Mass Fraction predicted with the coupled soot formation model at range of pressure conditions.

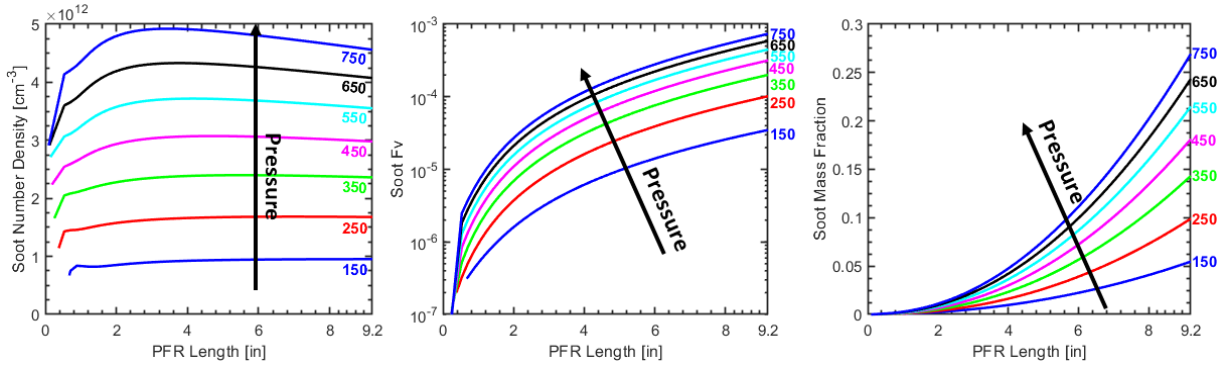

Figure 5.15 Soot Number Density [Left], Volume Fraction [Center] and Mass Fraction [Right] predicted with the coupled soot formation model at a range of pressure conditions.

Higher PFR pressures result in higher temperature and acetylene mass fractions, as expected. However, the increase between each 100 psia increment gets smaller – as can be seen by inspecting Figure 5.14 and noticing the curves get closer together with increased pressure. The reason for this is the increase in soot with increase in pressure gets smaller. The Figure 5.15 plots of soot volume fraction and mass fraction show this behavior with pressure. Surface growth is the dominant process in increasing soot mass. Figure 5.16 plots the calculated soot number density and soot mass density source rates. As the soot mass density source shows, surface growth is several orders of magnitude higher than nucleation. The surface growth kinetic rates taper off with increase in pressure, due to increased consumption of gas phase species, and in turn the increase in amount of soot formed with increase in pressure gets smaller. As a result, effects of soot on gas phase solution also taper off with pressure because the amount of soot formed with increase in pressure tapers off. Soot growth along the PFR length can result in large amount of soot though

and have a significant effect on gas properties. The soot volume fraction approaches 1e-3 and mass fraction are over 0.25. As previously mentioned, if an actual engine was to operate at these conditions then the performance loss would become significant at high pressures as the chamber gets longer or residence time increases. Section 5.3.2 discusses the effect of residence time in more detail.

Additionally, the soot number density is predicted to increase initially but then slowly drop along the PFR length, as shown on the right plot of Figure 5.15. Higher pressures are also predicted to produce higher soot number densities. This was not quite as originally expected, because it was thought coagulation would become more significant with pressure and decrease the number densities to form less but larger aggregate soot particle. However, as shown in Figure 5.16, the nucleation rates of the smallest soot particle also increase with pressure and the coagulation rates are about equal. At fuel rich conditions, the amount of smallest soot particles formed seems to keep up with the coagulation rates that act to decrease the soot number density. The net effect is to produce a relatively constant soot number density profile within the plug flow reactor domain.

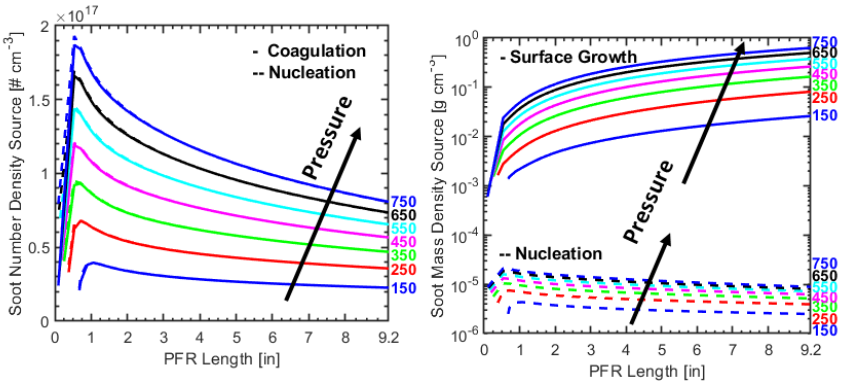

Figure 5.16 Volumetric Soot Source Terms for Number Density [Left] and Mass Density [Right].

The bulk PFR and soot solution was used to calculate the soot mass deposition rate due to deposit surface growth, thermophoretic diffusion, and Brownian diffusion via the approach discussed in sections 3.5 and 3.7. The mass deposition rate was found by multiplying the predicted mass flux by the WSR reactor surface area in the PFR chain.

The 2-D axisymmetric results from section 5.2 showed that predicted wall HACA rates are significantly lower than in the original PFR model because boundary layers allow the local gas chemistry to approach closer to equilibrium. To account for this effect – in a hand-wavy way – the

solution in each WSR in the PFR chain was integrated in a constant pressure reactor for time equal to ten times the residence time in the PFR. This is roughly what the extra residence time that the boundary layer provides. This is a very rough approach though, and it would be desirable to explore other approaches for accounting for boundary layer effects in the future. The thermophoretic and Brownian deposition rates were calculated directly with the plug flow reactor solution as described in section 3.7. Figure 5.17 shows the magnitude of the three different deposition mechanisms at a range of pressures; and Figure 5.18 and Figure 5.19 show a close up of each mechanisms.

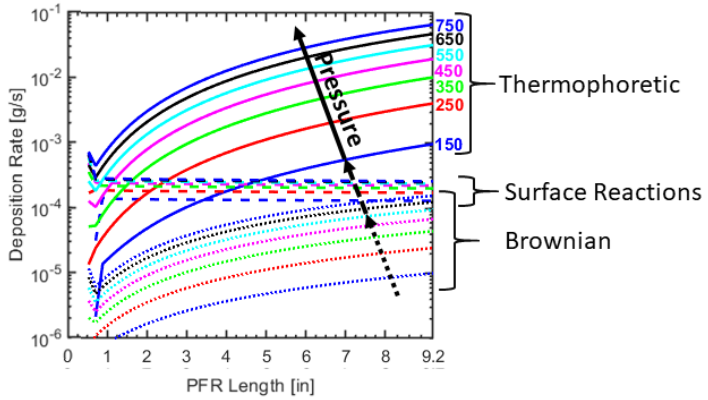

Figure 5.17 Predicted thermophoretic, surface reaction and Brownian contributions to total soot mass deposition rate at a constant wall temperature of 300 K at a range of pressure conditions (in psia)

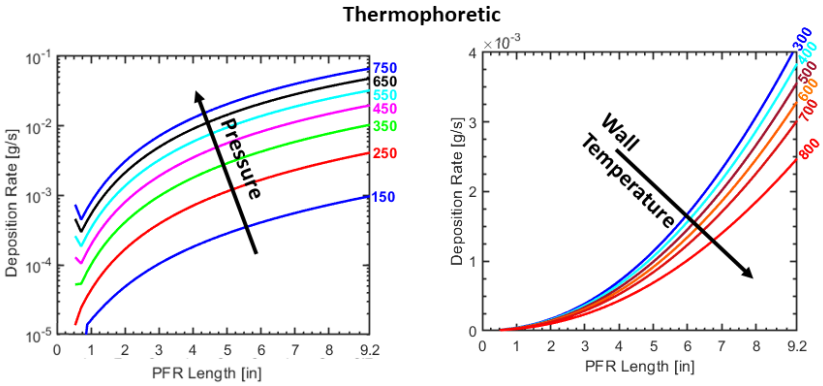

Figure 5.18 Predicted thermophoretic soot mass deposition rate at a wall temperature of 300 K and range of pressure conditions (in psia) [Left] and range of wall temperatures (in K) at 250 psia [Right].

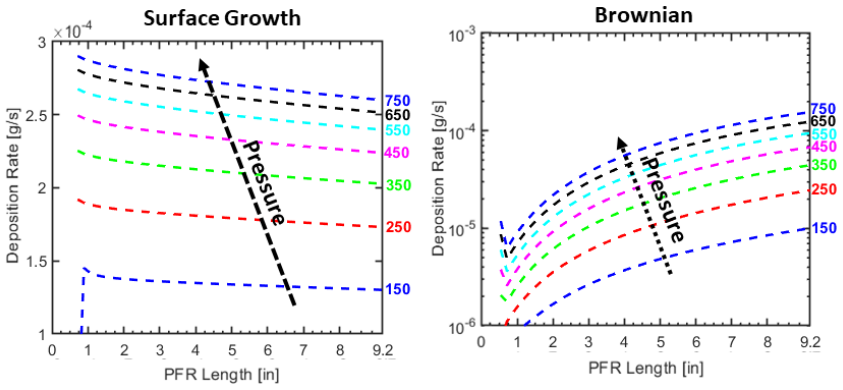

Figure 5.19 Predicted surface growth [Left] and Brownian [Right] mass deposition rates at a range of pressure conditions (in psia).

The deposition rate calculations show that that thermophoretic deposition is the dominant mechanism in the PFR. The thermophoretic deposition rate at the PFR exit is roughly an order of magnitude higher than due to soot deposit surface reactions, and two orders of magnitude higher compared to Brownian diffusion. Surface reactions on the deposit surface contribute to a higher soot mass growth rate initially in the PFR, when the concentration of acetylene is high, and the amount of soot formed is small - but as higher amount of soot is formed thermophoresis becomes more significant. Even with the rough correction to account for boundary layer effects, the surface reactions are still likely overpredicted at the higher-pressure conditions compared to 2-D CFD. The correction doesn't capture the behavior observed in the CFD, where the soot growth rates were predicted to increase with pressure until about 500 psia and then decrease afterwards. Hence, thermophoretic deposition is likely significantly more dominant at higher pressures. As soot volume fraction and mass fraction calculations in Figure 5.15 show, the amount of soot formed is at least an order of magnitude higher at the exit compared to the initial WSR in the PFR chain. The thermophoretic and Brownian diffusion deposit rates were predicted to increase by roughly the same amount as seen in Figure 5.18 and Figure 5.19. The predicted surface reaction contribution to the soot slowly decreases with axial length because of a drop in acetylene concentration. All the three deposit mechanisms produce higher soot deposition with increased pressure, however thermophoresis results in the largest increase in comparison. Thermophoretic deposition increases by about two orders of magnitude from 150 psia to 750 psia, whereas surface growth reactions only increase by about a factor of two for the same pressure increase – corresponding to about the same increase in acetylene concentration as shown in Figure 5.14. But the soot surface growth

reaction rate increase with pressure is likely not physical as described previously. Pressure also increases Brownian diffusion, but the deposit rates are much smaller in comparison to the other two mechanisms. The deposition rate due to Brownian diffusion at a pressure of 750 psia approaches that of surface growth reactions at a pressure of 150 psia at the exit of the reactor. Hence, Brownian diffusion can be considered a negligible source of soot deposition for the conditions in the PFR. Additionally, the reactor surface temperature affects the thermophoretic deposition rate as shown on the right of Figure 5.18. This is because the temperature gradient, which drives the thermophoretic deposition of submicron particles, decreases. However, the difference between a reactor wall temperature of 300 K and 800K is not significant until near the exit of the PFR, where the soot particle sizes are larger. The difference at the exit is within a factor of two. The higher temperature still produces higher soot deposition rates though than due to surface growth reactions.

The effect of coupling the MOMIC soot model to the PFR on the deposition calculations was also examined by running both the coupled and uncoupled model and then calculating the deposition rates. The results for the thermophoretic, surface growth and Brownian diffusion deposition rates between the coupled and uncoupled model are shown in Figure 5.20. The deposition trends with pressure agree between both models, however the uncoupled model predicts higher deposition rates. The difference is small at the lower pressures, where soot volume fractions are lower, but the difference becomes significant at higher pressures. Hence, coupling soot to the gas phase equations in the PFR becomes important with increased pressures.

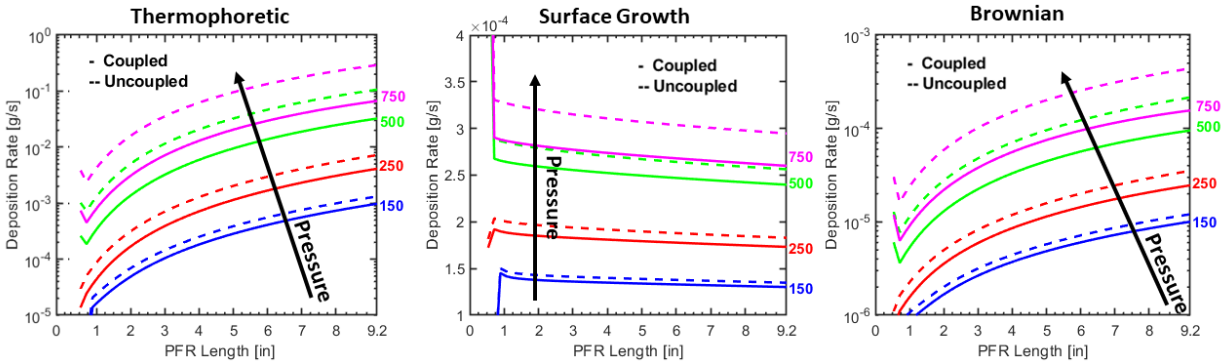

Figure 5.20 Effect of coupling soot to PFR on predicted soot mass deposition rate due to thermophoresis [Left], surface growth [center], and Brownian diffusion at a roughly constant residence time and range of pressures (in psia).

5.3.2 Effect of Residence Time

Residence time is another significant parameter that affects the amount of soot generated in a PFR. Increased residence time provides longer time for surface growth reactions to increase the mass of the soot particle size distribution. At the same, higher residence time results in increased consumption of gas phase species and greater affects the gas phase solution. To quantify the effect of residence time, the model was solved at various residence times at a constant pressure condition of 250 and 500 psia. The same inputs for the 250 and 500 psia conditions from the previous pressure study were used in this residence time study. However, the residence time in this case was altered by modifying the overall PFR reactor length from 9.2 inch to a range of values in between 5 inch - 13 inch. The residence time could also have been altered by varying both the mass flow rate and outlet throat area – with a constant chamber length of 9.2 inch. This approach though allowed studying the effect of residence time at constant mass flow rate and for an adiabatic reactor would have the same effect on the bulk flow – the governing equations are indistinguishable. Changing the PFR length also made coding this parametric study slightly simpler. All the results presented in this section nondimensionalized the axial location of the PFR solution by the length of the PFR in order to consistently compare the results. The deposit rate flux was also reported instead of the overall deposit to make comparison of different reactor lengths clearer. The total PFR residence time as a function of chamber length could be calculated as:

$$\tau_{res} = \frac{P}{\dot{m}RT} A_c L_{PFR} \tag{5.6}$$

The model conditions for this residence time study are shown in Table 5.4. The necessary number of well stirred reactors in each case was determined by first solving the model with 100 reactors and then increasing the number of reactors by 50 until the absolute and relative differences in the outlet solution was less than 1e-5 for temperature, pressure, species and moments.

Table 5.4 Reduced Order Soot Model residence time conditions at constant non-sooty pressure conditions

Outlet choke Diameter (inch)	Chamber Length (inch)	**Gas Pressure without Soot (psia)**	**τ_{res} without soot (milliseconds)**	Total Mass Flow Rate (g/s)
0.312	5 -13	250	3-8	36
		500		60

The effect of coupling the MOMIC soot model to the PFR was first explored at a range of residence time conditions. The PFR bulk gas temperature and acetylene concentrations for both the coupled and uncoupled models are shown in Figure 5.21; and soot properties between both models shown in Figure 5.22.

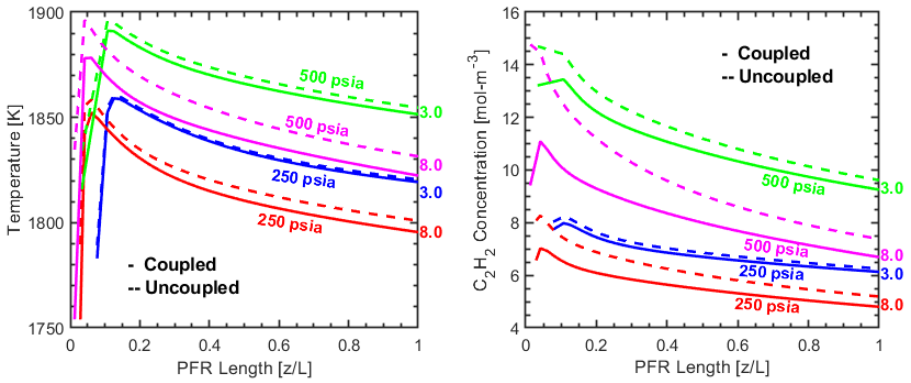

Figure 5.21 Effect of coupling soot to PFR on Temperature [Left] and C_2H_2 concentration [Right] at a range of residence time conditions (in milliseconds) and non-sooty pressure conditions of 250 psia, and 500 psia.

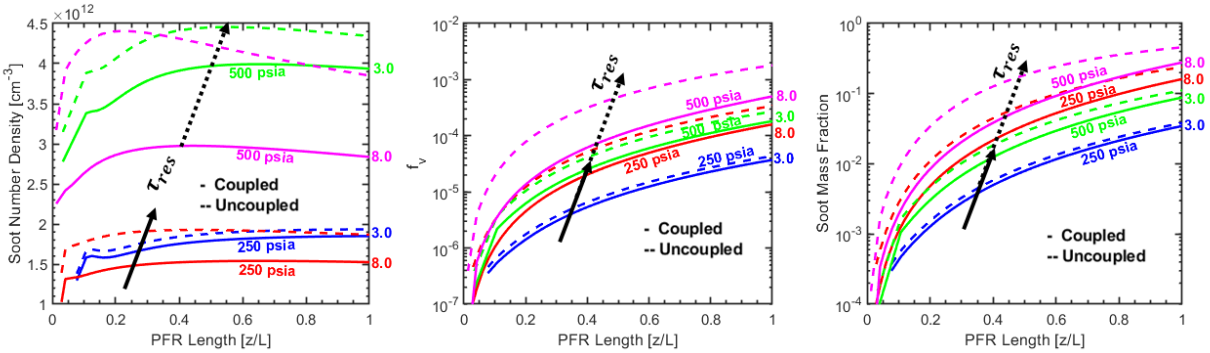

Figure 5.22 Effect of coupling soot to PFR on Soot Number Density [Left], Volume Fraction [Center] and Mass Fraction [Right] at a range of residence times and non-sooty pressure conditions of 250 psia, and 500 psia.

The gas solution in Figure 5.21 between the coupled and uncoupled PFR models shows little difference at small residence times – because the amount of soot formed is low, as shown in Figure 5.22. However, as both pressure and residence time increase, the amount of soot formed increases. As discussed in section 5.3.1, soot formation consumes gas moles to form solid phase soot, which produces a drop in pressure because of a decrease in gas density. There is also enthalpy

loss in forming soot and heat transfer between gas and soot phase. These effects become more noticeable in the gas phase as the amount of soot increases with higher pressure or residence time.

Coupling becomes important for predicting soot volume fractions as well as the amount of soot increases. As shown in Figure 5.21, the number densities, soot volume fractions, and mass fractions are higher for the uncoupled model for all conditions. This difference increases with both pressure and residence time. Consumption of gas phase species in forming soot, as well as gas enthalpy loss, results in smaller soot growth rates as the amount of soot increases. By not accounting for this decrease, the soot growth rates are higher in the uncoupled model. For small soot volume fractions, the error is not too significant. However, the volume fraction can be off by an order of magnitude at high pressure and residence time.

Furthermore, soot formation can contribute to considerable pressure drop in a combustion chamber. In a non-sooting environment, increased residence time allows for gas-phase reactions to approach closer to completion – which results in higher combustion performance and increased reactor pressure. The uncoupled approach predicts this behavior for the PFR, as shown in Figure 5.23. However, inclusion of soot formation in the gas-phase equations results in the opposite behavior and can produce large difference as the soot volume fractions increase at higher residence times - this prediction has been experimentally validated as discussed in section 5.5.1. Hence, not accounting for soot formation at fuel rich conditions can produce erroneous reactor pressure predictions at high pressure or long residence times.

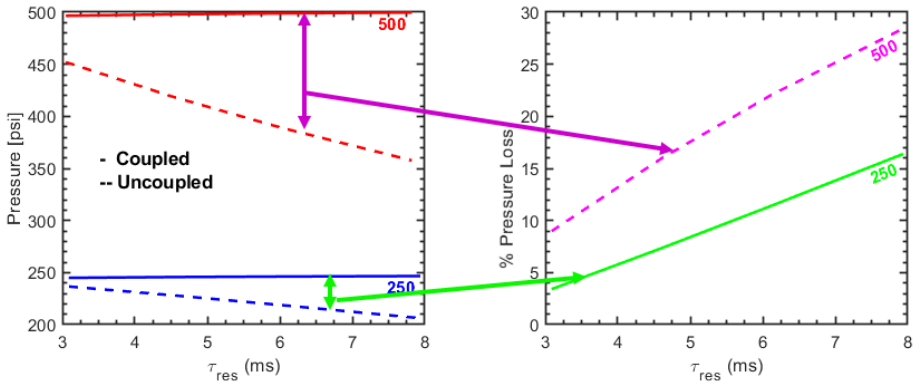

Figure 5.23 Effect of coupling soot to PFR on reactor pressure [Left] and percent pressure loss [Right] at a range of residence times and non-sooty pressure conditions of 250 psia, and 500 psia.

The effect of residence time on the coupled gas phase and soot particle solutions at larger number of conditions are shown in Figure 5.24 and Figure 5.25, respectively. These were run for the same conditions listed in Table 5.4. The pressure labels in the plot, correspond to the reactor pressure if no soot was formed at these conditions as listed in Table 5.4.

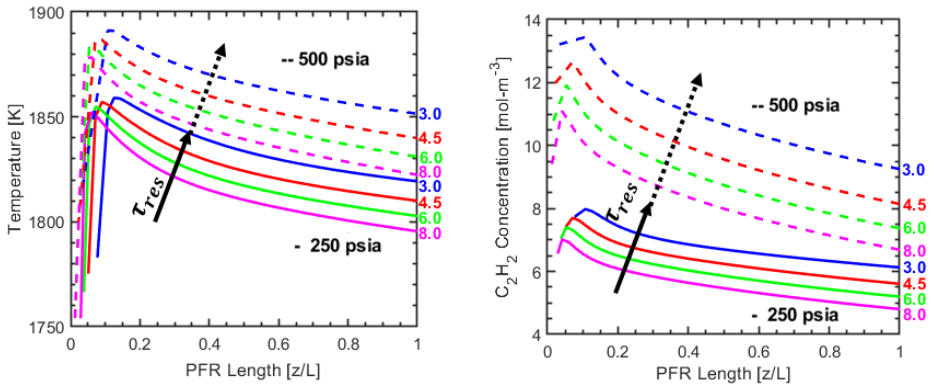

Figure 5.24 Predicted PFR Bulk Temperature [Left] and C_2H_2 [Right] Mass Fraction with soot formation at range of residence time conditions and non-sooty pressure conditions of 250 psia, and 500 psia.

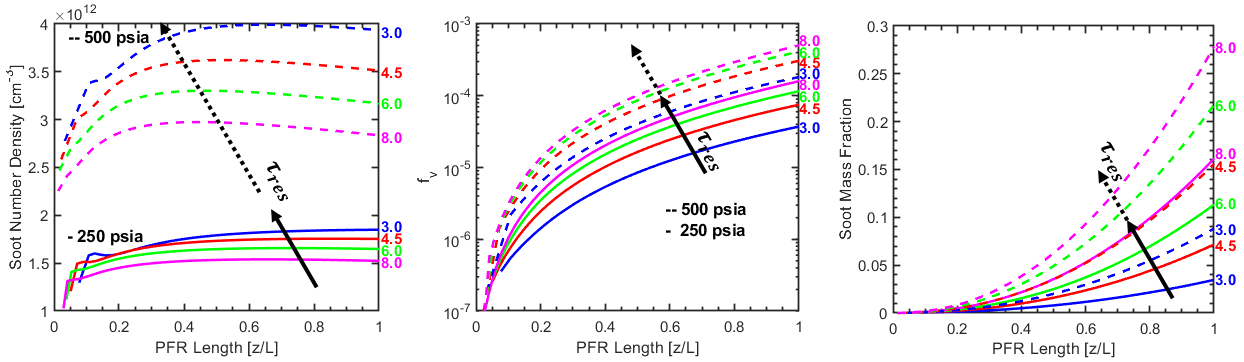

Figure 5.25 Soot Number Density [Left], Volume Fraction [Center] and Mass Fraction [Right] predicted with the coupled soot formation model at a range of residence time conditions and non-sooty pressure conditions of 250 psia, and 500 psia.

Residence time affects the amount of soot formed and in turn affects the gas phase. As discussed in the previous section, most of the soot mass at the high pressure arises from surface growth. As particles get larger, the reaction surface area increases, and this further drives the mass increase of soot particles. Higher residence times allow the surface growth reactions to occur for longer to form larger volume fractions. Increased residence time also results in larger soot particles due to coagulation of smaller particles – as evidenced by the drop in number density. The soot

volume and mass fractions increase by about an order of magnitude between residence time of 3 to 8 milliseconds. This physically results in large increase in soot for a reactor at 250 psia, and even higher at 500 psia - the soot can account for a significant amount of the reactor mass at longer residence times. This large amount of soot can significantly reduce gas temperatures and affect gas species concentrations. The overall effect of increased residence time in high pressure fuel rich combustion is it produces colder and denser flow – and decays engine performance by increasing pressure loss as shown in Figure 5.23.

The effect that residence time has on chamber wall deposition rates due to surface growth, thermophoretic diffusion, and Brownian diffusion was calculated with the PFR solution via the approach discussed in sections 3.5 and 3.7. Similarly to the approach discussed in the previous section, the soot growth rates due to heterogenous surface reactions were calculated by first integrating the solution from each WSR in a separate constant pressure reactor for a time equal to ten times the residence time of the PFR to account, in a very hand-wavy approach, for boundary layer effects. Afterwards, this solution was used in the surface growth reactor to calculate soot deposit growth flux. The thermophoretic and Brownian deposition rate fluxes were calculated directly with the plug flow reactor solution. Figure 5.26 shows the magnitude of the three different deposition mechanisms at a range of residence times; and Figure 5.27 shows a close-up of each mechanism.

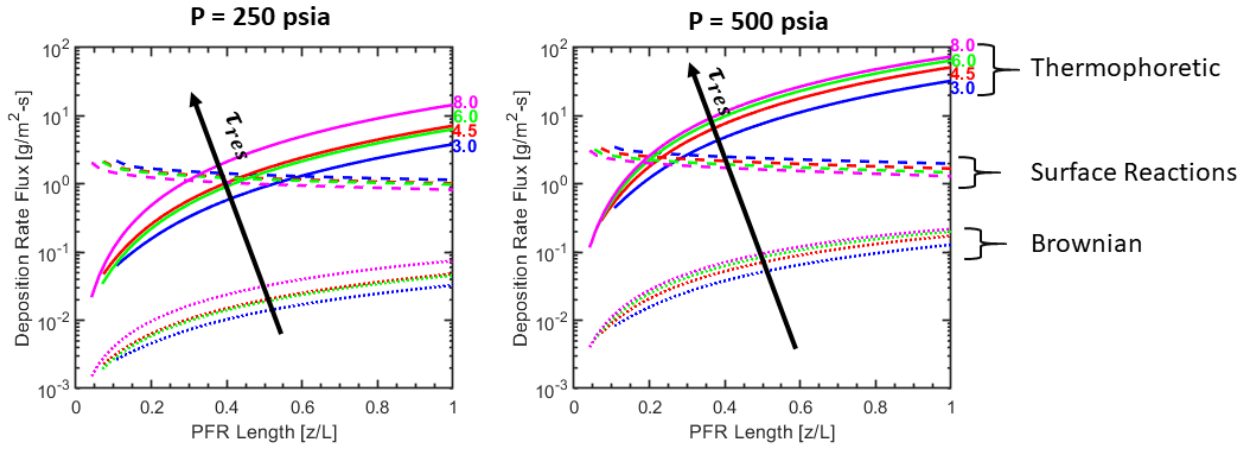

Figure 5.26 Predicted thermophoretic, surface reaction and Brownian contributions to total soot mass deposition rate at a constant wall temperature of 300 K at a range of residence time conditions (in milliseconds), and non-sooty pressure conditions of 250 psia, and 500 psia.

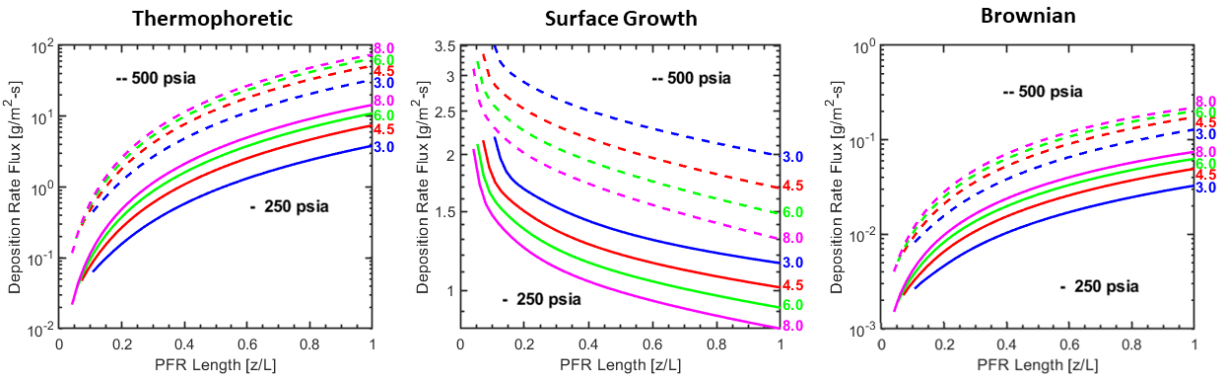

Figure 5.27 Predicted thermophoretic soot mass deposition rate at a wall temperature of 300 K [Left], surface growth [Center] and Brownian [Right] mass deposition rates at a range of residence time conditions (in milliseconds), and non-sooty pressure conditions of 250 psia, and 500 psia.

The predicted deposition results confirm the predictions from the previous section that thermophoresis is the dominant deposit mechanism and Brownian diffusion of soot to the chamber surface is negligible even at high residence times. Higher PFR residence times also produce higher deposits due to thermophoresis and Brownian diffusion because the amount of bulk soot increases with residence time as shown in Figure 5.25. Increased bulk soot also results in increased consumption of acetylene, as well as lower gas temperatures, and this decreases the rate of soot growth due to heterogenous surface growth reactions. Heterogenous reactions on the soot deposit surface can be an important source of soot growth and comparable to thermophoretic deposition at short residence times, however as residence times increase, it becomes overshadowed by thermophoretic deposition. Hence longer residence times are predicted to be dominated by thermophoretic deposits and produce significantly higher soot deposition because of higher soot volume fractions in the bulk flow.

The effect of coupling soot to the gas phase equations on deposit predictions was also explored to get an idea of how important it becomes with residence time. The results for the thermophoretic, surface growth and Brownian diffusion deposition rate fluxes between the coupled and uncoupled models are shown in Figure 5.28. Just like discussed in the previous section, soot coupling becomes important when the amount of soot formed becomes large. At small residence times of 3 milliseconds, the difference between coupled and uncoupled solution is not very significant – though it does increase with pressure. However, at higher residence times of 8 milliseconds, the difference becomes more substantial. Coupling reduces the thermophoretic deposit by about a factor of three at a pressure of 250 psia, and by an order of magnitude for the

500 psia case. The predicted surface growth and Brownian deposits are also lower for the coupled case, but these rates are small in comparison. Any error in predicting these deposits at larger residence times doesn't significantly affect the overall deposit predictions – even if these models were completely neglected.

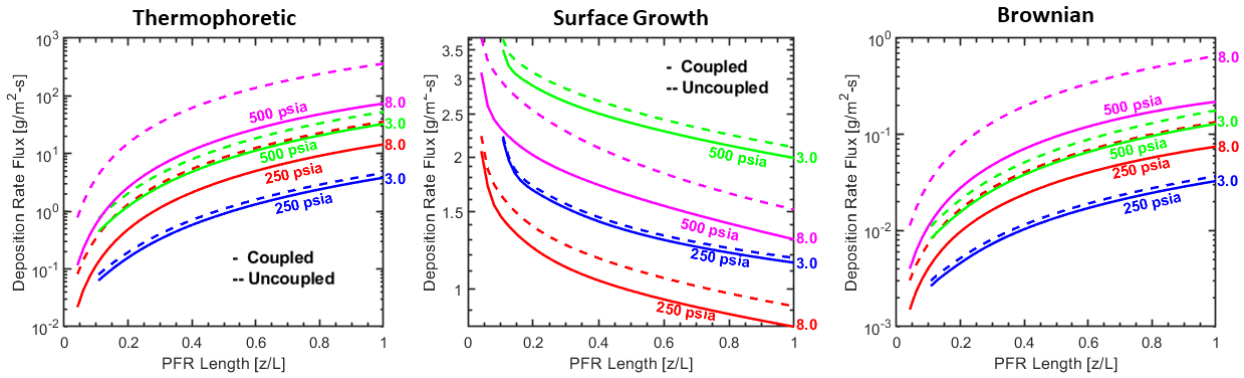

Figure 5.28 Effect of coupling soot to PFR on predicted soot mass deposition rate due to thermophoresis [Left], surface growth [center], and Brownian diffusion at a range of residence time conditions (in milliseconds), and non-sooty pressure conditions of 250 psia, and 500 psia.

5.4 Experimental Results

5.4.1 Experimental Conditions

The soot deposit experiment, that was discussed in chapter 4, was run to get model validation data. The experimental conditions are summarized in Table 5.5. The testing included running the combustor at a range of pressure conditions but at roughly constant residence times – for test #: 1,2,6,7; and roughly the same pressure condition but at variable residence times – for test #: 1,2,4,5,10. Additionally, two different sample materials were used to verify the effect of wall temperature on carbon deposits – for test #: 1,2,3,8. The same chamber configuration, with a total chamber length of 9.2 inch, was used for all the tests except for the last two. Test #9 was run to verify the prediction that soot formation is negligible at ambient combustion conditions and was run without a choke plate. Test #10 was run at the same conditions as test #1,2 but with a chamber extension – extending the chamber length to 13.8 inch.

Table 5.5. Soot Experiment Test Matrix

Test #	**Sample Material**	**Target Pressure* (psia)**	**Target Propellant Flow Rate (g/s)**		**τ_{res}** (ms)**	**Choke Plate Diameter (in)**
			GOx	**RP-2**		
1	Cu	250	30	30	6.1	0.312
2	Cu	250	30	30	6.1	0.312
3	SS	250	30	30	6.1	0.312
4	Cu	250	25	25	7.3	0.281
5	Cu	250	42	42	4.2	0.367
6	Cu	150	18	18	6.1	0.312
7	Cu	350	42.5	42.5	6.1	0.312
8	SS	250	30	30	6.1	0.312
9	Cu	14.7	30	30	Small	Open Chamber
10	Cu	250	30	30	9.2	0.312

* Target Pressure w/o torch Purge Flow, purge flow adds extra mass flow and increases chamber pressure – calculated assuming no soot formation and equilibrium conditions

** Residence time calculated assuming equilibrium conditions within the chamber, non-equilibrium and soot formation can slightly affect residence time.

These conditions were run with the feed system configuration shown in Table 5.6. All the flow parameters were the same, except for discharge coefficient of the RP-2 Venturi. The discharge coefficient varied by ~0.005 between the lowest and highest flow conditions in the test series as measured by waterflow test. The feed pressures to supply the required mass flow rates in Table 5.5 were set the values listed in Table 5.7.

Table 5.6 Soot Experiment Feed System Configuration and Venturi/Torch Injector Discharge Coefficients

Test #	Main GOx		Main RP-2	
	A_t (in)	C_d*	A_t (in)	C_d
1	0.088	0.985	0.018	0.986
2	0.088	0.985	0.018	0.986
3	0.088	0.985	0.018	0.986
4	0.088	0.985	0.018	0.988
5	0.088	0.985	0.018	0.983
6	0.088	0.985	0.018	0.988
7	0.088	0.985	0.018	0.983
8	0.088	0.985	0.018	0.986
9	0.088	0.985	0.018	0.986
10	0.088	0.985	0.018	0.986

* Discharge coefficient assumed based on Flowmaxx venturi vendor information

Table 5.7 Feed Pressures in the Soot Experiment

Test #	Set Pressures	
	GOx	RP-2
1	470	985
2	470	985
3	470	985
4	385	684
5	645	1931
6	385	365
7	646	1977
8	470	985
9	470	985
10	470	985

5.4.2 Experimental Bulk Pressure Measurements

The chamber pressure measurements for all the experimental test conditions are shown in Figure 5.29. All the test conditions showed a spike in chamber pressure when the torch igniter was turned on, and then a slight overpressure after ignition due to both torch and main propellant flow before dropping off once the torch was turned off. Test #6 did not show an overpressure because ignition occurred right as the torch was turned off. Additionally, the chamber pressure reading showed some initial transients before approaching a steadier reading. This transient was mostly traced back to the ER3000 GOx pressure regulator. As described in section 4.5, the ER regulator required tuning the PID controller to provide a smooth pressure response. The regulator was also designed for operation at much higher flowrates compared to this experiment - where the flow rate response to pressure is less sensitive. Due to the smaller flowrates in this experiment, a small pressure difference created a larger percent difference in the flow rate. This in turned affected the amount of flow delivered to the combustion chamber and thus the chamber pressure. This effect was evident in most of the tests, however the ER3000 response stabilized after a few seconds to deliver a steadier response.

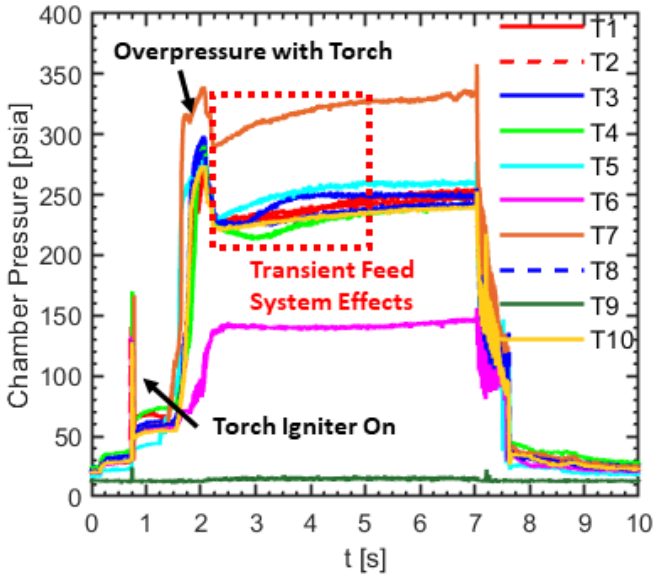

Figure 5.29 Measured chamber pressure for all the experimental conditions in the experimental combustor

The RP-2 and GOx mass flow rates that were delivered to the chamber during each hot-fire were calculated with the critical flow and cavitating venturi equations discussed in section 4.5.1 with the measured upstream venturi pressure and temperature. Figure 5.30 plots the calculated mass flow rates for all the tests and the injected mixture ratio. All the tests also had a nitrogen torch purge on for the entire duration – with the purge flow limited at the torch oxygen injector and the hydrogen orifice. Unfortunately, no temperature or pressure measurements were taken upstream of the restrictions to calculate the actual delivered nitrogen purge mass flow rate. Instead, the mass flow was estimated with the compressible 1-D mass flow relation based on the injector properties and set pressures shown in Table 5.6 and Table 5.7. As a verification, the torch chamber pressure was estimated from the estimated nitrogen mass flowrates and compared with the measured torch igniter chamber pressure at the beginning of the hotfire – when only the purges were flowing. The predicted chamber pressures with purge on agreed with the measured chamber pressure for all the tests.

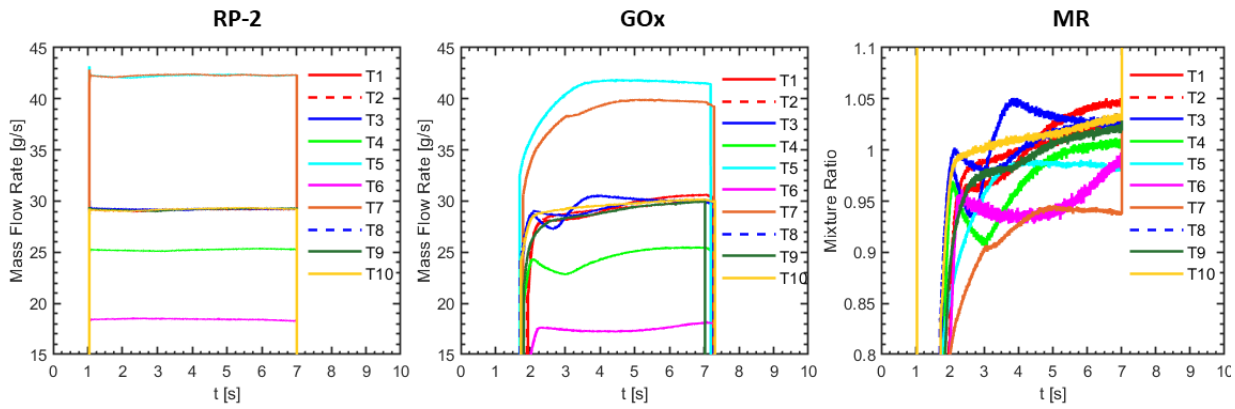

Figure 5.30 RP-2 [Left] and GOx [Center] mass flows and overall injected mixture ratio [Right] for all the test conditions calculated with the upstream venturi pressure and temperature measurements

As mentioned, the GOx ER3000 regulator tuning affected the response of the GOx flowrate. This is evident in the center of Figure 5.30, where the GOx flow rate takes a few seconds to reach a steady value. The RP-2 flow rate was regulated with an ER3000 as well, however, the density of RP-2 is orders of magnitude higher than GOx and the mass flow rate response is in turn less sensitive to small variations in pressure. As such, the RP-2 ER regulator provided a smoother flow rate response. Due to differences in the two propellant responses, the mixture ratio delivered to the chamber was not completely consistent for the first few seconds, as shown on the right of Figure 5.30. This transient response made comparison with the soot model more difficult. To simplify this effort, the mass flow rates of RP-2 and GOX were averaged for the last second of run time – from 6 to 7 seconds. These averaged values, shown in Figure 5.8, were then used as inputs for modeling the experiment.

Table 5.8 Averaged Propellant Injection Flow Rates from experimental measurements

Test #	RP-2 Mass Flow Rate (g/s)	GOx Mass Flow Rate (g/s)	Mixture Ratio
1	29.2	30.5	1.04
2	29.2	29.9	1.03
3	29.2	30	1.03
4	25.3	25.4	1.01
5	42.3	41.6	0.98
6	18.3	17.9	0.98
7	42.3	39.8	0.94
8	29.2	30.1	1.03
9	29.3	29.8	1.02
10	29.2	30.1	1.03

Snapshots from recorded test video for test #1 and test #9 are shown in Figure 5.31 and Figure 5.32, respectively. The amount of soot formed between each test was significantly different. The higher-pressure conditions in test #1 produced greater amount of soot and chamber deposit compared to the open chamber ambient pressure conditions in Test #9. Test #9 was run with the torch turned on for the entire duration to prevent blowout. This test was predicted to produce very little soot and to potentially damage the stainless-steel combustion chamber – both predictions were verified. As seen in Figure 5.32, there is no indication of dark sooty smoke but there is a light blue color in the flame indicating burning of stainless steel chamber – an indication verified by inspection of the hardware post-test.

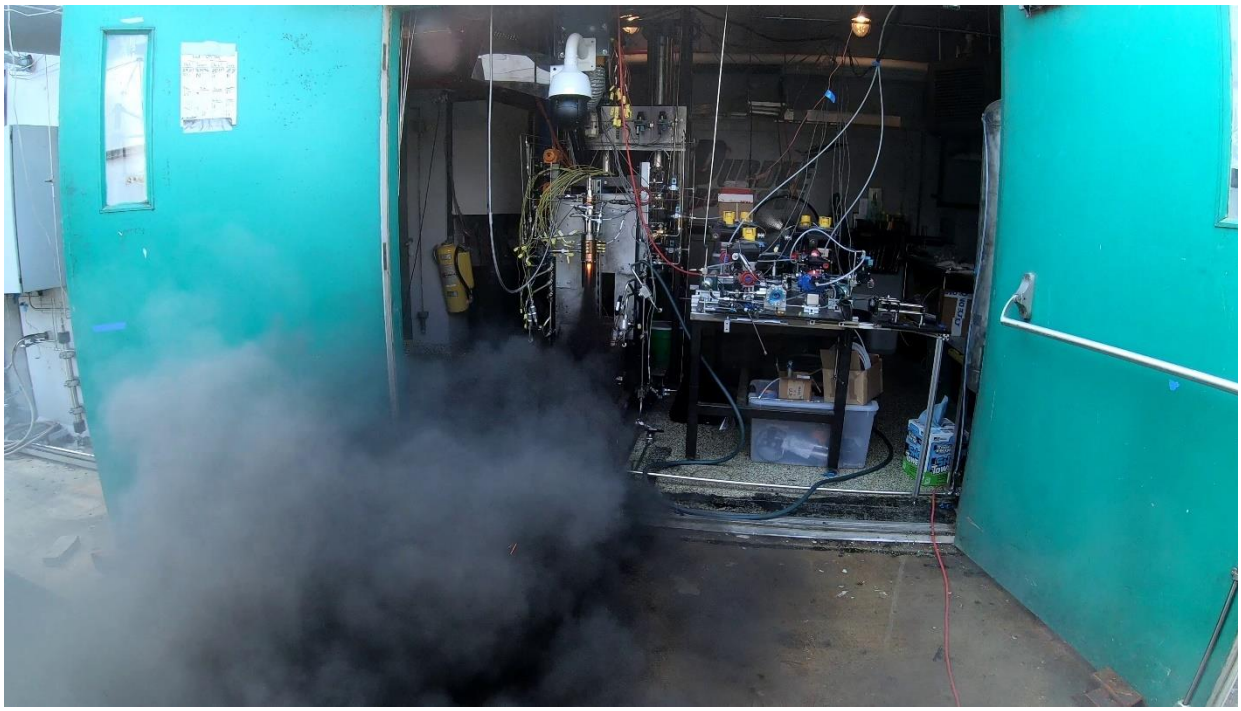

Figure 5.31 Test #1 showing a thick sooty exhaust from the very fuel rich combustion regime

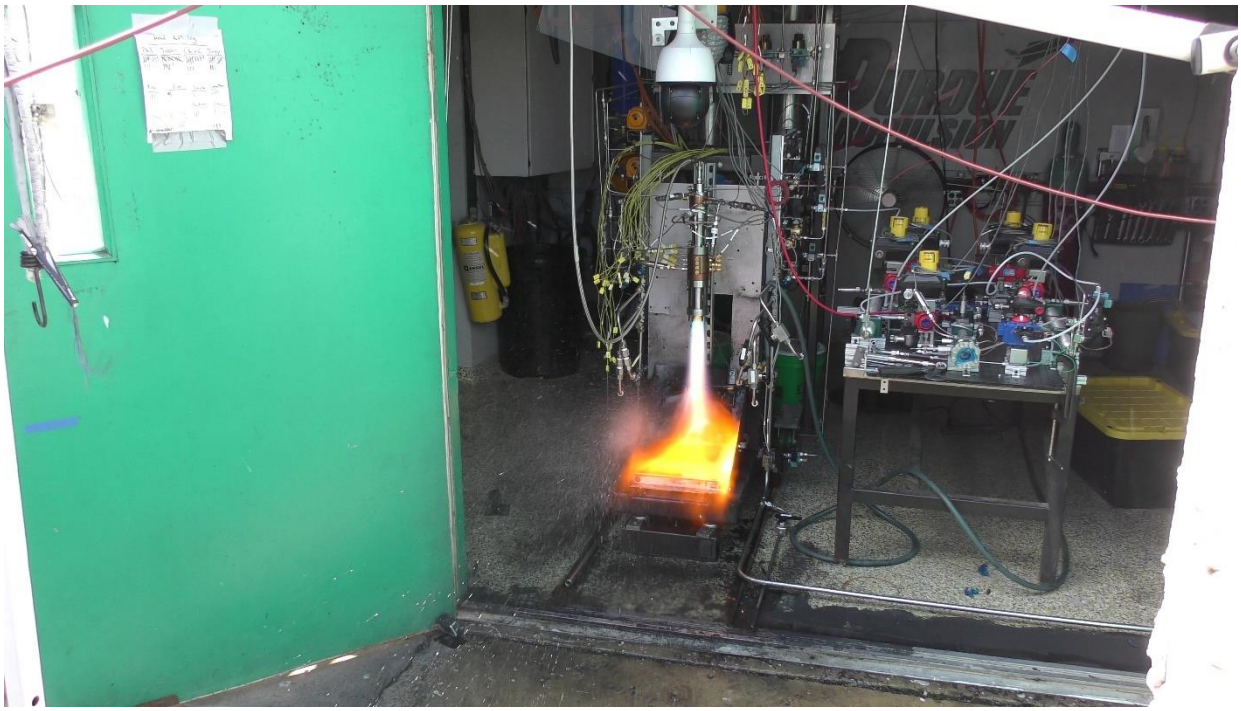

Figure 5.32 Test #9 showing a much cleaner flame with no thick soot production – and some hardware rich burning of the stainless-steel combustion chamber due to higher heat fluxes

5.4.3 Sample post-processing

Ten tests were run to get soot deposit mass and thickness measurements at the different conditions. The bulk soot deposit mass was obtained with a very simple method- by measuring the mass of the sample tube before and after the hot fire. These sample measurements for all the test conditions are shown in Table 5.9.

Table 5.9 Sample Mass Measurements

Test #	Initial Mass (g)	Post-test Mass (g)	Δmass (g)
1	92.78	93.23	0.45
2	91.92	92.35	0.43
3	82.66	83.02	0.36
4	92.28	92.79	0.51
5	92.68	93.03	0.35
6	92.98	93.11	0.13
7	92.48	93.23	0.75
8	81.95	82.33	0.38
9	92.73	92.70	-0.03
10	92.82	93.05	0.23

Measuring the deposit thickness was more involved, as shown in Figure 5.33. The sample tube was first cut into 4x6 sextant sections with a rotary cutter at a slow speed setting with 30 second cutting increments within a 5-minute interval in order to reduce disruption to the soot deposit or excessive heating of the sample tube. Each copper tube took about 3-4 hours to cut, and the stainless-steel tubes took twice as long. Once cut, the surface of each sample was scratched tangentially with a metallic razer, in order to reveal the chamber surface for comparing deposit thickness to. The samples were then imaged with the Zygo Zegage optical profilometer to generate an XYZ height-map. The image scan required running with dual light, with the exposure calibrated to a dark soot location and to the exposed copper surface in order to properly capture the soot surface.

Since the sample was not flat, sample curvature needed to be considered to accurately determine the soot thickness from the measured XYZ height-map. A Matlab code was written to

post-process this data further. The code first found the location of the tangential razer cut path via a simple optimization approach. First the minimum z-height at every y-slice of the image was located via the Matlab findpeaks function. Then a line was fit to all these points. Afterwards, the image was swept through each y-slice again, except now several candidate valley points in the image were found with the findpeaks function. Then the valley points closest to the fitted line were selected. If the new set of points after the sweep was the same as before, these were assumed to be the points on the razer line. Otherwise, this process was repeated until the points did not change with iteration. Once the razer points were located, they were fit to a convex quadric surface in the form of:

$$\begin{bmatrix} x \\ y \end{bmatrix} = \begin{bmatrix} ax^2 + by^2 + cxy + dx + ey + g \\ ax^2 + by^2 + cxy + dx + ey + g \end{bmatrix} \quad 5.7$$

The fitted surface was assumed to be equal to the metal sample surface and hence formed a reference surface to which soot deposit could be compared to. The profilometer z-coordinates were subtracted from the reference surface to flatten the image and generate a height map –the sample curvature effects were subtracted. The last part involved manually selecting regions on the height map and averaging the heights in the region. This averaged height was then compared with the soot deposit model predictions.

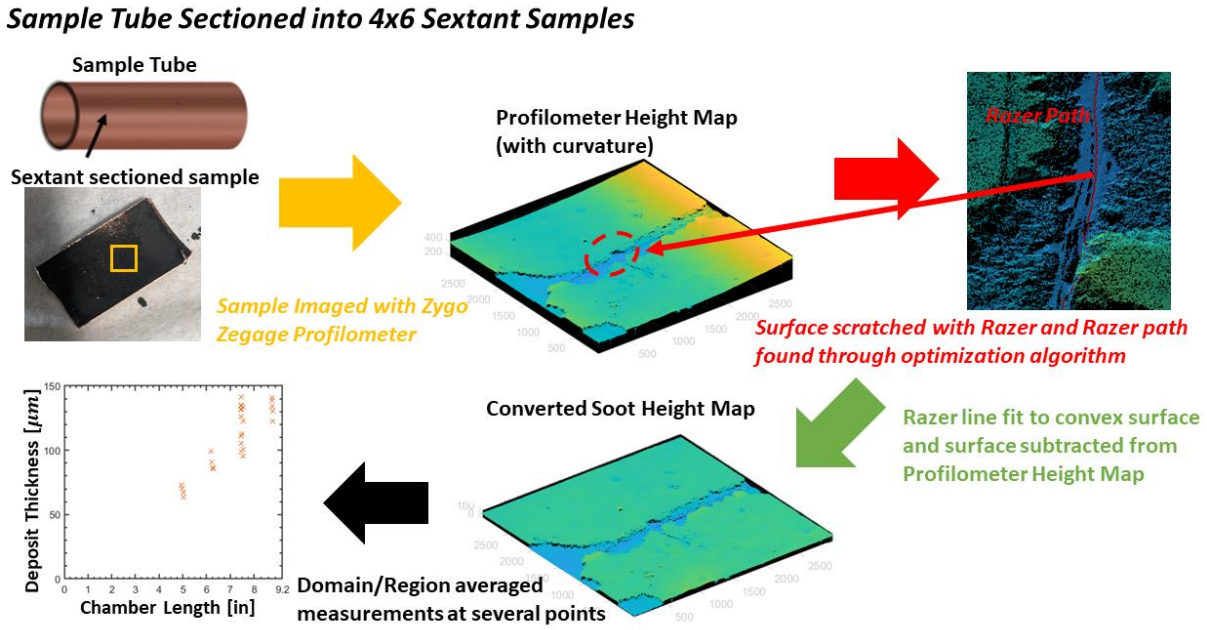

Figure 5.33 Soot profilometry procedure

5.4.4 Heat Flux Estimation

The sample backwall temperature was measured in all the tests, from which the heat flux was estimated via solution of the inverse heat transfer problem with several simplifying assumptions. The approach to solving the inverse heat transfer problem could be summarized as a guess and check, where the heat flux was guessed at the inner sample wall and then the heat diffusion equation solved to predict the backwall temperature. If the predicted temperature was lower, then the value of the heat flux guess was increased or vice versa. In this guess and check approach, heat transfer was assumed to be purely one-dimensional. This is computationally cheaper than solving a 2-D or 3-D inverse problem but introduces a potential source of error. Furthermore, perfect contact was assumed between the thermocouple in the experiment and the outer sample wall. Loctite anti-seize was applied to the tip of the thermocouple to improve contact with the outer chamber wall, however this contact resistance was not quantified. Assuming perfect contact is a simplification but produces a lower heat flux estimate than in reality. The thermal conductivity, density and specific heat property values for the stainless steel and copper samples were the same as discussed in section 4.2.1. With these assumptions, the thermal model was setup as shown in Figure 5.34 and the cylindrical form of the heat diffusion equation solved:

$$\frac{1}{r}\frac{\partial}{\partial r}\left(k(T)r\frac{\partial T}{\partial r}\right) = \rho c_p(T)\frac{\partial T}{\partial t} \tag{5.8}$$

With the following boundary conditions:

$$-k\frac{\partial T}{\partial r}\Big|_{\substack{inner\\wall}} = \dot{Q}''? \tag{5.9}$$

$$-k\frac{\partial T}{\partial r}\Big|_{\substack{outer\\wall}} = h_{out}\left(T_{\substack{outer\\wall}} - T_\infty\right) \tag{5.10}$$

Where the inner wall heat flux value was unknown and guessed, whereas the outer wall assumed a heat transfer coefficient of 10 $\frac{W}{m-k}$ for stagnant air and temperature of 300 K.

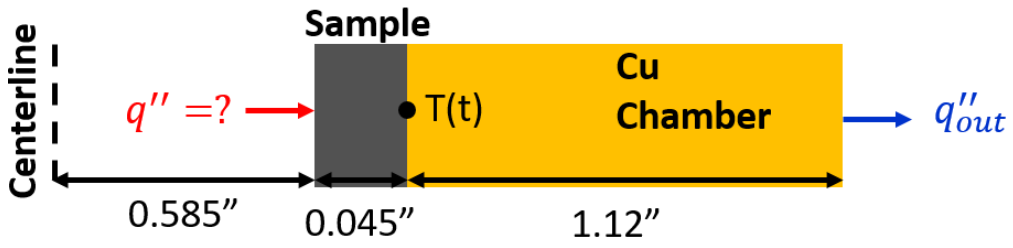

Figure 5.34 Inverse heat transfer problem setup for estimating heat flux in experiment

The heat diffusion equation was solved with the Matlab partial differential equation toolbox with the pdepe solver [129]. The model was written to accept a heat flux input at every 0.1 seconds and output a temperature response. The Matlab nonlinear least-squares lsqnonlin function was then used to find the heat flux values that matched the experimental temperature at every 0.1 seconds. There are probably more efficient and much faster methods for solving this problem. However, this approach was easy to code without requiring extensive research into inverse heat flux methods. It took about 4 hours on 6 cpu cores to find the optimal heat flux values starting with an initial heat flux guess of 1 MW. Better initial guesses decreased the run time by more than half.

The inverse heat transfer problem was solved for the 250 psia nominal chamber pressure condition for both the copper and stainless-steel samples. The results are shown in Figure 5.35. The predicted heat-flux shows a large spike around two seconds for both cases before dropping off. This occurred when the torch and main propellants were on but then dropped off as soon as the torch was turned off. This heat flux produced a temperature history at the outer sample wall that matched the experimentally measured temperature as shown on the right of Figure 5.35. As expected, the stainless-steel wall temperatures were higher than copper because of differences in thermal conductivity. However, it was interesting to see the heat flux decay with time – a result of soot deposition on the inner chamber wall. Furthermore, the decrease in heat flux was more significant than originally predicted. As discussed in section 4.4.4, the original heat transfer analysis for chamber design assumed dense soot deposits and in turn only produce a small effect on deposit. The experimental results though showed a much larger decrease in heat flux, suggesting the deposits were highly porous.

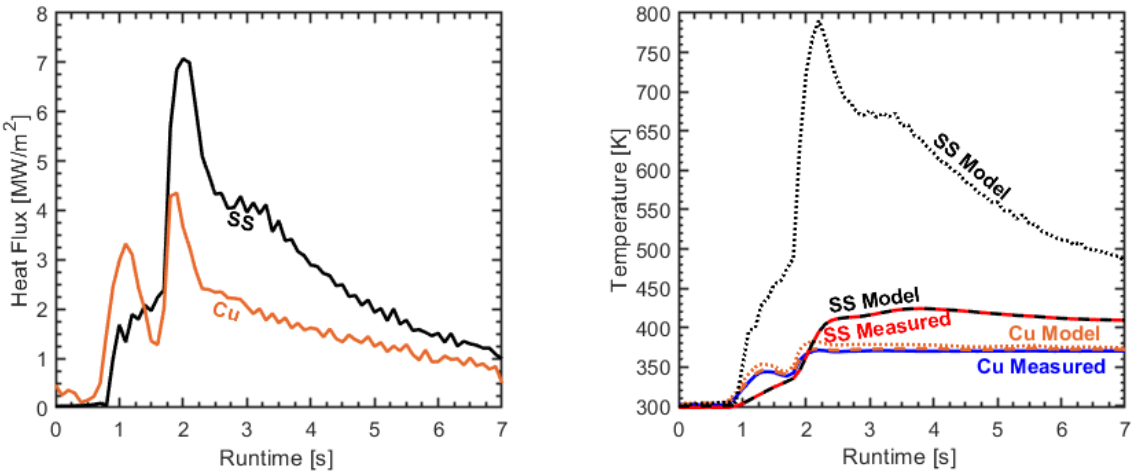

Figure 5.35 Predicted heat flux [Left] for copper and stainless steel samples and the calculated inner and outer wall surface temperatures [Right].

The increase in thermal resistance due to soot deposition was estimated from the inverse heat transfer solution. The resistance was estimated based on plug flow reactor bulk gas temperature T_g, the inverse heat flux calculated surface temperature T_w and the calculated heat flux q'' as shown:

$$R_{experiment} = \frac{T_g - T_w}{q''} \tag{5.11}$$

In addition, the thermal resistance was also estimated purely from the 1-D plug flow reactor soot model based on initial inner wall radius r_w, soot deposition rate $\dot{t}_{soot}$, and thermal conductivity of the soot deposit $k_{deposit}$:

$$R_{deposit} = \frac{r_w - \dot{t}_{soot}}{k_{deposit}} ln\left(\frac{r_w}{r_w - \dot{t}_{soot}}\right) \tag{5.12}$$

The thermal resistance from the model in equation 5.12 was calculated with a deposit conductivity of 0.5 W/m-K, and with a conductivity adjusted to match the predicted resistance from equation 5.11. As shown in Figure 5.36, the deposit conductivity that results in a solution close to that predicted with equation 5.11 was an order of magnitude smaller than conductivity of the soot particle. The most likely explanation for this result was the deposit was highly porous and contained trapped gas that had a lower conductivity than the soot particles.

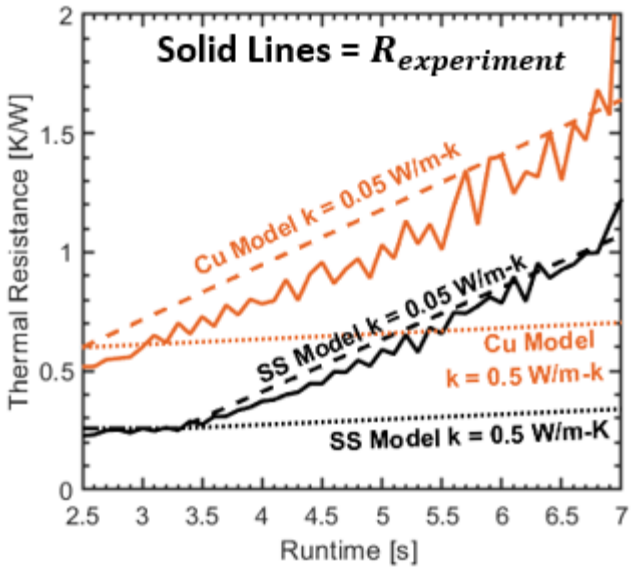

Figure 5.36 Thermal resistance predictions during

The porosity from the thermal calculation resistance was estimated from relation for equivalent gas conductivity in porous materials [180,181]:

$$k_{deposit} = k_{soot}\left[(1+\epsilon)^{1.5} + \epsilon^{0.25}\frac{k_{gas}}{k_{soot}}\right] \quad 5.13$$

Where the equivalent deposit conductivity $k_{deposit}$ is a function of the soot porosity ϵ, soot conductivity k_{soot} and porous gas conductivity k_{gas}. The porous gas conductivity was calculated from the transport properties of the HyChem POSF5433 mechanism. The resulting porosity was estimated to be about 90% porous. However, this value was not experimentally verified. It would be beneficial to measure soot porosity in future investigations.

5.5 Numerical and Experimental Comparison

5.5.1 Bulk Pressure Comparison

The bulk PFR pressure predictions were verified with the measured chamber pressure from all the experimental tests. As discussed in section 5.3, soot formation results in a chamber pressure loss because gas moles get converted to solid phase soot. Higher pressure and higher chamber residence times conditions are predicted to result in higher pressure loss because of increased soot formation, as shown in Figure 5.13 and Figure 5.23. These predictions were verified with the bulk

chamber pressure measurements, which were averaged for the last second of RP-2/GOx flow. The PFR model was run assuming adiabatic conditions with the propellant mass flows shown in Table 5.8. Additionally, the discharge coefficient of the choke plate exit was set to 0.95 to account for nozzle losses based on the simulation results of Sabirzyanov et al. [182]. Comparison of measured results with the model predictions are shown in Figure 5.37.

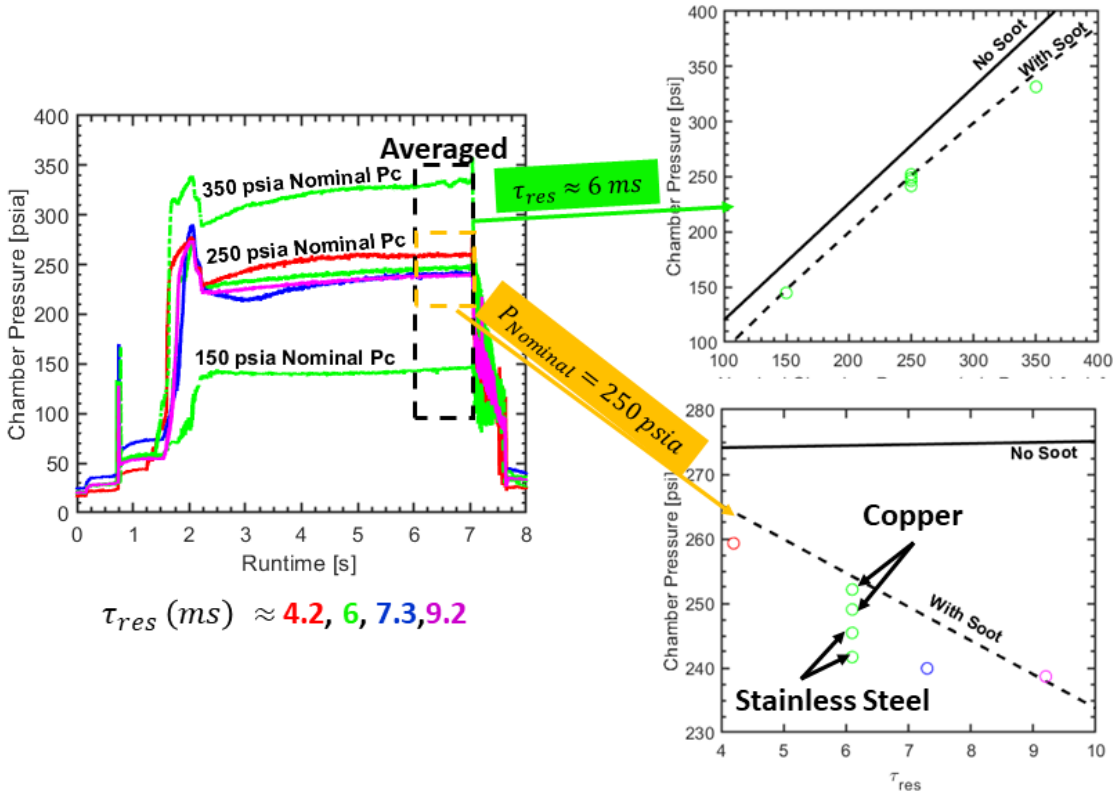

Figure 5.37 Comparison between measured chamber pressure reading and predicted with 1-D Plug Flow Reactor Model at different pressure and residence time conditions. The experimental pressure readings were averaged for the last second before shutdown for model comparison.

The measured chamber pressure readings match the pressure and residence time trends predicted by the sooty PFR model. The measured chamber pressure is lower than calculated for pure gas-flow with no soot formation, with the difference increasing with pressure and residence time. This is due to a higher amount of soot formed, as discussed in section 5.3.

Differences between the model and measurements are likely due to a few reasons. First, the model assumes perfect mixing in the radial direction and the conditions in the chamber may not have been as well mixed or axisymmetric. However, an even larger reason was likely the model assumed adiabatic boundary conditions for simplicity, whereas heat transfer to the walls was likely

important. Modeling the heat transfer accurately would require solving conjugate heat transfer and considering the effect that soot deposit has on heat flux – which section 5.4.4 has shown is important. This could be a future work item. Furthermore, another significant source of error was the torch igniter nitrogen purge. The nitrogen purge set pressures were sized such that the same percent of purge flow would flow in all the different conditions – with less purge for the lower RP-2/GOx flow rates and vice versa. The purges were limited by the torch gaseous oxygen injector and hydrogen orifice. However, the pressure upstream of these flow limiting devices was not measured during the testing as it was not thought to be a necessary measurement during the experiment design or test readiness review. Later modeling though showed that this difference could potentially impact the chamber pressure reading and it is possible that less purge flowed than modeled due to droop– leading to a higher predicted chamber pressure. Future experiments with a similar combustor should measure the purge flow in order to more accurately estimate the total mass injected into the chamber. The measured chamber pressure readings with the stainless-steel samples also showed slightly smaller measured chamber pressure readings compared to copper. This was thought to be due to variations in the experiment or to higher heat loss with the stainless-steel sample. Higher heat loss in the stainless sample doesn't make sense at first since stainless has a lower thermal conductivity, however if soot deposits were lower on stainless, then the heat loss to the wall could be higher. Section 5.5.2 verified that deposits are lower on stainless steel. But this difference during the short duration test sequence is likely small and the most likely suspected cause is variability in the experiment.

5.5.2 Soot Deposit Thickness Comparison

Soot deposit mass and thickness measurements were obtained at the different experimental conditions as discussed in section 5.4.3. These measurements were compared with soot deposit predictions from the sooty plug flow reactor model. Deposit thickness and bulk mass comparison with test #1 and test #3, which ran at the same operating conditions but used different sample materials, are shown in Figure 5.38 and Figure 5.39, respectively. Comparison of deposit thickness at variable pressure at constant residence time, and variable residence time at similar pressure conditions are shown in Figure 5.40 and Figure 5.41, respectively. Bulk deposit mass comparison between the experiment and model are shown in Figure 5.42. Even though the reactor solution was

run as adiabatic, the thermophoretic calculations were done with a wall temperature equal to the average inner wall temperature calculated from the inverse heat transfer solution.

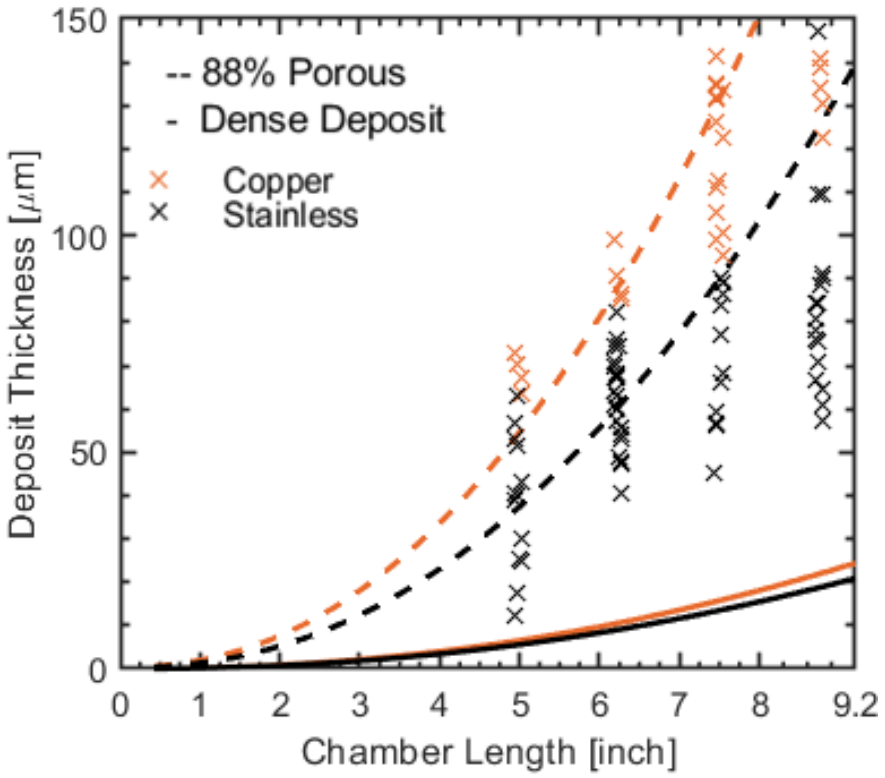

Figure 5.38 Comparison of measured soot deposit thickness on **stainless steel** and **copper** samples with soot plug flow reactor model, assuming both dense ($\rho_s = 1800\,\frac{kg}{m^3}$) and 88% porous deposits

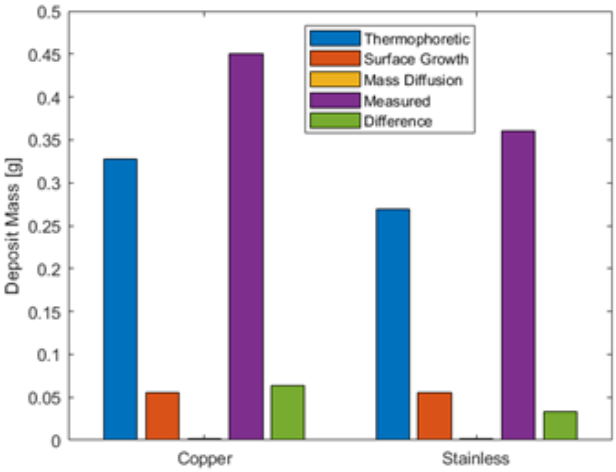

Figure 5.39 Comparison of predicted soot deposit masses from thermophoretic, surface growth, and mass diffusion on copper and stainless steel with bulk sample measurement

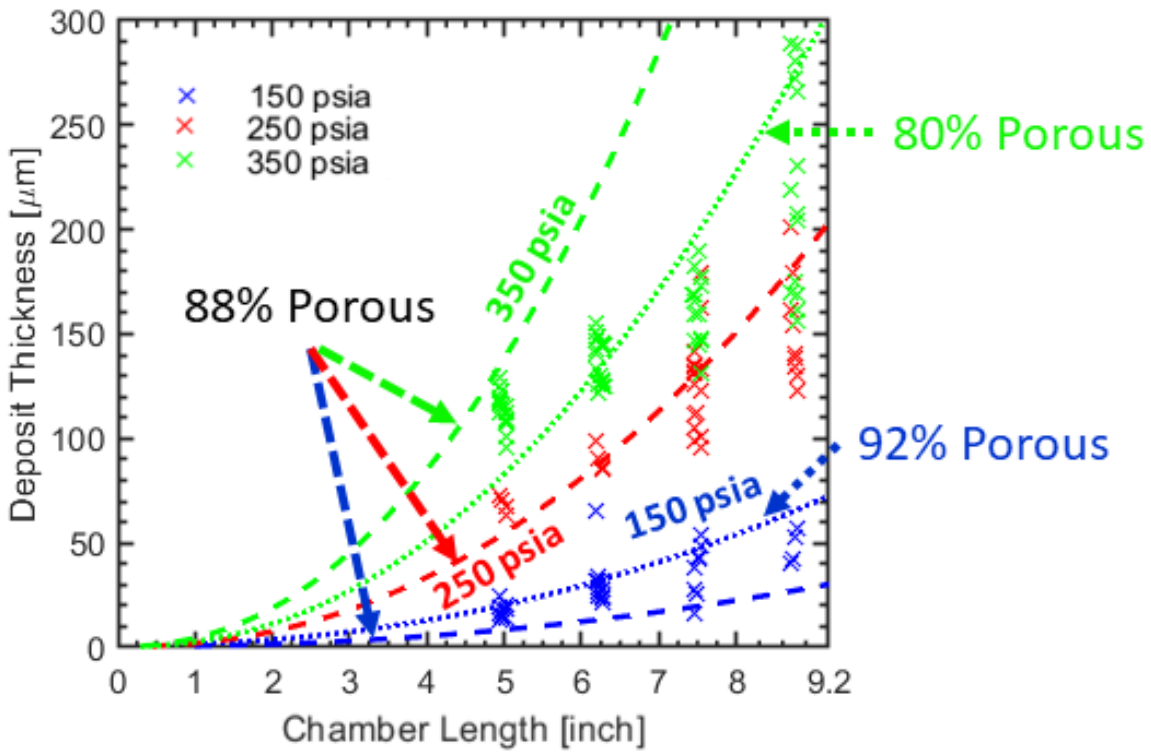

Figure 5.40 Comparison of measured soot deposit thickness at **150 psia**, **250 psia**, and **350 psia** with soot plug flow reactor model, with porosity tuned to match experimental data.

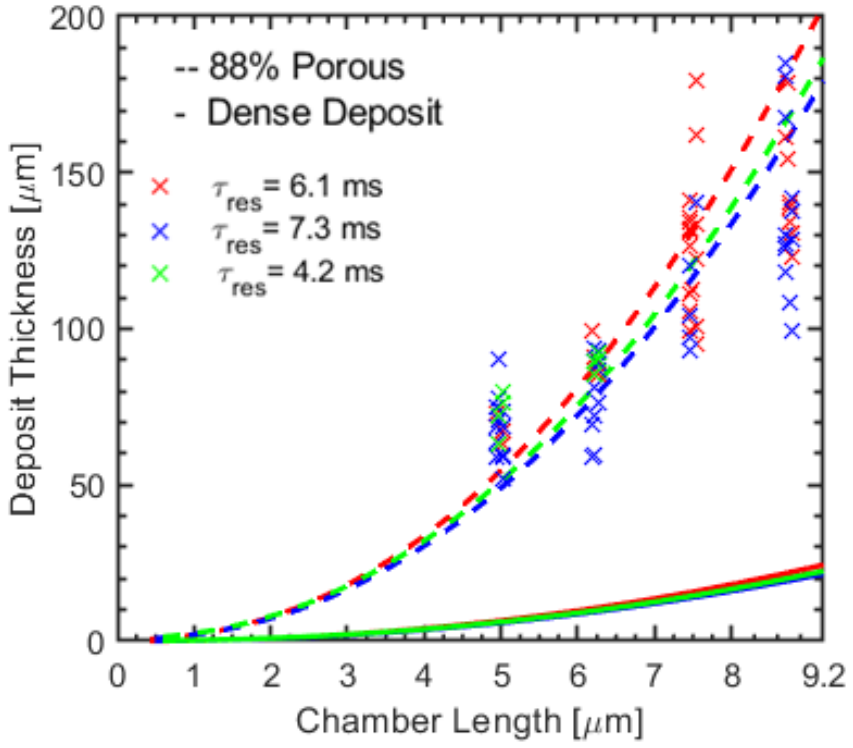

Figure 5.41 Comparison of measured soot deposit thickness at **7.3 ms**, **6.1 ms**, and **4.2 ms** residence time conditions with soot plug flow reactor model, assuming both dense ($\rho_s = 1800 \frac{kg}{m^3}$) and 88% porous deposits

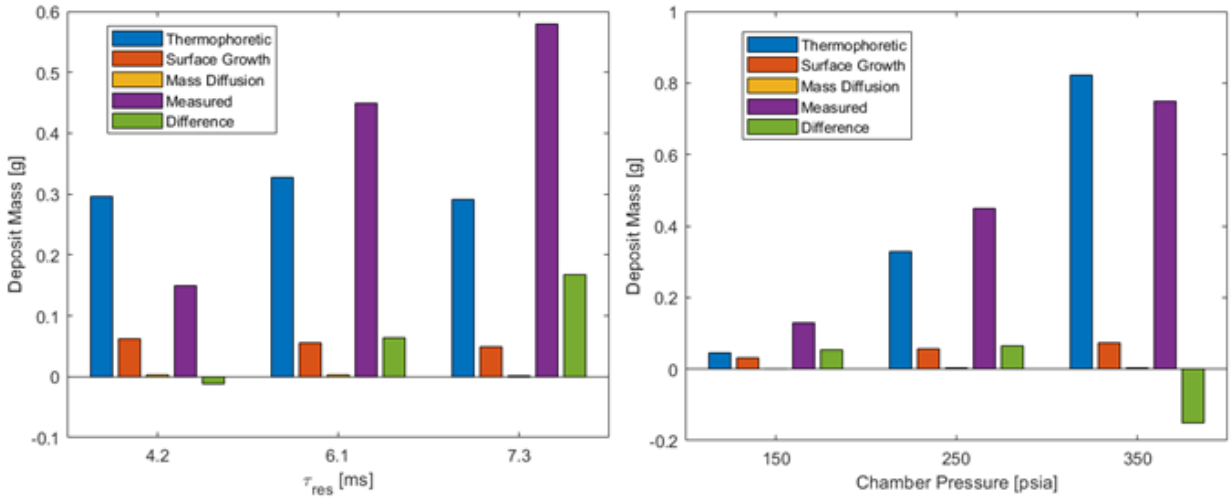

Figure 5.42 Comparison of predicted soot deposit masses from thermophoretic, surface growth, and mass diffusion with bulk sample measurement for variable residence time [Left] and variable pressure [Right] conditions.

Comparison of the deposit measurements on the stainless steel and copper samples, at the same operating conditions, showed copper to have a higher deposit as evidenced in Figure 5.38. The primary difference between these two tests is copper has a higher thermal conductivity – which resulted in a lower inner wall temperature as discussed in section 5.4.4. The lower wall temperature creates a larger near wall temperature gradient and induces a higher thermophoretic force. The experiment agreed with the predicted trend in the PFR model. In the model, the copper wall temperature was assumed to be at a constant 400 K and the stainless steel assumed to be 650 K, which was estimated to be the average sample inner wall temperature during the experiment duration from the inverse heat transfer solution. However, something that was not directly predictable by the model is the deposit porosity. As shown in Figure 5.38, porosity has a significant effect on soot deposit thickness. Though the copper sample was still predicted to have higher soot deposit than stainless steel, the predicted thickness is significantly lower than measured if a dense soot deposit is assumed - with density equal to 1800 $\frac{kg}{m^3}$. Setting the porosity to 88%, effectively assuming an average density of 216 $\frac{kg}{m^3}$ for the soot, provided better model prediction. This porosity agrees with the heat transfer results in section 5.4.4 as well as from internal discussion on an Air Force STTR Phase II carbon deposition project. It would be valuable though for future investigations to experimentally measure the porosity and develop a sub model for predicting the it since it's a critical parameter to accurately model deposit thickness.

In contrast to thickness comparison, the predicted bulk deposit mass due to thermophoresis, surface growth and mass diffusion on both samples was lower than measured by about 30%. This suggested that another deposition mechanism may be present that had not been considered. The difference in the deposit mass was lower on stainless, which was predicted to have a higher inner wall temperature, suggesting the missing mechanism has some temperature dependence. A likely culprit was thought to be condensation of heavy PAH's such as pyrene. Modeling this deposition mechanism was briefly investigated but not included in the current model due to several numerical related difficulties. Section 6.2.1 discusses this further.

The effect of pressure on soot deposition was subsequently investigated and compared with the model. As shown in Figure 5.40, higher pressure produced larger soot deposit thickness. This trend matched model predicts for all the tested pressure conditions. However, the results showed that a 12% porosity, which provided good agreement for the 250 psia case, underpredicted the soot

thickness at 150 psia and overpredicted for the 350 psia case. Manually tuning the porosity to 8% and 20% for the 150 psia and 350 psia cases, respectively, provided better agreement. This suggested that porosity is pressure dependent and decreases with pressure. The finding qualitatively matched the observed deposit in EGR coolers, where porosity from deposit at near ambient conditions has been measured to be ~2% [109,183] , and the higher pressure Air Force STTR Phase II project where the porosity was measured to be much lower. Higher pressure produces larger soot particle sizes and possibly results in better packing of particles. However, this porosity was determined by tuning the model to match the experimental data – and other modeling or experimental errors could be present that affect these results. Thus, additional work is necessary to measure the soot porosity and to possibly incorporate a physics based sub-model for porosity in the overall sooty plug flow reactor model. It was also interesting to observe that prediction of the bulk soot mass was off from the measured values by about the same amount for the 150 and 250 psia case. As previously mentioned, another deposit mechanism was suspected, and these results show the deposit mechanism may be pressure independent – at least at pressures below 250 psia. The higher-pressure case however resulted in overprediction of soot deposit mass by about ~0.15 g. There are two things that were suspected for this result. First, the higher-pressure test was run with a larger nitrogen purge pressure for safety considerations. The higher purge could possibly have resulted in higher shear stresses on the soot surface at shutdown that stripped away some of the soot. If this was the case, and the deposited mass was lost, then the modeled porosity would have been higher than predicted – and closer to the 250 psia condition. Another possibility is higher radiation transfer to the wall at larger pressures because the core soot volume fractions were larger. The higher radiation transfer would have resulted in significantly more heat loss to the wall compared to the other cases. This additional heat loss would introduce an energy loss that lowers gas temperature and decreases soot volume fractions in the core. It would also decrease the thermophoretic driving force by heating up the chamber walls and in turn reduce deposit rates. This was not yet done for the high-pressure condition but the chamber wall for this condition should be estimated via inverse heat transfer to determine if this was true. The model should also be run with heat transfer calculation to predict this effect in the model.

Finally, residence time effects were also investigated with both the model and experiments. The residence time in the experiment was varied by changing the propellant mass flow rate and the choke plate. As shown in Figure 5.41, residence time was not predicted, nor measured, to

significantly affect soot deposition. This was unintuitive at first glance, at least for me, because it was thought that higher residence time would result in higher soot formation in the core and in turn higher deposits. The MOMIC coupled plug flow reactor model does predict higher soot mass fractions at higher residence times, as shown on the left of Figure 5.43. However, as shown on the same figure, the thermophoretic velocity is lower with increased residence time. The reason for this is because the temperature gradient near the wall is lower at lower mass flow rates. In turn, the thermophoretic force is lower. Hence, the combined effect of higher bulk soot but lower thermophoretic velocity at increased residence time does not significantly affect deposits.

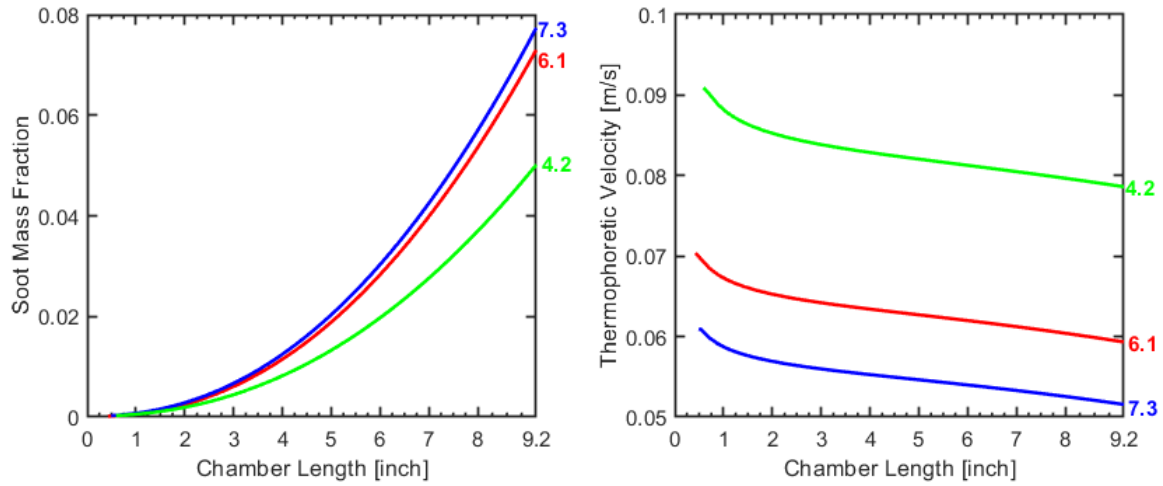

Figure 5.43 Predicted Soot Mass Fraction [Left] and Thermophoretic Velocity [Right] for the constant pressure and variable residence time conditions at **4.2**, **6.1**, **7.3** ms

5.5.3 Condensation Mechanism

The predicted soot deposit mass with the plug flow reactor model showed discrepancy with experimental measurements, suggesting that another deposition mechanism was present. After additional literature review, condensation of heavy PAH's was suspected. Soot deposit in EGR coolers has been observed to consist of 2 layers with dense and porous soot [183]. Assuming the unknown mechanism was condensation of pyrene PAH, the condensed deposit thickness would need to be about 20% of the deposit thickness in order to account for the missing mass in the copper and stainless samples – calculated with density of pyrene. This calculation is qualitatively in agreement with measurements of the EGR cooler, and with another Air Force Phase II STTR project performed at Zucrow laboratories.

The deposition flux due to condensation can be modeled by considering the rate of arrival from the vapor phase to the liquid-vapor interface and rate of departure from the liquid. Collier et. al provides a simple expression to calculate the condensation rate based on gas properties and mass fractions in the bulk and liquid-vapor interface [184]:

$$\dot{m}'' = K_g \rho_g \, ln \frac{1 - y_{g,i}}{1 - y_{g,o}} \tag{5.14}$$

Where K_g is the mass transfer coefficient, $y_{g,i}$ is the species mass fraction at the interface and $y_{g,o}$ is the mass fraction at the wall. K_g is can be evaluated from heat transfer coefficient h_g via analogy between heat and mass transfer as:

$$K_g = \left(\frac{h_g}{\rho_g c_{p,g}}\right)\left(\frac{P_r}{S_c}\right)^{\frac{2}{3}} \tag{5.15}$$

The heat transfer coefficient can be determined from correlation such as Dittus-Boelter, described in section 4.2.1, and the rest of the parameters in the mass transfer coefficient from gas properties. The species mass fraction at the interface can be determined based on partial pressure at the interface as:

$$y_{g,i} = \frac{P_v}{P} \tag{5.16}$$

Where P is the bulk pressure and P_v is the vapor pressure. The vapor pressure can be determined from the Antoine equation and the species-specific coefficients taken from the NIST database:

$$\log_{10} P_v = A - \frac{B}{T_{interface} + C} \tag{5.17}$$

The tricky part in predicting the condensation with this approach is calculating the mass fraction of the bulk PAH. This requires a reaction mechanism that includes PAH chemistry. The HyChem POSF5433 RP-2 reaction mechanism that was used for most of the PFR simulations does not have these steps. An attempt to splice the mechanism with the ABF mechanism for C2 Hydrocarbons [126], which contains PAH steps, was unsuccessful. The combined mechanism provided erroneous results in a WSR simulation. Further work is necessary to incorporate PAH steps in the HyChem mechanism. As a simpler approach, the 1-D plug flow reactor soot model was modified to solve the initial WSR with the HyChem mechanism, and then the remainder of the WSR in the PFR chain with the ABF mechanism. This is illustrated in Figure 5.44. The ABF

mechanism does not have RP-2 pyrolysis steps and thus to ensure complete pyrolysis, the initial WSR was sized such that the outlet mass fraction of RP-2 was less than 1e-5.

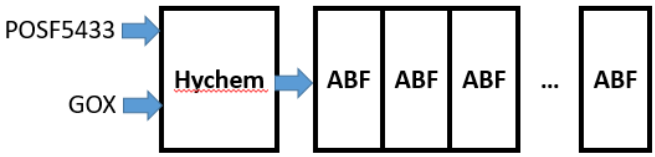

Figure 5.44 Plug flow reactor model modification to solve with HyChem and ABF mechanism

The predicted PAH condensation contribution towards the overall soot deposit for the copper and stainless-steel samples at the nominal chamber pressure of 250 psia are shown in Figure 5.45. This calculation was done assuming an interface temperature equal to the inner wall temperature from the inverse heat transfer solution. The predicted condensation rate with this model is higher for the copper than the stainless sample because the surface temperature was lower. The deposition flux also increases with axial length, as a larger amount of PAH is produced in the flow. The mass contribution of PAH condensation to the overall soot deposit and comparison with experiment is shown in Figure 5.46. Condensation seems to account for the observed mass discrepancy.

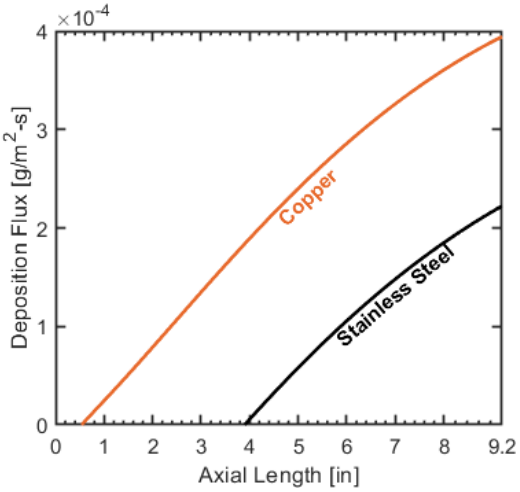

Figure 5.45 Pyrene condensation contribution towards overall soot deposit flux for copper and stainless steel samples at the nominal 250 psia pressure condition

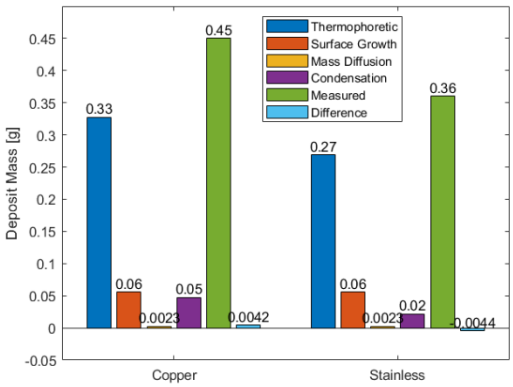

Figure 5.46 Comparison of predicted soot deposit masses from thermophoretic, surface growth, mass diffusion, and condensation on copper and stainless steel with bulk sample measurement

However, despite PAH condensation appearing to account for the mass on the copper and stainless samples at a nominal pressure of 250 psia, it's not the case for the other conditions. The condensation predictions at variable pressure and variable residence time conditions are shown in Figure 5.47. Condensation flux was predicted to increase with pressure. The deposit mass predictions for these conditions, shown in Figure 5.42, on the other hand showed different behavior. Condensation could not account for the discrepancy in the mass at the 150-350 psia pressures – where the discrepancy was roughly equivalent for 150 and 250 psia pressures and was lower than predicted for the 350 psia pressure. The higher residence time cases also resulted in larger mass deposit discrepancy compared to predictions, which condensation could not account for.

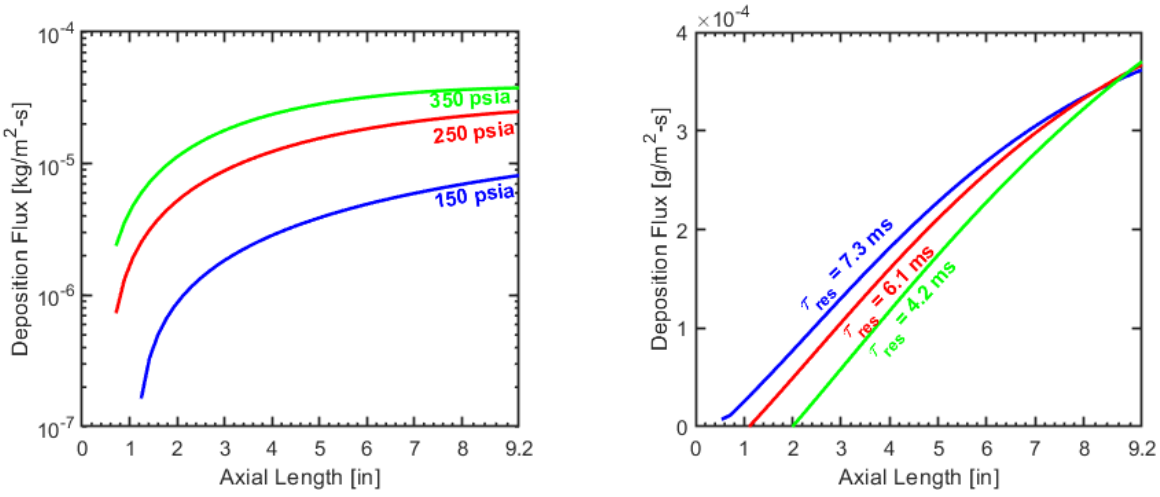

Figure 5.47 Pyrene condensation contribution towards overall soot deposit flux for copper and stainless steel samples at a roughly constant residence time of 6.2 ms and variable pressure [Left] and nominal pressure of 250 psia but variable residence time [Right]

6. CONCLUSIONS AND FUTURE WORK

6.1 Conclusions

A combined experimental and computational study of soot formation and deposition at fuel rich kerosene combustion conditions was performed over the last four and a half years. Specifically, a mixture ratio of unity was explored because it was thought to produce the largest amount of soot based on initial literature review. Though this condition may not be realistic of an actual propulsive system – fuel rich kerosene gas generators for example typically operate around mixture ratios of ~0.5, where soot formation is limited because the bulk gas temperatures are low – a mixture ratio of unity increased soot production and deposition. The higher amount of soot facilitated comparison of measurements with model to discern deposition mechanisms. These deposit mechanisms were initially thought to primarily be driven by thermophoretic and Brownian diffusion of core flow soot to the wall, and heterogenous surface growth reactions on the deposited soot surface layer. However, comparison of experimental results with the modeling predictions suggested that condensation of polycyclic aromatic hydrocarbons to the cold chamber wall may be important. Condensation was modeled with a rough approach and it seemed to better match soot deposit mass predictions with the experiment at some conditions but there was still some discrepancy – suggesting that another deposit mechanism could be present, or other effects such as soot removal. Modeling soot removal, among several additional improvements, is left as a future work item for improving the deposit model predictability.

The study started with a simplified reactor type modeling to predict bulk gas conditions in fuel rich conditions. These results showed that fuel rich combustion occurs at non-equilibrium conditions and consideration of chemical kinetics is important. Unless the residence times in a fuel rich system are very long, assuming equilibrium properties – such as with NASA chemical equilibrium with applications [13] – would provide erroneous prediction of the bulk gas state. Consequently, soot would be significantly underpredicted since species such as acetylene, which is involved in formation of soot-precursors and soot surface growth, can decrease by several orders of magnitude as equilibrium is approached. An initial plug flow reactor model, developed using the Cantera toolbox, was used to predict bulk gas property distribution in a combustor at chemical non-equilibrium. Soot surface growth reaction rates were then calculated with the surface

hydrogen-abstraction-acetylene-addition mechanism using the bulk solution. The results showed that soot surface growth rates are high initially in the reactor, where the heat release reactions produce higher temperatures and higher concentrations of acetylene, but slowly decrease with axial length – though very long reactor lengths are required to achieve equilibrium rates. The model also showed soot deposition to be sensitive to pressure and deposit growth rates to increase with increasing pressure.

Two-dimensional reacting flow CFD simulations were subsequently run to model fuel rich kerosene combustion with higher fidelity. Due to the high cost of running reacting CFD, and the limited available computational resources, the model was solved in a two-part approach. The previous plug flow reactor was used to ignite the kerosene and oxygen mixture and then this solution was used to generate an inlet boundary condition for CFD to model the residual reactions. By not directly computing ignition in the CFD, the time-step, and hence the computational effort, could be decreased by a hundred-fold. Steady state CFD results showed a drastic difference between the near wall soot surface growth rates and that of the plug flow reactor predictions, by about an order of magnitude. An examination of the results showed that boundary layers can significantly affect the reactions by providing a longer residence time for reactions to occur. For flows where the reaction residence time is short, such as stoichiometric combustion, this is not a significant effect. However, for fuel rich combustion, where reactions require very long residence times to reach equilibrium, any increase in residence time would have a significant effect on the gas state. As the initial plug flow reactor results showed, increasing residence time results in decreased soot production. This was the reason for lower predicted soot growth rates in CFD, suggesting that modeling near wall gas chemistry requires either CFD or considering the extra residence time provided by the boundary layer. The CFD results however showed that the bulk gas predictions of temperature, species, and calculated soot growth rates with the bulk state agree well with the plug flow reactor model. This insight allowed for predicting core flow soot formation and transport to the walls with the computationally cheaper reactor modeling approach.

The final part in the numerical approach was development of a reduced pseudo-two-dimensional plug-flow reactor model coupled to soot formation and deposition sub models. Bulk volumetric soot was modeled with the Method of Moments with Interpolative Closure and the particle size distribution calculated with the gas phase solution from the Plug Flow Reactor. The soot model was coupled with the plug flow reactor mass, energy and species equations to account

for mass, species and energy exchange between the gas and soot particles. In addition, the Kazakov aggregation model was incorporated in the Method of Moments with Interpolative Closure model to predict soot aggregation – which becomes important at high pressures and fuel rich conditions. Chamber wall deposit was modeled with surface growth reactions, like in the initial plug flow reactor model, as well as with thermophoretic and Brownian diffusion. The simplified model was able to compute deposit properties in ~1-2 minutes on a single intel Core i7-8750H cpu. The model showed that coupling soot to gas phase chemistry becomes important as the soot volume fraction become larger at either higher pressure or higher residence time. The decoupled approach produces higher soot volume fractions, mainly because consumption of acetylene, which increases as soot volume fractions increase, is not considered. Additionally, coupling soot to gas phase shows that soot can account for significant pressure loss at higher pressures or higher temperatures because gas species are consumed to form higher density solid soot. Soot deposit was also predicted to follow the same trends as the bulk soot volume fraction and thermophoretic deposition to be the most dominant source of soot mass deposit, followed by surface growth reactions. Brownian diffusion was predicted to be much smaller and negligible in comparison.

Simultaneously with the experimental effort, a fuel rich kerosene combustion and soot deposition experiment was designed and run to obtain soot deposit measurements at various conditions on a sample liner within the sample chamber. This experiment was designed to be ignited with a hydrogen and oxygen torch igniter, which was designed based on previous igniter designs with 0-D analysis. However, initial testing resulted in significant hardware damage and post-test CFD analysis showed significant design flaws. This igniter was redesigned based on additional CFD and worked successfully in all subsequent test firing. One of the outcomes of the experimental effort in this work involved developing a better understanding of important considerations in designing a successful hydrogen and oxygen torch igniter for kerosene ignition, with the results described in section 4.4.1. The experiment was designed together with the feed system and was guided by the modeling effort. Several months were spent designing, machining and then plumbing the feed system to run the tests. Afterwards, the experiment was run and chamber pressure measurements, sample backwall temperature measurements and deposits collected at various conditions. The chamber pressure was directly compared the bulk pressure predictions from the sooty plug flow reactor model. The sample inner wall temperature and heat flux was determined via inverse heat transfer, and the sample inner wall temperature used as input

in the thermophoretic deposit model calculation. The deposit thickness was measured with an optical profilometer and compared with model predictions.

The predicted bulk chamber pressures matched the trends in the experiment. Higher pressure resulted in lower chamber pressure compared to a pure gaseous no soot case, and higher residence time resulted in higher pressure loss. This was because soot formation decreased the amount of gas moles to form solid phase soot. The predicted chamber pressures though were slightly higher than measured. The difference was likely due to two reasons. First the model was run as adiabatic, whereas in the experiment heat loss to the wall – especially via soot radiation – would have contributed to gas energy loss and in turn resulted in lower pressure. Secondly, in the experiment there was always torch nitrogen purge, and it was sized to provide the same percent of total flow in all the experiments. Regulator effects though, such as drooping, could have resulted in lower nitrogen mass flow than anticipated and in turn lower chamber pressure. Unfortunately, pressure measurements were not taken upstream of the nitrogen purge flow restriction and instead the flow was calculated based on the reading of the regulator outlet gauge.

The deposit measurements showed higher deposit thickness on copper samples compared to stainless steel. This was verified with the model, however, the model required tuning the soot porosity to match the experimental data. A porosity of 88% seemed to provide good agreement with the measurements and was set based on internal discussion with another carbon deposition project, as well as heat flux estimates from inverse heat transfer solution. The porosity though is not something is directly modeled and modeling it based on bulk PFR predictions should be investigated for future work – since it can significantly affect deposit thickness. In addition, the predicted bulk deposit mass was about 10% lower than measured, suggesting that another deposition mechanism is present. The difference was also smaller for the stainless-steel sample, which was estimated to have a higher inner chamber wall temperature, suggesting that mechanism is temperature dependent. A likely source was thought to be condensation of heavy polycyclic aromatic hydrocarbons such as pyrene and including a model for this effect seemed to account for the mass discrepancy. However, there was still discrepancy in deposit mass at the variable pressure and residence time conditions which should be investigated in future work. Furthermore, the deposit thickness was higher with increased pressure. The model was able to predict the behavior with axial length along the combustor – though it again required tuning the porosity to match the trends. The tuning showed that porosity possibly increases with chamber pressure and this result

made intuitive sense since higher pressure is thought to produce better packing of the soot particles. But the effect of porosity with pressure needs to be investigated further before drawing conclusions. In addition, the model underpredicted soot deposit mass for the 150 and 250 psia chamber pressures but overpredicted for 350 psia. The underprediction was thought to be due to the extra PAH condensation mechanism and suggesting that it's pressure independent. The overprediction though was thought to potentially be due to either removal mechanisms stripping soot particles away or due to soot radiation becoming more important at increased pressure and resulting in lower soot volume fractions. Both hypotheses require further investigation. Finally, the variable residence time cases, where residence time was varied by varying mass flow, showed soot deposition to be insensitive to residence time. This was unanticipated as it was thought higher residence time would result in higher bulk soot and in turn higher deposition. The predicted behavior matched the model though and further examination showed that even though the soot volume fractions are higher at lower residence time, the temperature gradient at the wall – which drives thermophoretic deposition – was lower. In turn the net effect was negligible change on deposition with increased residence time.

Overall, the reduced pseudo-two-dimensional soot plug-flow reactor model was shown to be able to successfully predict soot deposit trends at conditions between 150-350 psia and residence times between 4.2-7.3 ms. The thickness deposit trends were successfully predicted – and provided good agreement with absolute measurements after tuning the deposit porosity. This was a significant numerical result since it showed that this inexpensive model, which takes 1-2 minutes to compute on a laptop processor, can predict soot formation and deposition behavior without requiring complex and expensive CFD, that would take days or weeks to run per condition. The model doesn't predict all the details of the CFD, and probably predicts soot properties with less accuracy, but it can be used to optimize a system or identify system conditions for running more detailed CFD without needing an expensive CFD parametric study. However, more work is necessary to improve the predictive capability of the model as the next section describes.

6.2 Future Work

The outcome from this research showed that reduced order plug flow reactor models can predict bulk soot deposition trends in a pressure range of 150-350 psia. However, additional work is necessary to improve predictive capability of deposit mass. There are also open questions

remaining about applicability higher pressure conditions were real gas effects and diffusion limited behavior become important. This section discusses possible avenues for both computational and experimental work to improve the model and the understanding of the carbon deposition phenomena.

6.2.1 Suggestions for further numerical investigation

The predicted soot deposit mass with the plug flow reactor model showed discrepancy with experimental measurements, suggesting that another deposition mechanism was present. Condensation of heavy PAH was explored as the likely mystery source, and inclusion of condensation in the model showed closer agreement to experiment at some conditions. However, condensation could not account for deposit mass discrepancy in the variable residence time and variable pressure cases. This suggested that still another mechanism could be present which needs to be hypothesized and explored.

Furthermore, most of the simulations were run with adiabatic boundary conditions in order to investigate effects of the bulk parameters on soot deposition. It would be beneficial for future work to run a parametric study with varying heat transfer to investigate how it affects the bulk volumetric soot and deposition predictions. Additionally, it would be interesting to incorporate conjugate heat transfer in the model to see how deposit properties varies with time as the chamber wall heats up and to see if the model is capable of matching the heat flux predictions from the inverse heat transfer estimates.

As the results showed, soot deposit porosity influences deposit thickness, and it seems to vary with pressure. As of now, the porosity was simply fit to match the experimental data – which is not necessarily a good approach for predicting deposit properties at unknown conditions. It would be extremely beneficial if this porosity could be modeled and predicted from chemistry and physics based on bulk gas properties and/or soot particle diameters. At the very least, an empirical correlation from literature review or compilation would substantially improve model predictability.

In addition, the current model assumes ideal gas to calculate gas density. However, this may not be appropriate for high pressure conditions and as such a real gas model like Peng-Robinson could be incorporated in the model to investigate how high-pressure conditions impact soot formation. In addition, a sort of resistance can potentially be added to the model to account for diffusion limited behavior in soot formation, where the kinetics rates would be slowed down

as bulk conditions become diffusion limited. Both modifications would improve model predictability for actual rocket conditions.

Finally, it would be very valuable to incorporate the method of moments in a CFD approach to verify the bulk soot volume fraction and deposit model predictions. The 2-D axisymmetric CFD that was discussed in this dissertation showed boundary layers can affect chemical reaction rates. However, since most of the bulk soot is formed in the core, it was not thought that boundary layers would have substantial effect on near wall deposit mass. A CFD simulation, with the boundary layer resolved, would verify this hypothesis.

6.2.2 Suggestions for further experimental investigation

The experiment part of this work was designed to provide as much useful model comparison on a budget and so several interesting features were not possible in the experiment. As described in Chapter 4, an original idea was to build a calorimetric chamber where the wall temperature could be precisely controlled. However, the design of this system was too expensive and not feasible within the allowable NSTRF project budget and so the cheaper approach to vary temperature was to run with different sample materials. It would be advisable for a future project, with a higher budget, to go with a calorimetric approach because it would provide a well-defined chamber surface temperature and make discerning wall temperature effects on soot deposit significantly clearer.

Additionally, an idea that I did not have time nor budget to achieve was to directly measure heat flux at the wall. This could be done via either coaxial thermocouples or potentially via thermocouples instrumented at several depths within the copper heat sink chamber. The inverse heat transfer results from this work showed that soot deposits seem to significantly affect heat transfer and directly measuring heat flux would provide this effect in-situ.

The average thermal conductivity through the soot deposit layer could also potentially be measured with heat flux measurements, or. In the combustor like the one used in this work, this could be done first by running purely the hydrogen and oxygen torch and measuring the response time of the thermocouples. Afterwards, once soot has been deposited and the chamber cooled down to ambient conditions the torch can be turned on again and the temperature response measured again. A thermal model can then be fit to the temperature response and the soot thermal conductivity pulled out from the fitting parameters. The experiment can be run at several mixture

ratios, propellant combinations, pressures, to investigate how this affects conductivity due to differences in soot porosity or composition. An empirical model can then be constructed to predict the conductivity and in turn this can be incorporated in a thermal or CFD model to better predict wall heat transfer in a rocket engine.

The flow rates in the experiments in this work were also small in order to limit soot removal effects. It would be valuable for future testing to run a similar combustor at a variety of flow rates and bulk velocity conditions to verify whether the amount of soot deposited remains independent of bulk velocity, like the results in Figure 5.41 suggest, or if effects such as removal become important at some bulk velocity. These measurements would aid with modeling removal in the numerical effort and in turn improve model predictability in more realistic flow conditions.

APPENDIX A. DERIVATION OF THE METHOD OF MOMENTS WITH INTERPOLATIVE CLOSURE

The method of moments is a statistical approach to solving for the average properties of a particle size distribution. For flow with soot the particle size distribution is discrete, and it can be assumed that the i[th] size particles have mass $m_i = im_1$ and $v_i = iv_1$ where $m_1$and v_1 are the mass and volume of the smallest soot particle. The time evolution of this soot particle population undergoing coagulation, with no reactions, can be described by the Smoluchowski master equations [99,100]:

$$\frac{dN_i}{dt} = -\sum_{j=1}^{\infty} \beta_{i,j} N_i N_j \qquad i = 1 \tag{A.1}$$

$$\frac{dN_i}{dt} = \frac{1}{2}\sum_{j=1}^{i-1} \beta_{j,i-j} N_j N_{i-j} - \sum_{j=1}^{\infty} \beta_{i,j} N_i N_j \qquad i = 2,3,\dots,\infty \tag{A.2}$$

Where N_i is the number density of particle size i, $\beta_{i,j}$ is the collision coefficient between particle sizes i and j. The negative term represents the decrease in the i[th] particle size number density due to collisions with other particle sizes and the positive term represents the gain in the i[th] particle size due to collisions with smaller particles. These terms are dependent on the collision coefficient which in general is a function of $\beta_{i,j}(N_i, N_j, m_i, m_j)$ where m_i are the mass of particle size i.

If all particle classes $N_1, N_2, .. N_\infty$ can be solved for then the particle size distribution is known. However, solving the equations would be extremely expensive as the number of coupled ODE's required would be as large as the number of particle sizes. Furthermore, determining the collision coefficient between all the particle sizes would also not be trivial and the dependence of the collision coefficient on the particle size evolution would make it difficult to form a closed-form solution for the Smoluchowski equations.

The r[th] concentration moment for this particle size distribution can be defined as:

$$M_r = \sum_{i=1}^{\infty} m_i^r N_i \tag{A.3}$$

Where m_i is the particle mass of the i[th] size class. In this formulation, the 0[th] moment is $M_0 = \sum_{i=1}^{\infty} N_i$ and corresponds to the total particle number density. The 1[st] moment is $M_1 = \sum_{i=1}^{\infty} m_i N_i$ and corresponds to the total particle mass density. From this the volume fraction can be calculated as $f_v = \frac{M_1}{\rho_{soot}}$. Higher order moments correspond to the variance, skewness, kurtosis and other statistical properties of the distribution. By knowing all integer moments ($r = 0,1,2, \dots, \infty$), the particle size distribution is known. However, most of the properties of particle size distribution can be determined with accuracy for just a few moments. Hence this approach results in a significantly reduced numerical cost to calculating soot distribution properties.

Equations describing the evolution of the moments due to coagulation can be obtained by multiplying equations A.1 and A.2 by m_i^r and then summing over all the particle size classes:

$$\frac{d}{dt}\left(\sum_{i=1}^{\infty} m_i^r N_i\right) = G_r \qquad r = 0,2,3, \dots, \infty \tag{A.4}$$

By assuming that $m_i = i m_1$, the equations describing the effect of coagulation on the moments can then be written as:

$$G_0 = \frac{1}{2}\sum_{i=1}^{\infty}\sum_{j=1}^{\infty} \beta_{i,j} N_i N_j \tag{A.5}$$

$$G_r = \frac{1}{2}\sum_{k=1}^{r-1}\binom{r}{k}\sum_{i=1}^{\infty}\sum_{j=1}^{\infty} m_i^k m_j^{r-k} \beta_{i,j} N_i N_j \qquad r = 2,3, \dots, \infty \tag{A.6}$$

With G_1=0, since the overall mass, and mass density M_1, of the system is conserved in coagulation. The difficulty in the method of moments is solving for these summations since the collision coefficients $\beta_{i,j}$ are nonadditive and have a complicated form, which depends on the coagulation regime. The coagulation regime depends on the Knudsen number defined as $K_n = \frac{2\lambda_f}{d_p}$ where $\lambda_f$is the gas mean free path and $d_p$is the gas particle diameter.

Coalescent Coagulation

Coalescent coagulation occurs when particles collide with each other and coalesce to form larger particles. Initially, while the particle sizes are small (and assumed to be spherical), the coalescent coagulation results in larger nearly spherical particles. However, after they grow into a large enough particle diameter, particle collisions produce fractal aggregates via aggregation. This

behavior has been observed in molecular dynamics simulations [97] and these growth assumptions have been successfully used in other method of moments via interpolative closure implementations [45,95,104,185]. Coalescent coagulation will be discussed in this section and particle aggregation discussed in the aggregation section.

Particle coagulation is usually modeled in the limits of free-molecular and continuum regimes, and the appropriate collision coefficient $\beta_{i,j}$ derived for coagulation term in the moment equations.

In the free molecular regime, where $Kn \gg 1$, the particle diameter is much smaller than the mean free path. This is generally true during the initial coagulation, when the particle size is small. In this limit, the collision coefficient for the coalescence of spherical particles is given by Seinfeld et al [99]:

$$\beta_{i,j}^{FM} = K_f \sqrt{\frac{1}{m_i} + \frac{1}{m_j}} \left(m_i^{\frac{1}{3}} + m_j^{\frac{1}{3}} \right)^2 \tag{A.7}$$

Where $K_f = \epsilon \sqrt{\frac{6k_B T}{\rho}} \left(\frac{3}{4\pi\rho} \right)^{\frac{1}{6}}$, k_B is the Boltzmann constant and ϵ is the Van Der Waals enhancement factor, which is dependent on particle size. However Harris et al. found that once particle inception has ceased, there is no significant loss in accuracy by using a constant size-independent enhancement factor of 2.2 [186].

Substituting the free molecular collision coefficient into the moment equations produces the following double summation term:

$$\sum_{i=1}^{\infty} \sum_{j=1}^{\infty} \left(m_i + m_j \right)^{\frac{1}{2}} m_i^{\frac{1}{2}} m_j^{\frac{1}{2}} \left(m_i^{\frac{1}{3}} + m_j^{\frac{1}{3}} \right)^2 N_i N_j \tag{A.8}$$

This summation is impossible to perform because of the $\left(m_i + m_j \right)^{\frac{1}{2}}$ term and expansion of the term is infinite. To calculate this term, Frenklach used a double interpolation scheme by first defining the following grid function [95,102][1]:

$$f_l^{(x,y)} = \sum_{i=1}^{\infty} \sum_{j=1}^{\infty} \left(m_i + m_j \right)^l \frac{m_i^x m_j^y}{m_i^{\frac{1}{2}} m_j^{\frac{1}{2}}} \left(m_i^{\frac{1}{3}} + m_j^{\frac{1}{3}} \right)^2 N_i N_j \tag{A.9}$$

The coagulation rates can then be expressed in terms of the grid function as:

[1] Note, the original MOMIC publication has a typo in the grid function $f_l^{(x,y)}$

$$G_0^{FM} = \frac{1}{2} K_f M_0^2 f_{\frac{1}{2}}^{0,0} \tag{A.10}$$

$$G_r^{FM} = \frac{1}{2} K_f M_0^2 \sum_{k=1}^{r-1} \binom{r}{k} f_{\frac{1}{2}}^{k,r-k}, \quad r = 2,3,\ldots \tag{A.11}$$

The grid function can be easily calculated at integer values of l and then the fractional values, which are needed in the growth rate terms, are interpolated via Lagrange polynomial using the log grid function values at the integer points as:

$$\log f_{\frac{1}{2}}^{x,y} = L_{\frac{1}{2}}\left(\log\left(f_0^{x,y}\right), \log\left(f_1^{x,y}\right), \log\left(f_2^{x,y}\right), \ldots\right) \tag{A.12}$$

Where the $L_{\frac{1}{2}}$ operator is the Langrange interpolation with respect to 1/2. Frenklach provides a set of parameterization of the grid functions for the five-moment model that gives smaller interpolation error, which was determined via trial and error [95].

In the continuum regime, where $Kn \ll 1$, the particle diameter is much larger than the mean free path. The collision coefficient for spherical particles is given by Seinfeld et al [99]:

$$\beta_{ij}^C = K_c \left(\frac{C_i}{m_i^{\frac{1}{3}}} + \frac{C_j}{m_j^{\frac{1}{3}}} \right) \left(m_i^{\frac{1}{3}} + m_j^{\frac{1}{3}} \right) \tag{A.13}$$

Where $K_c = \frac{2k_B T}{3\eta}$, $\eta = \frac{1}{\lambda}$, and C is the Cunningham slip correction factor and can expressed as $C = 1 + 1.257Kn$ [114]. Substituting the collision coefficient into the 0^{th} moment coagulation equation results in:

$$G_0^C = K_c \left(M_0^2 + M_{\frac{1}{3}} M_{-\frac{1}{3}} + K_c' \left(M_{-\frac{1}{3}} M_0 + M_{\frac{1}{3}} M_{-\frac{2}{3}} \right) \right) \tag{A.14}$$

Where $K_c' = 2.514\lambda \left(\frac{\pi \rho_{soot}}{6}\right)^{\frac{1}{3}}$, λ is the mean free path and ρ_{soot} is the soot density, and the definition of the moment is extended to include any real value of r. Furthermore, reduced moments are defined as:

$$\mu = \frac{M_r}{M_0} \tag{A.15}$$

The moment coagulation equations for the continuum regime can then be written as:

$$G_0^C = K_c M_0^2 \left(1 + \mu_{\frac{1}{3}} \mu_{-\frac{1}{3}} + K_c' \left(\mu_{-\frac{1}{3}} + \mu_{\frac{1}{3}} \mu_{-\frac{2}{3}} \right) \right) \tag{A.16}$$

$$G_r^C = K_c M_0^2 \sum_{k=1}^{r-1} \binom{r}{k} (2\mu_k \mu_{r-k} + \mu_{k+\frac{1}{3}} \mu_{r-k-\frac{1}{3}} + \mu_{k-\frac{1}{3}} \mu_{r-k+\frac{1}{3}} + Kc'(\mu_{k-\frac{1}{3}} \mu_{r-k} + \mu_k \mu_{r-k-\frac{1}{3}} + \mu_{k+\frac{1}{3}} \mu_{r-k-\frac{2}{3}} + \mu_{k-\frac{2}{3}} \mu_{k+\frac{1}{3}})) \quad \text{A.17}$$

In order to obtain closure to these coagulation rate equations, the fractional order reduced moments need to be determined. In the method of moments via interpolative closure, these fractional order moments are determined via interpolation from the integer moments, whose value is known at each integration step of the moment equations. The positive-order reduced moments are determined via Lagrange interpolation using the logarithms of the integer moments as [95]:

$$\log(\mu_P) = L_P\left(\log(\mu_0), \log(\mu_1), \ldots, \log\left(\mu_{r_{max}}\right)\right) \; p > 0 \quad \text{A.18}$$

Where the L_p operator is the same Lagrange operator as before, except with respect to P. The coagulation equations require knowledge of the $r_{max} + \frac{1}{3}$ moment and slight extrapolation is required. However Frenklach shows that dependence of $\log(\mu_r)$ vs r is close to linear above r of 3 and hence produces little error [95]. Furthermore, the coagulation equations also require some extrapolation for the negative moments, for which reasonably accurate results can be obtained by extrapolation of the first three moments as [95]:

$$\log\left(\mu_p\right) = L_p(\log(\mu_0), \log(\mu_1), \log(\mu_1)) \quad \text{A.19}$$

The coagulation rates for the transition regime, where $0.1 < Kn < 1$, were determined via the approximation of Pratsinis [187] as a harmonic mean of the free molecular and continuum limit values:

$$G_r^{TR} = \frac{G_r^{FM} G_r^C}{G_r^f + G_r^c} \; r = 0,2,3, \ldots \quad \text{A.20}$$

Where the superscripts TR, FM and C refer to transitional, free molecular and continuum regimes, respectively. This approximation was tested by Kazakov and Frenklach and was found to be within 20% compared to more complex methods and is satisfactory for most applications [104].

Nucleation

Thus far, the moment discussion involved solely the effect of coagulation on a particle size distribution. However, nucleation needs to occur to first generate the smallest particle size N_1. An equation to describe the initial nucleation process can be written as [95]:

$$\frac{dN_1}{dt} = R_{N_1} - G_{N_1} - \frac{k_s s_1}{\Delta m} N_1 \qquad \text{A.21}$$

In this formulation, R_{N_1} is the chemical pathway for generating the smallest soot particle, G_{N_1} is the reduction of the particles by coagulation and then last term describes oxidation of the soot particle with the k_s term being the reaction rate and s_1 the surface area of the particle.

This equation is not in the form of moment equations and in order to apply it for the moment calculations, it needs to be transformed into the form:

$$\frac{dM_r}{dt} = R_r + G_r \qquad \text{A.22}$$

Where R_r describes the nucleation rate. Detailed models to describe this process exist such as the model of Frenklach and Wang that involves additional moment equations for the PAH distribution [21,22]. However, this approach is computationally expensive and involves modeling on the order of 100 species and 500 reactions. Frenklach and Harris proposed treating the nucleation equation A.21 as an additional moment equation and modeling each term separately. With this approach, it could be assumed that soot particle nucleation is governed by PAH coagulation. This would then involve modeling PAH coalescence into a dimer and deriving the formulation rates of several possible dimers. Furthermore, the PAH formation rates and number densities would need to be calculated to predict the moment nucleation rates.

The PAH are formed from acetylene and as a simplification, Lindstedt et al. instead assumed a simple nucleation step that is dependent solely on the concentration of acetylene [101]:

$$R_r = \frac{2N_A}{C_{min}} k_n(T)[C_2H_2] \qquad \text{A.23}$$

Where N_A is Avogadro's constant and C_{min} is the number of carbon molecules in the smallest PAH that coagulates into a dimer to form the smallest soot particle. This approach is significantly cheaper computationally as it doesn't require mechanisms containing PAH reactions. Mehta ran pre-mixed flame simulations and compared PAH with acetylene nucleation mechanisms and showed that while the predicted number density was a factor of two higher with an acetylene based nucleation mechanism, the soot volume fractions were also higher but closer in agreement [45]. Simulations in diffusion flames however showed that the nucleation mechanism is almost

independent of nucleation mechanism and most of the soot production results from surface reactions. This was similarly observed by Leung et al. [93].

For the soot modeling in this work, the simplified nucleation step was used to reduce the computational cost. Furthermore, in all the simulations, it was observed that the nucleation rates are significant at low residence times on the order of 1e-5-1e-4 seconds. Coagulation and surface growth rates significantly dominate the moment rates at the higher residence times that are closer to the soot experiment conditions.

Surface Growth

In the soot population evolution discussed thus far, nucleation is responsible for generating the smallest primary particles and coagulation affects the number density. The particle size however can be affected further via heterogenous surface growth reactions. This can result in either surface growth at fuel rich conditions, or in oxidation at lean conditions. The form of surface growth rate that is suitable for the method of moments is given by Frenklach [95]:

$$\frac{dN_1}{dt} = -\frac{r_s N_1 s_1}{\Delta m} \tag{A.24}$$

$$\frac{dN_i}{dt} = \frac{r_s}{\Delta m}(N_{i-1}s_{i-1} - N_i s_i) \tag{A.25}$$

Where k_s is the growth rate per unit area, s_i is the surface area of particle of size i, and Δm is the mass difference between adjacent bins. These equations describe how mass is transferred amongst the particle size bins. As soon as Δm amount of mass is added to a particle in the ith bin size, it shifts to bin i+1. Multiplying the equations by m_i^r and summing over all particle size classes, the equations can be recast into a form that can be directly incorporated into the moment's equations [21,102]:

$$\left(\frac{dM_r}{dt}\right)_{\substack{surface\\growth}} = W_r = \frac{k_s}{\Delta m}\sum_{k=0}^{r-1}\binom{r}{k}\sum_{i=1}^{\infty}\Delta m^{r-k} m_i^k N_i s_i\,, \qquad r = 1,2,\ldots \tag{A.26}$$

Where W_0 is equal to 0 because surface growth only affects the particle size but not the number density M_0. This term can be added to the total moment production rate term to describe the particle size evolution due to nucleation, coagulation and surface growth:

$$\frac{dM_r}{dt} = R_r + G_r + W_r \tag{A.27}$$

Several reaction mechanisms can be involved in surface growth, however the growth in the post-flame region of a combustion reactor is thought to occur predominately via the hydrogen abstraction and acetylene addition (HACA) mechanism [21,22,35]. In this model, surface growth was modeled with HACA mechanism. Furthermore, the HACA mechanism describes the growth of PAH molecules but the soot surface resembles the edge of a PAH molecule and chemical similarity is assumed between the two growth processes, which is a good assumption that has been in previous soot modeling efforts [21,45,87]. The mechanism and rate constants that were used in modeling the growth rates are shown in Table A.6.1. Growth is assumed to occur at the armchair surface site on the particle surface and consist of either saturated carbon atoms $C_{soot} - H$ or dehydrogenated $C_{soot} *$ reactive sites.

Table A.6.1. HACA reaction mechanism used for soot surface growth calculations. The rate coefficients are in the Arrhenius form of $k = AT^n exp\ (-\frac{E}{RT})$

#	Reaction	$A\ (\frac{cm^3}{mol-s})$	N	E $\left(\frac{kcal}{mol}\right)$	Ref
1f	$C_{soot} - H + H \rightarrow C_{soot^*} + H_2$	$4.17e13$	0.0	13.0	[21,87]
1r	$C_{soot^*} + H_2 \rightarrow C_{soot} - H + H$	3.9e12	0.0	11.0	[188,189]
2f	$C_{soot} - H + OH \rightarrow C_{soot^*} + H_2O$	$1.0e10$	0.734	1.43	[21,87]
2r	$C_{soot^*} + H_2O \rightarrow C_{soot} - H + OH$	3.68e8	1.139	17.1	[94,189]
3	$C_{soot^*} + H \rightarrow C_{soot} - H$	$2.0e13$	0	0	[21,87]
4a	$C_{soot^*} + C_2H_2 \rightarrow C_{soot} - H + H$	$8.0e7$	1.56	3.8	[21,87]
4b	$C_{soot^*} + C_2H_2 \rightarrow C_{soot} * + H$				[44]
5	$C_{soot^*} + O_2 \rightarrow 2CO + products$	$2.2e12$		7.5	[21,87]
6	$C_{soot} - H + OH \rightarrow CO + products$	reaction probability = 0.13			[21,87]

In the mechanism, reaction pathway 4a is an original HACA step [87] and results in mass addition to the soot particle while depleting the soot radical. However, reaction pathway 4b

preserves the radical. Wang et al. found that reaction 4a significantly under-predicted soot for laminar counter-flow diffusion flames, and 4b resulted in an over-prediction [44]. The conclusion was that reaction 4a and 4b occur simultaneously, and the pathway 4a applies to the high-temperature region of the flame where there is a high concentration of H radicals while 4b is important near the low-temperature region. For laminar pre-mixed flames, it was found that reaction 4a actually provides better prediction because the local conditions are similar to the high temperature and high H radical concentration regions of diffusion flames [45,190]. This reaction step is the default that is used for the soot calculation in this work, but the code that was developed has an option for either step.

Soot growth can also occur due to condensation of PAH molecules on the soot surface [44]. Modeling this term would require using a large gas chemistry mechanism that includes details of PAH formation. However in a parametric soot model study, Mehta showed that the overall contribution of PAH condensation is small compared to surface reactions for diffusion flames, and even smaller for premixed flames [45]. Hence in this work, it was assumed that PAH condensation can be safely neglected.

Assuming spherical particle growth, where surface area is a function of the particle diameter, the heterogenous gas-surface reaction contribution to the overall moment rates can then be modeled as:

$$W_r = \pi \left(\frac{6m_c}{\pi \rho_{soot}}\right)^{\frac{2}{3}} \frac{k_s}{\Delta m} M_0 \sum_{k=0}^{r-1} \binom{r}{k} \Delta m^{r-k} \mu_{r+\frac{2}{3}} \tag{A.28}$$

Where m_c is the mass of carbon and density of soot ρ_{soot} is set to 1.8 g/cm^3, which is the density of carbon black and has been used in previous modeling efforts [45,88,89,190]. This term can be separated into three components with contributions due to C_2H_2, O_2, and OH as:

$$W_r^{C_2H_2} = k_{4a}[C_2H_2]\alpha x_{c_{soot^*}} \pi \left(\frac{6m_c}{\pi \rho_{soot}}\right)^{\frac{2}{3}} M_0 \sum_{l=0}^{r-1} \binom{r}{l} \mu_{l+\frac{2}{3}} (2)^{r-l} \tag{A.29}$$

$$W_r^{O_2} = k_5[O_2]\alpha x_{c_{soot^*}} \pi \left(\frac{6m_c}{\pi \rho_{soot}}\right)^{\frac{2}{3}} M_0 \sum_{l=0}^{r-1} \binom{r}{l} \mu_{l+\frac{2}{3}} (-2)^{r-l} \tag{A.30}$$

$$W_r^{OH} = \gamma_{OH}[OH] \sqrt{\frac{\pi k_b T}{2m_{OH}}} N_A \left(\frac{6m_c}{\pi \rho_{soot}}\right)^{\frac{2}{3}} M_0 \sum_{l=0}^{r-1} \binom{r}{l} \mu_{l+\frac{2}{3}} (-1)^{r-l} \tag{A.31}$$

In these relations, α is soot surface site fraction that is available for reaction, γ_{OH} is the collision probability for the OH radical, given for reaction 6 in Table A.6.1, m_{OH} is the mass of OH radical, and $x_{c_{soot*}}$ is the number density of surface radicals. The soot surface site fraction α accounts for the difference between the soot growth rates in low and high temperature flames [35,87]. It quantifies the changing morphology of the soot particle surface as the particle surface temperature changes. Previous modeling effort included using a constant for α [21,30], where there was no change in soot surface. A temperature dependent value has also been used by Appel et al [87] based on experimental results from eight laminar premixed flames, calculated as:

$$\alpha = \tanh\left(\frac{a(T)}{log\,\mu_1} + b(T)\right) \quad \text{A.32}$$

Where a and b are model parameters that are function of temperature. From the best-fit relations to the experimental data, the a and b parameters were expressed as:

$$a = 12.65 - 0.00563T \quad \text{A.33}$$

$$b = -1.38 + 0.00068T \quad \text{A.34}$$

In the soot model for this work, this temperature dependent relation was assumed, but the developed soot code allows for constant value to be set. Furthermore, the number density of soot particles was calculated $x_{c_{soot*}}$ via a kinetic steady-state assumption as:

$$x_{c_{soot*}} = x_{c_{soot-H}}\left(\frac{k_1[H] + k_2[OH]}{k_{1r}[H_2] + k_{2r}[H_2O] + k_3[H] + k_{4a}[C_2H_2] + k_5[O2]}\right) \quad \text{A.35}$$

Where $x_{c_{soot-H}}$ is the number density of soot radical sites and set to a value of 2.3e15 sites/cm^3, based on Frenklach's estimate of the number of carbon-carbon bonds of benzene PAH per unit area [29].

The total source term due to surface growth and oxidation is then:

$$W_r = W_r^{C_2H_2} + W_r^{O_2} + W_r^{OH} \quad \text{A.36}$$

Furthermore, the consumption rate for the bulk species can be expressed as the following:

$$\omega_{C_2H_2} = -\frac{W_0^{C_2H_2}}{2N_A} \quad \text{A.37}$$

$$\omega_{O_2} = -\frac{W_0^{O_2}}{2N_A} \quad \text{A.38}$$

$$\omega_{OH} = -\frac{\left(k2r[H_2O]x_{c_{soot^*}} - k2f[OH]x_{c_{soot}}\right)\alpha\pi d_c^2 M_0 \mu_{\frac{2}{3}} + W_0^{OH}}{N_A} \quad \text{A.39}$$

$$\omega_H = \frac{\left((k1r[H2] + k4f[C_2H_2] - k3[H])x_{c_{soot^*}} - k1f[H]x_{c_{soot}}\right)\alpha\pi d_c^2 M_0 \mu_{\frac{2}{3}}}{N_A} \quad \text{A.40}$$

$$\omega_{H_2} = \frac{\left(k1f[H]x_{c_{soot}} - k1r[H2]x_{c_{soot^*}}\right)\alpha\pi d_c^2 M_0 \mu_{\frac{2}{3}}}{N_A} \quad \text{A.41}$$

$$\omega_{H_2O} = \frac{\left(k2f[OH]x_{c_{soot}} - k2r[H2O]x_{c_{soot^*}}\right)\alpha\pi d_c^2 M_0 \mu_{\frac{2}{3}}}{N_A} \quad \text{A.42}$$

$$\omega_{CO} = -\frac{W_0^{O_2} + W_0^{OH}}{N_A} \quad \text{A.43}$$

Particle Aggregation

The previous discussion focused on the coalescent regime, where particle coagulation and growth are assumed to be perfectly spherical. However, especially at high pressures and fuel rich conditions, after an initial period of coalescent growth, the particles start agglomerating to form chain like structures. The aggregate structure is composed of nearly spherical and equal-sized primary particles [95], that obeys the fractal relationship [103]:

$$n = k_F\left(\frac{2R_g}{d_p}\right)^{D_F} \quad \text{A.44}$$

Where n is the number of primary particles, from the coalescent limit, k_f is the fractal pre-factor, R_g is the radius of gyration of the aggregate, d_p is primary particle diameter, and D_f is the fractal dimension. Typically the fractal dimensions of the agglomerates are close to 1.8. [104,191,192] A constant value of 1.8 was used in this work.

In modeling the particle aggregation, the particle distribution becomes a two-dimensional function of the aggregate particle mass, m, and aggregate number of primary particles, n. Then in addition to solving for the particle mass moments M and reduced moment μ, Kazakov and Frenklach introduced new moments for the primary particles and the corresponding reduced moments, P and π as [95,104]:

$$P = \sum_{i=1}^{\infty} n_i^r N_i \tag{A.45}$$

$$\pi_r = \frac{P_r}{P_0} \tag{A.46}$$

Which are solved for via the following equations:

$$\frac{dP_1}{dt} = R_0 \tag{A.47}$$

$$\frac{dP_r}{dt} = R_0 + H_r, \qquad r = 2,3,\ldots, \tag{A.48}$$

These equations are solved simultaneously with the M moment equations. Furthermore, $P_0 = \sum_i^{\infty} N_i = M_0$, the particle number density. R_0 is the particle nucleation rate and is the same as equation A.23. H_r is the aggregate coagulation contribution and can be expressed as:

$$H_r = \frac{1}{2}\sum_{k=1}^{r-1}\binom{r}{k}\left(\sum_{i=1}^{\infty}\sum_{j=1}^{\infty} n_i^k n_j^{r-k}\beta_{ij}^a N_i N_j\right) \tag{A.49}$$

In this relation, $\beta_{i,j}$ is the collision frequency of aggregates and similarly to the coalescent coagulation, it depends on the coagulation regime. For the free-molecular regime, the aggregate coagulation rate is provided by Kazakov [104] as:

$$H_r^{FM} = \frac{1}{2}K_f M_0^2 h_{\frac{1}{2}}^r \tag{A.50}$$

Where h is a grid function defined as:

$$\begin{aligned} h_l^r = \sum_{k=0}^{l}\binom{l}{k}\sum_{q=1}^{r-1}\binom{r}{q}\Big(&\langle m^{k+\frac{1}{6}} n^{q+\frac{2}{D_f}-\frac{2}{3}}\rangle \langle m^{l-k-\frac{1}{2}} n^{r-q}\rangle \\ &+ 2\langle m^{k-\frac{1}{6}} n^{q+\frac{1}{D_f}-\frac{1}{3}}\rangle \langle m^{l-k-\frac{1}{6}} n^{r-q+\frac{1}{D_f}-\frac{1}{3}}\rangle \\ &+ \langle m^{k-\frac{1}{2}} n^{q}\rangle \langle m^{l-k+\frac{1}{6}} n^{r-q+\frac{2}{D_f}-\frac{2}{3}}\rangle\Big) \end{aligned} \tag{A.51}$$

The $\langle m^r n^r\rangle$ terms appearing in this equation are binary moments for the two-dimensional particle size distribution and can be approximated as $\langle m^r n^r\rangle \approx \langle m^r\rangle\langle n^{r'}\rangle = \mu_r \pi_{r'}$ with an error not exceeding 20% [95,104]. The grid function is evaluated similarly to the approach for the coalescent free-molecular grid function. In the continuum regime, the aggregate coagulation rate is provided by Kazakov [104] as:

$$H_r^C = \frac{1}{2}K_c M_0^2 \sum_{k=1}^{r-1} \binom{r}{k} \Bigg(2\pi_k \pi_{r-k} + \langle m^{\frac{1}{3}} n^{k+\frac{1}{D_f}-\frac{1}{3}} \rangle \langle m^{-\frac{1}{3}} n^{r-k+\frac{1}{3}-\frac{1}{D_f}} \rangle + \langle m^{-\frac{1}{3}} n^{k+\frac{1}{3}-\frac{1}{D_f}} \rangle \langle m^{\frac{1}{3}} n^{r-k+\frac{1}{D_f}-\frac{1}{3}} \rangle + K_c' \Bigg(\langle m^{-\frac{1}{3}} n^{k+\frac{1}{3}-\frac{1}{D_f}} \rangle \pi_{r-k} + \pi_k \langle m^{-\frac{1}{3}} n^{r-k+\frac{1}{3}-\frac{1}{D_f}} \rangle + \langle m^{\frac{1}{3}} n^{k+\frac{1}{D_f}-\frac{1}{3}} \rangle \langle m^{-\frac{2}{3}} n^{r-k+\frac{2}{3}-\frac{2}{D_f}} \rangle + \langle m^{-\frac{2}{3}} n^{k+\frac{2}{3}-\frac{2}{D_f}} \rangle \langle m^{\frac{1}{3}} n^{r-k+\frac{1}{D_f}-\frac{1}{3}} \rangle \Bigg) \Bigg) \quad \text{A.52}$$

Furthermore, the calculation of the coagulation rates G, have a modified form during particle aggregation because the aggregate diameter is larger than a spherical particle with the same mass. Furthermore, the collision diameter for calculating the coagulation coefficient is also not a function of the volume anymore and depends on the fractal shape of the aggregate. The modified grid function that accounts for these effects for the free molecular coagulation rate calculation during particle aggregation is given by Kazakov [104] as:

$$f_l^{x,y} = \sum_{k=0}^{l} \binom{l}{k} \Bigg(\langle m^{x+k+\frac{1}{6}} n^{\frac{2}{D_f}-\frac{2}{3}} \rangle \mu_{y+l-k-\frac{1}{2}} + 2 \langle m^{x+k-\frac{1}{6}} n^{\frac{1}{D_f}-\frac{1}{3}} \rangle \langle m^{y+l-k-\frac{1}{6}} n^{\frac{1}{D_f}-\frac{1}{3}} \rangle + \mu_{x+k-\frac{1}{2}} \langle m^{y+l-k+\frac{1}{6}} n^{\frac{2}{D_f}-\frac{2}{3}} \rangle \Bigg) \quad \text{A.53}$$

For continuum regime, the coagulation rates have the following form:

$$G_0^{C,A} = K_c M_0^2 \Bigg(1 + \langle m^{\frac{1}{3}} n^{\frac{1}{D_f}-\frac{1}{3}} \rangle \langle m^{-\frac{1}{3}} n^{\frac{1}{3}-\frac{1}{D_f}} \rangle + K_c' \Bigg(\langle m^{-\frac{1}{3}} n^{\frac{1}{3}-\frac{1}{D_f}} \rangle + \langle m^{\frac{1}{3}} n^{\frac{1}{D_f}-\frac{1}{3}} \rangle \langle m^{-\frac{2}{3}} n^{\frac{2}{D_f}-\frac{2}{3}} \rangle \Bigg) \Bigg) \quad \text{A.54}$$

$$G_r^{C,A} = \frac{1}{2}K_c M_0^2 \Bigg(1 + \langle m^{\frac{1}{3}} n^{\frac{1}{D_f}-\frac{1}{3}} \rangle \langle m^{-\frac{1}{3}} n^{\frac{1}{3}-\frac{1}{D_f}} \rangle + K_c' \Bigg(\langle m^{-\frac{1}{3}} n^{\frac{1}{3}-\frac{1}{D_f}} \rangle + \langle m^{\frac{1}{3}} n^{\frac{1}{D_f}-\frac{1}{3}} \rangle \langle m^{-\frac{2}{3}} n^{\frac{2}{D_f}-\frac{2}{3}} \rangle \Bigg) \Bigg) \quad \text{A.55}$$

For the transition regime during aggregation, the free molecular $G_r^{FM,A}$ and continuum $G_r^{C,A}$ coagulation terms are harmonically averaged via the same approach as described for the transitional coalescent coagulation calculation. The free-molecular and continuum aggregation terms H_r^{FM} and H_r^{C} are also averaged the same way for the transitional regime.

Particle aggregation produces a larger surface area than the spherical particle with the same mass and as a result affects the surface growth calculation. The modified surface growth term can then be written as:

$$W_r^A = \pi \left(\frac{6m_c}{\pi \rho_{soot}}\right)^{\frac{2}{3}} \frac{k_s}{\Delta m} M_0 \sum_{k=0}^{r-1} \binom{r}{k} \left(\Delta m^{r-k} \langle m^{k+\frac{2}{3}} n^{\frac{1}{3}} \rangle\right) \quad \text{A.56}$$

With the assumption that the binary moments can be expressed as a product of the reduced moments $\langle m^{k+\frac{2}{3}} n^{\frac{1}{3}} \rangle = \mu_{k+\frac{2}{3}} \pi_{\frac{1}{3}}$, this can be written as:

$$W_r^A = W_r^{Coalescent} = \pi_{\frac{1}{3}} W_r^{Coalescent} \quad \text{A.57}$$

In calculating the soot properties, the coalescent growth model was first used to calculate the soot growth and only after the primary particle diameter was above a critical diameter d* were aggregate calculations turned on, in accord with the approach described by Frenklach and Kazakov [95,104].

APPENDIX B. SOOT EXPERIMENT MACHINE DRAWINGS

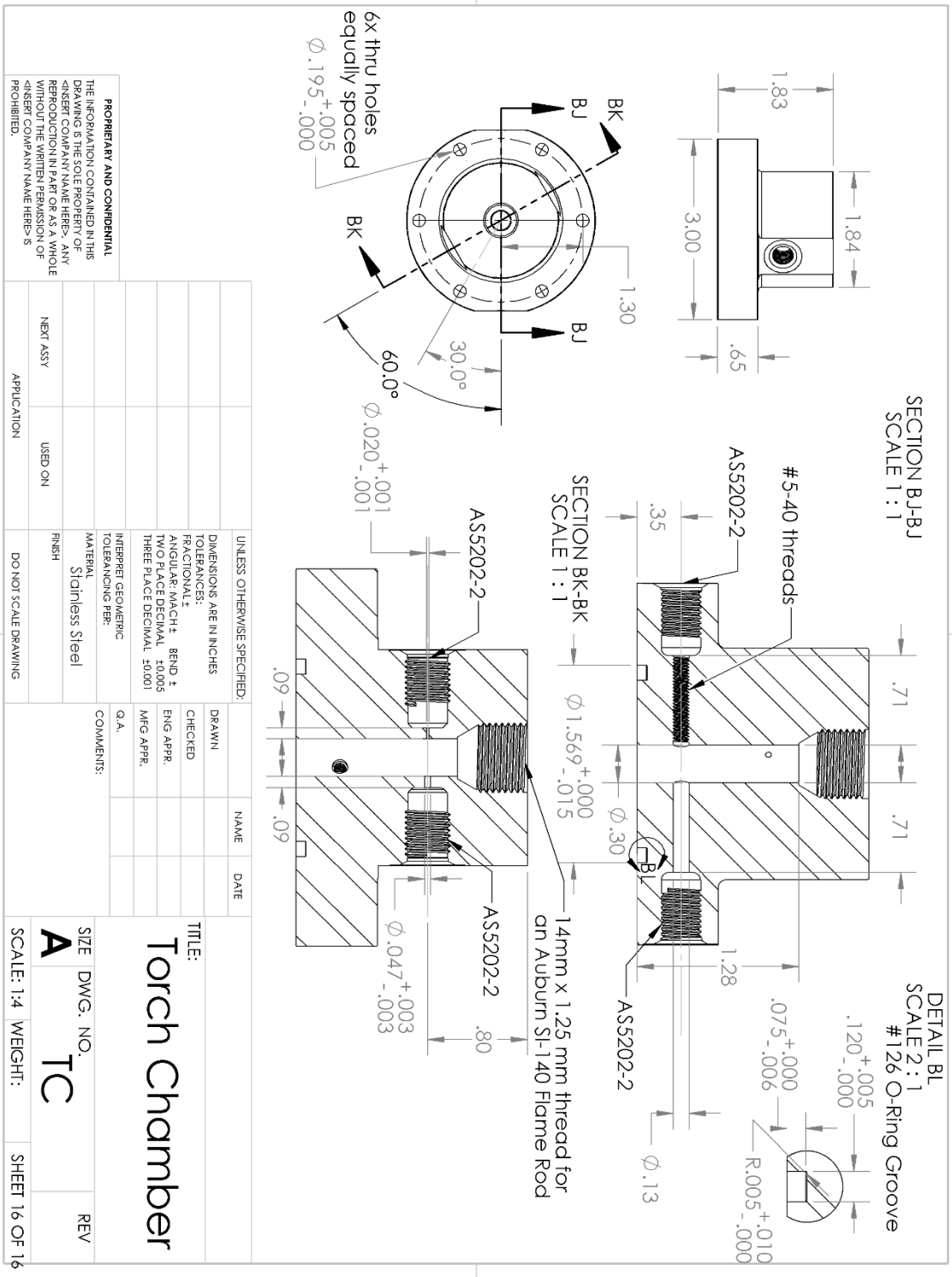

Figure B.1 Torch Chamber

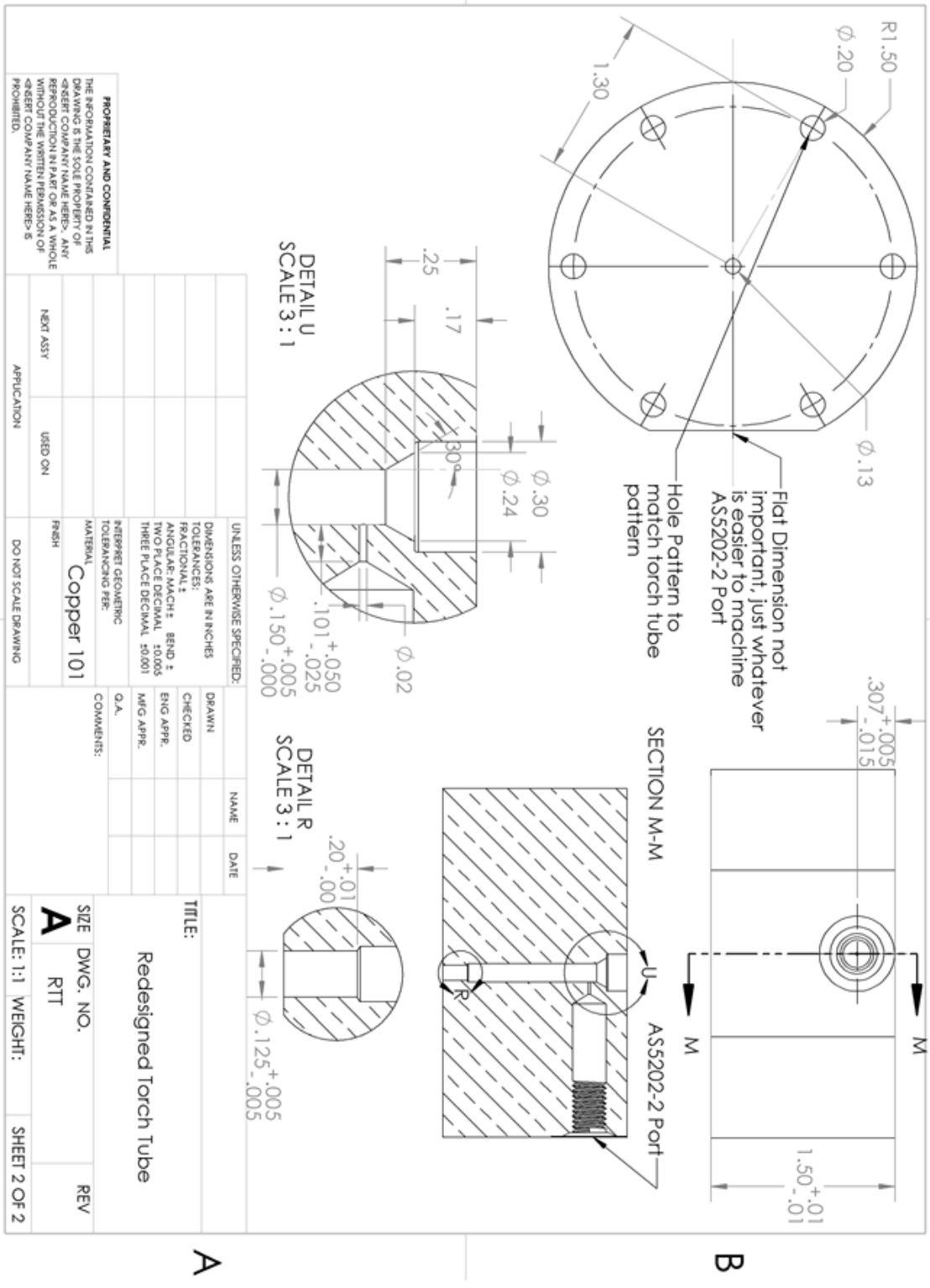

Figure B.2 Redesigned Torch Tube

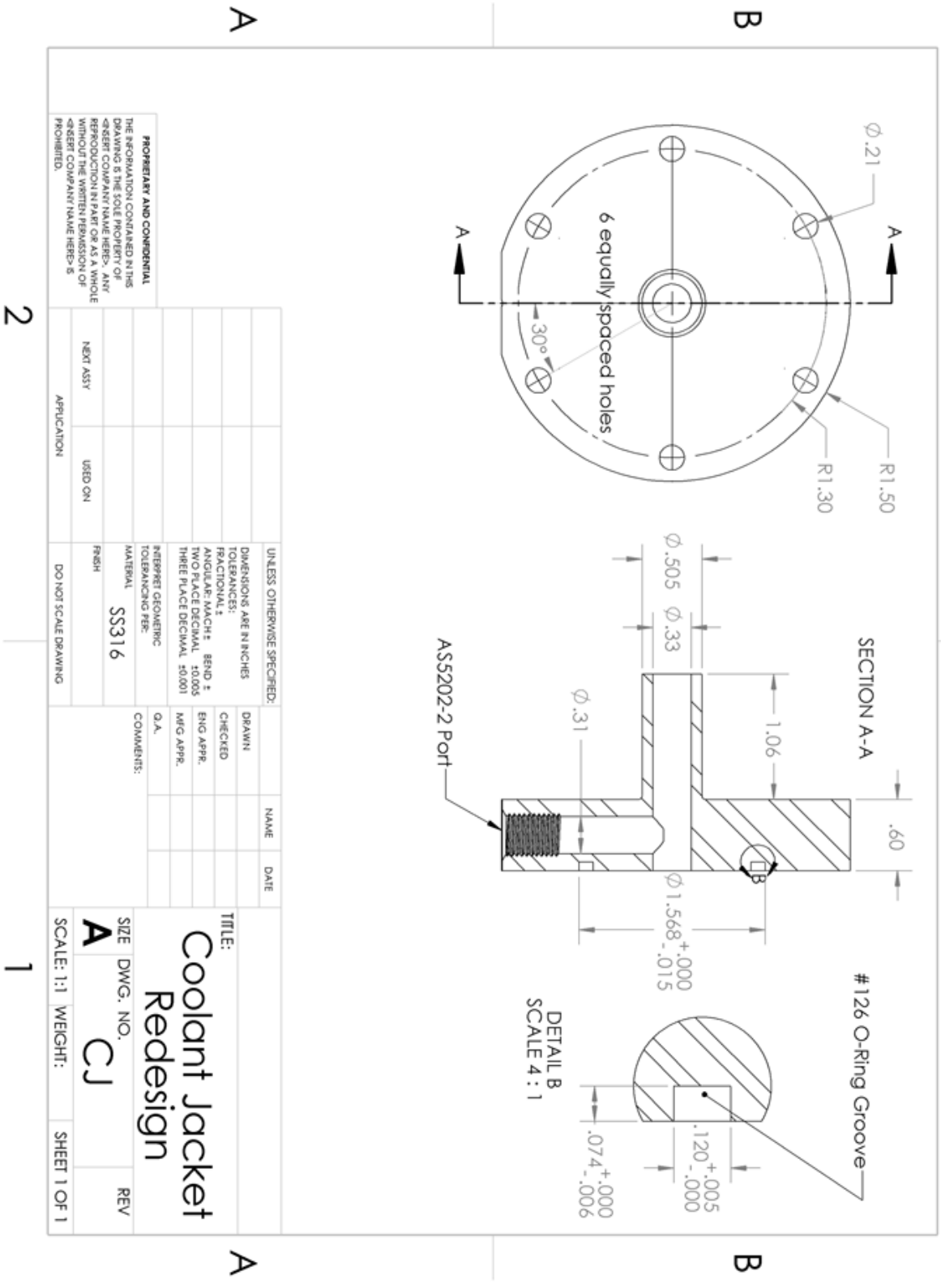

Figure B.3 Torch Coolant Jacket

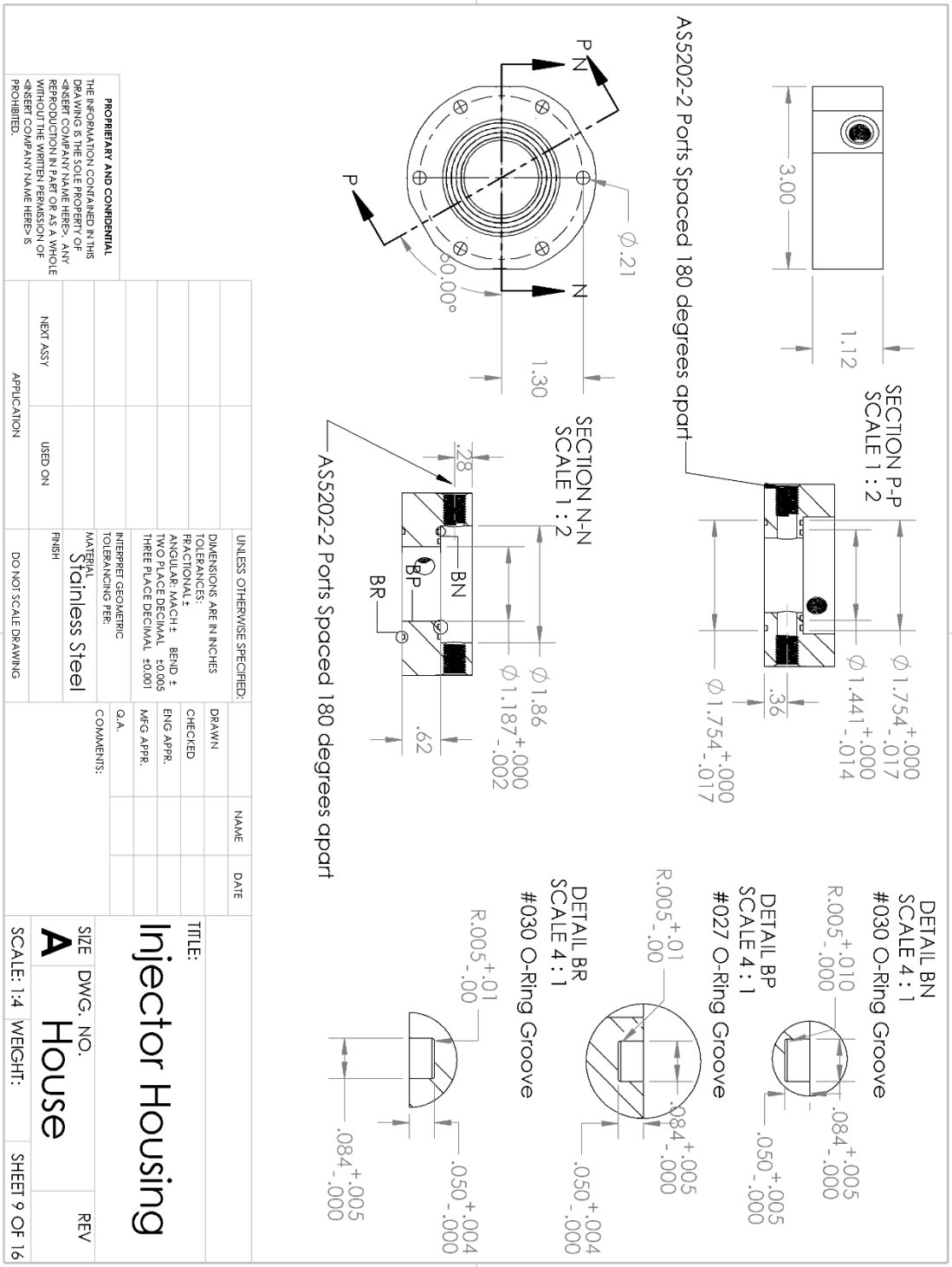

Figure B.4 Injector Housing

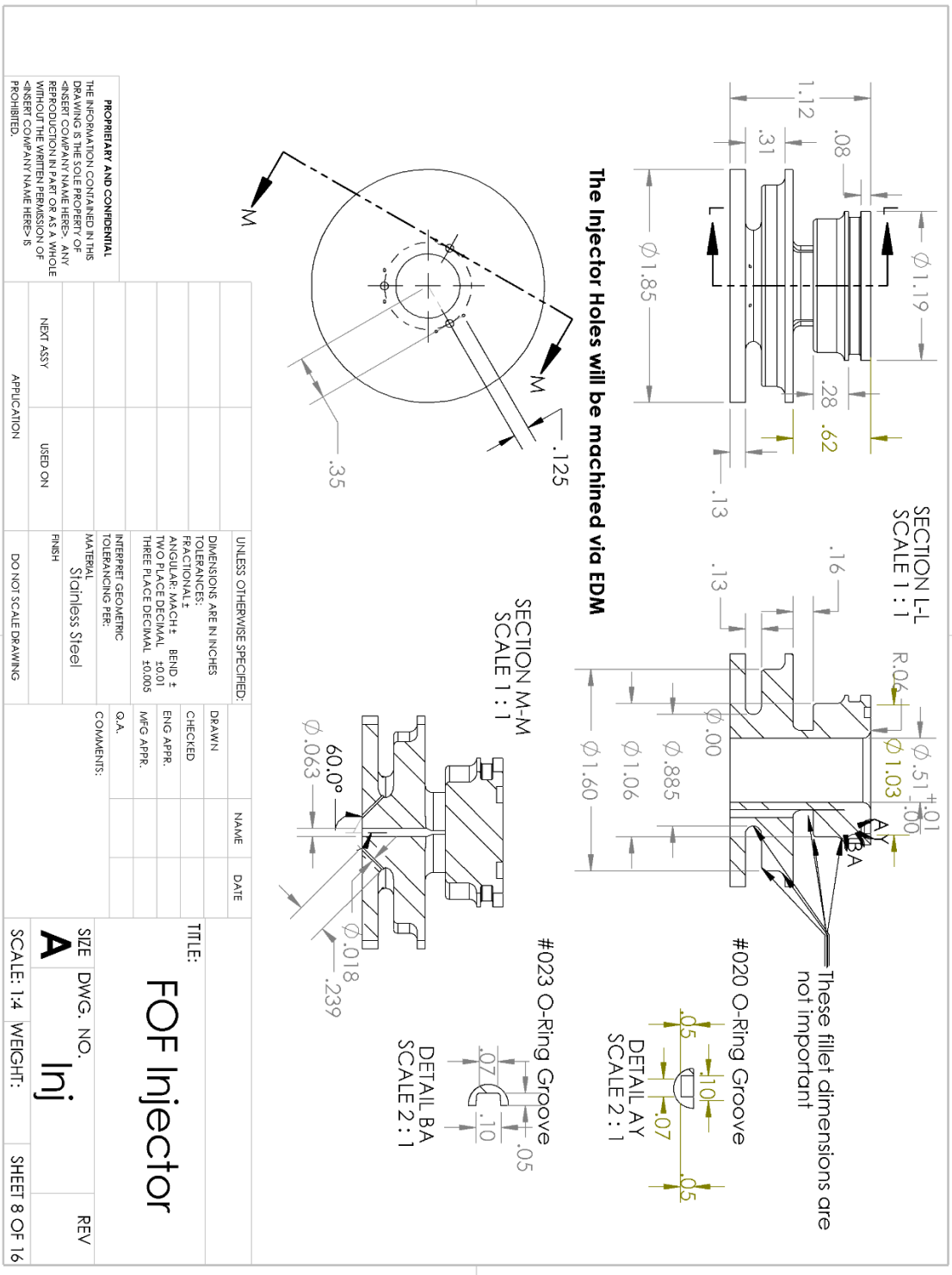

Figure B.5 Injectors

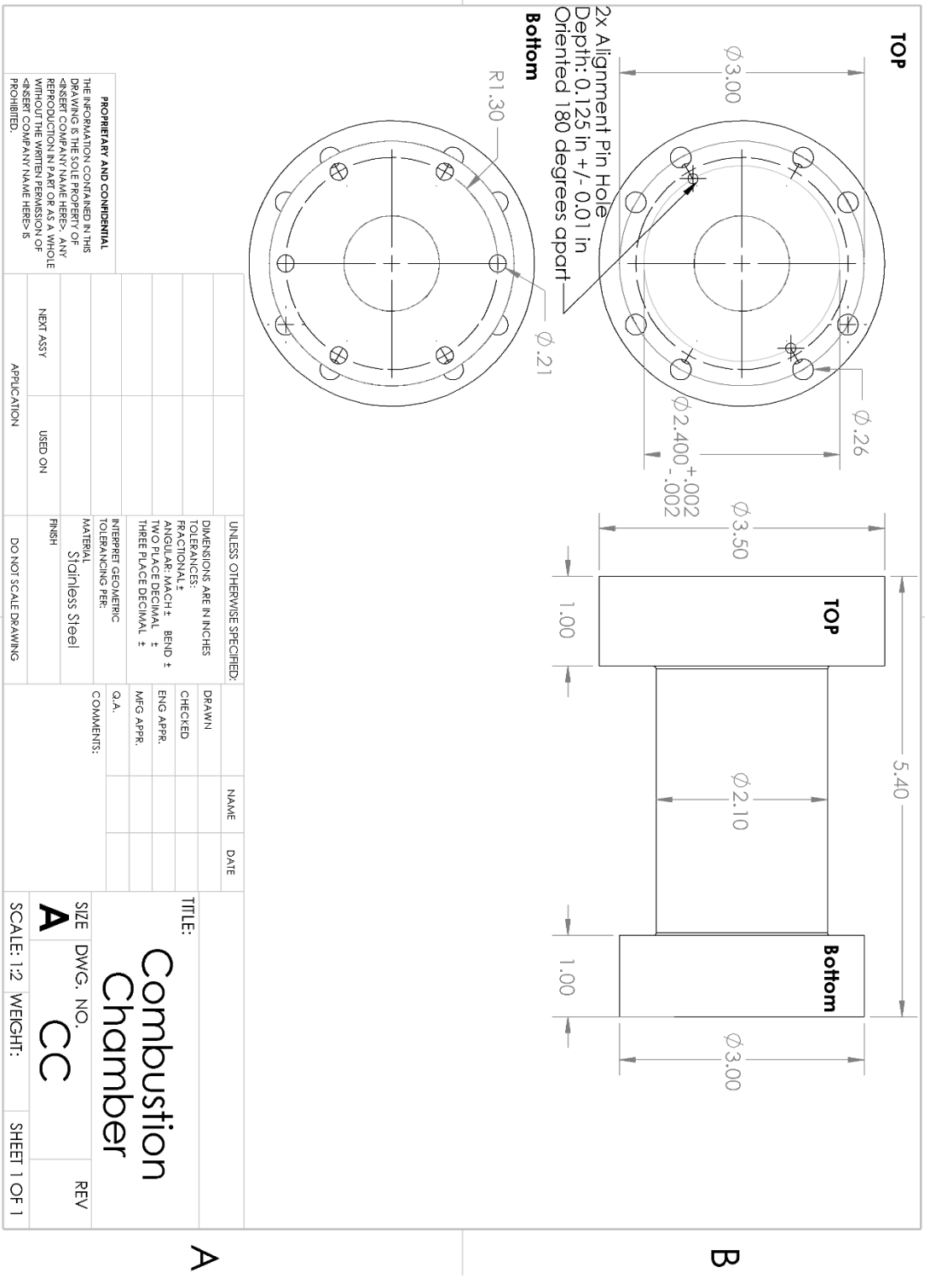

Figure B.6 Combustion Chamber

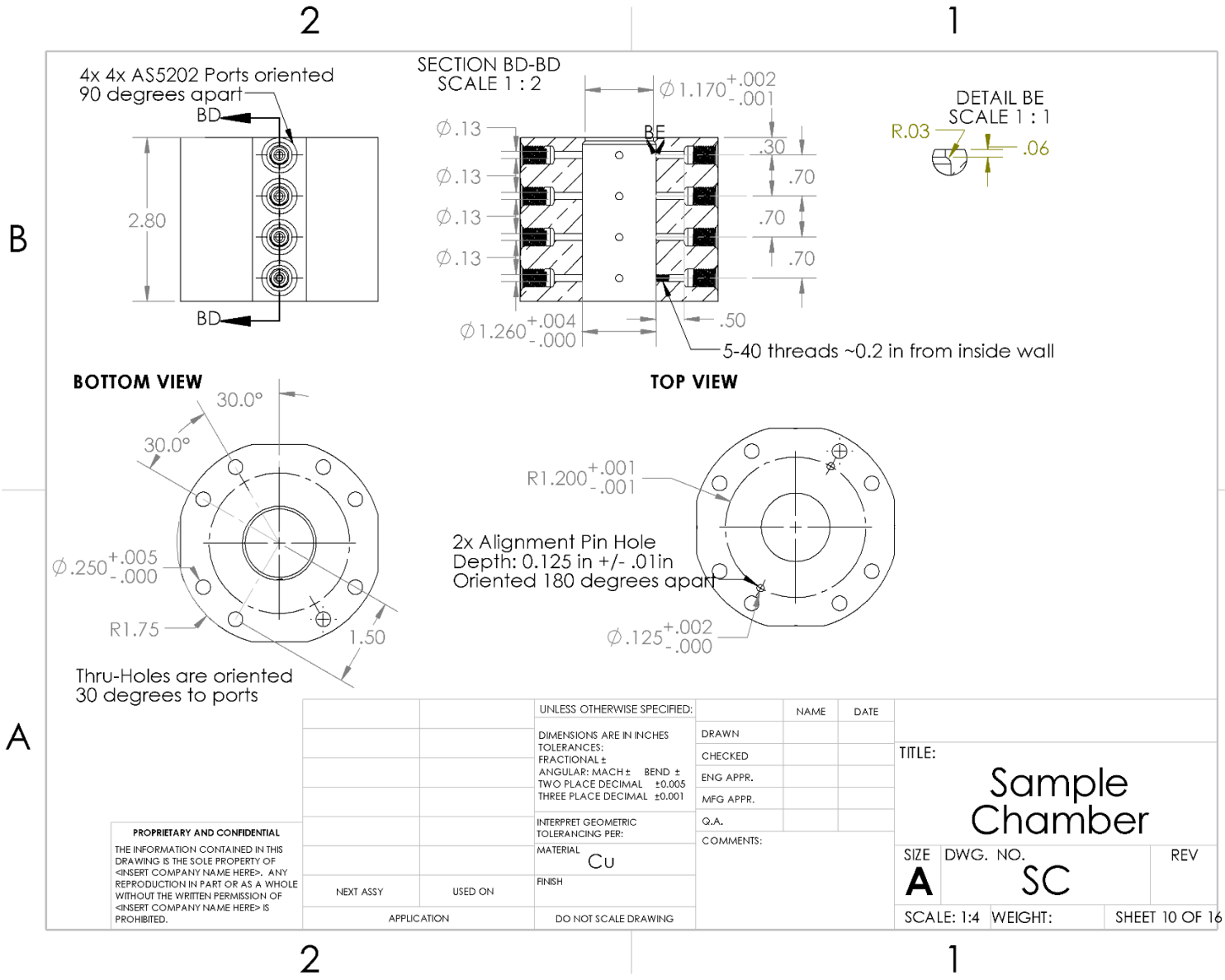

Figure B.7 Sample Chamber

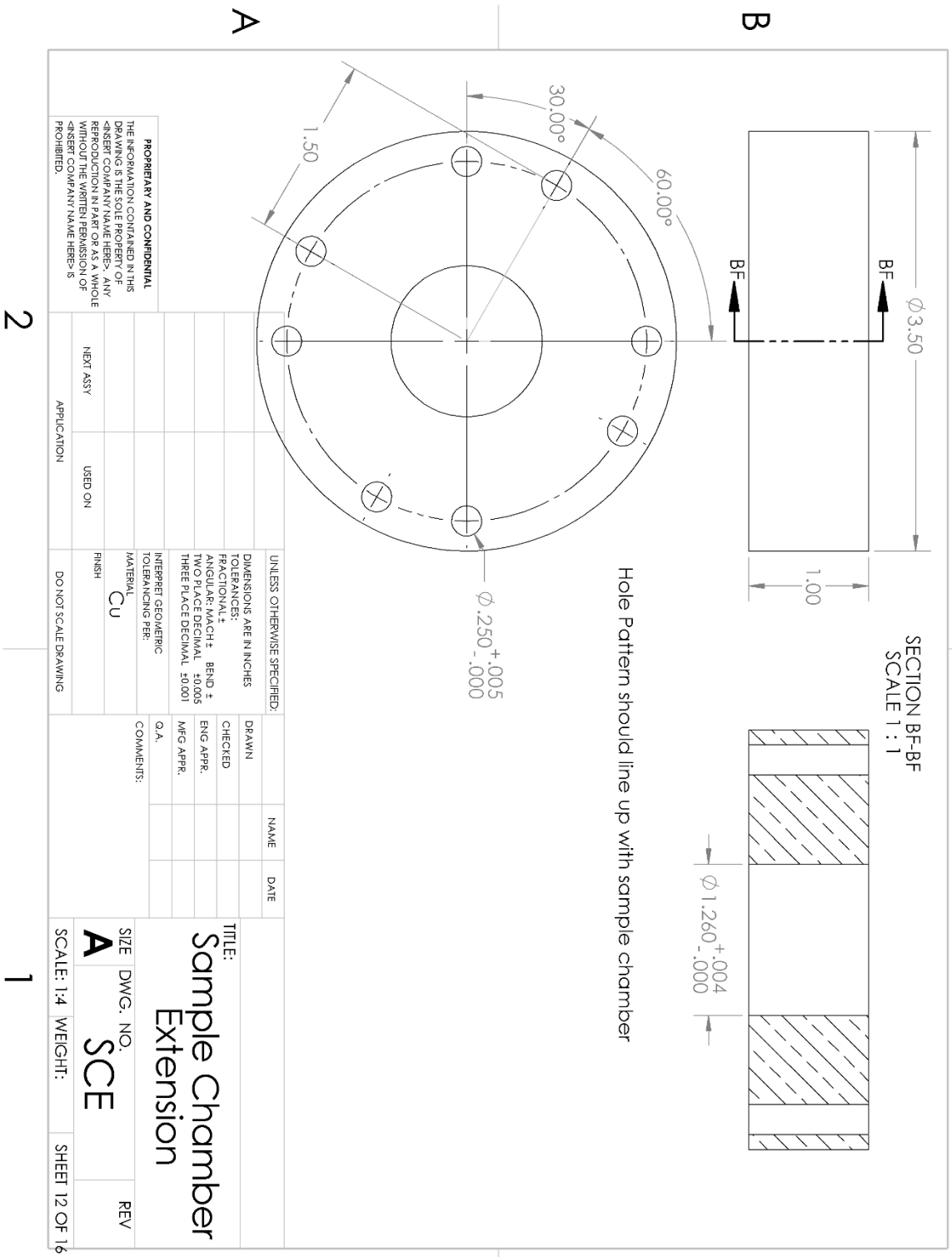

Figure B.8 Sample Chamber Extension

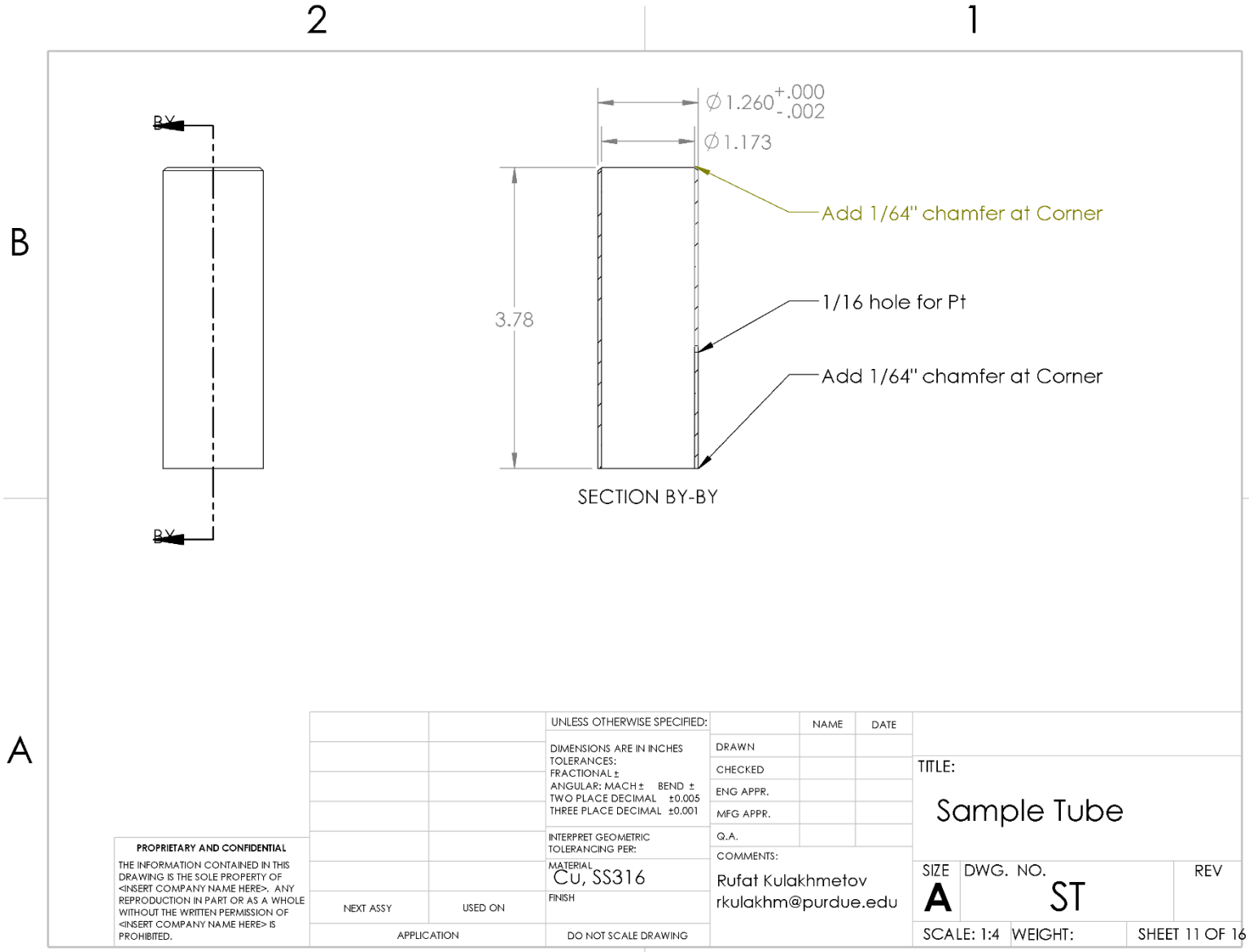

Figure B.9 Sample Tube

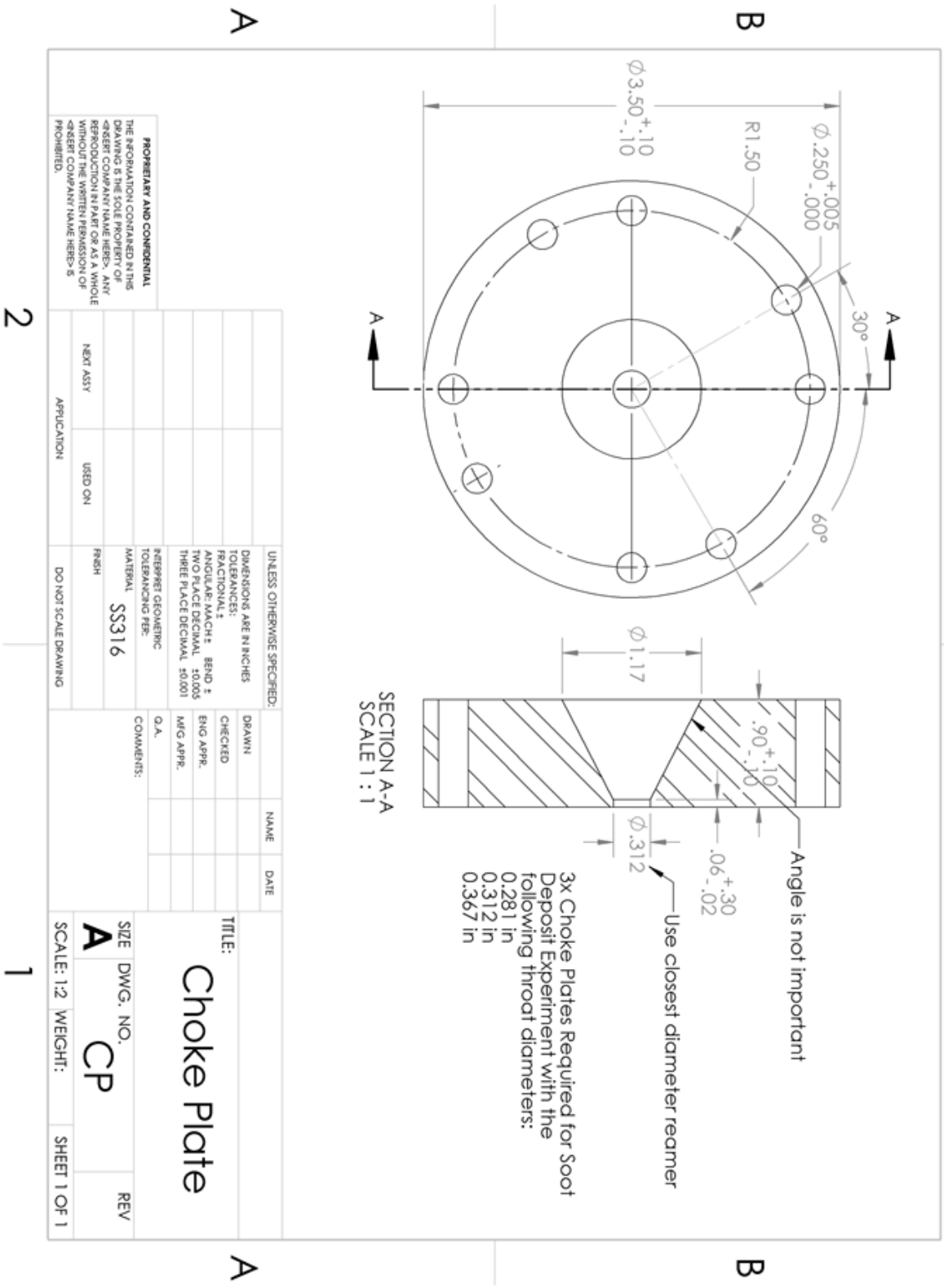

Figure B.10 Choke Plate

APPENDIX C. EXPERIMENTAL PLUMBING AND INSTRUMENTATION

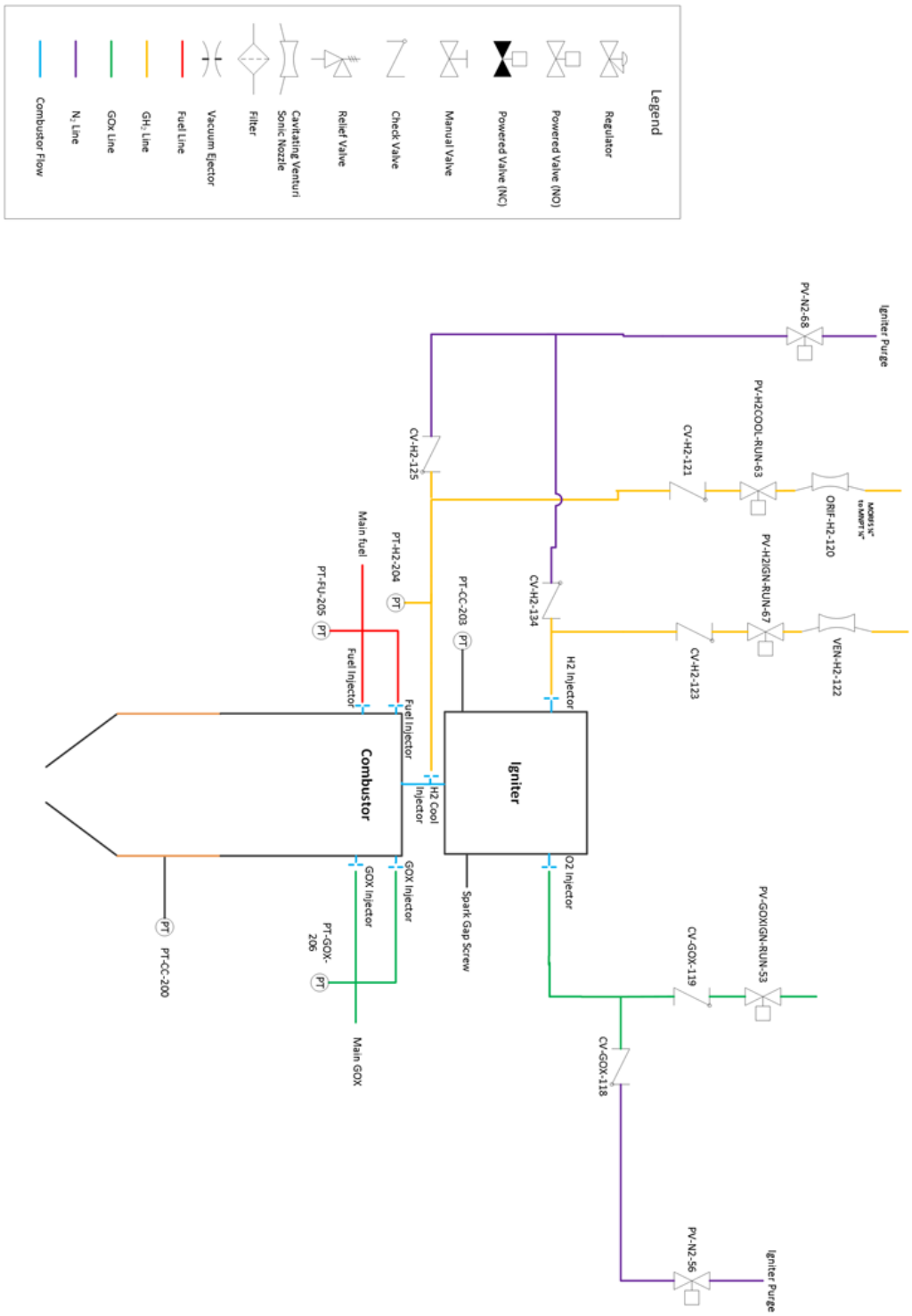

Figure C.1 Main Combustor Plumbing & Instrumentation Diagram

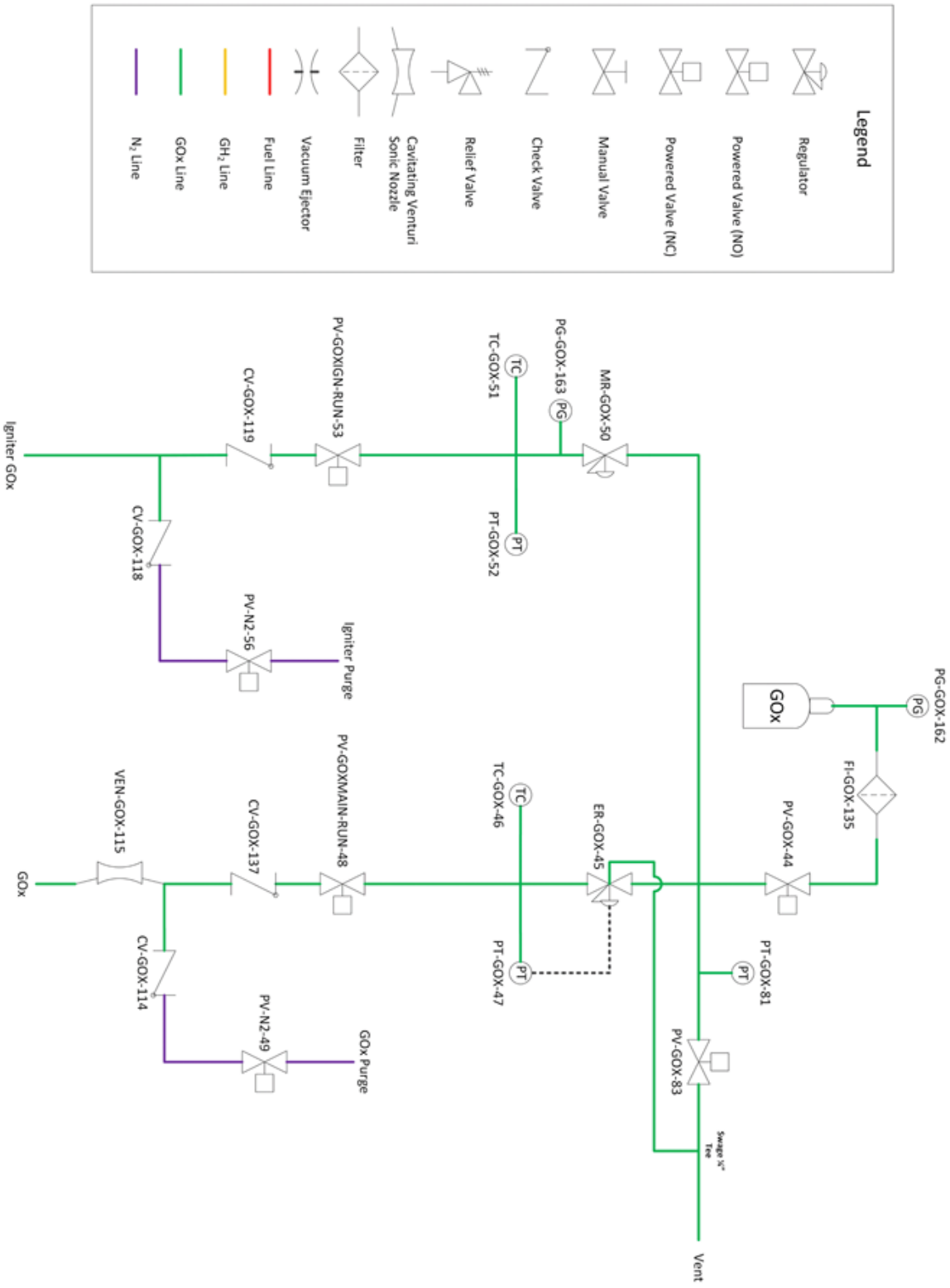

Figure C.2 Gaseous Oxygen Plumbing & Instrumentation Diagram

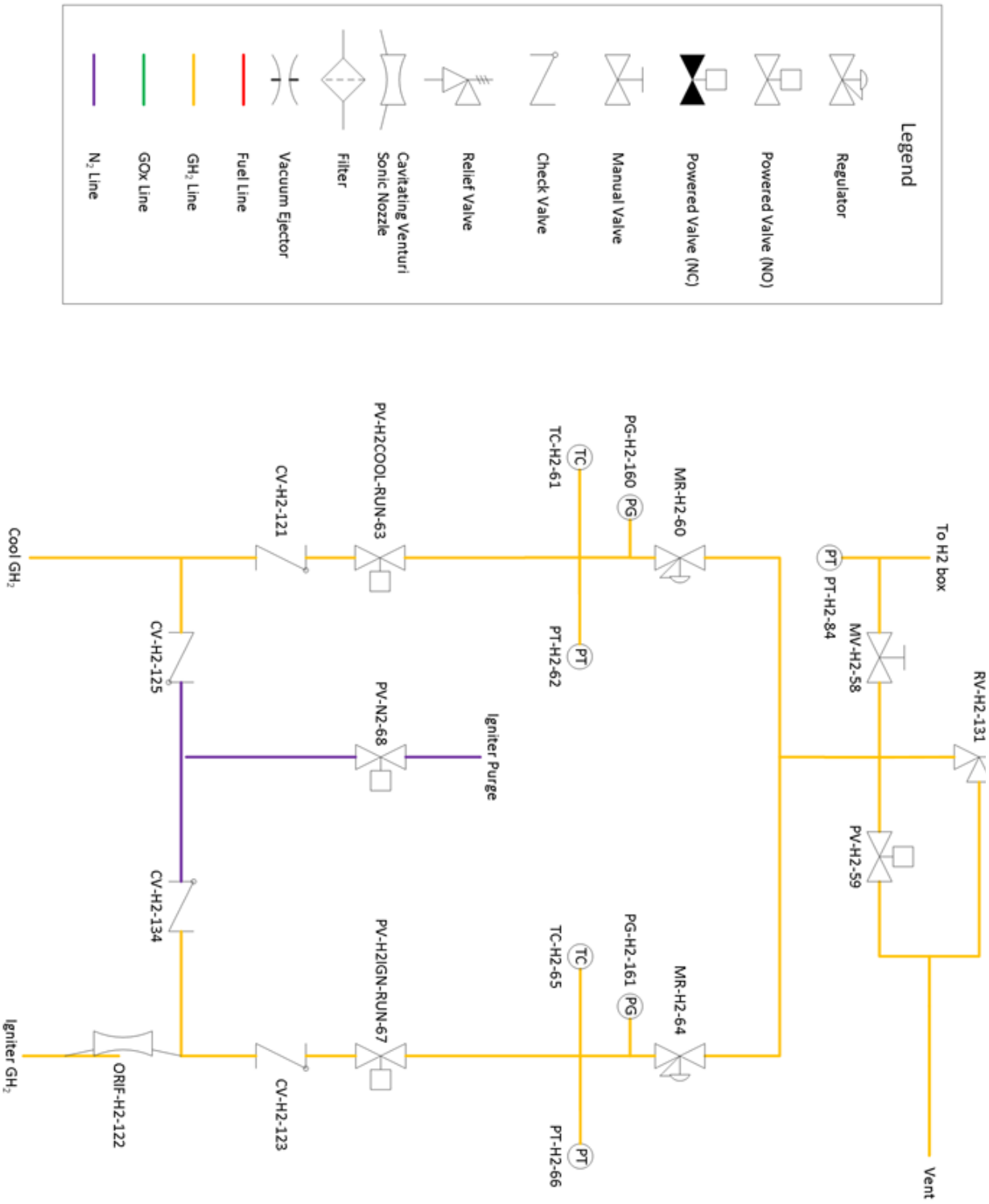

Figure C.3 Gaseous Hydrogen Plumbing & Instrumentation Diagram

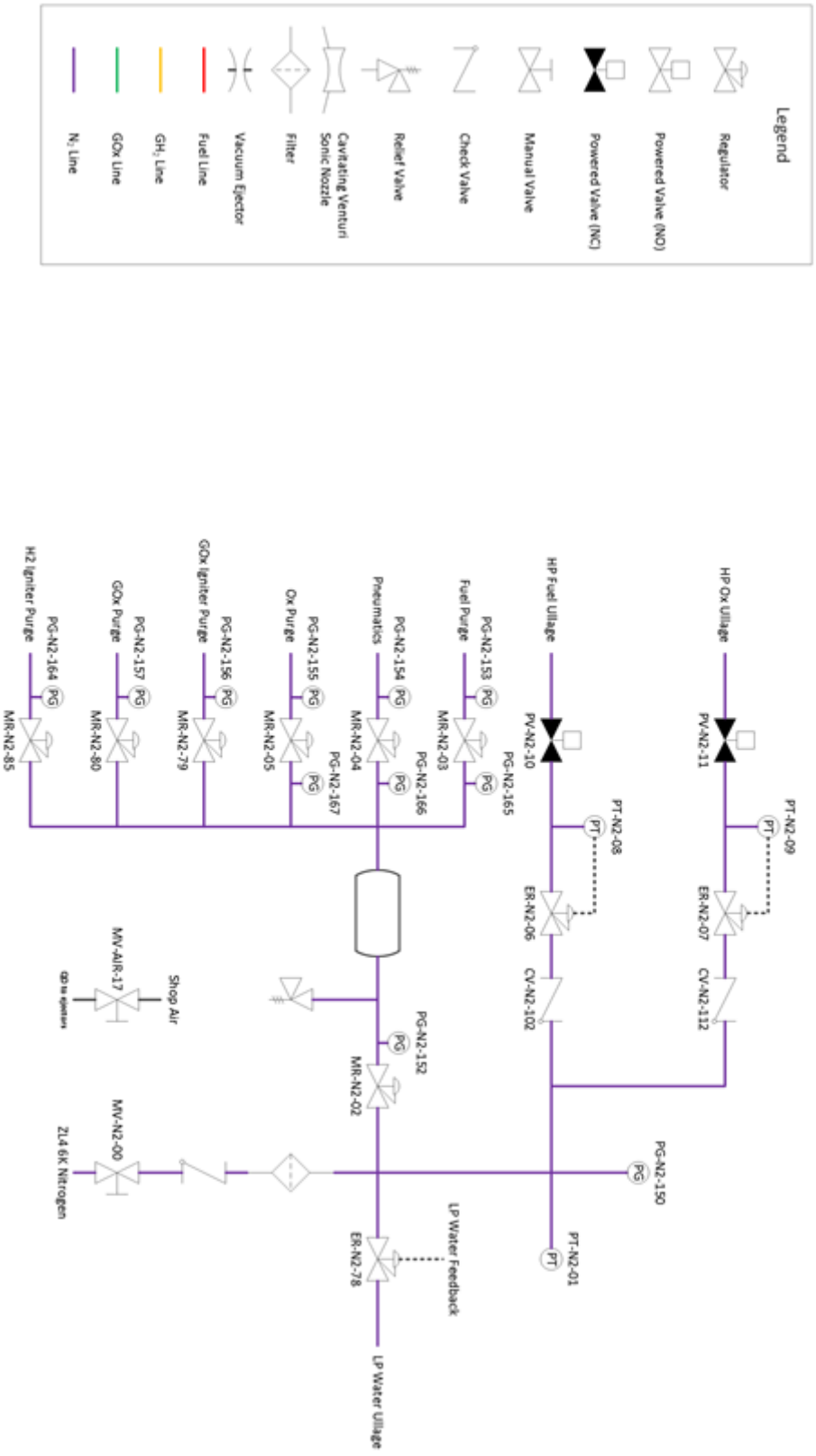

Figure C.4 Gaseous Nitrogen Plumbing & Instrumentation Diagram

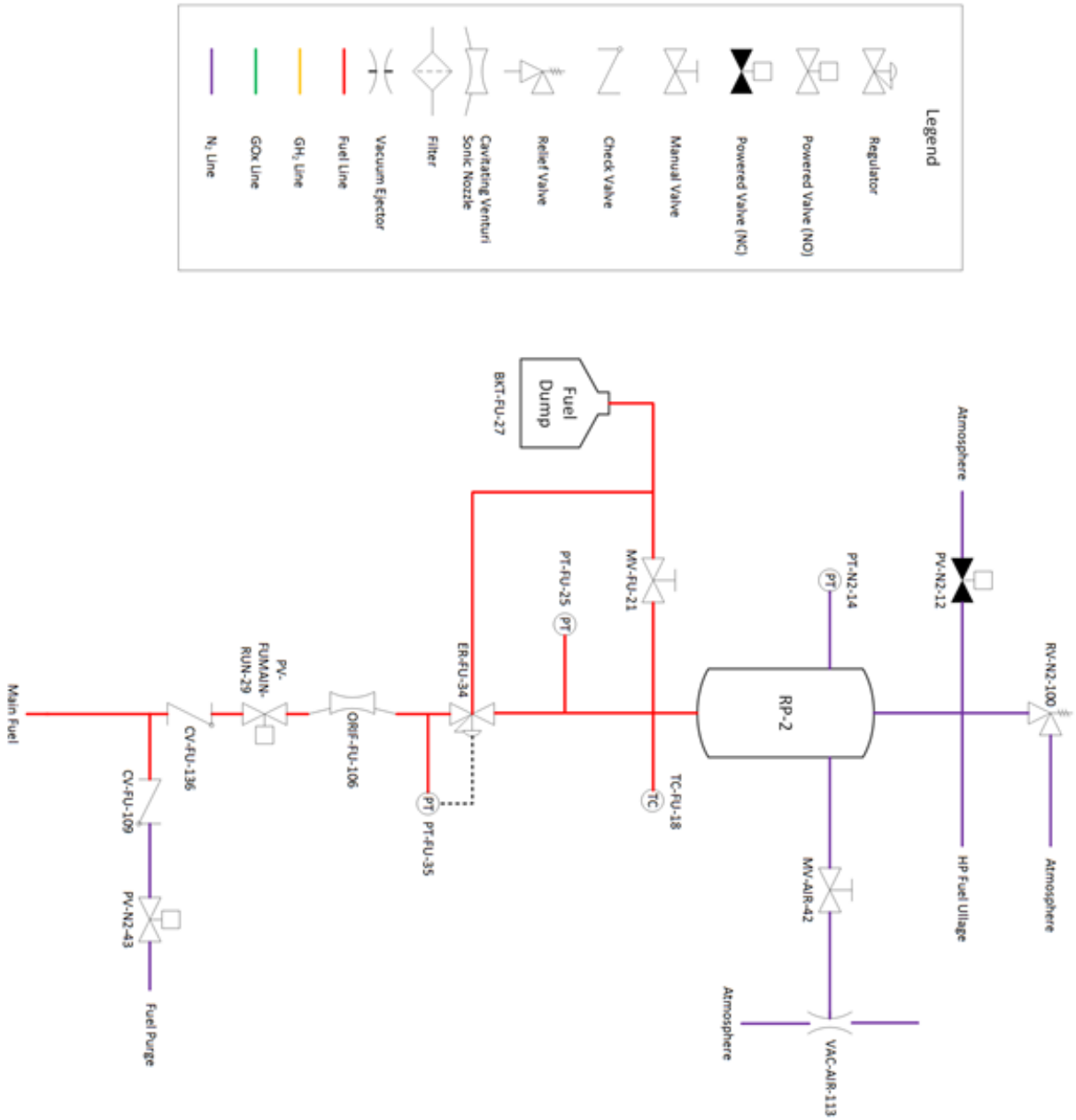

Figure C.5 Kerosene Plumbing & Instrumentation Diagram

APPENDIX D. SUPPLEMENTARY DESIGN CONSIDERATIONS

Sealing

The experiment consisted of multiple parts which required seal consideration to prevent leakage. Silicon O-rings were used for most of the parts since they are inexpensive and easy to replace. However, O-rings require machining grooves in the part for them to sit in, which can affect the mechanical design since the parts need to be thick enough for a groove and the groove diameter is constrained to only standard O-ring sizes. The O-ring groove geometry for the components were designed via the Parker O-Ring handbook [193]. Parker guidelines also suggest using double O-rings at high pressure applications. The initial operating conditions that were considered for the experiment included chamber pressures above 1000 psia and hence double O-rings were used for smaller sizes in the experiment design. This provided some headache of the manifold, injector and torch assembly design because the parts were highly integrated and changing the O-ring size for one of the parts required modifying the entire assembly. In addition, O-rings have a maximum temperature limitation, the Silicon O-rings used in the experiment had a maximum operating temperature 260°C, and placement required consideration of heat transfer. This was not an issue for most of parts, as they would only see room temperature fluid, except for torch igniter. The O-ring diameter size for the torch igniter was determined by running the heat transfer analysis at the highest heat flux condition and finding the diameter where the temperature remained below 260°C for the duration of the test.

Furthermore, a smooth sealing surface is required with O-rings, a scratch or deformity could be a potential leak path. Additionally, sealing between the combustion chamber and injector/manifold faces would have required four O-rings, in accordance with the Parker guidelines, and in turn the geometry would have needed to modify to have room to fit four concentric O-rings. Instead, for this section and for the sample chamber section, which is removed after every test and has a higher risk of getting scratched, a round graphite gasket was used. The graphite gasket can seal against a larger surface area and is not as sensitive to small scratches. It can also tolerate higher temperatures and can be placed closer to the inner chamber walls. However, the seal in graphite gasket is created by crushing the gasket via compression against the two opposite sealing surfaces and thus it can’t be reliably used again after compressive force is

relieved. A gasket can also blow out if it is not thick enough to withstand the chamber pressure. To prevent this, the gasket thickness and diameter were sized via a blowout calculation [194]. Multiple graphite gaskets were also cut from a flat graphite sheet with a waterjet at the BIDC machine shop and replaced after every test.

Bolt sizing

The experimental hardware was machined with flanges and designed to be held together with threaded bolts through all the flanges. The bolt hole pattern on the flanges was designed to be uniform to provide uniform compressive pressure on the parts. The torch assembly had 6 uniform spaced holes. However, the bolt hole pattern for the combustion and sample chamber was designed with a pattern of 4x 2 bolt holes that were 30 degrees apart so the bolts would not interfere with the measurement ports on the sample chamber.

The bolts in the experiment were sized with the approach discussed in the Mechanical Engineering Design textbook [195]. This first involved determining the bolt pre-load force and the chamber separation force. The pre-load is the tensile force that arises from tightening the bolt. A pre-load of 75% of the proof load is typically recommended for nonpermanent connections [195,196]. The proof load can be calculated from the area of the bolt and the proof strength of the bolt as:

$$F_{PBolt} = A_{bolt} S_p \tag{D.1}$$

The tensile force exerted on the bolts at pressure can be determined by calculating the chamber separation force, based on sealing surface area and chamber pressure, and scaling by the number of bolts as:

$$F_{SBolt} = \frac{A_{seal} P_c}{N_{bolts}} \tag{D.2}$$

The combined force on the bolt at pressure is the sum of the pre-load and chamber separation force contribution. The stress on the bolt can then be calculated as:

$$\sigma_{Bolt} = \frac{F_{PBolt} + F_{SBolt}}{A_{bolt}} \tag{D.3}$$

The bolt material and sizes for the torch/injector assembly and combustion/sample chamber assemblies were selected so the factor of safety with respect to the bolt proof strength was 1.5 or greater at the highest chamber pressure condition.

Furthermore, the torque spec for the preload was determined via:

$$T_{Bolt} = K_{lube} F_{PBolt} d_{Bolt} \quad \text{D.4}$$

Where the bolt torch spec is calculated from the bolt lubrication constant, desired pre-load and bolt diameter. The bolt lubrication constant accounts for friction, surface smoothness and lubrication of the fastener. A value of 0.2 is recommended by Shigley for general bolt fasteners [195].

Machining

Machinability is an important consideration for designing any hardware. The experiment design was guided in part via internal group discussion and discussion with machinists to make sure the parts were fabricable. However, the importance was not quite as realized as when I personally started machining the components. This section provides some advice that I accumulated over the course of this project on machining on a budget with the intent of aiding the design of future experiments.

If a specific material grade is not important, then the more machinable grade would make fabrication easier and cheaper. The soot experiment design required some components to be made from stainless steel, however the specific grade such as 304 or 316 was not critical as the thermal properties are similar and would have fine to use. Stainless 316 ended up being used mostly because it was on sale and cheaper than the other grades during material purchasing. Machining the stainless 316 on a lathe however required running at slower tool feed rates compared to other grades of stainless and in turn added significant amount of time. The overall time I spent to machine the stainless parts in the experiment was over 50 hours, if stainless 303 was used instead then the machining time could have been reduced by ~25%. Hence, choosing machinable material even if it's more expensive could result in significantly less machining time and end up being cheaper to manufacture.

Furthermore, it's helpful to understand how and which machining tools are used for making a part. As I discovered, a significant amount of time in machining is spent mounting the part on

the mill or lathe and setting up the tool, or making a custom tool, to machine the stock material. Speaking with the machinist for advice or learning about the tooling used can help with making an affordable machinable design. Making most of the design features machinable with just one or two tools is advantageous. If there are multiple different features, such as different diameter holes or different angles of the surfaces, then the machining time would be higher because of needing to replace tooling. So, if possible, it's advantageous to use the same features in the design. A design is also more affordable if the features can be made with standard machining tools without needing to make custom tooling. The tooling can be looked up online on various vender websites. For example, if certain diameter hole of certain depth is required, one can look up to see if there is a drill bit with a long enough shank. From one of many discussions with Toby Lamb at the Zucrow Laboratories, the recommended hole diameter to depth was within the range of 5-10. If it's larger, then the tool might wander and not produce a straight hole. This is especially true for smaller diameter holes since the drill bit has a smaller moment of inertia. Also, a thru-hole that's deeper than this criterion can be possible to machine by machining from opposite sides, but it may not be completely concentric because of variation in how the stock is mounted on opposite sides.

Complexity also adds extra time and cost, especially if the part was to experience hardware damage during test and needed to be re-machined. A part, such as the injector in my experiment, might be hard to fix and would need to be re-machined if it was to fail. Therefore, if a part has high potential to fail for reasons such as high heat flux, clogging, fracturing from overpressure, then it would be helpful to design it so re-machining a new part would be cheap. Other parts, such as a straight tube would be easy to clean up in most cases with an inside turning tool.

Additionally, if parts are personally machined then it helps to practice a certain technique on a sacrificial part before applying it to the final design piece. When I first tried machining O-ring grooves on torch tube, the tool approach into the part, along with the feeds and speeds were not optimal, which resulted in end mill shattering in the O-ring groove. The end mill was carbide tipped and carbide bits were dispersed in the machining region. Since there were carbide particles, trying to machine over it would have resulted in destruction of another endmill. Hence it was not possible to salvage the part and it needed to be thrown out and a new part started again from scratch. Machining each torch tube took about 10-15 hours of work.

REFERENCES

[1] Himansu, A., Coy, E., Sankaran, V., and Danczyk, S. Modeling of Fuel Film Cooling on Chamber Hot Wall. 2014.

[2] Edwards, T., and Meyer, M. Propellant Requirements for Future Aerospace Propulsion Systems. In *38th AIAA/ASME/SAE/ASEE Joint Propulsion Conference & Exhibit*, American Institute of Aeronautics and Astronautics, 2002.

[3] Sutton, G. P., and Biblarz, O. *Rocket Propulsion Elements*. John Wiley & Sons, 2010.

[4] Cook, R. T. *Advanced Cooling Techniques for High-Pressure Hydrocarbon-Fueled Engines*. Publication CR-159790. National Aeronautics and Space Administration, 1979.

[5] Giovanetti, A. J., Spadaccini, L. J., and Szetela, E. J. "Deposit Formation and Heat-Transfer Characteristics of Hydrocarbon Rocket Fuels." *Journal of Spacecraft and Rockets*, Vol. 22, No. 5, 1985, pp. 574–580.

[6] Giovanetti, A. J., Spadaccini, L. J., and Szetela, E. J. *Deposit Formation and Heat Transfer in Hydrocarbon Rocket Fuels*. United Technologies Corp., East Hartford, CT, 1983.

[7] Billingsley, M. C., Lyu, H. Y., and Bates, R. W. Experimental and Numerical Investigations of RP-2 Under High Heat Fluxes. Presented at the JANNAF 54th Propulsion Meeting, 2007.

[8] Kleinhenz, J. E., Deans, M. C., Stiegemeier, B. R., and Psaras, P. M. Thermal Stability of RP-2 for Hydrocarbon Boost Regenerative Cooling. Presented at the JANNAF 60th Propulsion Meeting, 2013.

[9] Mehta, R. S., Kulakhmetov, R., Pourpoint, T., Sengupta, D., Wang, H., and Himansu, A. Surface Coking in Fuel-Film Cooled Liquid Rocket Engines - Measurement and Modeling. Presented at the JANNAF Conference, Phoenix, 2016.

[10] Hernandez, R., and Mercer, S. Carbon Deposition Characteristics of LO2/HC Propellants. In *23rd Joint Propulsion Conference*, American Institute of Aeronautics and Astronautics, 1987.

[11] Abarham, M., Zamankhan, P., Hoard, J. W., Styles, D., Sluder, C. S., Storey, J. M. E., Lance, M. J., and Assanis, D. "CFD Analysis of Particle Transport in Axi-Symmetric Tube Flows under the Influence of Thermophoretic Force." *International Journal of Heat and Mass Transfer*, Vol. 61, 2013, pp. 94–105. https://doi.org/10.1016/j.ijheatmasstransfer.2013.01.071.

[12] Reza Razmavar, A., and Reza Malayeri, M. "A Simplified Model for Deposition and Removal of Soot Particles in an Exhaust Gas Recirculation Cooler." *Journal of Engineering for Gas Turbines and Power*, Vol. 138, No. 1, 2015, pp. 011505-011505–10. https://doi.org/10.1115/1.4031180.

[13] McBride, B. J., and Gordon, S. *Computer Program for Calculation of Complex Chemical Equilibrium Compositions and Applications: II*. Nationa Aeronautics and Space Administration, Office of Management, Scientific and Technical Information Program, 1996.

[14] Wang, H., Xu, R., Wang, K., Bowman, C. T., Hanson, R. K., Davidson, D. F., Brezinsky, K., and Egolfopoulos, F. N. "A Physics-Based Approach to Modeling Real-Fuel Combustion Chemistry-I. Evidence from Experiments, and Thermodynamic, Chemical Kinetic and Statistical Considerations." *Combustion and Flame*, Vol. 193, 2018, pp. 502–519.

[15] Xu, R., Wang, K., Banerjee, S., Shao, J., Parise, T., Zhu, Y., Wang, S., Movaghar, A., Lee, D. J., Zhao, R., Han, X., Gao, Y., Lu, T., Brezinsky, K., Egolfopoulos, F. N., Davidson, D. F., Hanson, R. K., Bowman, C. T., and Wang, H. "A Physics-Based Approach to Modeling Real-Fuel Combustion Chemistry – II. Reaction Kinetic Models of Jet and Rocket Fuels."

Combustion and Flame, Vol. 193, 2018, pp. 520–537. https://doi.org/10.1016/j.combustflame.2018.03.021.
[16] Celis, C., and Silva, L. F. F. da. "On the Non-Equilibrium Behavior of Fuel-Rich Hydrocarbon/Air Combustion Within Perfectly Stirred Reactors." *Combustion Science and Technology*, Vol. 189, No. 4, 2017, pp. 732–746. https://doi.org/10.1080/00102202.2016.1248239.
[17] Albrecht, B. A., Kok, J. B. W., Dijkstra, N., and Meer, T. van der. "Prediction and Measurement of the Product Gas Composition of the Ultra Rich Premixed Combustion of Natural Gas: Effects of Equivalence Ratio, Residence Time, Pressure, and Oxygen Concentration." *Combustion Science and Technology*, Vol. 181, No. 3, 2009, pp. 433–456. https://doi.org/10.1080/00102200802612351.
[18] Wang, H., Xu, R., Wang, K., Bowman, C. T., Hanson, R. K., Davidson, D. F., Brezinsky, K., and Egolfopoulos, F. N. "A Physics-Based Approach to Modeling Real-Fuel Combustion Chemistry-I. Evidence from Experiments, and Thermodynamic, Chemical Kinetic and Statistical Considerations." *Combustion and Flame*, Vol. 193, 2018, pp. 502–519.
[19] Bozzano, G., Dente, M., Faravelli, T., and Ranzi, E. "Fouling Phenomena in Pyrolysis and Combustion Processes." *Applied thermal engineering*, Vol. 22, No. 8, 2002, pp. 919–927.
[20] Schuetz, C. A., and Frenklach, M. "Nucleation of Soot: Molecular Dynamics Simulations of Pyrene Dimerization." *Proceedings of the Combustion Institute*, Vol. 29, No. 2, 2002, pp. 2307–2314.
[21] Frenklach, M., and Wang, H. Detailed Mechanism and Modeling of Soot Particle Formation. In *Soot formation in combustion*, Springer, 1994, pp. 165–192.
[22] Frenklach, M. "Reaction Mechanism of Soot Formation in Flames." *Physical Chemistry Chemical Physics*, Vol. 4, No. 11, 2002, pp. 2028–2037. https://doi.org/10.1039/B110045A.
[23] Abarham, M., Hoard, J., Assanis, D., Styles, D., Curtis, E. W., and Ramesh, N. "Review of Soot Deposition and Removal Mechanisms in EGR Coolers." *SAE International Journal of Fuels and Lubricants*, Vol. 3, No. 1, 2010, pp. 690–704.
[24] Huffman, H. D. "The Reconstruction of Aerosol Light Absorption by Particle Measurements at Remote Sites: An Independent Analysis of Data from the IMPROVE Network — II." *Atmospheric Environment*, Vol. 30, No. 1, 1996, pp. 85–99. https://doi.org/10.1016/1352-2310(95)00242-Q.
[25] Kennedy, I. M. "Models of Soot Formation and Oxidation." *Progress in Energy and Combustion Science*, Vol. 23, No. 2, 1997, pp. 95–132. https://doi.org/10.1016/S0360-1285(97)00007-5.
[26] Bockhorn, H. *Soot Formation in Combustion: Mechanisms and Models*. Springer Science & Business Media, 2013.
[27] Haynes, B. S., and Wagner, H. Gg. "Soot Formation." *Progress in Energy and Combustion Science*, Vol. 7, No. 4, 1981, pp. 229–273. https://doi.org/10.1016/0360-1285(81)90001-0.
[28] Wang, H. "Formation of Nascent Soot and Other Condensed-Phase Materials in Flames." *Proceedings of the Combustion Institute*, Vol. 33, No. 1, 2011, pp. 41–67. https://doi.org/10.1016/j.proci.2010.09.009.
[29] Wang, H., and Frenklach, M. "A Detailed Kinetic Modeling Study of Aromatics Formation in Laminar Premixed Acetylene and Ethylene Flames." *Combustion and Flame*, Vol. 110, No. 1, 1997, pp. 173–221. https://doi.org/10.1016/S0010-2180(97)00068-0.

[30] Colket, M. B., and Hall, R. J. Successes and Uncertainties in Modeling Soot Formation in Laminar, Premixed Flames. In *Soot Formation in Combustion: Mechanisms and Models* (H. Bockhorn, ed.), Springer Berlin Heidelberg, Berlin, Heidelberg, 1994, pp. 442–470.
[31] Calcote, H. F. "Mechanisms of Soot Nucleation in Flames—A Critical Review." *Combustion and Flame*, Vol. 42, 1981, pp. 215–242. https://doi.org/10.1016/0010-2180(81)90159-0.
[32] Böhm, H., and Jander, H. "PAH Formation in Acetylene–Benzene Pyrolysis." *Physical Chemistry Chemical Physics*, Vol. 1, No. 16, 1999, pp. 3775–3781. https://doi.org/10.1039/A903306H.
[33] Lindstedt, R. P., and Meyer, M. P. "A Dimensionally Reduced Reaction Mechanism for Methanol Oxidation." *Proceedings of the Combustion Institute*, Vol. 29, No. 1, 2002, pp. 1395–1402. https://doi.org/10.1016/S1540-7489(02)80171-7.
[34] Frenklach, M., Clary, D. W., Gardiner, W. C., and Stein, S. E. "Effect of Fuel Structure on Pathways to Soot." *Symposium (International) on Combustion*, Vol. 21, No. 1, 1988, pp. 1067–1076. https://doi.org/10.1016/S0082-0784(88)80337-0.
[35] Frenklach, M., and Wang, H. "Detailed Modeling of Soot Particle Nucleation and Growth." *Symposium (International) on Combustion*, Vol. 23, No. 1, 1991, pp. 1559–1566. https://doi.org/10.1016/S0082-0784(06)80426-1.
[36] Lignell, D. O. *Direct Numerical Simulation of Soot Formation and Transport in Turbulent Nonpremixed Ethylene Flames*. 2008.
[37] Johansson, K., Head-Gordon, M., Schrader, P., Wilson, K., and Michelsen, H. "Resonance-Stabilized Hydrocarbon-Radical Chain Reactions May Explain Soot Inception and Growth." *Science*, Vol. 361, No. 6406, 2018, pp. 997–1000.
[38] Zhao, B., Uchikawa, K., and Wang, H. "A Comparative Study of Nanoparticles in Premixed Flames by Scanning Mobility Particle Sizer, Small Angle Neutron Scattering, and Transmission Electron Microscopy." *Proceedings of the Combustion Institute*, Vol. 31, No. 1, 2007, pp. 851–860. https://doi.org/10.1016/j.proci.2006.08.064.
[39] Wersborg, B. L., Howard, J. B., and Williams, G. C. "Physical Mechanisms in Carbon Formation in Flames." *Fourteenth Symposium (International) on Combustion*, Vol. 14, No. 1, 1973, pp. 929–940. https://doi.org/10.1016/S0082-0784(73)80085-2.
[40] Harris, S. J., and Weiner, A. M. "Chemical Kinetics of Soot Particle Growth." *Annual Review of Physical Chemistry*, Vol. 36, No. 1, 1985, pp. 31–52. https://doi.org/10.1146/annurev.pc.36.100185.000335.
[41] Xu, F., Sunderland, P. B., and Faeth, G. M. "Soot Formation in Laminar Premixed Ethylene/Air Flames at Atmospheric Pressure." *Combustion and Flame*, Vol. 108, No. 4, 1997, pp. 471–493. https://doi.org/10.1016/S0010-2180(96)00200-3.
[42] Xu, F., Lin, K.-C., and Faeth, G. M. "Soot Formation in Laminar Premixed Methane/Oxygen Flames at Atmospheric Pressure." *Combustion and Flame*, Vol. 115, No. 1, 1998, pp. 195–209. https://doi.org/10.1016/S0010-2180(98)00017-0.
[43] Xu, F., and Faeth, G. M. "Soot Formation in Laminar Acetylene/Air Diffusion Flames at Atmospheric Pressure." *Combustion and Flame*, Vol. 125, No. 1, 2001, pp. 804–819. https://doi.org/10.1016/S0010-2180(01)00221-8.
[44] Wang, H., Du, D. X., Sung, C. J., and Law, C. K. "Experiments and Numerical Simulation on Soot Formation in Opposed-Jet Ethylene Diffusion Flames." *Symposium (International) on Combustion*, Vol. 26, No. 2, 1996, pp. 2359–2368. https://doi.org/10.1016/S0082-0784(96)80065-8.

[45] Mehta, R. S. *Detailed Modeling of Soot Formation and Turbulence–Radiation Interactions in Turbulent Jet Flames*. PhD Dissertation. Pennsylvania State University, 2008.
[46] Kee, R. J., Coltrin, M. E., Glarborg, P., and Zhu, H. *Chemically Reacting Flow: Theory, Modeling, and Simulation*. John Wiley & Sons, 2017.
[47] *Chemical-Kinetic Mechanisms for Combustion Applications*. https://web.eng.ucsd.edu/mae/groups/combustion/mechanism.html Mechanical and Aerospace Engineering (Combustion Research), University of California at San Diego (http://combustion.ucsd.edu).
[48] Sirjean, B., Dames, E., Sheen, D. A., Egolfopoulos, F. N., Wang, H., Davidson, D. F., Hanson, R. K., Pitsch, H., Bowman, C. T., and Law, C. K. "JetSurF Version 1.1." *A high-temperature chemical kinetic model of n-alkane oxidation*, 2009.
[49] Wang, H., Dames, E., Sirjean, B., Sheen, D. A., Tangko, R., Violi, A., Lai, J. Y. W., Egolfopoulos, F. N., Davidson, D. F., and Hanson, R. K. "JetSurF Version 2.0." *A High-Temperature Chemical Kinetic Model of n-alkane (up to n-dodecane), cyclohexane, and methyl-, ethyl-, n-propyl, and n-butyl-cyclohexane Oxidation at High Temperatures*, 2010.
[50] Wang, T.-S. "Thermophysics Characterization of Kerosene Combustion." *Journal of Thermophysics and Heat Transfer*, Vol. 15, No. 2, 2001, pp. 140–147.
[51] Smith, G. P., Golden, D. M., Frenklach, M., Moriarty, N. W., Eiteneer, B., Goldenberg, M., Bowman, C. T., Hanson, R. K., Song, S., and Gardner, W. C. "GRI-Mech 3.0 Mechanism." *Berkley University, USA*, 1999.
[52] Goodwin, D. G., Speth, R. L., Moffat, H. K., and Weber, B. W. *Cantera: An Object-Oriented Software Toolkit for Chemical Kinetics, Thermodynamics, and Transport Processes*. 2018.
[53] Reaction Design. "CHEMKIN Theory Manual." *San Diego, CA*, 2007.
[54] Bergman, T. L., Incropera, F. P., DeWitt, D. P., and Lavine, A. S. *Fundamentals of Heat and Mass Transfer*. John Wiley & Sons, 2011.
[55] Winterton, R. H. "Where Did the Dittus and Boelter Equation Come From?" *International journal of heat and mass transfer*, Vol. 41, Nos. 4–5, 1998, pp. 809–810.
[56] Hindmarsh, A. C., Brown, P. N., Grant, K. E., Lee, S. L., Serban, R., Shumaker, D. E., and Woodward, C. S. "SUNDIALS: Suite of Nonlinear and Differential/Algebraic Equation Solvers." *ACM Transactions on Mathematical Software (TOMS)*, Vol. 31, No. 3, 2005, pp. 363–396.
[57] Jones, E., Oliphant, T., Peterson, P., and others. *SciPy: Open Source Scientific Tools for Python*. 2001.
[58] Virtanen, P., Gommers, R., Oliphant, T. E., Haberland, M., Reddy, T., Cournapeau, D., Burovski, E., Peterson, P., Weckesser, W., Bright, J., van der Walt, S. J., Brett, M., Wilson, J., Jarrod Millman, K., Mayorov, N., Nelson, A. R. J., Jones, E., Kern, R., Larson, E., Carey, C., Polat, İ., Feng, Y., Moore, E. W., Vand erPlas, J., Laxalde, D., Perktold, J., Cimrman, R., Henriksen, I., Quintero, E. A., Harris, C. R., Archibald, A. M., Ribeiro, A. H., Pedregosa, F., van Mulbregt, P., and Contributors, S. 1. 0. "SciPy 1.0–Fundamental Algorithms for Scientific Computing in Python." *arXiv e-prints*, 2019, p. arXiv:1907.10121.
[59] Byrne, G. D., and Hindmarsh, A. C. "A Polyalgorithm for the Numerical Solution of Ordinary Differential Equations." *ACM Trans. Math. Softw.*, Vol. 1, No. 1, 1975, pp. 71–96. https://doi.org/10.1145/355626.355636.
[60] Turns, S. R. "An Introduction to Combustion," Second Edition, McGrew-Hill, New York." 2006.

[61] Molin, P., and Gervais, P. “Convergence of a Series of Well-Stirred Reactors to Plug-Flow Reactor.” *AIChE Journal*, Vol. 41, No. 5, 1995, pp. 1346–1348. https://doi.org/10.1002/aic.690410533.
[62] Foelsche, R. O., Keen, J. M., Solomon, W. C., Buckley, P. L., and Corporan, E. “Nonequilibrium Combustion Model for Fuel-Rich Gas Generators.” *Journal of Propulsion and Power*, Vol. 10, No. 4, 1994, pp. 461–472.
[63] Yu, J., and Lee, C. “Prediction of Non-Equilibrium Kinetics of Fuel-Rich Kerosene/LOX Combustion in Gas Generator.” *Journal of Mechanical Science and Technology*, Vol. 21, No. 8, 2007, pp. 1271–1283. https://doi.org/10.1007/BF03179044.
[64] Song, E., and Song, J. “Modeling of Kerosene Combustion under Fuel-Rich Conditions.” *Advances in Mechanical Engineering*, Vol. 9, No. 7, 2017, p. 1687814017711388. https://doi.org/10.1177/1687814017711388.
[65] Ingebo, R. D. *Drop-Size Distributions for Impinging-Jet Breakup in Airstreams Simulating the Velocity Conditions in Rocket Combustors*. National Advisory Committee for Aeronautics, Lewis Flight Propulsion Lab, 1958.
[66] Magee, J. W., Bruno, T. J., Friend, D. G., Huber, M. L., Laesecke, A. R., Lemmon, E. W., McLinden, M. O., Perkins, R. A., Widegren, J. A., and others. *Thermophysical Properties Measurements and Models for Rocket Propellant RP-1: Phase I*. 2007.
[67] Lefebvre, A. H., and McDonell, V. G. *Atomization and Sprays, Second Edition*. CRC Press, 2017.
[68] Williams, A. “Fundamentals of Oil Combustion.” *Progress in Energy and Combustion Science*, Vol. 2, No. 3, 1976, pp. 167–179. https://doi.org/10.1016/0360-1285(76)90011-3.
[69] Avedisian, C. T. “Recent Advances in Soot Formation from Spherical Droplet Flames at Atmospheric Pressure.” *Journal of Propulsion and Power*, Vol. 16, No. 4, 2000, pp. 628–635.
[70] Ranz, W. E., and Marshall, W. R. “Evaporation from Drops.” *Chem. eng. prog*, Vol. 48, No. 3, 1952, pp. 141–146.
[71] Lawver, B. “Testing of Fuel/Oxidizer-Rich, High-Pressure Preburners.” 1982.
[72] Schoenman, L. “Fuel/Oxidizer-Rich High-Pressure Preburners.[Staged-Combustion Rocket Engine].” 1981.
[73] Rohatgi, A. *Webplotdigitizer: Version 4.3*. 2020.
[74] Harvazinski, M. E. *Modeling Self-Excited Combustion Instabilities Using a Combination of Two- and Three-Dimensional Simulations*. PhD Thesis. 2012.
[75] Choi, Y.-H., and Merkle, C. L. “The Application of Preconditioning in Viscous Flows.” *Journal of Computational Physics*, Vol. 105, No. 2, 1993, pp. 207–223. https://doi.org/10.1006/jcph.1993.1069.
[76] Sardeshmukh, S. V., and Heister, S. D. Reacting Opposed Jets of Hypergolic Propellants MMH and RFNA. Presented at the 50th AIAA/ASME/SAE/ASEE Joint Propulsion Conference, Cleveland, OH, 2014.
[77] Mikoshiba, K., Sardeshmukh, S. V., and Heister, S. D. “On the Response of Annular Injectors to Rotating Detonation Waves.” *Shock Waves*, 2019. https://doi.org/10.1007/s00193-019-00900-8.
[78] Wilcox, D. C. “Formulation of the K-w Turbulence Model Revisited.” *AIAA Journal*, Vol. 46, No. 11, 2008, pp. 2823–2838. https://doi.org/10.2514/1.36541.
[79] McBride, B. J. Z. *NASA Glenn Coefficients for Calculating Thermodynamic Properties of Individual Species*. 2002.

[80] Mathur, S., Tondon, P., and Saxena, S. “Thermal Conductivity of Binary, Ternary and Quaternary Mixtures of Rare Gases.” *Molecular physics*, Vol. 12, No. 6, 1967, pp. 569–579.
[81] Bird, R. B., Stewart, W. E., and Lightfoot, E. N. “Transport Phenomena. 1960.” *Madison, USA*, 1960.
[82] Sardeshmukh, S. V. *Comprehensive Computational Modeling of Hypergolic Propellant Ignition*. Purdue University, West Lafayette, 2013.
[83] Bruce Munson, Rothmayer, A., and Okiishi, T. *Fundamentals of Fluid Mechanics*. 2012.
[84] Xu, R., Wang, K., Banerjee, S., Shao, J., Parise, T., Zhu, Y., Wang, S., Movaghar, A., Lee, D. J., Zhao, R., Han, X., Gao, Y., Lu, T., Brezinsky, K., Egolfopoulos, F. N., Davidson, D. F., Hanson, R. K., Bowman, C. T., and Wang, H. “A Physics-Based Approach to Modeling Real-Fuel Combustion Chemistry – II. Reaction Kinetic Models of Jet and Rocket Fuels.” *Combustion and Flame*, Vol. 193, 2018, pp. 520–537. https://doi.org/10.1016/j.combustflame.2018.03.021.
[85] Ansys, I. “CFD.” *ICEM CFD theory guide, Ansys inc*, 2015.
[86] Karypis, G., and Kumar, V. “Metis.” *A Software Package for Partitioning Unstructured Graphs, Partitioning Meshes, and Computing Fill-Reducing Orderings of Sparse Matrices, Version*, Vol. 4, 1998.
[87] Appel, J., Bockhorn, H., and Frenklach, M. “Kinetic Modeling of Soot Formation with Detailed Chemistry and Physics: Laminar Premixed Flames of C 2 Hydrocarbons.” *Combustion and Flame*, Vol. 121, No. 1, 2000, pp. 122–136.
[88] Karasevich, Y., Tanke, D., Tappe, M., Thienel, T., Wagner, H. G., and others. Soot Formation at Elevated Pressures and Carbon Concentrations in Hydrocarbon Pyrolysis. No. 25, 1994, pp. 627–634.
[89] Graham, S. “The Modelling of the Growth of Soot Particles during the Pyrolysis and Partial Oxidation of Aromatic Hydrocarbons.” *Proc. R. Soc. Lond. A*, Vol. 377, No. 1769, 1981, pp. 119–145.
[90] TAKAHASHI, F., and GLASSMAN, I. “Sooting Correlations for Premixed Flames.” *Combustion Science and Technology*, Vol. 37, Nos. 1–2, 1984, pp. 1–19. https://doi.org/10.1080/00102208408923743.
[91] Calcote, H. F., and Manos, D. M. “Effect of Molecular Structure on Incipient Soot Formation.” *Combustion and Flame*, Vol. 49, No. 1, 1983, pp. 289–304. https://doi.org/10.1016/0010-2180(83)90172-4.
[92] Kennedy, I. M., Kollmann, W., and Chen, J.-Y. “A Model for Soot Formation in a Laminar Diffusion Flame.” *Combustion and Flame*, Vol. 81, No. 1, 1990, pp. 73–85. https://doi.org/10.1016/0010-2180(90)90071-X.
[93] Leung, K. M., Lindstedt, R. P., and Jones, W. P. “A Simplified Reaction Mechanism for Soot Formation in Nonpremixed Flames.” *Combustion and Flame*, Vol. 87, No. 3, 1991, pp. 289–305. https://doi.org/10.1016/0010-2180(91)90114-Q.
[94] Guo 1, H., Liu, F., and Smallwood, G. J. “Soot and NO Formation in Counterflow Ethylene/Oxygen/Nitrogen Diffusion Flames.” *Combustion Theory and Modelling*, Vol. 8, No. 3, 2004, pp. 475–489. https://doi.org/10.1088/1364-7830/8/3/003.
[95] Frenklach, M. “Method of Moments with Interpolative Closure.” *Chemical Engineering Science*, Vol. 57, No. 12, 2002, pp. 2229–2239. https://doi.org/10.1016/S0009-2509(02)00113-6.
[96] Balthasar, M., and Kraft, M. “A Stochastic Approach to Calculate the Particle Size Distribution Function of Soot Particles in Laminar Premixed Flames.” *Combustion and*

Flame, Vol. 133, No. 3, 2003, pp. 289–298. https://doi.org/10.1016/S0010-2180(03)00003-8.
[97] Mitchell, P., and Frenklach, M. "Particle Aggregation with Simultaneous Surface Growth." *Phys. Rev. E*, Vol. 67, No. 6, 2003, p. 061407. https://doi.org/10.1103/PhysRevE.67.061407.
[98] Devore, J. L. *Probability and Statistics for Engineering and the Sciences*. Cengage learning, 2011.
[99] Seinfeld, J. H., Pandis, S. N., and Noone, K. "Atmospheric Chemistry and Physics: From Air Pollution to Climate Change." *Physics Today*, Vol. 51, 1998, p. 88.
[100] "The Mechanics of Aerosols. By N. A. Fuchs. Translated by R. E. Daisley and Marina Fuchs; Edited by C. N. Davies. London (Pergamon Press), 1964. Pp. Xiv, 408; 82 Figures; 40 Tables. £6." *Quarterly Journal of the Royal Meteorological Society*, Vol. 91, No. 388, 1965, pp. 249–249. https://doi.org/10.1002/qj.49709138822.
[101] Lindstedt, R. P., and Louloudi, S. A. "Joint-Scalar Transported PDF Modeling of Soot Formation and Oxidation." *Proceedings of the Combustion Institute*, Vol. 30, No. 1, 2005, pp. 775–783. https://doi.org/10.1016/j.proci.2004.08.080.
[102] Frenklach, M., and Harris, S. J. "Aerosol Dynamics Modeling Using the Method of Moments." *Journal of Colloid and Interface Science*, Vol. 118, No. 1, 1987, pp. 252–261. https://doi.org/10.1016/0021-9797(87)90454-1.
[103] Jullien, R., and Botet, R. "Aggregation and Fractal Aggregates." *Ann. Telecomm.*, Vol. 41, 1987, p. 343 (short version).
[104] Kazakov, A., and Frenklach, M. "Dynamic Modeling of Soot Particle Coagulation and Aggregation: Implementation with the Method of Moments and Application to High-Pressure Laminar Premixed Flames." *Combustion and Flame*, Vol. 114, Nos. 3–4, 1998, pp. 484–501.
[105] Wang, E., Zhang, Q., Shen, B., Zhang, G., Lu, X., Wu, Q., and Wang, Y. Intel Math Kernel Library. In *High-Performance Computing on the Intel® Xeon Phi™*, Springer, 2014, pp. 167–188.
[106] Adhikari, S., Sayre, A., and Chandy, A. J. "A Hybrid Newton/Time Integration Approach Coupled to Soot Moment Methods for Modeling Soot Formation and Growth in Perfectly-Stirred Reactors." *Combustion Science and Technology*, Vol. 188, No. 8, 2016, pp. 1262–1282. https://doi.org/10.1080/00102202.2016.1177035.
[107] Guha, A. "Transport and Deposition of Particles in Turbulent and Laminar Flow." *Annual Review of Fluid Mechanics*, Vol. 40, No. 1, 2008, pp. 311–341. https://doi.org/10.1146/annurev.fluid.40.111406.102220.
[108] Mehravaran, M., and Brereton, G. Modeling of Thermophoretic Soot Deposition and Stabilization on Cooled Surfaces. 2011.
[109] Abarham, M. "A Combined Modeling and Experimental Investigation of Nan-Particulate Transport in Non-Isothermal Turbulent Internal Flows." 2011.
[110] Hamaker, H. C. "The London—van Der Waals Attraction between Spherical Particles." *Physica*, Vol. 4, No. 10, 1937, pp. 1058–1072. https://doi.org/10.1016/S0031-8914(37)80203-7.
[111] Talbot, L., Cheng, R. K., Schefer, R. W., and Willis, D. R. "Thermophoresis of Particles in a Heated Boundary Layer." *Journal of Fluid Mechanics*, Vol. 101, No. 4, 1980, pp. 737–758. https://doi.org/10.1017/S0022112080001905.
[112] Kim, J. H., Mulholland, G. W., Kukuck, S. R., and Pui, D. Y. "Slip Correction Measurements of Certified PSL Nanoparticles Using a Nanometer Differential Mobility

Analyzer (Nano-DMA) for Knudsen Number from 0.5 to 83." *Journal of Research of the National Institute of Standards and technology*, Vol. 110, No. 1, 2005, p. 31.
[113] Batchelor, G. K., and Shen, C. "Thermophoretic Deposition of Particles in Gas Flowing over Cold Surfaces." *Journal of Colloid and Interface Science*, Vol. 107, No. 1, 1985, pp. 21–37. https://doi.org/10.1016/0021-9797(85)90145-6.
[114] Friedlander, S. K. *Smoke, Dust, and Haze*. Oxford university press New York, 2000.
[115] Nishiwaki, K. Unsteady Thermal Behavior of Engine Combustion Chamber Deposits. 1988.
[116] Gnielinski, V. "New Equations for Heat and Mass Transfer in Turbulent Pipe and Channel Flow." *Int. Chem. Eng.*, Vol. 16, No. 2, 1976, pp. 359–368.
[117] Petukhov, B. *Advances in Heat Transfer, Eds. Irvine, TF and Hartnett, JP, Vol. 6*. Academic Press, New York, 1970.
[118] Einstein, A. "On the Motion of Small Particles Suspended in Liquids at Rest Required by the Molecular-Kinetic Theory of Heat." *Annalen der physik*, Vol. 17, 1905, pp. 549–560.
[119] Berger, F. P., and Hau, K.-F. F.-L. "Mass Transfer in Turbulent Pipe Flow Measured by the Electrochemical Method." *International Journal of Heat and Mass Transfer*, Vol. 20, No. 11, 1977, pp. 1185–1194. https://doi.org/10.1016/0017-9310(77)90127-2.
[120] von Zedtwitz, P., Lipiński, W., and Steinfeld, A. "Numerical and Experimental Study of Gas–Particle Radiative Heat Exchange in a Fluidized-Bed Reactor for Steam-Gasification of Coal." *Fluidized Bed Applications*, Vol. 62, No. 1, 2007, pp. 599–607. https://doi.org/10.1016/j.ces.2006.09.027.
[121] Qiao, L., Xu, J., Sane, A., and Gore, J. "Multiphysics Modeling of Carbon Gasification Processes in a Well-Stirred Reactor with Detailed Gas-Phase Chemistry." *Combustion and Flame*, Vol. 159, No. 4, 2012, pp. 1693–1707. https://doi.org/10.1016/j.combustflame.2011.12.002.
[122] Xu, J. "Coal Gasification for Fuel Synthesis: Multiphysics Modeling and New Concepts." 2014.
[123] Guo, Y. C., Chan, C. K., and Lau, K. S. "Numerical Studies of Pulverized Coal Combustion in a Tubular Coal Combustor with Slanted Oxygen Jet☆." *Fuel*, Vol. 82, No. 8, 2003, pp. 893–907. https://doi.org/10.1016/S0016-2361(02)00367-8.
[124] Brown, N. J., Revzan, K. L., and Frenklach, M. "Detailed Kinetic Modeling of Soot Formation in Ethylene/Air Mixtures Reacting in a Perfectly Stirred Reactor." *Symposium (International) on Combustion*, Vol. 27, No. 1, 1998, pp. 1573–1580. https://doi.org/10.1016/S0082-0784(98)80566-3.
[125] Kazakov, A., Wang, H., and Frenklach, M. "Detailed Modeling of Soot Formation in Laminar Premixed Ethylene Flames at a Pressure of 10 Bar." *Combustion and Flame*, Vol. 100, No. 1, 1995, pp. 111–120. https://doi.org/10.1016/0010-2180(94)00086-8.
[126] Appel, J., Bockhorn, H., and Frenklach, M. "Kinetic Modeling of Soot Formation with Detailed Chemistry and Physics: Laminar Premixed Flames of C 2 Hydrocarbons." *Combustion and Flame*, Vol. 121, No. 1, 2000, pp. 122–136.
[127] Vaughn, C. B. *Formation of Soot and Polycyclic Aromatic Hydrocarbons in a Jet-Stirred Reactor*. PhD Thesis. Massachusetts Institute of Technology, 1988.
[128] Heidermann, T., Jander, H., and Wagner, H. G. "Soot Particles in Premixed C 2 H 4–Air-Flames at High Pressures (P= 30–70 Bar)." *Physical Chemistry Chemical Physics*, Vol. 1, No. 15, 1999, pp. 3497–3502.

[129] 2017b. *Matlab Partial Differential Equation Toolbox*. The MathWorks, Inc., Natick, Massachussets.
[130] White, G. K., and Collocott, S. J. "Heat Capacity of Reference Materials: Cu and W." *Journal of Physical and Chemical Reference Data*, Vol. 13, No. 4, 1984, pp. 1251–1257. https://doi.org/10.1063/1.555728.
[131] Abu-Eishah, S. I. "Correlations for the Thermal Conductivity of Metals as a Function of Temperature." *International Journal of Thermophysics*, Vol. 22, No. 6, 2001, pp. 1855–1868. https://doi.org/10.1023/A:1013155404019.
[132] Franssen, J.-M., and Real, P. V. *Fire Design of Steel Structures: Eurocode 1: Actions on Structures; Part 1-2: General Actions–Actions on Structures Exposed to Fire; Eurocode 3: Design of Steel Structures; Part 1-2: General Rules–Structural Fire Design*. John Wiley & Sons, 2012.
[133] Ellis, D., Keller, D., and Nathal, M. "Thermophysical Properties of GRCop-84." 2000.
[134] Bartz, D. R. "Survey of the Relationship between Theory and Experiment for Convective Heat Transfer from Rocket Combustion Gases." 1968.
[135] Olson, D. B., and Madronich, S. "The Effect of Temperature on Soot Formation in Premixed Flames." *Combustion and Flame*, Vol. 60, No. 2, 1985, pp. 203–213. https://doi.org/10.1016/0010-2180(85)90008-2.
[136] Langenkamp, P. N., van Oijen, J. A., Levinsky, H. B., and Mokhov, A. V. "Growth of Soot Volume Fraction and Aggregate Size in 1D Premixed C2H4/Air Flames Studied by Laser-Induced Incandescence and Angle-Dependent Light Scattering." *Journal of Combustion*, Vol. 2018, 2018, p. 13.
[137] Prado, G. P., Lee, M. L., Hites, R. A., Hoult, D. P., and Howard, J. B. "Soot and Hydrocarbon Formation in a Turbulent Diffusion Flame." *Symposium (International) on Combustion*, Vol. 16, No. 1, 1977, pp. 649–661. https://doi.org/10.1016/S0082-0784(77)80360-3.
[138] Savage, P. E., Gopalan, S., Mizan, T. I., Martino, C. J., and Brock, E. E. "Reactions at Supercritical Conditions: Applications and Fundamentals." *AIChE Journal*, Vol. 41, No. 7, 1995, pp. 1723–1778.
[139] Gülder, Ö. L., Intasopa, G., Joo, H. I., Mandatori, P. M., Bento, D. S., and Vaillancourt, M. E. "Unified Behaviour of Maximum Soot Yields of Methane, Ethane and Propane Laminar Diffusion Flames at High Pressures." *Combustion and Flame*, Vol. 158, No. 10, 2011, pp. 2037–2044. https://doi.org/10.1016/j.combustflame.2011.03.010.
[140] Mathis, U., Mohr, M., Kaegi, R., Bertola, A., and Boulouchos, K. "Influence of Diesel Engine Combustion Parameters on Primary Soot Particle Diameter." *Environmental Science & Technology*, Vol. 39, No. 6, 2005, pp. 1887–1892. https://doi.org/10.1021/es049578p.
[141] Will, S., Schraml, S., and Leipertz, A. "Two-Dimensional Soot-Particle Sizing by Time-Resolved Laser-Induced Incandescence." *Optics Letters*, Vol. 20, No. 22, 1995, pp. 2342–2344. https://doi.org/10.1364/OL.20.002342.
[142] Kulakhmetov, R. F., and Pourpoint, T. L. Numerical Investigation of Bulk Velocity and Pressure on Near Wall Chemistry in Fuel Rich RP-2/GOX Combustion. Presented at the AIAA Propulsion and Energy 2019 Forum, Indianapolis, IN, 2019.
[143] Kulakhmetov, R. F., and Pourpoint, T. L. 1D Plug Flow Reactor Modeling Approach of Soot Formation and Deposition in a Fuel Rich Kerosene Combustor. In *AIAA Scitech 2020 Forum*.

[144] Kulakhmetov, R. F., and Pourpoint, T. L. Preliminary Modeling Approach of Carbon Deposits in Fuel Rich RP-2/GOX Combustion at Rocket Conditions. Presented at the AIAA Scitech 2019 Forum, San Diego, CA, 2019.
[145] Kulakhmetov, R. F., Gabl, J. R., and Pourpoint, T. L. Design, Analysis and Testing of a Low Cost Hydrogen/Oxygen Augmented Spark Igniter for Kerosene Ignition. Presented at the AIAA Propulsion and Energy 2020 Forum, 2020.
[146] Ellis, D. L. *GRCop-84: A High-Temperature Copper Alloy for High-Heat-Flux Applications*. NASA Glenn Research Center, 2005.
[147] Sanchez, T. "Experimental Study of a Kerosene Fuelled Internal Combustion Engine." *A disserta-tion of the degree of Master, Lausanne: Industrial Energy Systems Laboratory of the Federal Institute of Technology in Lausanne*, 2008.
[148] Moesl, K. G., Vollmer, K. G., Sattelmayer, T., Eckstein, J., and Kopecek, H. "Experimental Study on Laser-Induced Ignition of Swirl-Stabilized Kerosene Flames." *Journal of Engineering for Gas Turbines and Power*, Vol. 131, No. 021501, 2008. https://doi.org/10.1115/1.2981181.
[149] Hooper Peter. "Experimental Experience of Cold Starting a Spark Ignition UAV Engine Using Low Volatility Fuel." *Aircraft Engineering and Aerospace Technology*, Vol. 89, No. 1, 2017, pp. 106–111. https://doi.org/10.1108/AEAT-09-2014-0137.
[150] Suhy, P. J., Evers, L. W., Morgan, E. J., and Wank, J. E. The Feasibility of a Kerosene Fueled Spark Ignited Two-Stroke Engine. 1991.
[151] Singh, R., and McChesney, R. Development of Multi-Fuel Spark Ignition Engine. 2004.
[152] Repas, G. A. "Hydrogen-Oxygen Torch Ignitor." 1994.
[153] Helderman, D. *Measurement and Analysis in a Subscale Rocket Combustor*. Purdue University, 2009.
[154] Helderman, D. PURDUE IGNITOR DESIGN AND OPERATIONS MANUAL.
[155] Lim, D. *Experimental Studies of Liquid Injector Response and Wall Heat Flux in a Rotating Detonation Rocket Engine*. Purdue University Graduate School, 2019.
[156] Gejji, R. M. *An Experimental Investigation of a Hydrogen Oxygen Flame Steam Generator*. Purdue University, 2011.
[157] Fortin, F.-A., Rainville, F.-M. D., Gardner, M.-A., Parizeau, M., and Gagné, C. "DEAP: Evolutionary Algorithms Made Easy." *Journal of Machine Learning Research*, Vol. 13, 2012, pp. 2171–2175.
[158] Paschen, F. "Ueber Die Zum Funkenübergang in Luft, Wasserstoff Und Kohlensäure Bei Verschiedenen Drucken Erforderliche Potentialdifferenz." *Annalen der Physik*, Vol. 273, No. 5, 1889, pp. 69–96. https://doi.org/10.1002/andp.18892730505.
[159] Nugent, N. J. *Breakdown Voltage Determination of Gaseous and near Cryogenic Fluids with Application to Rocket Engine Ignition*. PhD Thesis. Purdue University, 2009.
[160] Ó Conaire, M., Curran, H. J., Simmie, J. M., Pitz, W. J., and Westbrook, C. K. "A Comprehensive Modeling Study of Hydrogen Oxidation." *International journal of chemical kinetics*, Vol. 36, No. 11, 2004, pp. 603–622.
[161] Ben-Yakar, A., and Hanson, R. K. "Cavity Flame-Holders for Ignition and Flame Stabilization in Scramjets: An Overview." *Journal of Propulsion and Power*, Vol. 17, No. 4, 2001, pp. 869–877. https://doi.org/10.2514/2.5818.
[162] Repas, G. A. "Hydrogen-Oxygen Torch Ignitor." 1994.
[163] Helderman, D. *Measurement and Analysis in a Subscale Rocket Combustor*. Purdue University, 2009.

[164] Vladimir Bazarov. AAE690A Liquid Propellant Rocket Engine Injectors. Purdue University, , 2006.
[165] Cheng, G. C., Davis, R. R., Johnson, C. W., Muss, J. A., and Griesen, D. A. *Development of GOX/Kerosene Swirl-Coaxial Injector Technology*. SIERRA ENGINEERING INC CARSON CITY NV, 2003.
[166] Kim, S., Khil, T., Kim, D., and Yoon, Y. "Effect of Geometric Parameters on the Liquid Film Thickness and Air Core Formation in a Swirl Injector." *Measurement Science and Technology*, Vol. 20, No. 1, 2008, p. 015403.
[167] Salgues, D., Mouis, A.-G., Lee, S.-Y., Kalitan, D., Pal, S., and Santoro, R. Shear and Swirl Coaxial Injector Studies of LOX/GCH4 Rocket Combustion Using Non-Intrusive Laser Diagnostics. 2006.
[168] Davis, D. W. *On the Behavior of a Shear-Coaxial Jet, Spanning Sub-to Supercritical Pressures, with and without an Externally Imposed Transverse Acoustic Field*. Pennsylvania State University, University Park, 2006.
[169] Mehegan, P. F., Campbell, D. T., and Scheuerman, C. H. *Investigation of Gas-Augmented Injectors*. Rocketdyne, a division of North American Rockwell Corporation, 1970.
[170] Gill, G. S., and Nurick, W. H. "Liquid Rocket Engine Injectors." 1976.
[171] Mehegan, P. F. "Two-Stage Bipropellant Injection System Studies Final Report." 1967.
[172] Huang, D. H. H. *Design of Liquid Propellant Rocket Engines Second Edition*. 1971.
[173] Deridder, M. A., and Anderson, W. E. "Heat Flux and Pressure Profiles in an Oxygen/Hydrogen Multielement Rocket Combustor." *Journal of Propulsion and Power*, Vol. 26, No. 4, 2010, pp. 696–705.
[174] *High-Temperature Characteristics of Stainless Steels*. American Iron and Steel Institute.
[175] Meters, A. S. C. for the M. of F. F. U. S. B. P. O. *Measurement of Fluid Flow Using Small Bore Precision Orifice Meters*. American Society of Mechanical Engineers, 1995.
[176] Ghassemi, H., and Fasih, H. F. "Application of Small Size Cavitating Venturi as Flow Controller and Flow Meter." *Flow Measurement and Instrumentation*, Vol. 22, No. 5, 2011, pp. 406–412. https://doi.org/10.1016/j.flowmeasinst.2011.05.001.
[177] Ordin, P. M. "Safety Standard for Oxygen and Oxygen Systems-Guidelines for Oxygen System Design, Materials Selection, Operations, Storage, and Transportation." *NASA NSS*, Vol. 1740, 1996.
[178] McBride, B. J., and Gordon, S. *Computer Program for Calculation of Complex Chemical Equilibrium Compositions and Applications: II*. Nationa Aeronautics and Space Administration, Office of Management, Scientific and Technical Information Program, 1996.
[179] Gülder, Ö. L., Intasopa, G., Joo, H. I., Mandatori, P. M., Bento, D. S., and Vaillancourt, M. E. "Unified Behaviour of Maximum Soot Yields of Methane, Ethane and Propane Laminar Diffusion Flames at High Pressures." *Combustion and Flame*, Vol. 158, No. 10, 2011, pp. 2037–2044. https://doi.org/10.1016/j.combustflame.2011.03.010.
[180] Litovsky, E., Shapiro, M., and Shavit, A. "Gas Pressure and Temperature Dependences of Thermal Conductivity of Porous Ceramic Materials: Part 2, Refractories and Ceramics with Porosity Exceeding 30%." *Journal of the American Ceramic Society*, Vol. 79, No. 5, 1996, pp. 1366–1376. https://doi.org/10.1111/j.1151-2916.1996.tb08598.x.
[181] CIRO, W. D., EDDINGS, E. G., and SAROFIM, A. F. "EXPERIMENTAL AND NUMERICAL INVESTIGATION OF TRANSIENT SOOT BUILDUP ON A CYLINDRICAL CONTAINER IMMERSED IN A JET FUEL POOL FIRE." *Combustion*

Science and Technology, Vol. 178, No. 12, 2006, pp. 2199–2218. https://doi.org/10.1080/00102200600626108.

[182] Sabirzyanov, A. N., Glazunov, A. I., Kirillova, A. N., and Titov, K. S. "Simulation of a Rocket Engine Nozzle Discharge Coefficient." *Russian Aeronautics*, Vol. 61, No. 2, 2018, pp. 257–264. https://doi.org/10.3103/S1068799818020150.

[183] Lance, M. J., Sluder, C. S., Wang, H., and Storey, J. M. E. Direct Measurement of EGR Cooler Deposit Thermal Properties for Improved Understanding of Cooler Fouling. 2009.

[184] Collier, J. G., and Thome, J. R. *Convective Boiling and Condensation, 3rd Edn. Clarendon*. Oxford, 1996.

[185] El-Asrag, H. A. E.-R. *Large Eddy Simulation Subgrid Model for Soot Prediction*. PhD Thesis. Georgia Institute of Technology, 2007.

[186] Harris, S. J., and Kennedy, I. M. "The Coagulation of Soot Particles with van Der Waals Forces." *Combustion Science and Technology*, Vol. 59, Nos. 4–6, 1988, pp. 443–454. https://doi.org/10.1080/00102208808947110.

[187] Pratsinis, S. E. "Simultaneous Nucleation, Condensation, and Coagulation in Aerosol Reactors." *Journal of Colloid and Interface Science*, Vol. 124, No. 2, 1988, pp. 416–427. https://doi.org/10.1016/0021-9797(88)90180-4.

[188] Hwang, J. Y., and Chung, S. H. "Growth of Soot Particles in Counterflow Diffusion Flames of Ethylene." *Combustion and Flame*, Vol. 125, No. 1, 2001, pp. 752–762. https://doi.org/10.1016/S0010-2180(00)00234-0.

[189] Rezvan, K. L., Brown, N. J., and Frenklach, M. *Soot Formation Codes*.

[190] Dasgupta, A. K. "Numerical Simulation of Axisymmetric Laminar Diffusion Flames with Soot." 2015.

[191] Netzell, K., Lehtiniemi, H., and Mauss, F. "Calculating the Soot Particle Size Distribution Function in Turbulent Diffusion Flames Using a Sectional Method." *Proceedings of the Combustion Institute*, Vol. 31, No. 1, 2007, pp. 667–674. https://doi.org/10.1016/j.proci.2006.08.081.

[192] Netzell, K. *Development and Applications of Detailed Kinetic Models for the Soot Particle Size Distribution Function*. PhD Thesis. Lund University, 2006.

[193] Parker, O., and Handbook, R. "ORD 5700." *Parker Hannifin Corporation, Cleveland, Ohio*, 2007.

[194] Wacker, R. *Prevent Gasket Blowout—What's Most Important?* Pumps & Systems, http://www.fluidsealing.com/sealingsense/Apr14.pdf, 2014, pp. 80–82.

[195] Shigley, J. E. *Shigley's Mechanical Engineering Design*. Tata McGraw-Hill Education, 2011.

[196] "Fastener Facts." *Bowman Distribution-Barnes Group*, , 1985, p. 90.

VITA

Rufat F. Kulakhmetov

Education

Purdue University, School of Aeronautics and Astronautics *West Lafayette, IN*
PhD in **Aeronautics and Astronautics,** Minor in Aerodynamics 2016 – 2020
- Advisor: Dr. **Timothée Pourpoint** ***GPA:*** *3.76/4.00*
- **Dissertation**: Measurement and Modeling of Soot Formation and Deposition in Fuel Rich High Pressure Kerosene Combustion
    - *Supported by **NASA Space Technology Research Fellowship***

M.S in **Aeronautics and Astronautics,** Minor in Aerodynamics 2014 – 2016
- Advisor: Dr. **Timothée Pourpoint** ***GPA****:3.73/4.00*
- Research Project: Measurement of Surface Coking in Fuel Film Cooled Liquid Rocket Engines

University of Connecticut, School of Mechanical Engineering *Storrs, CT*
B.S in **Mechanical Engineering** 2011-2014
- Developed and tested a Cold Gas RCS thruster for senior design ***GPA****: 3.88/4.00*
- Advisor**:** Dr. **Brice Cassenti**
- Graduated with Magna Cum Laude

Research and Work Experience

Purdue University *West Lafayette, IN*
PhD Candidate/NASA Space Technology Research Fellow - Maurice J**. Zucrow** Laboratories **Fall 2016 – Present**
- Researching fuel rich **RP-2** kerosene soot deposit via an **experimental** and **numerical** approach:
- Designed a high-pressure torch-ignited kerosene experiment in **SolidWorks,** wrote 0-D **Object-Oriented** combustion analysis codes using **Cantera** to predict/size combustor and fluid lines, and ran 2-D **reacting URANS** simulations with an in-house **CFD** code to understand experiment flow field
- Machined experimental hardware with a lathe and mill; installed high pressure **kerosene, oxygen, hydrogen** fluid system (tubes/valves/regulators); and wired/set up a **LabView** data acquisition system
- Wrote a **Fortran Method of Moments** soot formation model and coupled to **Well Stirred Reactor/Plug Flow models** using **Cantera toolbox** to predict soot deposition in a reduced order model approach
    - Predictions have been validated with profilometer measurements of soot deposit

Graduate Research Assistant – Maurice J. **Zucrow** Laboratories **Fall 2015 – Spring 2016**
- Researched **surface coking in fuel film cooled liquid rocket engines** for an Air Force Phase I STTR for my M.S.
- Developed and tested a **90% hydrogen peroxide bi-propellant dump combustor** to measure **RP-2** and **JP-8** carbon buildup
- Phase II STTR awarded based on this effort

Graduate Teaching Assistant - School of Aeronautics and Astronautics **Fall 2014 – Spring 2015**
- Reviewed and graded assignments, and held help sessions for Rocket Propulsion and Aircraft Design/Build/Test classes

Air Force Research Laboratory *Edwards, CA*
NSTRF Visiting Technologist – AFRL/RQRC Combustion Devices Branch **Summer 2019**
- Wrote a Soot Particle Distribution code in **Fortran 90** using the **Method of Moments with Interpolative Closure**
- Ran **0-D** and **1-D kinetic** simulations with **Cantera** to predict volumetric soot rates

Summer 2018
- Modeled **chemically reacting flow** via **2-D URANS** with the **Fortran** Generalized Equation and Mesh Solver **(GEMS) CFD** code
- Investigated influence of several reduced kerosene reaction mechanisms on flow-field structure

NASA Marshall Space Flight Center *Huntsville Al*

Visiting Technologist – ER36 Engine Components Development and Technology Branch **Summer 2017**

- Investigated methane engine failure via 3-D **reacting URANS/LES** calculation on NASA Pleiades supercomputer
- Generated surface meshes in **ANSA**, unstructured volumetric mesh in **AFLR3**, and solved with **Loci/Chem 3.0**

Propulsion Academy Research Assistant - *Spacecraft Propulsion Systems Department* **Summer 2013**

- Developed a **90% Hydrogen Peroxide** 10 lbf reaction control system test article for the Nano Launch 1200
- Designed thruster in SolidWorks, performed 1-D thermal and structural design analysis, performed cold flow tests of the machined article, set up and calibrated instruments including FLIR, pressure transducers, thermocouples

Aerojet Rocketdyne *Canoga Park, CA*

Graduate Intern – Systems Verification and Test Branch **Summer 2015**

- Supported planning and Functional Readiness Test (**FRT**) data review for **RS-25** engine test program.
- **Automated** FRT using **MATLAB** to reduce over 100-hour workload per test to about 1 hour.

University of Connecticut *Storrs, CT*

Undergraduate Research Assistant – Combustion and Gas Dynamics Laboratory **Spring 2012 – Spring 2014**

- Measured bluff-body stabilized flames via Particle Image Velocimetry (PIV) and Planar Laser-Induced Fluorescence (PLIF)
- Wrote image processing tools in **MATLAB** to identify flame location and shape during post-processing

Undergraduate Grader for ME5320 Graduate Compressible Flow **Spring 2014**

- Reviewed homework assignments for errors and graded problem sets

NASA Glenn Research Center *Cleveland, OH*

Undergraduate Student Research Program Intern – ER23 Combustion & Reacting Systems Branch **Summer 2012**

- Measured flame lifting and blowout limits for simple fuels in a jet co-flow burner for comparison with the Structure and Liftoff in Combustion Experiment (SLICE) on the Internal Space Station
- Applied electric fields to methane flames to characterize flame structure in 1g and refine the test matrix for the Advanced Combustion via Microgravity Experiment (ACME) on the International Space Station

NASA Goddard Space Flight Center *Greenbelt, MD*

High School INSPIRE Intern - Satellite Servicing Capabilities Office at Goddard Space Flight Center **Summer 2011**

- Formulated and constructed servo-actuated camera imaging system concepts for the Robotic Refueling Mission

Awards & Honors

NASA Space Technology Research Fellowship (2016-2020), Air Force Research Lab Challenge Coin Recipient (2018), Rocketdyne Mission Success Award (2015), American Savings Foundation Scholarship (2011-2014), University of Connecticut New England Scholar (2013), Saybrook Charitable STEM Scholarship (2012) , University of Connecticut Engineering Merit Scholarship (2012), Dean's List in the School of Engineering (2011-2013)

Activities

Purdue Space Day Activity Head (2014-2019), Zucrow Student Association Social Chair (2018-2019), AIAA Student Chapter Founder at UCONN (2012-2014), Connecticut Invention Convention Judge (2013, 2014), Civil Air Patrol (2012-2014)

Memberships

AIAA Student Member	NASA Academy Alumni Association	Tau Beta Pi Engineering Honor Society	Phi Kappa Phi National Honor Society	Alpha Lambda Delta National Honor Society

Relevant Skills and Qualifications

- Proficient with SolidWorks, Autodesk Inventor, MATLAB, Python, Cantera, Fortran, Linux
- Familiar with C++, Chemkin Pro, LabView, IcemCFD, Fluent, Star-CCM CFD, Comsol, Loci/Chem
- Experienced with chemical kinetics and reacting flow modeling
- Laboratory experience with setting up and testing liquid propellants including hydrogen peroxide, kerosene, and methane
- Basic experience with electronics, circuits, Raspberry PI and Arduino
- Fluent in Russian, Beginner in Spanish

PUBLICATIONS

Journal

- Kulakhmetov, R. F., and Pourpoint, T. L. “Boundary Layer Effects on Soot Growth Chemistry in Fuel Rich Kerosene Combustion.” Combustion Science and Technology (In Preparation)

- Kulakhmetov, R. F., and Pourpoint, T. L. “Modeling Aggregate Soot Formation in a Well Stirred Reactor.” Combustion and Flame (In Preparation)

- Kulakhmetov, R. F., and Pourpoint, T. L. “Measurement and Modeling of Soot Formation and Deposition in a Plug Flow Reactor.” Combustion and Flame (In Preparation)

- Mikoshiba K., Kulakhmetov, R. F., Pourpoint, T. L and S.D. Heister “Comparison of Soot Formation in Rotating Detonation Engines with Constant Pressure Combustion.” Combustion Science and Technology (In Preparation)

- Tinker D.C., Kulakhmetov, R. F., Pourpoint, T. L and Pitz R.W. “Design guidelines for a successful hydrogen and oxygen augmented spark torch igniter.” Combustion Science and Technology (In Preparation)

Conference

- Kulakhmetov, R. F., Gabl, J. R., and Pourpoint, T. L. Design, Analysis and Testing of a Low Cost Hydrogen/Oxygen Augmented Spark Igniter for Kerosene Ignition. Presented at the AIAA Propulsion and Energy 2020 Forum, 2020.

- Kulakhmetov, R. F., and Pourpoint, T. L. 1D Plug Flow Reactor Modeling Approach of Soot Formation and Deposition in a Fuel Rich Kerosene Combustor. Presented at the AIAA Scitech 2020 Forum, Orlando, FL, 2020.

- Kulakhmetov, R. F., and Pourpoint, T. L. Numerical Investigation of Bulk Velocity and Pressure on Near Wall Chemistry in Fuel Rich RP-2/GOX Combustion. Presented at the AIAA Propulsion and Energy 2019 Forum, Indianapolis, IN, 2019.

- Kulakhmetov, R. F., and Pourpoint, T. L. Preliminary Modeling Approach of Carbon Deposits in Fuel Rich RP-2/GOX Combustion at Rocket Conditions. Presented at the AIAA Scitech 2019 Forum, San Diego, CA, 2019

- Mehta, R. S., Kulakhmetov, R., Pourpoint, T., Sengupta, D., Wang, H., and Himansu, A. Surface Coking in Fuel-Film Cooled Liquid Rocket Engines - Measurement and Modeling. Presented at the JANNAF Conference, Phoenix, 2016.